Dissertation
submitted to the
Combined Faculties of the Natural Sciences and Mathematics
of the Ruperto-Carola-University of Heidelberg, Germany
for the degree of
Doctor of Natural Sciences

Put forward by
M.Sc. Matthäus Krantz
born in: Halle an der Saale

Oral examination: 8. July 2020

Development of a metallic magnetic calorimeter with integrated SQUID readout

Referees: Prof. Dr. Christian Enss
Prof. Dr. Maurits W. Haverkort

This thesis describes the development of a high-resolution soft X-ray detector based on metallic magnetic calorimeters (MMCs). MMCs are cryogenic, energy dispersive particle detectors which consist of a particle absorber that is thermally coupled to a paramagnetic temperature sensor. The latter is placed in a weak magnetic field, hence exhibiting a temperature dependent magnetization $M(T)$. Upon X-ray photon absorption, the rise of detector temperature causes a change of sensor magnetization, which is usually read out with a current-sensing dc-SQUID via a superconducting flux transformer. Here, an imperfect transformer matching, as well as a transformer intrinsic energy coupling losses, limit the achievable energy resolution. To challenge this limit, a novel integrated detector was developed, in which the temperature sensor is integrated into a custom-designed dc-SQUID to maximize signal coupling. A major challenge of this configuration is the Joule heating of the SQUID, since heating effects prevent cooling of the detector and thus limit its performance. For this reason, the developed 32 pixel detector makes use of a newly developed thermalization scheme for the SQUID's shunt resistors, resulting in operation temperatures below 20 mK for the detector. With this kind of detector, a baseline energy resolution of $\Delta E_{\mathrm{FWHM}} = 1.3\,\mathrm{eV}$, and $\Delta E_{\mathrm{FWHM}} = 1.8\,\mathrm{eV}$ at 5.9 keV was achieved.

Entwicklung eines metallischen magnetischen Kalorimeters mit integrierter, SQUID-basierter Sensorauslese

In dieser Arbeit wird die Entwicklung eines Teilchendetektors basierend auf metallischen magnetischen Kalorimetern (MMCs) für die hochauflösende Spektroskopie von weicher Röntgenstrahlung beschrieben. MMCs sind kryogene, energiedispersive Teilchendetektoren, welche aus einem Teilchenabsorber bestehen, der in thermischen Kontakt mit einem paramagnetischen Temperatursensor steht. Letzterer befindet sich in einem schwachen Magnetfeld, wodurch er eine temperaturabhängige Sensormagnetisierung $M(T)$ besitzt. Die Absorption eines Röntgenphotons führt zu einer Erhöhung der Detektortemperatur, und damit folglich zu einer Änderung der Sensormagnetisierung, was überlicherweise über einen supraleitenden Flusstransformator mit einem SQUID-Stromsensor ausgelesen wird. Hierbei limitieren eine unvollkommene Transformatoranpassung, sowie fundamentale Grenzen in der transformatorgekoppelten Energiesensitivität, die erreichbare Energieauflösung. Um diese Einschränkung zu beseitigen, wurde ein integrierter Detektor entwickelt, bei dem der Temperatursensor in ein spezielles dc-SQUID integriert wurde, um die Signalkopplung zu maximieren. Eine große Herausforderungen bei dieser Direktauslese ist, den Detektor auf eine ausreichend niedrige Betriebstemperatur abzukühlen, da Heizeffekte, die durch die Ströme in den SQUID Shuntwiderständen erzeugt werden, einen relativ großen Wärmeeintrag in den Detektor darstellen. Aus diesem Grund wurde für den integrierten Detektor ein neuartiges Thermalisierungskonzept entwickelt, welches es erlaubt, den Detektor unter 20 mK abzukühlen. Damit konnte eine intrinsische Energieauflösung von $\Delta E_{\mathrm{FWHM}} = 1.3\,\mathrm{eV}$, und $\Delta E_{\mathrm{FWHM}} = 1.8\,\mathrm{eV}$ bei 5.9 keV demonstriert werden.

Contents

1. Introduction

The scientific field of modern spectroscopy was pioneered by Sir Isaac Newton [New30], Joseph von Fraunhofer [Fra17], Gustav Kirchhoff and Robert Bunsen [Kir60] over the course of more than 100 years. Since then, tremendous advancements were achieved in this field of science that led to a wide range of applications, and also created instruments that allow for an investigation not only of distant astronomical phenomena, but of the quantum realm as well, fundamentally enhancing our understanding of the universe. With the application of modern spectroscopy, the boundaries of our knowledge are expanded in a multitude of natural sciences, for instance in biology [Day69, Fis02], chemistry [Lic87, Coh05], material sciences [Fel07, Liu14] and astronomy [Mer34, Cam10]. In atomic physics for example, X-ray spectroscopy is used in order to verify or refute predictions that are provided by the theory of quantum electrodynamics (QED) [Dun88]. These investigations are usually done on heavy highly charged ions (HCI) [Epp07], as the QED corrections ΔE [Lam47] to the binding energy E of bound electrons that is predicted from the Dirac-theory [Dir28] scale with $\Delta E \sim Z^4/n^3$ [Joh85]. Here Z denotes the nuclear charge and n is the principal quantum number. The thereby investigated transition energies range from the lower keV regime up to more than 100 keV. But also the X-ray spectroscopy of lighter highly charged ions with transition energies $< 10\,\text{keV}$ is of interest, for instance in order to develop astrophysical and cosmological models, as these lighter HCI's can be found in stars and their atmosphere, in near-stellar clouds, or other astrophysical environments [Gab74, Bö10]. Therefore, they are also investigated via X-ray spectroscopy in earth-bound laboratories [Sha16, Mic18]. Thus, a precise determination of the transition energy E for these research fields requires instruments with an appropriate quantum efficiency, as well as an excellent resolution.

Two types of detectors are commonly used for the X-ray spectroscopy on highly charged ions. Commercially available semiconductor based detectors have a good quantum efficiency for a wide energy bandwidth, but provide only a limited energy resolution down to 100 eV [Lut06, Aal16] in the lower keV range, that further degrades with $\sqrt{E}$. Crystal spectrometers have a very low quantum efficiency, as well as a small energy bandwidth, but provide a superior resolution down to 1 eV in the lower keV energy range [Kub14]. Highly promising contenders to these established instruments are micro-calorimeters from the field of cryogenic particle detectors. The idea behind these detectors was first proposed by F. Simon [Sim35] in 1935 and is based on measuring the temperature increase that results from the absorption of a single particle. Today, several unique concepts exist how this temperature increase is determined in modern cryogenic micro-calorimeters. Often used are semiconductor thermistors [Mos84, McC05, Kra17], transition edge sensors [Irw05, Smi12, Smi20] and metallic magnetic calorimeters [Ens00, Fle09, Kem18]. The latter are at the center of discussion in this thesis.

Metallic magnetic calorimeters (MMCs) combine the high energy bandwidth and quantum efficiency of semiconductor detectors with the excellent energy resolution of crystal spectrometers. The outstanding developments of this type of detector in the last two decades already yielded a wide range of applications for MMCs. For instance, they are used for the high resolution X-ray spectroscopy at electron beam ion traps [Geo12, Sch12] and storage rings [Hen15], or for the detection of massive high-energetic molecules [Gam16]. Furthermore, they are involved in the determination of the neutrino mass [Ale19, Vel19] as well as in meteorological precision measurements [Pau19], and are planned to contribute in future dark matter research [Arm19].

For these applications, state-of-the-art MMCs are typically operated at millikelvin temperatures and make use of a particle absorber that is in good thermal contact with a paramagnetic temperature sensor. The latter is placed in a weak magnetic field, giving rise to a temperature dependent sensor magnetization $M(T)$. Placed in close proximity to the temperature sensor is a closed superconducting pickup loop, that forms a superconducting flux transformer together with the input coil of a current sensing dc-SQUID. When $M(T)$ changes upon particle absorption, the resulting magnetic flux change $\delta\Phi$ in the pickup loop is coupled via the superconducting flux transformer into the dc-SQUID. Such a device can be described as a flux-to-voltage transducer that can achieve a quantum-limited noise performance, making it the best presently available wideband sensor for magnetic flux. Making use of this energy dispersive particle detection scheme, MMCs demonstrated a fast signal response time below 100 ns [Kem18], a close to perfect linear behavior [Kem18], as well as a record resolving power of $E/\Delta E \approx 6100$ at 60 keV [Gei19]. For the soft X-ray spectroscopy, the present day benchmark of metallic magnetic calorimeters is an energy resolution of $\Delta E_{\mathrm{FWHM}} = 1.6\,\mathrm{eV}$ for a photon energy of 5.9 keV [Kem18].

The work of this thesis focuses on the development of a new type of MMC detector, where the sensor element is integrated into a novel kind dc-SQUID, which has the potential to even surpass the current best performance of MMC detectors. For the commonly used readout scheme of this cryogenic detector, a major performance limitation can be found in the coupling between detector and dc-SQUID due to an imperfect matching of the superconducting flux transformer, as well as due to transformer intrinsic energy transfer limitations. By integrating the sensor element into the dc-SQUID, these limitations can be avoided. The main challenge for a high performance operation of such an integrated multi-pixel detector at millikelvin temperatures is the energy dissipation of the dc-SQUID. This energy, which is in the lower picowatt range, is dissipated in close proximity to the paramagnetic temperature sensor, which leads to a potential increase of the operation temperature of the detector, consequently limiting its energy resolution.

For the understanding of such an integrated detector, chapter 2 discusses the basics of metallic magnetic calorimeters. This includes their working principle, the thermodynamic properties of the particle absorber and paramagnetic temperature sensor, as well as the two already mentioned readout schemes. Furthermore, the detector response function, important noise contributions and the fundamental limit of the energy resolution is discussed. The chapter concludes with a brief overview of the state-of-the-art performance of MMCs.

The fundamentals of a dc-SQUID that is required for the development of an integrated detector are discussed in chapter 3. At first, one of their key components, the so called Josephson tunnel junction, is introduced. Afterwards, the working principle of a dc-SQUID, two common readout schemes, as well as general design considerations for such a device are discussed.

The cryogenic system that is used for detector operation is discussed in chapter 4. This chapter also includes a description of the used data acquisition system, a description of the radioactive calibration source that was used to characterize the developed detectors, as well as a depiction of the utilized data analysis method.

Important aspects that are related to the microfabrication of the dc-SQUIDs and metallic magnetic calorimeters in this thesis are discussed in chapter 5. This includes the fabrication and characterization of Josephson tunnel junctions, as well as surface investigations of metallic thin films with an atomic force microscope, that were performed in order to optimize the corresponding fabrication process for these tunnel junctions. Furthermore, new microfabrication processes that were developed for the realization of the first integrated detector that was developed within this thesis are illustrated.

In Chapter 6, this detector is discussed, which is an 8×8 pixel array that consists of 32 integrated detectors. At the beginning of this chapter, an overview of the detector design and its optimizations according to numerical simulations are presented. Furthermore, detector specific experimental methods are discussed, which includes the preparation procedure of the weak external magnetic field, as well as the experimental setup. At the end of this chapter, the main features of the detector are discussed and compared to the theoretical predictions, focusing on the impact of the on-chip energy dissipation on the achievable energy resolution, as well as on intrinsic factors that may limit its performance.

Based on these characterizations, the detector concept was refined and two new detectors were developed, which consist of 16 integrated detectors in a linear arrangement.

The first one is discussed in chapter 7, starting with a detailed description of the design improvements. Afterwards, this detector is characterized in detail and the results are compared to the theoretical model showing, that despite major improvements, the on-chip energy dissipation is still a limiting factor.

Chapter 8 discusses the second iteration of this detector development. Its special design characteristic is a novel custom-designed microfabricated thermalization for the dc-SQUID's energy dissipation and the isolation of the integrated detector in order to transport the dissipated energy as directly as possible to the heat sink at the sample holder. The characterization of this detector shows, that its energy resolution significantly improved and comparable with the best micro-calorimeter world wide.

2. Theoretical background of metallic magnetic calorimeters

In the framework of this thesis, several ultra-high-resolution X-ray detectors based on metallic magnetic calorimeters (MMCs) were developed. This chapter addresses the theoretical background required to understand this type of detector with a focus on its working principle, thermodynamic properties of its absorber and sensor materials, a commonly used readout scheme, and the detector geometry used within this thesis. In addition, the dominant noise contributions, as well as an estimation of the achievable energy resolution of such a detector, will be discussed.

2.1 Working principle of metallic magnetic calorimeters

A metallic magnetic calorimeter is an energy dispersive, single particle detector, which is usually operated at temperatures well below 100 mK. Its main constituents are schematically depicted in figure 2.1 a). It consists of a particle absorber which is in good thermal contact with a paramagnetic temperature sensor. The latter is connected to a thermal bath, that is kept at constant temperature T, via a weak thermal link. The sensor is also placed in a weak external magnetic field, so that the temperature senor exhibits a temperature dependent magnetization $M(T)$.

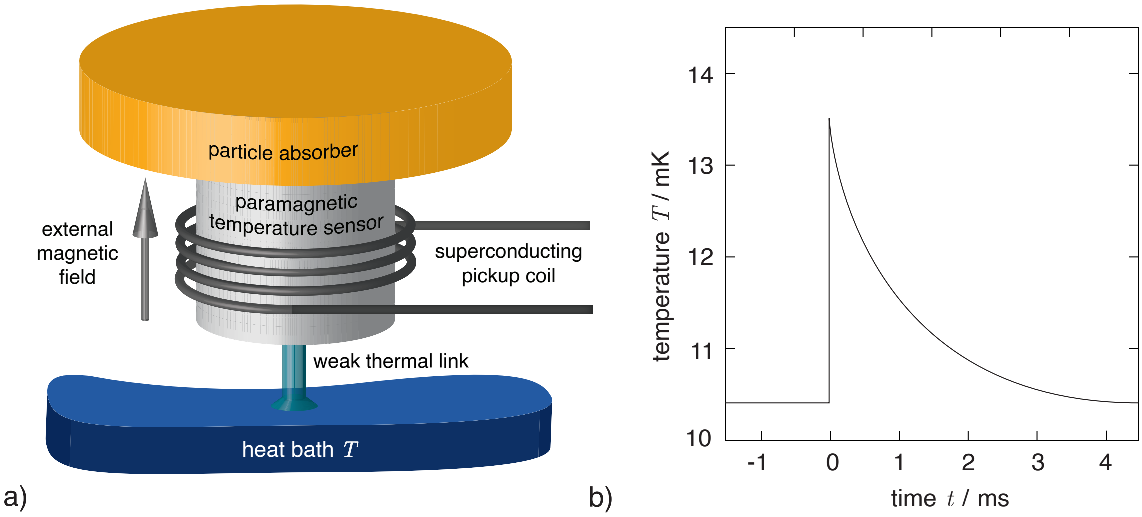

Figure 2.1: a) Schematic of a metallic magnetic calorimeter. b) Exemplary detector response after a particle has been absorbed.

After a particle with energy δE is absorbed, the detector temperature T increases by δT according to the first law of thermodynamics. A corresponding illustration of a detector response is depicted in figure 2.1 b), in which the very fast temperature rise is followed by a much slower thermalization back to the heat bath temperature. The speed of this thermalization can be adjusted by the thermal conductance of the thermal link between sensor and heat bath. In linear approximation, assuming $\delta T \ll T$, the temperature change of the detector is given by

$$\delta T \simeq \frac{\delta E}{C_{\mathrm{tot}}}\,, \tag{2.1}$$

where C_{tot} denotes the total heat capacity of the detector. The increased detector temperature leads to a change in sensor magnetization δM, which in turn causes a change of magnetic flux $\delta\Phi$ threading a superconducting pickup coil placed in close vicinity. This coil forms a closed superconducting loop together with the input coil of a current-sensing superconducting quantum interference device (SQUID). The latter, which is not shown in the schematic, can be described as a magnetic flux-to-voltage transducer. Within the closed superconducting pickup loop, a change of magnetic flux induces a screening current δI due to magnetic flux conservation

$$\delta I \propto \delta\Phi \propto \delta M \simeq \frac{\partial M}{\partial T}\frac{\delta E}{C_{\mathrm{tot}}}\,, \tag{2.2}$$

which in turn changes the magnetic flux threading the SQUID loop. This ultimately results in a voltage signal measurable by room temperature electronics. According to equation 2.2, in order to maximize the detector signal, the sensor magnetization must be highly sensitive to temperature changes, i.e. $\partial M/\partial T$ must be high, while the total heat capacity C_{tot} of the detector should to be as small as possible. Both conditions can be achieved at an operation temperature $T \ll 100\,\mathrm{mK}$, as the sensor magnetization follows Curie's Law ($M \propto 1/T$), while the phononic specific heat ($C_{\mathrm{ph}} \propto T^3$) and the electronic specific heat ($C_{\mathrm{el}} \propto T$) are greatly reduced.

2.2 Particle absorber

For the development of a metallic magnetic calorimeter for X-ray spectroscopy, the utilized particle absorber usually has to fulfill predetermined experimental requirements. These requirements include the quantum efficiency for the investigated photon energies E_γ, the rate of photons hitting the detector, and the required total detection area. These requirements can be met by adjusting the absorber thickness and the absorber material. The metallic magnetic calorimeters that were developed within the framework of this thesis are designed for soft X-ray spectroscopy of photons with $E_\gamma < 10\,\mathrm{keV}$. The stopping power of a material for X-rays depends on the cross section of the photoelectric effect $\sigma_{\mathrm{ph}} \propto Z^5$, which is the dominant absorption mechanism for photons with an energy $E < 500\,\mathrm{keV}$. In addition, the absorber should have a low heat capacity and a reliable fabrication should be possible for the chosen material. Furthermore, the detector signal should not show a position dependence of the location of particle absorption, which requires that the intrinsic absorber thermalization is much faster than the thermal coupling between absorber and temperature sensor.

With these requirements in mind, several possible absorber materials were investigated in the past, including dielectrics [McC93], metals [Ban93], and superconductors [Por11, Hen12], with high purity gold ($Z = 79$) being the present day material of choice [Fle05, Rot07, Kem18]. The noble metal is chemically inert, provides a high thermal conductance and possesses a very low intrinsic radioactivity, as there don't exist radioactive Au isotopes and Au can be separated very well from other potentially radioactive elements. Furthermore, the electro-chemical deposition of high purity gold is a well established process in the semiconductor industry and is commercially available as ready-to-use solutions, making a reliable fabrication of absorbers made of gold achievable. A possible, promising successor is bismuth ($Z = 83$) [Vai04, Got14, Rod14, Gad17], which shows a greatly reduced heat capacity compared to gold up to a factor of 150 [Col70], but shows a much slower thermal diffusion [Iyo04, Hoe06] and a slightly smaller stopping power [Bro08].

2.3 Temperature sensor

A temperature increase δT of the detector that follows upon particle absorption is converted into a change of magnetization δM by making use of a paramagnetic temperature sensor. The utilized sensor material for this should provide a reliable processability, exhibit a fast intrinsic thermal conductance and negligible radioactivity. Furthermore, the temperature dependence of the magnetization $\partial M/\partial T$ should be as large as possible. The alloys Au:Er and Ag:Er were found to provide a reasonable compromise between these requirements [Fle03, Bur08]. In these materials, the host metals Au and Ag are doped with a few hundred ppm of the rare-earth metal erbium. In this diluted solution, erbium ions occupy regular sites of the ffc lattice of the host metal and donates three electrons to the electron gas. The resulting electron configuration of the Er^{3+} ions is $[\mathrm{Kr}]4\mathrm{d}^{10}4\mathrm{f}^{11}5\mathrm{s}^2 5\mathrm{p}^6$. In this configuration, the unpaired electrons of the 4f-shell give rise to paramagnetic properties. Due to its small diameter of only 0.6 Å compared to a diameter of 2 Å of the 5s- and 5p-orbitals, the 4f-shell is shielded by the latter orbitals against the crystal field of the lattice of the host material [Abr12]. This allows for the application of Hund's rules to determine the total spin $S = 3/2$, angular momentum $L = 6$ and total angular momentum $J = L + S = 15/2$ of the 4f-electrons, resulting in a Landé factor of $g_\mathrm{J} = 6/5$. This gives rise to a magnetic moment of $\boldsymbol{\mu} = -g_\mathrm{J}\mu_\mathrm{B}\boldsymbol{J}$, a result which has been verified for temperatures above 100 K [Wil69]. Here, $\mu_\mathrm{B} = 9.27 \cdot 10^{-24}$ J/T denotes the Bohr magneton.

The 16-fold degenerate ground state of an Er^{3+} ion is split into several multiplets due to the influence of the crystal field, all of which are occupied at higher temperatures. The occupation of these energy levels decreases for temperatures $T < 100\,\mathrm{K}$ until only the lowest energetic state, called the Kramers-Γ_7 doublet, is occupied. It is separated from the next energetically higher multiplet by $\Delta E/k_\mathrm{B} \approx 17\,\mathrm{K}$ (Au) or $\Delta E/k_\mathrm{B} \approx 25\,\mathrm{K}$ (Ag) respectively [Hah92]. Here, $k_\mathrm{B} = 1.38 \cdot 10^{-23}$ J/K denotes the Boltzmann constant. Therefore, the erbium ions within the sensor can be described as a two level system with quasi-spin $\tilde{S} = 1/2$ and effective Landé g-factor $\tilde{g} = 6.8$, considering a typical operation temperature $T < 100\,\mathrm{mK}$ of MMCs and a sufficiently weak applied external magnetic field [Abr12, Tao71]. Furthermore, the erbium used for doping should be devoid of the isotope $^{167}\mathrm{Er}$, as its non-zero nuclear spin represents an additional degree of freedom, influencing the magnetization and heat capacity at temperatures below 100 mK [Ens00]. The sensor material used in this thesis is doped with ~ 400 ppm of Er enriched in $^{168}\mathrm{Er}$.

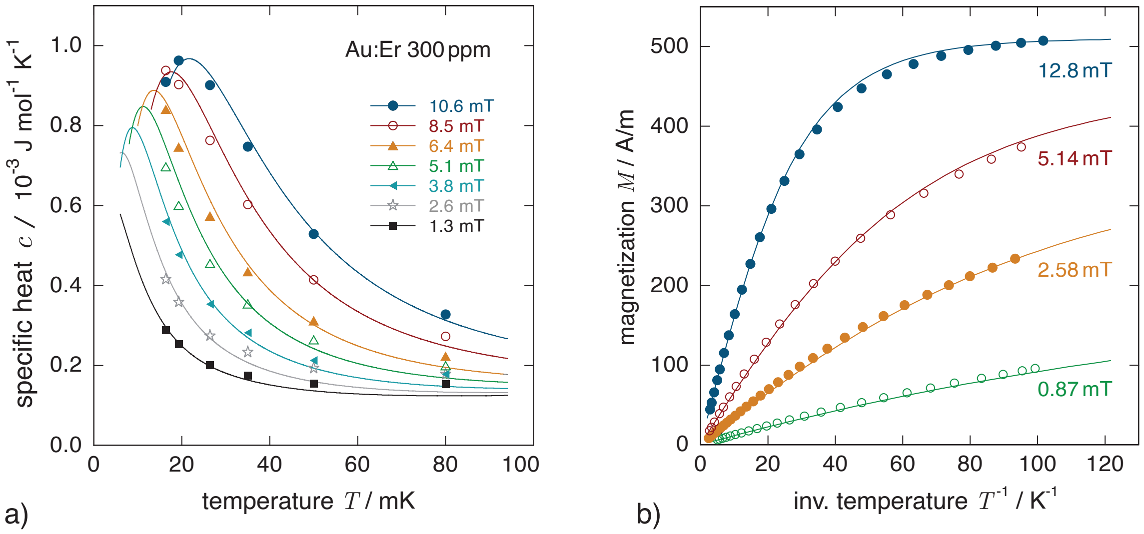

Figure 2.2: a) Specific heat $c(T)$ and b) temperature dependence of the magnetization $M(T^{-1})$ of a Au:Er sample with an Er concentration of $c_\mathrm{Er} = 300$ ppm made of milled bulk material for different magnetic fields H. The contineous lines are computed via Monte-Carlo simulations whereas the symbols represent measured data [Fle03].

The temperature dependence of the specific heat c at MMC operation temperatures is illustrated in figure 2.2 a) for an Au:Er sample milled from bulk material for a variety of applied external magnetic fields. Shown is measured data and Monte-Carlo simulations, in which dipole-dipole interactions and RKKY[1] interactions between the magnetic moments were considered [Sch00, Fle03]. Both of these interactions have a r^{-3} dependency, with r denoting the distance between the magnetic moments. Therefore, an interaction parameter $\alpha = \Gamma_{\mathrm{RKKY}}/\Gamma_{\mathrm{dd}}$ can be introduced to describe the relative interaction strength of the RKKY interactions and dipole-dipole interactions between magnetic moments in the sensor material. This parameter was determined to $\alpha_{\mathrm{Au:Er}} = 5$ for Au:Er [Fle03]. Figure 2.2 b) shows the measured and calculated magnetization for the same sample. As one can observe, the thermodynamic properties of Au:Er can be predicted, which allows for the optimization of the MMC performance by means of numerical simulations.

However, the metallic magnetic calorimeters that were developed within this thesis make use of Ag:Er as the sensor material. At the time of detector development, no numerical description existed for this material. It was shown in [Dan05], that the thermodynamic properties of Ag:Er can be sufficiently approximated for low erbium concentrations c_{Er} of a few hundred ppm via scaling from the numerical simulations of the thermodynamic properties of Au:Er, such that the specific heat $c_{\mathrm{E_z,Ag:Er}}$ of the magnetic moments in Ag:Er can be calculated to

$$c_{\mathrm{E_z,Ag:Er}}(B, T, c_{\mathrm{Er}}, \alpha_{\mathrm{Ag:Er}}) = \frac{\alpha_{\mathrm{Au:Er}}}{\alpha_{\mathrm{Ag:Er}}} \cdot c_{\mathrm{E_z,Au:Er}}\left(B, T, \frac{\alpha_{\mathrm{Ag:Er}}}{\alpha_{\mathrm{Au:Er}}} c_{\mathrm{Er}}, \alpha_{\mathrm{Au:Er}}\right). \tag{2.3}$$

Consequently, the sensor magnetization can be calculated to

$$M_{\mathrm{Ag:Er}}(B, T, c_{\mathrm{Er}}, \alpha_{\mathrm{Ag:Er}}) = \frac{\alpha_{\mathrm{Au:Er}}}{\alpha_{\mathrm{Ag:Er}}} \cdot M_{\mathrm{Au:Er}}\left(B, T, \frac{\alpha_{\mathrm{Ag:Er}}}{\alpha_{\mathrm{Au:Er}}} c_{\mathrm{Er}}, \alpha_{\mathrm{Au:Er}}\right). \tag{2.4}$$

The performance of several metallic magnetic calorimeters was successfully predicted in recent works [Hen17, Sch19] by calculating the thermodynamic properties of Ag:Er via this scaling, where an interaction parameter of $\alpha_{\mathrm{Ag:Er}} = 12.5$ for Ag:Er was determined.

2.3.1 Thermalization between absorber and sensor

The dominant absorption mechanism for photons in gold with an energy $E < 500\,\mathrm{keV}$ is the photoelectric effect, discussed in detail in [Koz12]. At first, the absorption of a photon results in a free, high energetic electron, which thermalizes via electron-electron scattering, creating additional athermal electrons. The latter then further thermalize via electron-phonon interaction with high energetic athermal phonons.

---

[1] **R**uderman-**K**ittel-**K**asuya-**Y**osida

These processes usually require a very small interaction volume within the absorber and perform on a faster timescale than a metallic magnetic calorimeter can resolve. Afterwards, the athermal phonons pass their energy to the conduction electrons, which represent the dominant system of heat capacity within the absorber at temperatures below 1 K. The absorbed energy is transmitted from the absorber to the sensor via the conduction electrons, where they interact with the magnetic moments of the temperature sensor, which represent the dominant contribution to the sensor heat capacity at the operation temperature of an MMC [Ens00]. The magnetic moments within the temperature sensor react to a temperature increase of the electron system with a relaxation time τ that can be calculated with the Korringa relation $\tau = \kappa/T$ for the case of a negligible heat capacity contribution C_z of the magnetic moments to the total heat capacity C_tot of the detector. However, as will be shown in section 2.6.4, the intrinsic energy resolution of an MMC is minimized for $C_\mathrm{z} = 0.5$ C_tot. In this case, the relaxation time can be calculated by

$$\tau \cong (1-\beta)\frac{\kappa}{T}\,. \tag{2.5}$$

Here, $\beta = C_\mathrm{z}/(C_\mathrm{z}+C_\mathrm{e})$ is the fraction of the heat capacity of the magnetic moments to the total heat capacity of the detector and $\kappa = 7\cdot 10^{-9}\,\mathrm{Ks}$ [Sjö75] is the Korringa constant of the sensor material. The magnetic moments react with a time constant of $\tau \approx 175\,\mathrm{ns}$ to a temperature increase of the conduction electrons, assuming an operation temperature of $T = 20\,\mathrm{mK}$ and $\beta = 0.5$.

Loss of athermal phonons

The interaction length required for a thermalization of the athermal phonons with the conduction electrons is on the order of a few micrometers at the operation temperatures of an MMC [Ens00]. As the thickness of absorber and sensor for the detectors developed in this thesis is $3\,\mu\mathrm{m}$ and $\sim 1\,\mu\mathrm{m}$ respectively, this means that athermal phonons can potentially traverse the absorber and sensor, depositing their energy into the substrate. Therefore, this lost energy can not contribute to the detector signal. This issue can be observed as a distinct low energy tail in a spectral line shape measured with a metallic magnetic calorimeter [Fle09]. In order to minimize this effect, the effective contact area between absorber and sensor can be reduced to a few percent by putting the absorbers on posts [Sch12].

2.4 Coupling schemes between MMC and SQUID

This section briefly discusses the relevant coupling schemes between a metallic magnetic calorimeter and a dc-SQUID that is used for signal readout.

2.4.1 Transformer coupled readout

Figure 2.3 a) illustrates a nowadays commonly used detection scheme for metallic magnetic calorimeters, in which the particle absorber is omitted for visibility. Shown is a paramagnetic temperature sensor with a superconducting pickup coil with inductance L_M in close proximity. An input coil with inductance L_in is connected in series to inductively couple the MMC to a current-sensor SQUID with inductance L_S via the mutual inductance M_in, creating a superconducting flux transformer. Both coils are connected to each other via wire bonds with inductance L_par, as MMC and SQUID are situated on separate substrates. In the externally applied inhomogeneous magnetic field B, the free electron spins of the Er^{3+} ions within the sensor partially align along the magnetic field lines, giving rise to a temperature dependent magnetization $M(T)$. When the temperature T of the sensor increases upon particle absorption in the absorber, the sensor magnetization $M(T)$ changes, consequently changing the magnetic flux $\delta\Phi$ that penetrates the pickup coil L_M. Due to magnetic flux conservation in closed superconducting loops, this induces a screening current δI_scr running through the input coil of the SQUID, given by

$$\delta I_\mathrm{scr} = \frac{\delta\Phi}{L_\mathrm{M} + L_\mathrm{in} + L_\mathrm{par}} \,. \tag{2.6}$$

This current is converted into a magnetic flux change $\delta\Phi_\mathrm{S}$ within the SQUID loop via the mutual inductance $M_\mathrm{in} = k\sqrt{L_\mathrm{in}L_\mathrm{S}}$, where k denotes a magnetic coupling coefficient. The thereby derived magnetic flux coupling between pickup coil and SQUID is [Kem18]

$$\frac{\delta\Phi_\mathrm{S}}{\delta\Phi} = \frac{M_\mathrm{in}}{L_\mathrm{M} + L_\mathrm{in} + L_\mathrm{par}} \,. \tag{2.7}$$

The readout scheme that is depicted in figure 2.3 b) is used for the detectors that are developed in this group. It uses two pickup coils of opposite winding directions, each with inductance L_M. The input coil of the dc-SQUID is connected in parallel to this coil arrangement. Such a scheme allows for a readout of two temperature sensor but reduces the flux coupling according to Kirchhoff's law to

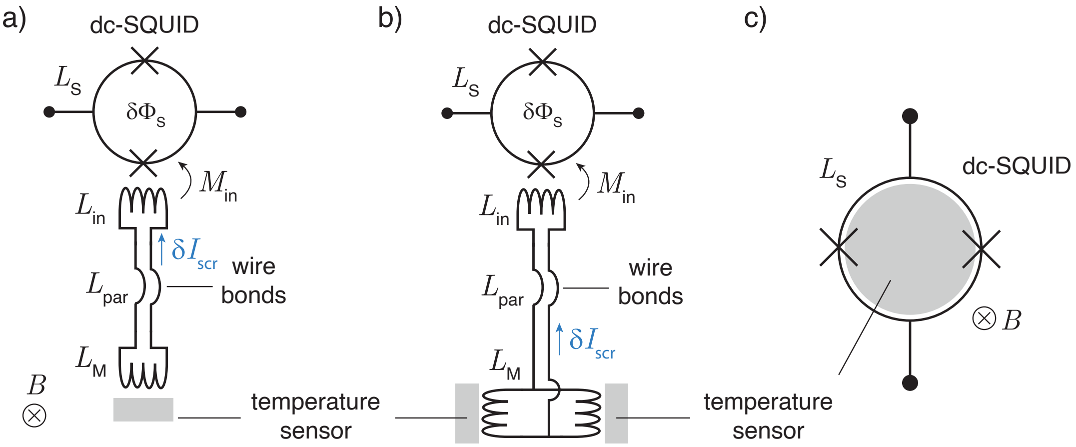

Figure 2.3: a) Schematic view of a transformer coupled readout of metallic magnetic calorimeter. One paramagnetic temperature sensor is placed in close vicinity to a superconducting pickup with inductance L_M. An input coil with inductance L_in is connected in series to inductively couple the MMC to a current-sensor SQUID with inductance L_S via the mutual inductance M_in. L_M and L_in are connected via via wire bonds with inductance L_par. b) Uses two pickup coils of opposite winding direction to read out two sensors, but with reduced flux coupling between L_M and L_S compared to a). c) The direct sensor readout: A paramagnetic temperature sensor is placed directly inside a SQUID loop in order to maximize the flux coupling.

$$\frac{\delta\Phi_\mathrm{S}}{\delta\Phi} = \frac{M_\mathrm{in}}{L_\mathrm{M} + 2(L_\mathrm{in} + L_\mathrm{par})}\,. \tag{2.8}$$

Equation 2.8 is maximized for $L_\mathrm{in} = L_\mathrm{M}/2 + L_\mathrm{par}$. Assuming inductance matching $L_\mathrm{in} = L_\mathrm{M}/2$, as well as a negligible parasitic inductance $L_\mathrm{par} = 0$, the maximum fraction of the magnetic energy transferred from the pickup coil to the SQUID is given by $k^2/4$ [Wei96], i.e. the energy transfer between MMC and SQUID has an upper limit of 25 % for the transformer coupled readout. However, inductance matching is not always achieved and $k < 1$ and $L_\mathrm{par} \geq 0.5\,\mathrm{nH}$ usually holds true for actual application, so that the actually achieved flux coupling is further reduced.

When the pickup coils of have an opposite winding direction, as it is the case for the presented readout scheme, they form a 1^{st}-order gradiometer in which the two temperature sensors that are placed in close proximity to each pickup coil create a signal of opposite polarity in the SQUID. This allows for a discriminate readout of two pixels within one detector. Furthermore, such a gradiometric setup suppresses external parasitic electromagnetic signals, as well as temperature variations of equal magnitude in both sensors, like infinitesimal temperature fluctuations of the cryogenic setup. Lastly, the transformer coupled readout provides the advantage of a spatial and thermal separation, as MMC and SQUID can be situated on separate substrates.

Otherwise the on-chip power dissipation required for SQUID readout, usually on the order of 10 pW to 1 nW, would have a negative impact on the detector's operation temperature.

2.4.2 Direct sensor readout

In order to circumvent the previously addressed coupling limitations of the transformer coupled readout scheme, one can place the paramagnetic temperature sensor directly inside the SQUID loop, as it is schematically depicted in figure 2.3 c). For this simple approach, the flux coupling $\delta\Phi_\mathrm{S}/\delta\Phi$ is 100%. The previously discussed gradiometric readout scheme can also be applied here, which reduces the flux coupling $\delta\Phi_\mathrm{S}/\delta\Phi$ to 50% [Boy09]. However, while the flux coupling is far superior to the transformer coupled readout, other potential challenges arise for an operation of such an integrated detector. The readout of a dc-SQUID, which will be discussed in detail in chapter 3, requires an on-chip power dissipation, which would occur in very close proximity to the temperature sensor, increasing its temperature with respect to the heat bath, possibly degrading the achievable energy resolution. Therefore, advanced thermalization concepts are required, making the fabrication more complex. The second drawback are parasitic effects originating from the capacitive coupling between sensor and SQUID, requiring a highly sophisticated SQUID design. The third drawback are very large signal heights due to the enhanced flux coupling, allowing for the signal rise to exceed the slew-rate of the readout chain, so that the signal rise is not fully resolvable. The main goal of this thesis was to face these challenges to exploit the full potential of the direct sensor readout of a metallic magnetic calorimeter in order to set a new benchmark energy resolution for MMCs for the soft X-ray spectroscopy.

2.5 Meander-shaped detector geometry

State-of-the-art metallic magnetic calorimeters are usually fabricated by means of photolithography and thin film deposition techniques, giving rise to several possible detector geometries. Planar meander-shaped pickup coils are nowadays most commonly used [Zin06, Bur08, Hen17, Sch19], while planar spiral-shaped pickup coils with superconducting ground plane are also reported in literature [Boy09, Fle09, Heu11]. The detectors that were developed in this thesis make use of meander-shaped pickup coils, which will be discussed in this section on the example of the direct sensor readout scheme. An unoptimized version of this idea was developed in the past [Sto05, Sch07], which was far away from reaching its full potential.

Figure 2.4 shows a schematic detector design with direct sensor readout that is similar

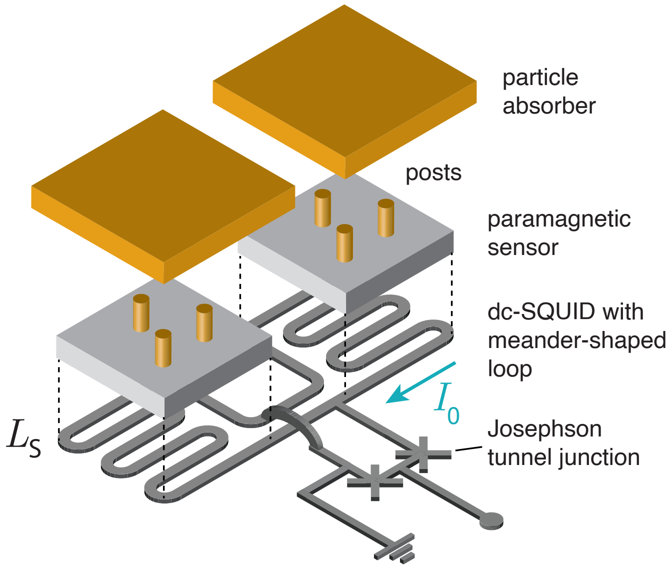

Figure 2.4: Schematic of a metallic magnetic calorimeter with direct sensor readout [Zak03, Sto05], similar to the designs that were developed in this thesis. Two paramagnetic temperature sensors are placed on top of a meander-shaped SQUID loop, which consists of two planar meander-shaped coils. A persistent current I_0 that is required to magnetize the sensor is injected into the meander-shaped loop.

to the detectors that were developed in the framework of this thesis. It consists of two paramagnetic temperature sensors with corresponding particle absorbers that are situated on top of planar meander-shaped pickup coils. Connected in parallel to that are two so called Josephson tunnel junctions. These are central elements of a dc-SQUID, as will be discussed in detail in chapter 3. The inductance of the detector, which means the inductance of the SQUID in this case, is therefore given by $L_\mathrm{S} = L_\mathrm{M}/2$. Furthermore, in order to create the magnetic field B that is required to magnetize the temperature sensor, a persistent current I_0 can be injected into the superconducting meander-shaped SQUID loop. The following sections will discuss how the simulation of the magnetic field distribution within the temperature sensor can be used to predict the energy resolution of a metallic magnetic calorimeter with such a meander-shaped detector geometry.

2.5.1 Magnetic field distribution within the sensor

It was shown in section 2.3, that the heat capacity and magnetization of the sensor depend on the applied magnetic field, i.e. $c_\mathrm{sens}(T,B)$ and $M(T,B)$. The magnetic field originates from the persistent current I_0 flowing in the meander-shaped pickup coil and exhibits a highly inhomogeneous field distribution within the sensor volume, making an analytical computation of $c_\mathrm{sens}(T,B)$ and $M(T,B)$ hardly possible. Hence, numerical simulation are used to determine the magnetic field distribution within the sensor volume in order to predict $c_\mathrm{sens}(T,B)$ and $M(T,B)$. These calculations were done with the program FEMM[2] in this thesis.

---

[2] **F**inite **E**lement **M**ethod **M**agnetics: www.femm.info

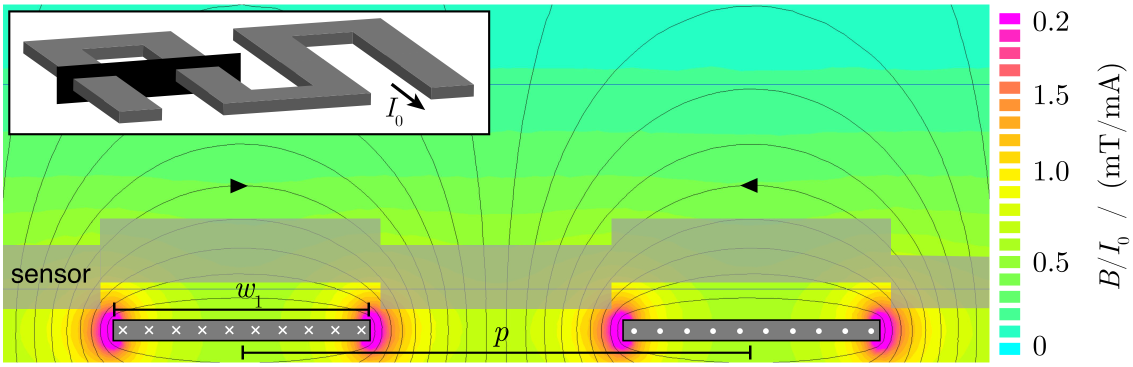

Figure 2.5: Pseudocolor plot of the calculated normalized magnetic field distribution for a cross section of two stripes of a meander-shaped pickup coil simulated using FEMM. The thickness of the stripes is 250 nm with a width $w = 5\,\mu$m and a pitch $p = 10\,\mu$m. The sensor is indicated by the grey semi-transparent area and has a height of 1 μm with a spatial separation of 300 nm between sensor and pickup coil. The depicted magnetic field is created by a persistent current $I_0 = 1\,$mA.

Figure 2.5 shows a pseudocolor plot of a numerically calculated magnetic field distribution for a cross section of two stripes of a meander-shaped pickup coil. There, $w = 5\,\mu$m denotes the stripe width of the pickup coil and $p = 10\,\mu$m represents the pitch, i.e. the horizontal center-to-center distance between two neighboring stripes of the meander. The meander stripes have a thickness of 250 nm. Only the magnetic field distribution that is created by a current I_0 flowing in two meander stripes has to be calculated due to periodic boundary conditions in horizontal direction, i.e. the magnetic field distribution in the entire temperature sensor can be described by a periodic repetition of the results shown in figure 2.5. The meander stripes are assumed to be of infinite length in the simulation, because FEMM can only simulate magnetic and electrostatic problems in two-dimensions. Furthermore, the meander stripes are superconducting with an assumed perfect diamagnetic behavior, neglecting any edge effects that might occur due to the London penetration depth λ_{L} [Hen77]. A persistent current of $I_0 = 1\,$mA flowing in the meander stripes was used to create the illustrated pseudocolor plot. The current enters the drawing plane in the left stripe and exits the drawing plane in the right stipe, as indicated by the crosses and dots respectively. The approximate location of the paramagnetic sensor, that is 1 μm thick, is indicated by the semi-transparent grey area, while the interstice between structures is filled with the insulator $\mathrm{SiO_2}$. That the sensor is not entirely flat is a result from the microfabrication techniques used for detector development, as will be discussed in section A.1. Any effect of the sensor material on the magnetic field is neglected due to its low susceptibility. From this FEMM simulation, the magnetic field distribution $P(B)$ within the sensor volume can be extracted by evaluating the magnetic field $B(\boldsymbol{r})$ for any number of points, depending on the required resolution.

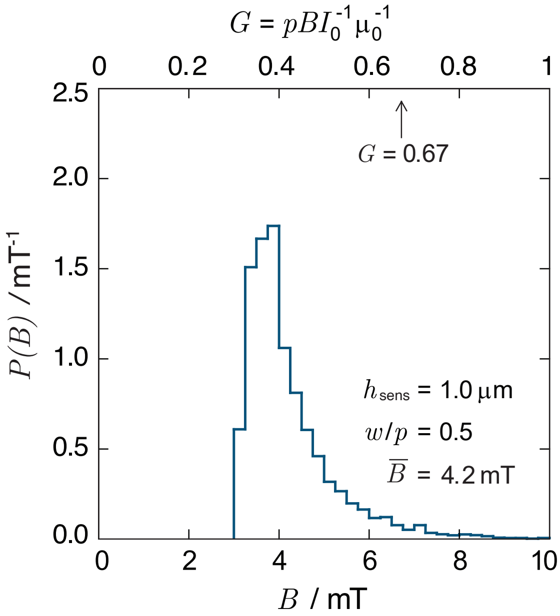

Figure 2.6: Probability distribution of the magnetic field amplitude within a sensor volume that has a thickness of 1 μm and a distance of 300 nm to the meander-shaped pickup coil below. The meander has a stripe width $w = 5\,\mu$m, a pitch $p = 10\,\mu$m and a thickness of 250 nm. The magnetic field is created by a current flowing in the meander of $I_0 = 50\,$mA.

The thereby created magnetic field distribution $P(B)$ is illustrated in figure 2.6 for the simulated meander-shaped geometry. The depicted distribution is created for a persistent current $I_0 = 50\,$mA flowing in the superconducting meander-shaped pickup coil. Also depicted is an average geometry factor G that can be extracted from the simulation, that represents a dimensionless factor which can be used to describe the average coupling strength between the spins within the sensor volume and the pickup coil below and is given by the relation [Bur04]:

$$B(\boldsymbol{r}) = \mu_0 G(\boldsymbol{r}/p)\frac{I_0}{p}\,. \tag{2.9}$$

Here, $\mu_0 = 4\pi \cdot 10^{-7}\,$Vs/Am denotes the magnetic constant, $B(\boldsymbol{r})$ is the magnetic field strength at location $\boldsymbol{r}$ and $G(\boldsymbol{r}/p)$ is the corresponding geometry factor at location $\boldsymbol{r}$. Thus, the magnetic field scales linearly with the persistent current I_0 and is inversely proportional to the pitch p of the meander stripes. The geometry fractor $G(\boldsymbol{r}/p)$ also scales inversely with p, showing that the coupling strength between sensor and pickup coil increases for a smaller pitch. It will be shown later, that the expected signal height of a metallic magnetic calorimeter can be computed by making use of the probability distribution $P(B)$.

2.6 Energy resolution

In order to predict the achievable energy resolution of a metallic magnetic calorimeter, the signal-to-noise ratio $SNR(f)$ of the detector has to be determined. This computation requires precise knowledge of the signal height $\delta\Phi/\delta E$ after a particle with energy δE has been absorbed, as well as knowledge of its signal shape $p(f)$ and the noise contributions of the detector. After the discussion of these three key factors, this chapter concludes with the derivation of an expression for the achievable energy resolution of an MMC.

2.6.1 Signal height

The signal height $\delta\Phi/\delta E$ represents the change of magnetic flux $\delta\Phi$ within the pickup coil of the detector after a particle with energy δE has been absorbed. According to equation 2.2, precise calculations of the expected signal height require knowledge of the temperature dependence of the sensor magnetization $M(T,B)$, as well as of the total heat capacity $C_{\mathrm{tot}}(T) = C_{\mathrm{Abs}}(T) + C_{\mathrm{sens}}(T,B)$ of the detector, where $C_{\mathrm{Abs}}(T)$ denotes the heat capacity of the particle absorber. In order to calculate the signal height $\delta\Phi/\delta E$, which denotes the change of magnetic flux threading the meander-shaped pickup coil per energy input, the sensor volume can be divided into infinitesimal small volume elements $\mathrm{d}V(\boldsymbol{r})$ located at position $\boldsymbol{r}$, whereby the magnetic field $B(\boldsymbol{r})$ can be determined for each volume element using the numerical simulations that were already discussed in the previous section. The amplitude $B(\boldsymbol{r})$ can be expressed by equation 2.9, which includes a dimensionless geometry factor $G(\boldsymbol{r}/p)$ that is also extracted from the magnetic field simulations. In order to calculate the magnetic flux change $\delta\Phi$ in the pickup coil, one has to sum over all magnetic flux changes $\mathrm{d}(\delta\Phi)$ in every volume element, with the flux change within one single volume element $\mathrm{d}V$ being [Fle05]

$$\mathrm{d}(\delta\Phi) = \mu_0 \frac{G(\boldsymbol{r}/p)}{p} \delta M(\boldsymbol{r}) \mathrm{d}V \, . \tag{2.10}$$

An expression for the signal height can be derived by combining the equations 2.2, 2.9 and 2.10, followed by an integration over the entire sensor volume V:

$$\frac{\delta\Phi}{\delta E} = \frac{1}{C_{\mathrm{abs}} + \int_V c_{\mathrm{sens}}(B(\boldsymbol{r}))\mathrm{d}^3 r} \int\limits_V \mu_0 \frac{G(\boldsymbol{r}/p)}{p} \frac{\partial M(B(\boldsymbol{r}))}{\partial T} \mathrm{d}^3 r. \tag{2.11}$$

Considering the fact that the heat capacity $c_{\mathrm{sens}}(B(\boldsymbol{r}))$ of the sensor and the magnetization $M(B(\boldsymbol{r}))$ both depend on the magnetic field, one can integrate equation 2.11 over the magnetic field distribution $P(B)$ that was introduced in section 2.5.1, instead of the sensor volume V. By making use of the weighted average

$$\langle X \rangle = \int\limits_0^\infty P(B) X \mathrm{d}B \, , \tag{2.12}$$

equation 2.11 can be written as

$$\frac{\delta\Phi}{\delta E} = \frac{V}{C_{\mathrm{abs}} + V \cdot \langle c_{\mathrm{sens}} \rangle} \left\langle \mu_0 \frac{G}{p} \frac{\partial M}{\partial T} \right\rangle . \tag{2.13}$$

2.6.2 Signal shape

A thermodynamic model of a metallic magnetic calorimeter can be compiled by treating the detector as a canonical ensemble with two sub-systems, as it is schematically depicted in figure 2.7. Here, it is assumed that one sub-system represents the conduction electrons within absorber and sensor and has a heat capacity C_{e} and temperature T_{e}. The other sub-system represents the magnetic moments within the sensor and has a heat capacity C_{z} and temperature T_{z}. Both sub-systems are thermally coupled to each other via the thermal conductance G_{ze}, while the conduction electrons are thermally coupled to a heat bath of constant temperature T_{b} via the thermal conductance G_{eb}. In addition, noise sources P_{ze} and P_{eb} exist in parallel to the respective thermal coupling, representing thermodynamic energy fluctuations between the corresponding systems. In this model, the the flow of energy can be described by the coupled differential equations [Fle05]

$$\dot{E}_{\mathrm{z}} = C_{\mathrm{z}}\dot{T}_{\mathrm{z}} = G_{\mathrm{ze}}\left(T_{\mathrm{e}} - T_{\mathrm{z}}\right) + P_{\mathrm{ze}} \tag{2.14}$$

$$\dot{E}_{\mathrm{e}} = C_{\mathrm{e}}\dot{T}_{\mathrm{e}} = G_{\mathrm{ze}}\left(T_{\mathrm{z}} - T_{\mathrm{e}}\right) - P_{\mathrm{ze}} + G_{\mathrm{eb}}\left(T_{\mathrm{e}} - T_{\mathrm{b}}\right) - P_{\mathrm{eb}} + E\delta(t) , \tag{2.15}$$

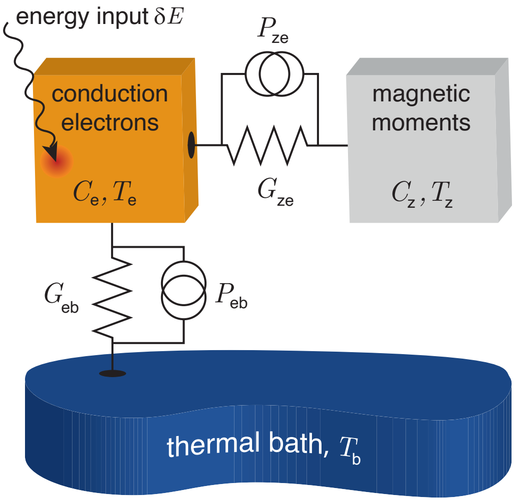

Figure 2.7: Schematic of a thermodynamic model of a metallic magnetic calorimeter which assumes, that the detector can be represented as a canonical ensemble with two sub-systems, one representing the conduction electrons and the other the magnetic moments. The depicted factors G, P, C and T are explained in the text.

with $E\delta(t)$ representing an external, instantaneous energy input into the system of the conduction electrons as $\delta(t)$ denotes the Dirac delta function. Solving the differential equations, assuming $G_{\mathrm{ze}} \gg G_{\mathrm{eb}}$ and $C_{\mathrm{e}} \approx C_{\mathrm{z}}$ while neglecting the intrinsic noise contributions P_{ze} and P_{eb}, yields the solution

$$E_{\mathrm{z}}(t) = E_0 p(t) = E_0 \beta \left(e^{-t/\tau_1} - e^{-t/\tau_0} \right) , \tag{2.16}$$

where $p(t)$ denotes the responsivity of the detector and $\beta = C_{\mathrm{z}}/(C_{\mathrm{z}} + C_{\mathrm{e}})$ is the fraction of the heat capacity of the magnetic moments to the total heat capacity of the detector. The time constant τ_0 represents the signal rise of the detector and is given by equation 2.5. The signal decay time $\tau_1 \simeq (C_{\mathrm{z}} + C_{\mathrm{e}})/G_{\mathrm{eb}}$ is defined by the thermal coupling between the conduction electrons and the thermal bath and can thereby be adjusted to fit experimental requirements.

2.6.3 Noise contributions

This section briefly discusses intrinsic noise sources of a metallic magnetic calorimeter, as well as the noise contribution originating from the dc-SQUID used for signal readout.

Thermodynamic energy fluctuations

The thermal noise sources P_{ze} and P_{eb} that were already mentioned in section 2.6.2 represent statistical, thermal energy fluctuations between the thermodynamic system of conduction electrons and the system of magnetic moments within the sensor, as well as between the system of conduction electrons and the heat bath, respectively. In analogy to the Nyquist-noise of an electrical resistor, the power spectral density of these noise sources is given by $S_{\mathrm{P}_i} = 4k_{\mathrm{B}}T^2G_i$, with G_i denoting the thermal coupling linked to the respective noise source, as depicted in figure 2.7. Solving the differential equations 2.14 and 2.15 for $E\delta(t) = 0$, i.e. neglecting an external energy input, under the assumption that $G_{\mathrm{ze}} \gg G_{\mathrm{eb}}$ and $C_{\mathrm{e}} \approx C_{\mathrm{z}}$, one finds the expression [Fle03]

$$S_{E_{\mathrm{Z}},\mathrm{TEF}}(f) = 4k_{\mathrm{B}}T^2C_{\mathrm{z}} \left(\frac{(1-\beta)\tau_0}{1+(2\pi\tau_0 f)^2} + \frac{\beta\tau_1}{1+(2\pi\tau_1 f)^2} \right) \tag{2.17}$$

for the power spectrum of the energy fluctuations of the magnetic moments as a function of frequency f. The spectrum of the energy fluctuations $\sqrt{S_{\mathrm{E_Z,TEF}}}$ therefore shows two distinct plateaus, the first having a cut-off frequency $(2\pi\tau_1)^{-1}$ at lower frequenies with and amplitude $\sqrt{4k_{\mathrm{B}}C_{\mathrm{z}}\tau_1T^2\beta}$. The second plateau has a cut-off frequency $(2\pi\tau_0)^{-1}$ at higher frequencies with an amplitude $\sqrt{4k_{\mathrm{B}}C_{\mathrm{z}}T^2\tau_0(1-\beta)}$. An example of the resulting noise spectrum is illustrated in figure 2.8, where it is marked as ”TEF”.

Magnetic Johnson noise

Free electrons in a normal conducting metal perform a Brownian motion due to thermal excitation. This random motion of charge carriers, in our case the movement of electrons within the temperature sensor and the absorber, therefore creates fluctuating magnetic fields, called magnetic Johnson noise. The resulting flux noise within the pickup coil of the detector is coupled into the readout SQUID via the superconducting flux transformer. The power spectral density of this noise contribution depends on the temperature T, the electrical conductance σ and volume V of the conductor material, and also on the detection geometry. The latter is taken into account by a geometry-dependent factor $\mathcal{C}$ that can be numerically calculated. For a paramagentic, metallic temperature sensor situated on top of a meander-shaped pickup coil, the expression

$$S_{\Phi,\mathrm{J}} = (\mu_0 \mathcal{C})^2 \sigma k_\mathrm{B} T V \tag{2.18}$$

can be derived [Fle05]. Numerical simulations show, that this noise contribution is usually negligible for the transformer coupled readout at operation temperatures below 100 mK [Pie08]. However, when the direct sensor readout is used, as discussed in section 2.4.2, this noise source can make a significant contribution to the white noise level of the overall noise spectrum.

Low-frequency noise due to Er ions

Previous measurements using metallic magnetic calorimeters, with either Au:Er or Ag:Er based temperature sensors, revealed a $1/f$-like noise contribution, whose amplitude scales with the amount of erbium within the sensor [Dan05]. Under the assumption that this noise contribution originates from the Er ions, each ion contributes $S_\mathrm{m}(f) \simeq 0.18\mu_\mathrm{B}^2/f^\nu$ to the spectral power density, independently whether Au or Ag is used as a host material [Bur08]. The noise exponent ν varies between 0.8 and 1 and slightly depends on the detector geometry and fabrication process of the sensor [Fle09]. These magnetic fluctuations result in a magnetic flux noise within the pickup coil of the detector that can be described by [Fle03]:

$$S_{\Phi,\mathrm{Er}}(f) = \frac{\mu_\mathrm{B}^2 \langle G^2 \rangle}{p^2} S_\mathrm{m}(f) N_\mathrm{Er} \,. \tag{2.19}$$

Here, p denotes the pitch between neighboring stripes of the meander-shaped pickup coil of the detector, G denotes the dimensionless geometry factor that was discussed in section 2.6.1 and N_Er is the number of erbium-ions within the sensor.

Total noise spectrum

In order to derive an expression for the expected energy resolution of a metallic magnetic calorimeter, the total noise of the system has to be computed. Since all of the discussed noise contributions are independent of each other, they can be incoherently summed up, creating an expression for the apparent magnetic flux noise in the readout SQUID:

$$S_{\Phi_\mathrm{S},\mathrm{tot}} = \left(\frac{\delta\Phi_\mathrm{S}}{\delta\Phi}\right)^2 \left[\left(\frac{1}{\beta}\frac{\delta\Phi}{\delta E}\right)^2 S_{E_\mathrm{Z},\mathrm{TEF}} + S_{\Phi,\mathrm{J}} + S_{\Phi,\mathrm{Er}}\right] + S_{\Phi_\mathrm{S},\mathrm{SQ}}\,. \tag{2.20}$$

Here, $S_{\Phi_\mathrm{S},\mathrm{SQ}}$ denotes the power spectral density of the intrinsic SQUID noise contribution, which consists of a frequency-dependend $1/f$-like noise contribution and a white noise contribution, which will be further discussed in detail in chapter 3. The different noise contributions, as well as the overall noise spectrum for an example detector with transformer coupled readout is shown in figure 2.8 a), where $\sqrt{S_{\Phi_\mathrm{S}}}$ is given in the units $\mu\Phi_0/\sqrt{\mathrm{Hz}}$. Here, $\Phi_0 = h/2e = 2.07\cdot 10^{-15}\,\mathrm{Tm}^2$ is defined as the magnetic flux quantum. In the displayed simulation, the absorber and sensor properties were assumed to be identical to the ones used for the first detector that was developed in the framework in this thesis. Therefore, the absorber dimensions are $150\times 150\times 3\,\mu\mathrm{m}^3$, the sensor dimensions are $50\times 50\times 1.2\,\mu\mathrm{m}^3$ with an erbium concentration of $c_\mathrm{Er} = 450\,\mathrm{ppm}$. The detector is coupled to the SQUID via a superconducting flux transformer. The gradiometric, meander-shaped pickup coil below the sensors has a pitch $p = 6\,\mu\mathrm{m}$, a meander stripe width $p = 3\,\mu\mathrm{m}$, whereas the inductance of each meander is $L_\mathrm{M} = 290\,\mathrm{pH}$. A persistent current of $I_0 = 33\,\mathrm{mA}$ was assumed. At an operation temperature of $T = 20\,\mathrm{mK}$, the resulting heat capacity of absorber and sensor is 0.1 pJ/K and 0.08 pJ/K, respectively. Furthermore, a signal rise time of $\tau_0 = 100\,\mathrm{ns}$ and a signal decay time of $\tau_1 = 10\,\mathrm{ms}$ was assumed.

The SQUID has an inductance of 130 pH, an input coil inductance of 1.1 nH and a coupling coefficient of $k = 0.95$ between the two constituents. Its white noise level was assumed to be a very low $S_{\Phi,\mathrm{w}} = 0.1\,\mu\Phi_0/\sqrt{\mathrm{Hz}}$ and its low frequency noise contribution to be $S_{\Phi,1/\mathrm{f}} = 3.0\,\mu\Phi_0/\sqrt{\mathrm{Hz}}/f^\alpha$, with $\alpha = 0.9$. The noise energy $\epsilon(f) = S_\Phi(f)/2L$ defines the energy resolution of a dc-SQUID, a property that will be further discussed in section 3.2.3. Calculating the noise energy for the hypothetical SQUID at higher frequencies shows, that $\epsilon_\mathrm{w} \approx 1.5\hbar$, with $\hbar$ denoting the reduced Planck's constant. Therefore, the dc-SQUID that was assumed for the noise simulations nearly has a so called quantum-limited noise performance. The latter would mean, that the energy resolution of the SQUID is only limited by the uncertainty principle $\Delta E\cdot\Delta t \geq \hbar/2$. The parasitic inductance contribution of the required bonding wires is assumed to be 0.5 nH.

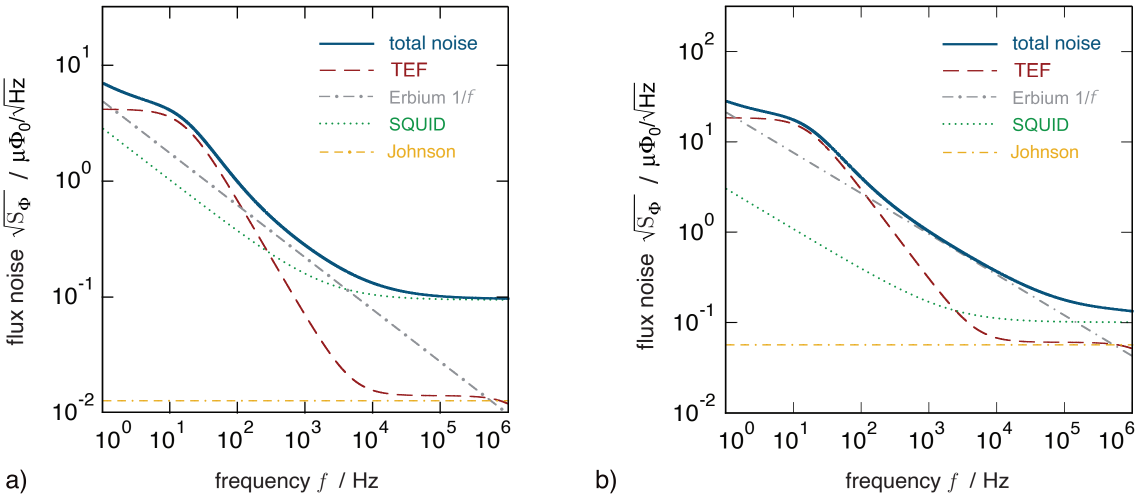

Figure 2.8: Calculated flux noise spectrum as well as the noise spectra of the individual noise sources present within an MMC. The basis for this calculation are an absorber and sensor with comparable properties to the ones developed in this thesis. a) MMC with transformer coupled readout. b) MMC with direct sensor readout. Further details are explained in the text.

For comparison, figure 2.8 b) shows a calculated noise spectrum for an MMC with direct sensor readout. For this ideal case, the same simulation parameters were used as in a). The noise simulations show, that for the transformer coupled readout, the SQUID noise is a significant contribution to the overall noise spectrum for all frequencies relevant to the discussion. At high frequencies, where a near quantum-limited noise performance was assumed, the SQUID dominates the noise spectrum and the Johnson noise of the sensor and absorber is still one order of magnitude smaller than the white noise of the SQUID. It becomes apparent, that by making use of the transformer coupled readout for metallic magnetic calorimeters, the achievable energy resolution, as derived in the following section, will usually not reach the lower limit that is set by the detector intrinsic noise contributions. For the direct sensor readout, it can be seen that the white noise contributions of the SQUID, the high frequency plateau of the thermodynamic energy fluctuations, and the Johnson noise are of a comparable magnitude, whereas the low frequency regime is completely dominated by the noise contributions of the MMC, and the $1/f$-like noise contribution of the SQUID is basically negligible. Therefore, the energy resolution of an MMC using the direct sensor readout is only effected by the noise contributions of the SQUID at higher frequencies, and to a significantly smaller degree than for the transformer coupled readout.

2.6.4 Energy resolution of metallic magnetic calorimeters

In the case for metallic magnetic calorimeters, the signal amplitude E_0 of a noisy signal with shape $s(t) = E_0 p(t) + n(t)$ can be determined via optimal filtering [McC05]. For an undisturbed signal that is described by an amplitude E_0 and by the responsivity $p(t)$ given in equation 2.16, the method of optimal filtering assumes, that such a signal can be superimposed by a noise term $n(t)$. When the noisy detector signal $E(t)$ is divided into N equidistant frequency intervals Δf in the frequency space, the Fourier transform of frequency interval i is given by

$$\tilde{s}_i = E_0 \tilde{p}_i + \tilde{n}_i \, . \tag{2.21}$$

Here, $\tilde{p}_i$ denotes the Fourier transform of the responsivity $p(f)$ of the frequency interval i, given by

$$|\tilde{p}(f)| = \frac{2\beta\tau_1}{\sqrt{1+(2\pi\tau_0 f)^2}\sqrt{1+(2\pi\tau_1 f)^2}} \, , \tag{2.22}$$

and $\tilde{n}_i$ denotes the noise amplitude of the frequency interval i. Each Fourier transform component $\tilde{s}_i$ is proportional to the amplitude E_0 of the detector signal. Since the noise in each frequency interval is uncorrelated, N approximations E_i can be made for the amplitude E_0. The latter is then determined by the weighted average

$$E_0 = \sum_i w_i E_i \quad \text{with} \quad w_i = \frac{{SNR_i}^2}{\sum\limits_j {SNR_j}^2} \, , \tag{2.23}$$

where SNR_i denotes the signal-to-noise ratio of the respective frequency interval i. The $SNR(f)$ can be calculated by

$$SNR(f) = \frac{|\tilde{p}(f)|}{\sqrt{S_{\Phi,\mathrm{tot}}(f)}} \, , \tag{2.24}$$

where the numerator $|\tilde{p}(f)|$ is given by equation 2.22, while the denominator $\sqrt{S_{\Phi,\mathrm{tot}}(f)}$ represents the total apparent flux noise in the SQUID. Therefore, frequency intervals with a higher SNR are also weighted higher for determining the signal amplitude. The standard deviation of the energy E_0, that is determined by equation 2.23, is a measure of the energy resolution of the detector:

$$\Delta E_{\mathrm{FWHM}} = 2\sqrt{2\ln 2}\left(\int\limits_0^\infty SNR^2(f)\,\mathrm{d}f\right)^{-1/2} \, . \tag{2.25}$$

When considering only the thermodynamic energy fluctuations of the MMC, an expression for the fundamental limit of its achievable energy resolution can be computed. This noise contribution can be calculated from equation 2.20 to

$$S_{\mathrm{E_Z,TEF}} = \beta^2 \left[\left(\frac{\delta \Phi_\mathrm{S}}{\delta \Phi} \right) \left(\frac{\delta \Phi}{\delta E} \right) \right]^{-2} S_{\Phi_\mathrm{S},\mathrm{tot}} \,. \tag{2.26}$$

Now, combining equation 2.24, 2.25, and 2.26 yields the expression

$$\Delta E_\mathrm{FWHM} = 2.35 \sqrt{4 k_\mathrm{B} T^2 C_\mathrm{e}} \left(\frac{1}{\beta(1-\beta)} \frac{\tau_0}{\tau_1} \right)^{1/4} , \tag{2.27}$$

that defines a fundamental limit of the achievable energy resolution of a metallic magnetic calorimeter. Equation 2.27 evidently shows, that a minimization of the achievable energy resolution requires a low operation temperature T, a fast signal rise τ_0 that is limited by the intrinsic thermalization between conduction electrons and magnetic moments, as it was discussed in section 2.3.1, and requires a slow signal decay τ_1 without reducing the count rate of the detector to be lower than experimentally required. In addition, $\beta = C_\mathrm{z}/(C_\mathrm{z} + C_\mathrm{e}) = 1/2$ should be fulfilled, i.e. the heat capacity of the conduction electrons of the absorber and sensor should be matched to the heat capacity of the magnetic moments of the sensor.

2.7 Linearity of metallic magnetic calorimeters

For a detector with perfect linearity, the signal height is given by the constant ratio $\delta\Phi/\delta E$, as discussed in section 2.6.1. However, as the temperature of the detector increases after a particle has been absorbed, its thermodynamic properties change with respect to the baseline temperature of the MMC during this heat pulse. Therefore, the heat capacity of the detector C_tot increases and the temperature dependence of the magnetization $\partial M/\partial T$ changes during the signal rise, i.e. until the detector is thermalized with the heat bath. Since the magnitude of this property change depends on the temperature increase δT, a non-linear behavior of the detector response arises for the absorption of particles with increasing energy. This non-linear behavior can be described by

$$E_\mathrm{m} = \left(\frac{\partial \Phi_\mathrm{S}}{\partial E} \right)^{-1} \delta \Phi_\mathrm{S} = (1 + \eta(E)) E \,, \tag{2.28}$$

where E_m denotes the measured energy and E denotes the actual photon energy. The non-linearity of the detector can be sufficiently approximated by [Pie12a]

$$\eta(E) = \frac{E}{2C_\mathrm{tot}} \left(\frac{\partial \Phi_\mathrm{S}}{\partial E}\right)^{-1} \frac{\partial}{\partial T} \frac{\partial \Phi_\mathrm{S}}{\partial E} \tag{2.29}$$

for metallic magnetic calorimeters, where $\partial/\partial T(\partial\Phi_\mathrm{S}/\partial E)$ is the partial derivative of the signal height with respect to the temperature.

2.8 State-of-the-art performance of MMCs

The main goal of this thesis is to improve the present-day benchmark of the energy resolution of metallic magnetic calorimeters for soft X-ray spectroscopy. This section therefore presents what the current benchmark performance is for MMCs for the spectroscopy of photons with an energy $E_\gamma < 10\,\mathrm{keV}$.

The maXs-20 detector

The maXs-20 detector was developed in [Sch12]. It is a 1×8 pixel linear array consisting of four metallic magnetic calorimeters. The MMCs use the meander-shaped detector geometry that was discussed in section 2.5, as well as the transformer coupled readout. The meander-shaped pickup coil has a width $w = 2.5\,\mu\mathrm{m}$ and a pitch $p = 5\,\mu\mathrm{m}$. Each absorber is made out of electroplated gold with the dimensions $250 \times 250 \times 5\,\mu\mathrm{m}^3$. Its temperature sensor is made of Au:Er with the dimensions $157 \times 157 \times 1.5\,\mu\mathrm{m}^3$ and an Er concentration of $c_\mathrm{Er} = 315\,\mathrm{ppm}$. With the maXs-20 detector, the fastest measured signal rise for metallic magnetic calorimeters was demonstrated. This achievement is depicted in Figure 2.9 a), which shows the magnetic flux change in the current-sensing SQUID that was used for detector readout, which resulted upon the absorption of X-rays ($E_{\mathrm{K}\alpha} = 5.9\,\mathrm{keV}$, $E_{\mathrm{K}\beta} = 6.49\,\mathrm{keV}$) emitted by an ^{55}Fe calibration source. The depicted signal rise is described by

$$\Delta\Phi_\mathrm{S} = E_0 \cdot (1 - e^{-t/\tau_0})\,, \tag{2.30}$$

with E_0 denoting the signal amplitude and a measured rise time $\tau_0 = 80\,\mathrm{ns}$. The measurement was performed at a temperature $T = 30\,\mathrm{mK}$ and a persistent current of $I_0 = 45\,\mathrm{mA}$. At these operation parameters, the heat capacity of absorber and temperature sensor were $C_\mathrm{abs} = 0.67\,\mathrm{pJ/K}$ and $C_\mathrm{sens} = 1.63\,\mathrm{pJ/K}$, respectively. The expected signal rise time can be estimated according to equation 2.5, resulting in a calculated $\tau_0 = 86\,\mathrm{ns}$, which is only $6\,\mathrm{ns}$ above the measured value. For this calculation, a $\beta = C_\mathrm{z}/(C_\mathrm{z} + C_\mathrm{e} + C_\mathrm{X}) \approx 0.63$ is required. The factor C_X is an

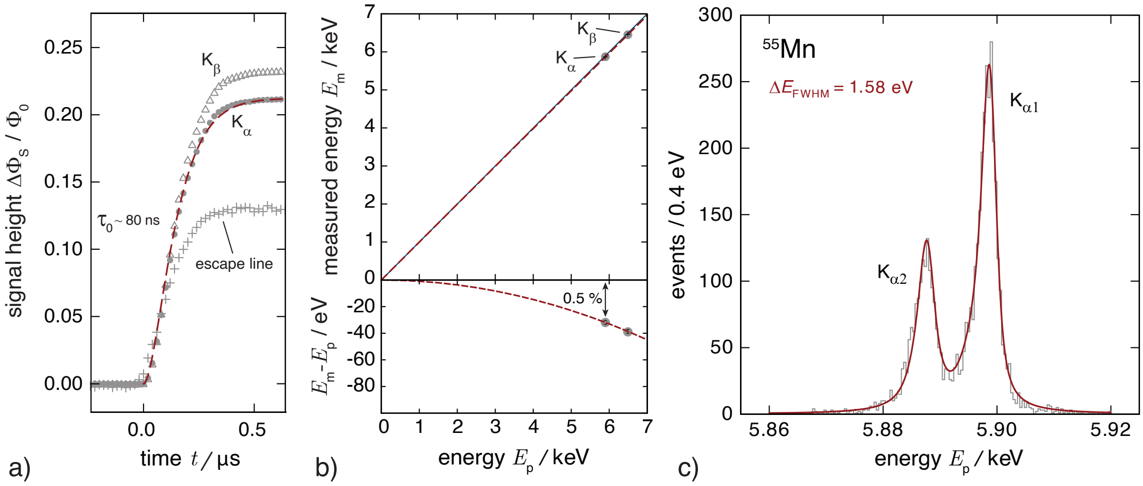

Figure 2.9: a) Signal rise of a maXs-20 detector measured with a current-sensing SQUID after X-rays from an ^{55}Fe callibration source have been absorbed. The data fit (red) shows the expected exponential signal rise with a time constant of $\tau_0 = 80\,\mathrm{ns}$. b) Measured energy E_m as a function of the actual photon energy E_p, illustrating a near perfect linear behavior of the detector with a non-linearity of only 0.5 %. c) Measured energy spectrum of the K$_\alpha$-line of an ^{55}Fe X-ray source. Fitted to the histogram is the expected lineshape when assuming an instrumental resolution of $\Delta E_\mathrm{FWHM} = 1.58\,\mathrm{eV}$. The energy spectrum was measured with a revised version of the maXs-20 detector that was developed in [Heu11].

additional contribution to the total detector heat capacity C_tot that was observed in [Sch12]. It was argued to originate from sputtered Au and Au:Er and was found to also depend on the persistent current I_0. For $I_0 = 45\,\mathrm{mA}$, $C_\mathrm{X} \approx 0.25\,\mathrm{pJ/K}$ was determined. The small deviation between the measured and the calculated τ_0 shows, that the signal rise of an MMC is very well understood and predictable. The maXs-20 detector, and MMCs in general, are the fastest kind of cryogenic microcalorimeters presently available.

Figure 2.9 b) depicts in the upper plot the measured photon energy E_m of the maXs-20 detector as a function of the actual photon energy E_p, with a second-order polynomial function (red dashed line) fitted to the data. The maXs-20 detector shows a close to perfect linear detector response, with a non-linearity $E_\mathrm{m} - E_\mathrm{p}$ of only 0.5 % for 5.9 keV photons, as it is depicted in the lower plot. The measurement was performed in [Sch12] at $T = 23\,\mathrm{mK}$ and $I_0 = 30\,\mathrm{mA}$. The calculated non-linearity given by equation 2.29 also yields an expected non-linearity of 0.5 %. The parameters used for this calculation from numerical simulations are a total detector heat capacity of $C_\mathrm{tot} = 1.84\,\mathrm{pJ/K}$, a signal height per energy input of $\delta\Phi/\delta E = 62.8\,\mu\Phi_0/\mathrm{eV}$, and a derivative of $\partial/\partial T(\partial\Phi_\mathrm{S}/\partial E) = -28.1\,\mathrm{m}\Phi_0/(\mathrm{eVK})$. This shows that the linearity of a metallic magnetic calorimeter a well understood and predictable property.

Revised maXs-20 detector

While the maXs-20 detector presents the MMC benchmark for a fast signal rise with excellent linearity, its signal-to-noise ratio is not sufficient to simultaneously present the benchmark for the best energy resolution achieved with an MMC for the spectroscopy of photon energies $E < 10\,\mathrm{keV}$. The detector that holds this record is a revised version of the maXs-20 detector that was developed in [Heu11]. In this revision, the absorber size is identical to the regular maXs-20 detector, but the meander-shaped detector geometry was replaced by a spiral-shaped pickup coil that is galvanically connected to a superconducting cap on top of the sensor, which has the colloquial expression ”sandwich geometry”. This detector geometry significantly enhances the signal coupling between the MMC and the current-sensing dc-SQUID used for signal readout, improving the signal-to-noise ratio and therefore the achievable energy resolution. However, the signal rise of this detector had to be artificially slowed down to a few microseconds by introducing a thermal bottleneck between absorber and sensor. Otherwise, the slew-rate limit of the readout chain would have been reached, i.e. a tracking of the resulting large signal heights would not have been possible with the employed readout chain. The achieved energy resolution of this revised maXs-20 for 5.9 keV photons is shown in figure 2.9 c). The plot shows the energy spectrum of the K_α-lines of a ^{55}Fe source measured at a temperature of $T = 13\,\mathrm{mK}$ [Kem18]. The curve fitted to the data is a convolution of the natural linewidth of the K_α-line and a Gaussian distribution with an instrumental energy resolution of $\Delta E_\mathrm{FWHM} = 1.58\,\mathrm{eV}$, resulting in a detector resolving power of $E/\Delta E_\mathrm{FWHM} \approx 3700$. Therefore, metallic magnetic calorimeters start to push towards the resolving power of the best crystal spectrometers available, which can be well over 10000 [See17], while simultaneously covering a significantly larger, detectable dynamic range than crystal spectrometers.

3. Superconducting Quantum Interference Device

This thesis focuses on the development of integrated detectors for the high resolution soft X-ray spectroscopy, where the paramagnetic temperature sensor of a metallic magnetic calorimeter shall be placed directly on top of a dc-SQUID. This also includes the development and optimization of the corresponding dc-SQUID. Therefore, the fundamentals that are required for the comprehension of such a device are discussed in this chapter.

3.1 Basics of Josephson tunnel junctions

Josephson tunnel junctions are a central element of a dc-SQUID and can be visualized as a plate capacitor consisting of two superconducting electrodes that are separated from each other by a few nanometer-thin insulation layer. The thickness of this thin layer has to be chosen such that the macroscopic wave functions of both superconducting electrodes overlap. The Josephson junctions fabricated within the framework of this thesis are made out of an $\mathrm{Nb/Al{-}AlO_x/Nb}$ trilayer, where the aluminium oxide represents the insulating barrier. In such a tunnel junction, Cooper pairs can coherently tunnel between both electrodes [Jos62], which is called the Josephson effect. The supercurrent I_s through the junction carried by the tunneling Cooper pairs is described by the first Josephson equation [Jos62]:

$$I_\mathrm{s} = I_\mathrm{c} \sin{(\phi)}\,. \tag{3.1}$$

There, I_c denotes the critical current of the tunnel junction and ϕ the gauge-invariant phase difference between the macroscopic wave functions Ψ_1 and Ψ_2 of both superconducting electrodes, given by

$$\phi = \theta_2 - \theta_1 - \frac{2\pi}{\Phi_0}\int\limits_1^2 \boldsymbol{A}\cdot \mathrm{d}\boldsymbol{l}\,, \tag{3.2}$$

with the magnetic vector potential $\boldsymbol{A}$ within the insulating barrier. θ_1 and θ_2 represent the phases of the macroscopic wave functions. In addition, the phase difference evolves in time for a finite voltage drop across the junction according to the second Josephson equation [Jos62]

$$U = \frac{\Phi_0}{2\pi}\dot{\phi}\,. \tag{3.3}$$

Equation 3.1 and 3.3 represent a foundation for many effects, with the most well known being the DC Josephson effect and the AC Josephson effect. Both of which shall be briefly described.

When an external current source is connected to a Josephson junction and a current $I < I_\mathrm{c}$ is applied, then this current can be carried by Cooper pairs and the constant phase difference ϕ of the two superconducting electrodes is adjusted according to equation 3.1. This means that no voltage drop occurs across the junction according to equation 3.3. This is called the DC Josephson effect. Increasing the externally applied current to $I > I_\mathrm{c}$ leads to an excess current $I_\mathrm{e} = I - I_\mathrm{c}$ that is carried by quasiparticles, resulting in a voltage drop U across the junction. As a result, the phase difference ϕ increases linearly with time according to equation 3.3, leading to the AC Josephson effect, which describes an alternating supercurrent

$$I_\mathrm{s} = I_\mathrm{c} \sin\left(\omega_\mathrm{J} t + \phi\right). \tag{3.4}$$

through the junction. The ac frequency is given by $f_\mathrm{J} = \omega_\mathrm{J}/(2\pi U) = 1/\Phi_0 \approx 485\,\mathrm{MHz}/\mu\mathrm{V}$ within the Josephson junction according to equation 3.1.

3.1.1 *IV*- characteristics of Josephson junctions

Figure 3.1 shows the current-voltage characteristic of a hysteretic Josephson junction which was fabricated within the framework of this thesis and characterized at $T = 4.2\,\mathrm{K}$ in a liquid helium transport dewar. The measurement was performed with a four wire sensing method. In addition, figure 3.1 also illustrates several figures of merit used to characterize a tunnel junction in order to determine its quality, as will be further discussed at the end of this section. As it can be seen, the voltage drop across the Josephson junction is $U = 0\,\mathrm{V}$ for $I < I_\mathrm{c}$. Once the current exceeds the the critical current, an additional quasiparticle flow I_e and a voltage drop across the junction occurs, indicated by the sharp voltage jump at the point marked by I_c and the red arrow pointing to the right in figure reffig:JJcharacteristic. In order for a cooper pair to break up into two quasiparticles, the energy $eU_\mathrm{g}(T) = [\Delta_1(T) + \Delta_2(T)]$ needs to be provided, for instance by an external circuit. Here, $\Delta_1(T)$ and $\Delta_2(T)$ denote the respective energy gap of the superconducting electrodes, and $U_\mathrm{g}(T)$ denotes the so called gap voltage of the Josephson tunnel junction. When the current I is increased further, so that $U \gg U_\mathrm{g}$, then the junction switches into its voltage state, where it exhibits an ohmic behavior. The excess quasiparticle current is then given by $I_\mathrm{e} = U/R_\mathrm{N}$, with R_N denoting the so called normal state resistance of the Josephson junction.

When the Josephson junction is in its voltage state and the current I is reduced, then the junction switches back into its zero-voltage state at a so called retrapping

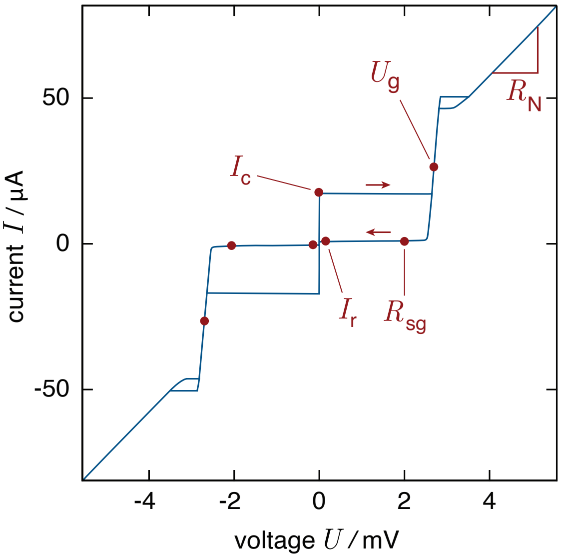

Figure 3.1: Measured current-voltage characteristic of an unshunted Josephson junction, which was fabricated within the framework of this thesis. In addition, several figures of merit are depicted that are used to discern the quality of a Josephson tunnel junction. These include the critical current I_c, the subgap resistance R_sg, the normal state resistance R_N, and the gap voltage U_g.

current $I_\mathrm{r} < I_\mathrm{c}$. In this case, the IV-characteristic moves along the so called subgap regime for $U < U_\mathrm{g}$, the path indicated by the red arrow pointing to the left, where a finite amount of quasiparticles exist due to thermal excitations at $T > 0\,\mathrm{K}$. This regime is denoted by a characteristic subgap resistance R_sg, a figure of merit used to discern the quality of a Josephson tunnel junction, as will be discussed later on.

3.1.2 RCSJ-model

The IV-characteristic of a Josephson tunnel junction can be described by the RCSJ[1] model [McC68, Ste68], in which the junction is represented by the equivalent circuit shown figure 3.2 a). The schematic depicts a parallel circuit consisting of an ideal Josephson junction with critical current I_c, a capacitance C, a resistance $R(U)$ and a noise current I_F. The resistance $R(U)$ is highly non-linear and has two different values depending on the voltage U across the junction, as was already indicated in the previous section. For $|U| > U_\mathrm{g}$, the resistance is given by the normal state resistance of the Josephson tunnel junction, i.e. $R(U) = R_\mathrm{N}$. For $|U| \leq U_\mathrm{g}$, the resistance is given by the subgap resistance $R(U) = R_\mathrm{g}$ of the Josephson tunnel junction. The noise current I_F originates from cooper pairs being broken up into quasiparticles due to thermal excitations at $T > 0\,\mathrm{K}$. According to the RSCJ-model, the total external current I running through a Josephson tunnel junction is given by

$$I = C\dot{U} + \frac{U}{R(U)} + I_\mathrm{s} + I_\mathrm{F}\,, \tag{3.5}$$

where the first term of the equation represents the displacement current, the second term denotes the flow of quasiparticles, the third term is the supercurrent given by

---

[1] **A**bbreviation for Resistively- and **C**apacatively-**S**hunted **J**unction

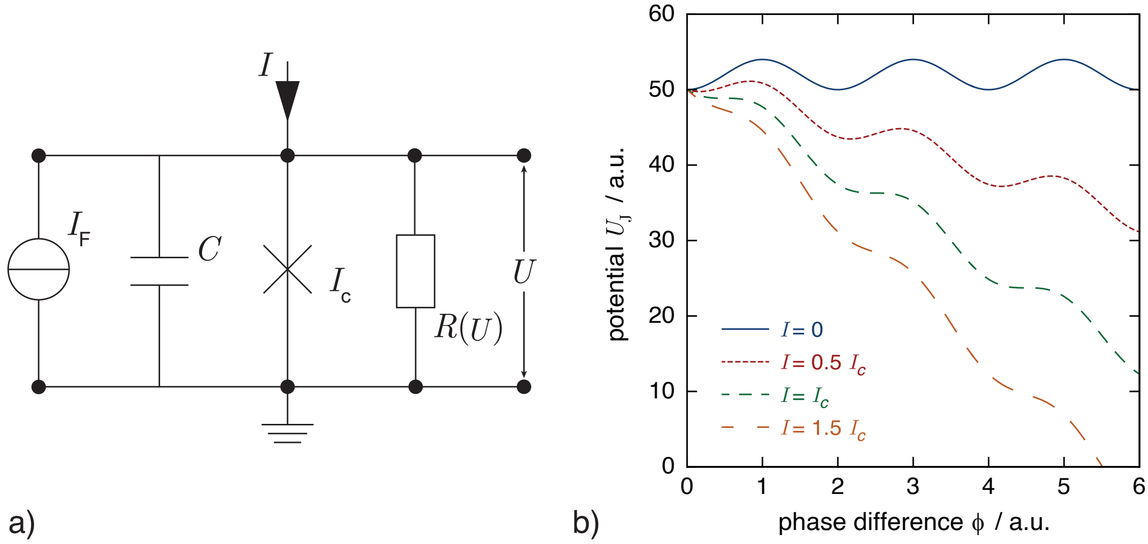

Figure 3.2: a) Equivalent circuit of a Josephson junction within the RCSJ-model. b) Tilted washboard potential U_J as a function of the gauge-invariant phase difference ϕ between both superconducting electrodes for different bias currents I through the Josephson tunnel junction.

the first Josephson equation 3.1 and the last term is the noise current I_F. Making use of equation 3.3 leads to an equation of motion for the gauge-invariant phase difference ϕ

$$I = I_\mathrm{c}\sin(\phi) + \frac{\Phi_0}{2\pi}C\ddot{\phi} + \frac{\Phi_0}{2\pi}\frac{1}{R(U)}\dot{\phi} + I_\mathrm{F}\,. \tag{3.6}$$

This equation is mathematically equivalent to equation of motion of a particle with mass $m = (\Phi_0/2\pi)C$, on which a friction force is exerted that is characterized by the damping coefficient $\nu = (\Phi_0/2\pi)/R$, and which is moving in the so-called tilted washboard potential U_J. This potential is depicted in figure 3.2 b) and is given by

$$U_\mathrm{J}(\phi) = \frac{\Phi_0}{2\pi}\Big[I_\mathrm{c}(1-\cos(\phi)) - (I + I_\mathrm{F})\phi\Big]\,. \tag{3.7}$$

The plot shows that the potential tilts further and further with increasing bias current I. For $I < I_\mathrm{c}$, the particle is trapped in one of the minima of the potential. Therefore, the time average of the phase difference $\langle\dot{\phi}\rangle$ vanishes, meaning no voltage drop occurs across the junction, i.e. it is in its zero-voltage state. For $I \geq I_\mathrm{c}$, the particle moves along the tilted washboard potential, leading to a voltage drop according to the second Josephson equation, which is consequently called the voltage-state. Reducing the current to a retrapping current $I_\mathrm{r} \leq I_\mathrm{c}$ leads to the particle being trapped again in one of the reoccurring minima of the potential, i.e. the junction switches back to the zero-voltage state. However, whether the particle is trapped again at $I_\mathrm{r} = I_\mathrm{c}$, or at $I_\mathrm{r} < I_\mathrm{c}$, depends on the mass and the damping coefficient of the particle.

This possible hysteretic behavior is described in the RCSJ model by introducing the dimensionless Stewart-McCumber parameter

$$\beta_\mathrm{c} = \frac{2\pi}{\Phi_0} I_\mathrm{c} R_\mathrm{N}^2 C\,. \tag{3.8}$$

For $\beta_\mathrm{c} \ll 1$, the Josephson tunnel junction is highly damped and the particle will be trapped in a potential minimum at $I_\mathrm{r} \approx I_\mathrm{c}$. For $\beta_\mathrm{c} \gg 1$, the junction is underdamped and the retrapping current I_r can be described by [Lik86]

$$\frac{I_\mathrm{r}}{I_\mathrm{c}} = \frac{4}{\pi\sqrt{\beta_\mathrm{c}}}\,. \tag{3.9}$$

In this case, the Josephson tunnel junction shows a hysteretic behavior as the retrapping current is close to zero [Cla04]. Such an IV-characteristic was already shown in figure 3.1. In order to suppress a hysteretic behavior, a shunt resistor $R_\mathrm{S} \gg R_\mathrm{N}$ can be connected in parallel to the Josephson junction. In this case, R_N is replaced by R_S in equation 3.8, making β_c an adjustable design parameter.

Sub gap voltage: The sub gap voltage $U_\mathrm{g}(T) = [\Delta_1(T)+\Delta_2(T)]/e$ depends on the energy gaps Δ_1 and Δ_2 of the superconducting electrodes of the tunnel junction, both of which are made out of niobium for the junctions fabricated during this thesis. For bulk niobium, the energy gap 2Δ reaches values between 2.92 meV and 3.02 meV for $T \to 0$ [Car90], and decreases with temperature according to the BCS[2] theory. The energy gap Δ, and with it the gap voltage U_g of a junction can be reduced through various means, including the proximity effect of the normal conducting aluminum within the junction [Hou93, Yam94], or via mechanical stress in the used materials [Kur88]. For Nb/Al-AlO$_\mathrm{x}$/Nb junctions at $T = 4.2\,\mathrm{K}$, values between 2.83 mV and 2.93 mV are expected for U_g, assuming the thickness of the Nb electrodes is larger than the London penetration depth λ_L.

$I_\mathrm{c}R_\mathrm{N}$ product: The critical current I_c of a Josephson tunnel junction depends on the coupling strength between the two superconducting electrodes. Therefore, I_c becomes larger when the insulating barrier within the junction becomes thinner. In addition, I_c scales linearly with the junction area A_J. In contrast to that, the normal state resistance R_N of a Josephson tunnel junction decreases when the insulating barrier becomes thinner and also decreases linearly with A_J. It is therefore assumed that the $I_\mathrm{c}R_\mathrm{N}$ product is independent of the barrier thickness and junction area. The Ambegaokar-Baratoff-theory [Amb63] provides an expectation for $I_\mathrm{c}R_\mathrm{N}$ when

---

[2] Abbreviation for **B**ardeen-**C**ooper-**S**chrieffer

the junction electrodes are made out of the same material with identical energy gap

$$I_\mathrm{c}R_\mathrm{N} = \frac{\pi}{2e}\Delta(T)\tanh\left[\frac{\Delta(T)}{2k_\mathrm{B}T}\right]. \tag{3.10}$$

For Nb/Al$-$AlO$_\mathrm{x}$/Nb junctions, the $I_\mathrm{c}R_\mathrm{N}$ product is expected to reach values between 2.29 mV and 2.37 mV for $T \to 0$. However, these values are not often reached in actual applications because the derivation of equation 3.10 assumes ideal Cooper pair tunneling with a rectangular potential barrier in the insulating layer. In reality, the potential barrier has sloped walls and an inhomogeneous barrier thickness across the junction area, resulting in a reduced value for an experimentally determined $I_\mathrm{c}R_\mathrm{N}$ product compared to the theoretical expectation.

Subgap resistance: For Nb/Al$-$AlO$_\mathrm{x}$/Nb Josephson tunnel junctions, the subgap resistance R_sg is usually defined as the resistance of the junction at a voltage drop of $U = 2\,\mathrm{mV}$. Its occurrence has multiple, non-trivial causes, like the flow of thermally excited quasi particles, Andreev-reflexions [Oct83], or multi-particle tunneling processes of Cooper pairs [Tay63, Sch63], all of which are not of importance for the present work and shall therefore not be discussed further. It is noted that, just like the $I_\mathrm{c}R_\mathrm{N}$-product, the ratio of the subgab to normal state resistance, $R_\mathrm{sg}/R_\mathrm{N}$, and the characteristic voltage $U_\mathrm{c} = R_\mathrm{sg} \cdot I_\mathrm{c}$, are parameters used to compare congeneric Josephsen junctions to each other. High quality junctions are indicated by $R_\mathrm{sg}/R_\mathrm{N} > 10$ and $U_\mathrm{c} > 30\,\mathrm{mV}$.

3.2 Basics of dc-SQUIDs

3.2.1 Working principle and design considerations

A basic schematic of a dc-SQUID is depicted in figure 3.3 a). It consists of a superconducting loop with inductance L_S, that is interrupted by two Josephson junctions, which are assumed to be identical in the description at hand. A shunt resistor R_S is connected in parallel to each junction to avoid a hysteretic junction behavior, as it was discussed in section 3.1.2.

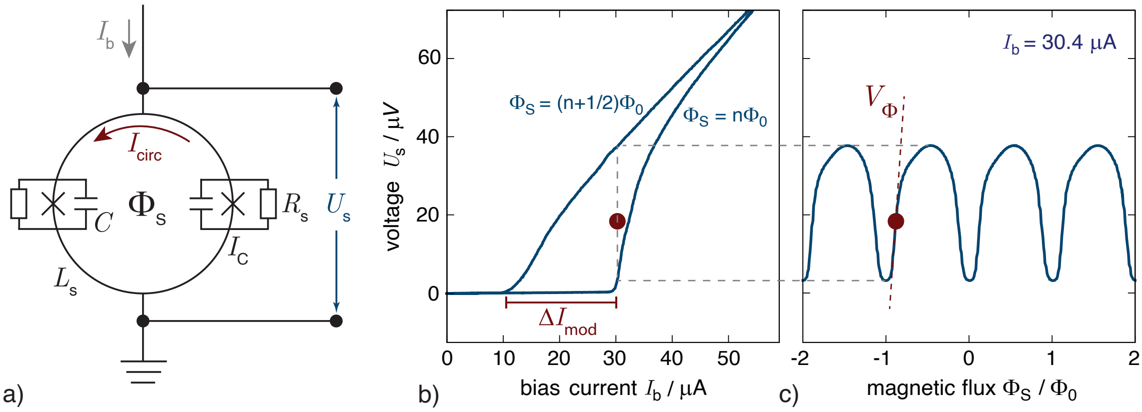

Figure 3.3: a) Schematic of a dc-SQUID consisting of a closed superconducting loop with inductance L_S that is interrupted by two Josephson junctions with critical current I_c. A shunt resistor R_S is connected in parallel to each junction, suppressing their hysteretic behavior. b) Exemplary current-voltage characteristics of a dc-SQUID shown for two values of the magnetic flux Φ_S threading the SQUID loop, that leads to a minimum or maximum critical current, respectively. c) Voltage-flux characteristic resulting from an applied bias current of $I_\mathrm{b} = 30.4\,\mu\mathrm{A}$.

The supercurrent through the dc-SQUID is given by [Cla04]

$$I_\mathrm{S} = 2 I_\mathrm{c} \cos\left(\frac{\pi \Phi_\mathrm{S}}{\Phi_0}\right) \sin\left(\phi_1 + \frac{\pi \Phi_\mathrm{S}}{\Phi_0}\right), \tag{3.11}$$

where ϕ_1 denotes the phase of one Josephson junction and Φ_S denotes the magnetic flux threading the SQUID loop. Φ_S has two constituents, one being the externally applied magnetic flux Φ_ext. The other constituent is a self-induced magnetic flux Φ_L, which results from a circulating current $I_\mathrm{circ} = -\Phi_\mathrm{ext}/L_\mathrm{S}$, that is induced in order to maintain flux quantization within the SQUID loop [Dol61]. The total magnetic flux Φ_S within the SQUID is then given by [Bar82]

$$\Phi_\mathrm{S} = \Phi_\mathrm{ext} + \Phi_\mathrm{L} = \Phi_\mathrm{ext} - L_\mathrm{S} I_\mathrm{c} \sin\left(\frac{\pi \Phi_\mathrm{S}}{\Phi_0}\right) \cos\left(\phi_1 + \frac{\pi \Phi_\mathrm{S}}{\Phi_0}\right). \tag{3.12}$$

The equations 3.11 and 3.12 only have analytical solutions when the SQUID is operated in the so called zero-voltage-state for $I_\mathrm{b} \ll I_\mathrm{c,SQ}$ and only for the two limiting cases $\Phi_\mathrm{L} \simeq 0$ and $\Phi_\mathrm{L} \gg \Phi_0$. However, actual practical application is done in the so called voltage-state. In this mode of operation, the bias current is usually fixed at a value $I_\mathrm{b} \geq 2I_\mathrm{c}$, leading to a quasiparticle current through the shunted Josephson junctions, resulting in a voltage drop across the SQUID. An exemplary IV-characteristic is plotted in figure 3.3 b), representing the voltage response of a dc-SQUID as a function of the applied bias current I_b. It can be seen, that the voltage response is maximized for $\Phi_\mathrm{S} = (n + 1/2)\Phi_0$, and minimized for $\Phi_\mathrm{S} = n\Phi_0$. Figure 3.3 c) shows the periodic $V\Phi$-characteristic of the SQUID at constant bias current with $I_\mathrm{b} = 30.4\,\mu\mathrm{A}$. The optimum performance is achieved when the SQUID is operated at the point of highest flux sensitivity, which is done by choosing the working point at which the figures of merit, given by

$$V_\Phi = \frac{\partial U}{\partial \Phi_\mathrm{S}} \qquad \text{and} \qquad I_\Phi = \frac{\partial I}{\partial \Phi_\mathrm{S}}\,, \tag{3.13}$$

are maximized. Here, V_Φ is the flux-to-voltage transfer coefficient at constant bias current (current-bias) and I_Φ is the flux-to-current transfer coefficient at constant bias voltage (voltage bias). With these two figures of merit, the so called dynamic resistance can be defined as $R_\mathrm{dyn} = V_\Phi/I_\Phi$, which is the slope of the IV-characteristic at the chosen working point. The optimum working point is marked in red in figure 3.3 b) and c) and can be adjusted by applying an appropriate external magnetic field. At this point, the SQUID has a linear voltage output $U_\mathrm{s} = V_\Phi \delta\Phi$ in response to additional flux changes $\delta\Phi$, assuming $\delta\Phi_\mathrm{S} \leq \pm\Phi_0/4$. In addition, the maximum modulation of the SQUID's critical current ΔI_mod as a response to a change of magnetic flux $\delta\Phi_\mathrm{S}$ is marked in figure 3.3 b). The magnitude of this modulation can be described by [Tes77]

$$\Delta I_\mathrm{mod} = \mathcal{A}(\beta_\mathrm{L}) \cdot 2I_\mathrm{c} \qquad \text{with} \qquad \beta_\mathrm{L} = \frac{2L_\mathrm{S}I_\mathrm{c}}{\Phi_0}\,, \tag{3.14}$$

where $\mathcal{A} \leq 1$ is a dimensionless number and β_L is the so called screening parameter. The latter is a measure of the contribution of the self-induced flux Φ_L to the total magnetic flux Φ_S. For the limiting case $\beta_\mathrm{L} \ll 1$, Φ_L can be neglected so that $\Phi_\mathrm{S} \approx \Phi_\mathrm{ext}$ and $\mathcal{A}$ approaches 1. For the other limiting case $\beta_\mathrm{L} \gg 1$, Φ_L makes a significant contribution to the overall SQUID behavior, as it strives towards flux quantization within the SQUID loop. In this case, $\mathcal{A}$ approaches zero and barely any critical current modulation occurs. In order to maximize ΔI_mod, β_L has to be as small as possible. This can be achieved by reducing the SQUID inductance L_S further and further. However, this rarely presents any practical application, as such a SQUID consequently shows only a negligible response to external magnetic fields. Numerical simulations show, that an optimized SQUID performance is achieved for $\beta_\mathrm{C}, \beta_\mathrm{L} \approx 1$ for $T = 4.2\,\mathrm{K}$ [Tes77]. At this point, the critical current modulation of the SQUID is $\Delta I_\mathrm{mod} = 0.96 \cdot I_\mathrm{c}$.

3.2.2 SQUID noise

Figure 3.4 shows a typical spectrum of the apparent flux noise of a dc-SQUID that was measured at $T = 20\,\mathrm{mK}$. It can be seen, that it is composed of a frequency-independent white noise contribution $\sqrt{S_{\Phi,\mathrm{w}}}$ and a frequency-dependent $1/f$-like noise contribution $\sqrt{S_{\Phi,1/f}}$. The origin of the white noise contribution $\sqrt{S_{\Phi,\mathrm{w}}}$ of a dc-SQUID is the Nyquist current noise of the shunt resistors connected in parallel to the Josephson junctions. The spectral power density of the Nyquist current noise of a resistor R is given by

$$S_I(f) = \frac{4k_\mathrm{B}T}{R}\,, \tag{3.15}$$

showing that it scales linearly with the temperature T, and is inversely proportional to the resistance R.

In a dc-SQUID, the current noise power spectral density S_I can be split into an in-phase contribution $S_I^\mathrm{in} = 4k_\mathrm{B}T/(R_\mathrm{S}/2)$ and into an out-of-phase contribution $S_I^\mathrm{out} = 4k_\mathrm{B}T/(2R_\mathrm{S})$. The former is related to the current fluctuations in both resistors having the same direction, i.e. the noise current is flowing through the entire SQUID, while the latter is related to the current fluctuations having opposite direction, i.e. they flow along the SQUID loop. The total white noise contribution is a superposition of both contributions, given by [Lik72, Koc80]

$$S_{V,\mathrm{w}} = S_I^\mathrm{in} \cdot R_\mathrm{dyn} + S_I^\mathrm{out} \cdot L_\mathrm{S}^2 V_\Phi^2 = \frac{4k_\mathrm{B}T}{R_\mathrm{S}} \left[2R_\mathrm{dyn}^2 + \frac{L_\mathrm{S}^2 V_\Phi^2}{2} \right]. \tag{3.16}$$

For an optimized dc-SQUID, i.e. $\beta_\mathrm{C}, \beta_\mathrm{L} \approx 1$, the approximations $R_\mathrm{dyn} \approx \sqrt{2}R_\mathrm{S}$ and $V_\Phi \approx R_\mathrm{S}/L_\mathrm{S}$ hold [Tes77, Bru82], resulting in a voltage power spectral density of the white noise

$$S_{V,\mathrm{w}} = 18k_\mathrm{B}TR_\mathrm{S}\,. \tag{3.17}$$

The apparent flux noise in the SQUID that results from this white noise contribution is given by

$$S_{\Phi,\mathrm{w}} = \frac{S_{V,\mathrm{w}}}{V_\Phi^2}\,. \tag{3.18}$$

The power spectrum of the $1/f$-like noise contribution can be described by

$$S_{\Phi,1/f}(f) = S_{\Phi,1/f}(1\,\mathrm{Hz})/f^\alpha\,, \tag{3.19}$$

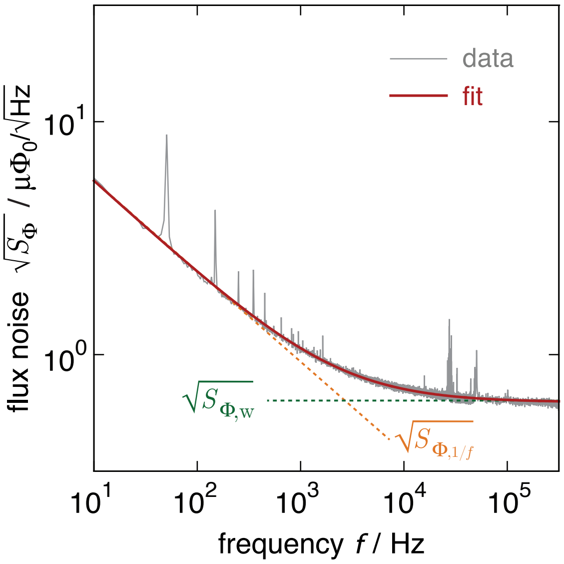

Figure 3.4: Exemplary spectrum of the apparent flux noise of a dc-SQUID measured at $T = 20\,\mathrm{mK}$. It is composed of a white noise contribution $\sqrt{S_{\Phi,\mathrm{w}}}$, marked as a green dotted line, and a $1/f$ noise contribution $\sqrt{S_{\Phi,1/f}}$, marked as an orange dotted line. Equation 3.20 is fitted to the data.

i.e. by the noise amplitude at 1 Hz divided by the frequency f^α, in which the noise exponent α typically has values between 0.4 and 1.5 for a variety of superconducting quantum devices [Kem16]. This low frequency excess flux noise was observed for the first time over 30 years ago [Koc83], and even after decades of investigation [Wel87, Hub97, Dru11], its definitive origin is still not well understood. The noise contribution might result from a random reversal of interacting surface spins [Koc07], that are most likely located at the interface of the metallic constituents and the oxide layer on their surface [Fao08]. These spins can result from metal-induced gap states [Cho09], dangling bonds [dS07], adsorbed oxygen [Wan15], or nuclear spins [LaF15].

The total apparent flux noise in the SQUID can be computed by

$$\sqrt{S_\Phi} = \sqrt{S_{\Phi,\mathrm{w}} + S_{\Phi,1/f}}\,. \tag{3.20}$$

3.2.3 Energy sensitivity

The energy sensitivity ϵ_s of a SQUID is a figure of merit used to compare the performance of SQUIDs with different loop inductances L_S with each other. It is defined as

$$\epsilon_\mathrm{s}(f) := \frac{S_\Phi(f)}{2L_\mathrm{S}} = \frac{S_\mathrm{V}(f)}{2L_\mathrm{S}{V_\Phi}^2}\,, \tag{3.21}$$

i.e. the voltage noise power density S_V divided by the SQUID inductance L_S and the flux-to-voltage transfer coefficient ${V_\Phi}^2$. Numerical simulations show, that the intrinsic energy sensitivity of a dc-SQUID reaches a minimum for $\beta_\mathrm{C} = \beta_\mathrm{L} \approx 1$ for

$T = 4.2\,\mathrm{K}$ [Tes77], and is given by

$$\epsilon_{\mathrm{s}}(f) \approx \frac{9k_{\mathrm{B}}TL}{R_{\mathrm{N}}} \simeq 16k_{\mathrm{B}}T\sqrt{\frac{L_{\mathrm{S}}C}{\beta_{\mathrm{C}}}} \simeq 16\sqrt{\pi}k_{\mathrm{B}}T\sqrt{\frac{\Phi_0 C_{\mathrm{j}}}{2\pi j_{\mathrm{c}}}}\,. \tag{3.22}$$

Here, $C_{\mathrm{j}} = C/A_{\mathrm{j}}$ is the specific junction capacitance and $j_{\mathrm{c}} = I_{\mathrm{c}}/A_{\mathrm{j}}$ is the critical current density of the Josephson tunnel junction. Apparently, in order to minimize the energy sensitivity in a SQUID design, the specific junction capacitance should be small, the critical current density should be as high as possible and the operation temperature T of the SQUID should be low. The energy sensitivity ϵ_{s} is usually given in the units of the reduced Planck's constant $\hbar = 1.05 \cdot 10^{-34}$ Js. SQUIDs can reach a quantum limited noise performance, where the energy sensitivity has the lower limit of $\epsilon_{\mathrm{s}} = \hbar$, i.e. it is limited by the uncertainty principle $\Delta E \cdot \Delta t \geq \hbar/2$ [Koc81, Dan83], making them the most sensitive wideband sensors for magnetic flux today.

3.3 Practical dc-SQUIDs

3.3.1 Resonances in SQUIDs

A SQUID loop with inductance L_{S} and the intrinsic capacitance C of the Josephson tunnel junctions form an LC circuit with resonance frequency $f_{\mathrm{res}} = 1/(2\pi\sqrt{L_{\mathrm{S}}C/2})$. The circuit is driven by the AC Josephson currents, as described in section 3.1, where an ac-current with frequency $f_{\mathrm{J}} = U_{\mathrm{s}}/\Phi_0$ occurs, with U_{s} denoting the voltage drop across the SQUID. The formed LC circuit is in resonance for

$$\frac{U_{\mathrm{s}}}{\Phi_0} = \frac{1}{2\pi\sqrt{L_{\mathrm{S}}C/2}}\,. \tag{3.23}$$

When the resonance condition is fulfilled, in the IV-characteristics of a dc-SQUID the two extremal voltage responses for $\Phi_{\mathrm{S}} = n\Phi_0$ and $\Phi_{\mathrm{S}} = (n+1/2)\Phi_0$ can intercept far below the ohmic regime of the characteristics. This is illustrated in figure 3.5 a), which shows an IV-characteristics of a washer SQUID with input coil that was developed in this group. The point of resonance is marked accordingly. In addition to this SQUID intrinsic resonance, coupling an input coil to a SQUID can also lead to parasitic effects in the IV-characteristics, resulting in so called resonant current steps [Enp92] that can also be observed in figure 3.5 a). Since SQUID loop and input coil are spatially separated by a thin insulating layer, a parasitic capacitance C_{p} is introduced, forming an LC circuit with the inductance L_{S} of the SQUID loop, which can also be driven by the ac-currents in the SQUID, potentially leading to resonances in the SQUID itself, or in its input coil. While a dc-SQUID that is developed for the direct sensor readout of a metallic magnetic calorimeter does not require an input coil, placing a paramagnetic temperature sensor directly on top of the SQUID loop can also introduce a parasitic capacitance C_p, potentially leading to the shown disturbing effects in the IV-characteristics. Resulting from these effects is a distortion of the $V\Phi$-characteristics, as illustrated in figure 3.5 b). Shown is the $V\Phi$-characteristics of the same SQUID for a bias current $I_\mathrm{b} = 11.1\,\mu\mathrm{A}$. As a consequence, the linear voltage response of the SQUID can be reduced to $\delta\Phi_\mathrm{S} \ll \pm\Phi_0/\pi$ and the flux-to-voltage transfer coefficient V_Φ is potentially reduced, consequently degrading the energy sensitivity ϵ_s of SQUID.

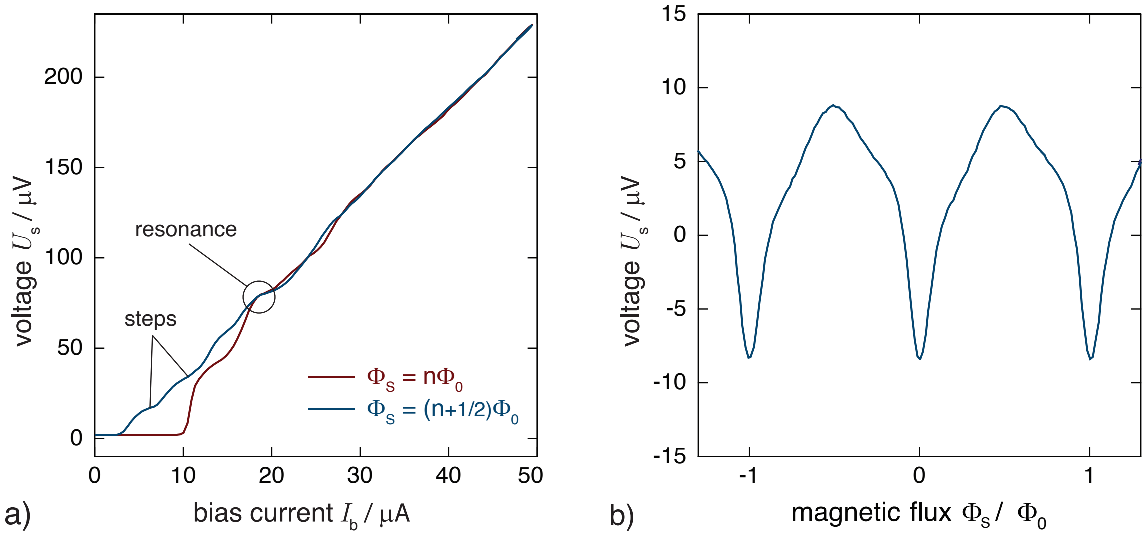

Figure 3.5: a) IV-characteristics of a washer SQUID with tightly coupled input coil that was developed in this group. The characteristics shows a point of resonance as well as resonant current steps. b) $V\Phi$-characteristic of the same SQUID for a bias current $I_\mathrm{b} = 11.1\,\mu\mathrm{A}$.

There exist several methods to adapt a SQUID design in order to dampen resonances occurring in its characteristics. A commonly employed method is the resistive damping of resonances, where a shunt resistor R_sh is connected in parallel to either the loop inductance L_S of the SQUID [Knu87, Fog89, Enp91]. As a result, the amplitude of the intrinsic resonance of the SQUID can be damped, so that it has no longer any derogatory effects on the SQUID performance at its optimum working point. In addition, resonant current steps in the IV-characteristics can be smoothed by the introduction of additional shunt resistors that are connected in parallel between each turn of the input coil inductance L_in , which dampens resonances occurring within the latter [Ono97].

3.3.2 Flux-locked loop operation

Metallic magnetic calorimeters have an excellent and predictable linearity, as was described in section 2.8. In order to benefit from this during detector operation, the employed readout chain should ideally not introduce additional non-linearities. An optimized dc-SQUID that is biased at its optimum working point has a linear voltage response for magnetic flux changes $\delta\Phi_{\mathrm{S}} \leq \pm\Phi_0/\pi$ [Cla04]. However, flux changes in the employed SQUID larger than Φ_0/π are not uncommon when reading out metallic magnetic calorimeters. In this case, the flux-to-voltage transfer coefficient V_Φ changes as the SQUIDs working point moves along its periodic $V\Phi$-characteristic. Not only is the voltage response non-linear for $\delta\Phi_{\mathrm{S}} \geq \pm\Phi_0/\pi$, the apparent flux noise in the SQUID also changes with V_Φ according to equation 3.20, consequently degrading the energy sensitivity ϵ_{s} according to equation 3.21.

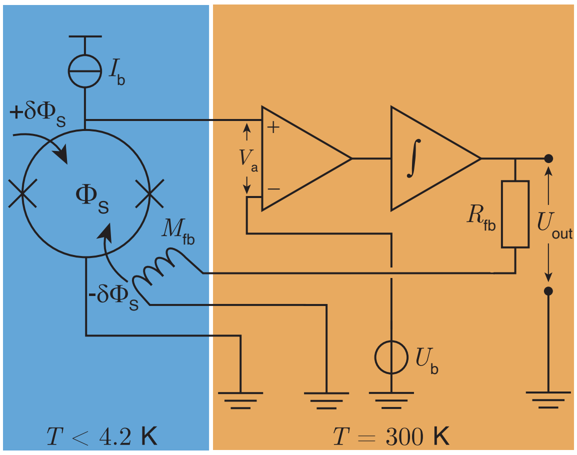

Figure 3.6: Schematic of a dc-SQUID that is read out using a flux-locked circuit. The output voltage of the SQUID is amplified, integrated, and transformed into a current via the feedback resistor R_{fb}. This current is running through a feedback coil that is coupled via the mutual inductance M_{fb} to the SQUID loop in order to compensate the initial flux change Φ_{S}.

In order to linearize $V(\Phi)$ for large signals, and to keep ϵ_{s} at its lowest value during operation at all times, a so called flux-locked loop (FLL) circuit can be used, as schematically illustrated in figure 3.6. The dc-SQUID is connected to a differential preamplifier, which is in turn connected to an integrator, both usually situated at room temperature. The reference voltage U_{b} is adjusted such that the input voltage V_{a} of the preamplifier vanishes at the optimum working point of the SQUID, so that $U_{\mathrm{out}} = 0\,\mathrm{V}$. When a signal $\delta\Phi_{\mathrm{S}}$ arrives in the SQUID, the corresponding voltage response is amplified, integrated, and converted into a feedback current I_{fb} via the feedback resistor R_{fb}. This feedback current compensates the initial magnetic flux change $\delta\Phi_{\mathrm{S}}$ in the SQUID via a feedback coil with mutual inductance M_{fb}, i.e. $\delta\Phi_{\mathrm{fb}} = M_{\mathrm{fb}}I_{\mathrm{fb}} = \text{-}\delta\Phi_{\mathrm{S}}$. This negative feedback loop keeps the magnetic flux Φ_{S} in the SQUID constant, so that it is locked at its optimum working point. The flux-to-voltage transfer coefficient U/Φ_0 of a SQUID operated in the FLL mode can be computed to

$$\frac{U}{\Phi_0} = \frac{R_{\mathrm{fb}}}{M_{\mathrm{fb}}} \,. \tag{3.24}$$

The room temperature preamplifier and the corresponding wiring between SQUID and preamplifier both introduce additional noise in the form of voltage noise $\sqrt{S_{\mathrm{U,rta}}}$ and current noise $\sqrt{S_{\mathrm{I,rta}}}$. The spectral power density of the total apparent flux noise in the SQUID is therefore given by

$$S_\Phi = S_{\Phi,\mathrm{SQ}} + \frac{S_{\mathrm{U,rta}}}{{V_\Phi}^2} + \frac{S_{\mathrm{I,rta}}}{{I_\Phi}^2} + \frac{S_{\mathrm{U,wire}}}{{V_\Phi}^2} + \frac{I_{\mathrm{I,wire}}}{{I_\Phi}^2} \,, \tag{3.25}$$

where $S_{\Phi,\mathrm{SQ}}$ denotes the SQUID noise. The room temperature electronics used in the work at hand is the commercially available Magnicon XXF-1[3]. Its intrinsic voltage noise has two plateaus, $\sqrt{S_{\mathrm{U,rta}}} \approx 0.33\,\mathrm{nV}/\sqrt{\mathrm{Hz}}$ at $f > 10^3\,\mathrm{Hz}$ and $\sqrt{S_{\mathrm{U,rta}}} \approx 0.5\,\mathrm{nV}/\sqrt{\mathrm{Hz}}$ at $f < 10^3\,\mathrm{Hz}$. Furthermore, a $1/f$-like voltage noise contribution is observed for $f < 1\,\mathrm{Hz}$ with $\sqrt{S_{\mathrm{U,rta}}(0.1\,\mathrm{Hz})} \approx 0.8\,\mathrm{nV}/\sqrt{\mathrm{Hz}}$. In addition, it has an intrinsic white current noise level of $\sqrt{S_{\mathrm{I,rta}}} \approx 2.6\,\mathrm{pA}/\sqrt{\mathrm{Hz}}$ at $f > 30\,\mathrm{Hz}$, and a $1/f$-like current noise contribution below $f = 30\,\mathrm{Hz}$ with $\sqrt{S_{\mathrm{I,rta}}(0.1\,\mathrm{Hz})} \approx 40\,\mathrm{pA}/\sqrt{\mathrm{Hz}}$ [Dru06]. The last two terms in equation 3.25 denote a Nyquist voltage noise contribution $S_{\mathrm{U,wire}}$ and a Nyquist current noise contribution $I_{\mathrm{I,wire}}$ of the wiring between 300 K and 4 K. In this setup, the voltage noise contribution of the XXF-1 electronics alone can already have a dominating role in the overall noise spectrum. Assuming a dc-SQUID with a flux-to-voltage transfer coefficient of $V_\Phi = 50\,\mu\mathrm{V}/\Phi_0$, the white voltage noise of the XXF-1 contributes with $\sqrt{S_{\mathrm{U,rta}}/V_\Phi^2} = 6.6\,\mu\Phi_0/\sqrt{\mathrm{Hz}}$ to the apparent flux noise, which is for instance more than one order of magnitude higher than the white apparent flux noise of the dc-SQUIDs that are developed in this group [Kem15].

3.3.3 Slew rate

A time delay t_{d} has to be considered between a magnetic flux input $\delta\Phi_{\mathrm{S}}$ into the SQUID and a corresponding feedback $\delta\Phi_{\mathrm{fb}}$, which originates from the transmission lines between SQUID and readout electronics, as well as from the integrator and other circuit elements. This time delay can cause a phase lag, causing the feedback to become positive at high frequencies. When the so called error flux $\delta\Phi_{\mathrm{e}} = \delta\Phi_{\mathrm{S}} - |\delta\Phi_{\mathrm{fb}}|$ in the SQUID becomes larger than the linear voltage response $\Delta\Phi_{\mathrm{lin}}$ of the SQUID, the SQUID no longer behaves like a linear element and the FLL operation can become

---

[3] Magnicon GmbH: www.magnicon.com/squid-electronics/XXF-1/

unstable. One can therefore define the so called maximum slew rate $\dot{\Phi}_{\mathrm{fb}}$ of a flux-locked loop circuit, which defines the maximum flux-feedback rate with which the electronics can compensate magnetic flux changes $\delta\Phi_{\mathrm{S}}$ in the SQUID. The maximum slew rate of the circuit shown in 3.6 can be derived to [Wel84, Wei96, Cla04]

$$\dot{\Phi}_{\mathrm{fb}}^{\mathrm{max}} = 2\pi\Delta\Phi_{\mathrm{lin}} V_{\Phi} \frac{M_{\mathrm{fb}}}{R_{\mathrm{fb}}} G_{\mathrm{A}} G_{\mathrm{I}} = 2\pi f_1 \Delta\Phi_{\mathrm{lin}}\,, \tag{3.26}$$

where G_{A} is the gain of the preamplifier. $G_{\mathrm{I}}(f) = f_1/(if)$ is the gain of the assumed one-pole integrator and f_1 denotes its unity-gain frequency of the integrator, i.e. $G_{\mathrm{I}}(f_1) = 1$, with i being the imaginary number. Under the idealized conditions of negligible gain errors at high frequencies, the frequency response of a one-pole integrator for instance is identical to the 3 dB cutoff frequency of a first-order RC lowpass filter, i.e. $f_1 = f_{\mathrm{c}}$. According to equation 3.26, a high system slew rate requires a large linear voltage response $\Delta\Phi_{\mathrm{lin}}$ of the employed SQUID, as well as a high unity-gain frequency f_1 of the integrator.

3.3.4 Two-stage SQUID readout

In order to reduce the impact of the noise contribution $\sqrt{S_{\Phi,\mathrm{rta}}}$ of the amplifier at room temperature, was was discussed at the end of section 3.3.2, an additional cryogenic amplification stage can be introduced, that boosts the output signal of the sensor SQUID. The corresponding circuit schematic is illustrated in figure 3.7. Shown in the first stage is a metallic magnetic calorimeter, that is inductively coupled to a front-end dc-SQUID via the mutual inductance M_{in}. The dc-SQUID is operated in the FLL mode and is connected in series to the input coil of the cryogenic amplifier situated on the second stage. Both are connected in parallel to a gain resistor R_{g} that is also situated on the second stage. The constant bias current I_{b1} splits up into the two branches of this circuit. The current $I_{\mathrm{FE}}(I_{\mathrm{c,SQ}}(\Phi), R_{\mathrm{S}}, R_{\mathrm{g}})$ running through the front-end SQUID depends on its critical current $I_{\mathrm{c,SQ}}(\Phi)$, on the shunt resistance R_{S} of the Josephson junctions, and on the gain resistance R_{g}. The current through the gain resistor is consequently given by $I_{\mathrm{g}} = I_{\mathrm{b1}} - I_{\mathrm{FE}}$. Once the SQUID detects a flux change $\delta\Phi_{\mathrm{S}}$, the modulation of its critical current, as discussed in section 3.2.1, also modulates the current in the input coil of the cryogenic amplifier. The maximum possible modulation is given by $\Delta I_{\mathrm{mod}} = I_{\mathrm{c,SQ}}(\mathrm{n}\Phi_0) - I_{\mathrm{c,SQ}}((\mathrm{n}+1/2)\Phi_0)$.

The cryogenic amplifier is an N-SQUID series array that is operated with a constant bias current I_{b2}. The magnetic flux change $\delta\Phi_{\mathrm{S}}$ in the front-end SQUID is coherently coupled into each SQUID cell of the N-SQUID series array via the mutual inductance M_{N}. Each of the identical SQUID cells within the array respond accordingly to the magnetic flux change with an output voltage $U_{\mathrm{N,out}}$. The resulting total voltage response of the array is given by $U_{\mathrm{N,out}} = N \cdot U_{\mathrm{N,out}}$. Therefore, an N-SQUID series array behaves like a single dc-SQUID with an enhanced flux-to-voltage transfer coefficient $V_{\Phi,\mathrm{N}}$. The spectral power density of the intrinsic voltage noise $S_{V,N}$ of the array is consequently also enhanced by the factor N. According to equation 3.20, the intrinsic magnetic flux noise $\sqrt{S_{\Phi,\mathrm{N}}}$ of the array scales with $1/\sqrt{N}$.

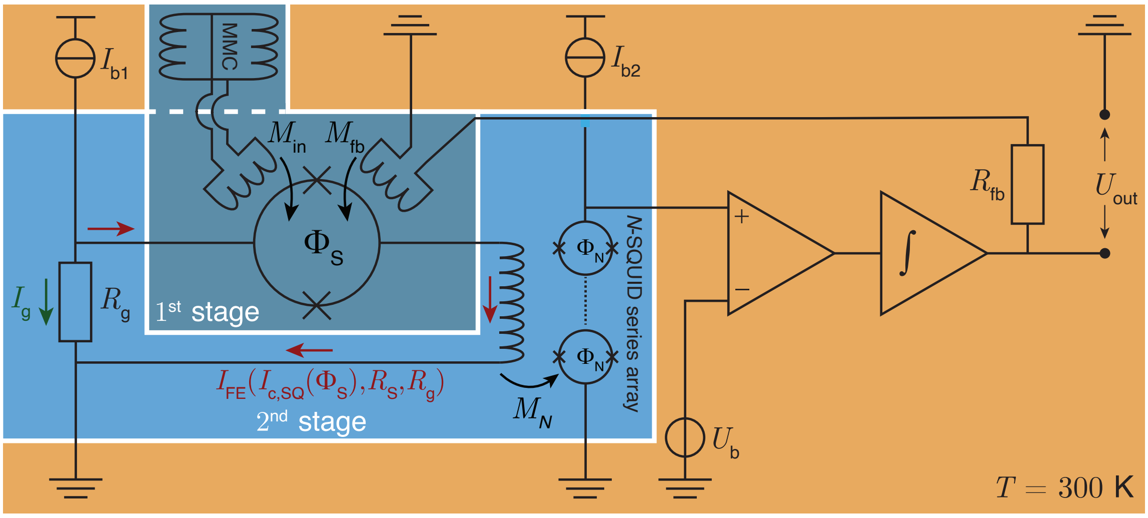

Figure 3.7: Schematic drawing of a two-stage SQUID configuration. Shown in the first stage is a single front-end SQUID used for detector readout, that is operated in the flux-locked loop mode. Situated in the second stage is an N-SQUID series array that functions as a cryogenic preamplifier.

One figure of merit of the two-stage SQUID readout is the flux-to-flux amplification given by

$$G_\Phi = \frac{\delta\Phi_{\mathrm{N}}}{\delta\Phi_{\mathrm{S}}} = \frac{M_{\mathrm{N}}}{R_{\mathrm{dyn,FE}} + R_{\mathrm{g}}} V_{\Phi,\mathrm{FE}}\,, \tag{3.27}$$

in which $V_{\Phi,\mathrm{FE}}$ denotes the flux-to-voltage transfer coefficient of the front-end SQUID and $R_{\mathrm{dyn,FE}}$ its dynamic resistance. Since $V_{\Phi,N} = G_\Phi V_{\Phi,\mathrm{FE}}$, a flux-to-flux amplification of $G_\Phi > 1$ must be achieved in order to enhance the flux-to-voltage transfer coefficient of the two-stage setup. However, the maximum achievable slew rate reduces with G_Φ, making an arbitrarily large amplification not desirable. The total spectral power density of the apparent flux noise in the front-end SQUID adds up to

$$S_\Phi = S_{\Phi,\mathrm{FE}} + \frac{1}{G_\Phi^2}\left[S_{\Phi,\mathrm{N}} + \frac{S_{\mathrm{U,300K}}}{V_{\Phi,\mathrm{N}}^2} + \frac{S_{\mathrm{I,300K}}}{I_{\Phi,\mathrm{N}}^2} + \frac{4k_{\mathrm{B}}TR_{\mathrm{g}}}{(R_{\mathrm{g}} + R_{\mathrm{dyn,FE}})^2} M_{\mathrm{N}}^2\right]. \tag{3.28}$$

The individual summands of this equation originate from, from left to right, the intrinsic noise of the front-end SQUID $\sqrt{S_{\Phi,\mathrm{FE}}}$, the intrinsic noise of the N-SQUID series array $\sqrt{S_{\Phi,\mathrm{x}}}$, the sum of the voltage noise $\sqrt{S_{\mathrm{U,300K}}} = \sqrt{S_{\mathrm{U,rta}} + S_{\mathrm{U,wire}}}$ and current noise $\sqrt{S_{\mathrm{I,300K}}} = \sqrt{S_{\mathrm{I,rta}} + S_{\mathrm{I,wire}}}$ of the room temperature electronics and its corresponding wiring, with $V_{\Phi,\mathrm{N}}$ and $I_{\Phi,\mathrm{N}}$ denoting the flux-to-voltage and flux-to-current transfer coefficient of the array, respectively. The gain resistor R_g generates a Nyquist current noise running through $R_\mathrm{g} + R_{\mathrm{dyn,FE}}$, consequently generating a flux noise in the N-SQUID series array via M_N. Therefore, the last term of equation 3.27 denotes the apparent flux noise contribution of the gain resistor R_g. Since it scales with temperature T, and usually $R_\mathrm{g} \ll R_{\mathrm{dyn,FE}}$, this term can be neglected. The arrays employed in the thesis are in-house fabricated 16-SQUID series arrays with a gain resistance of $R_\mathrm{g} = 0.2\,\Omega$.

3.3.5 Energy dissipation of a dc-SQUID

Figure 3.8 shows the measured IV-characteristics of a dc-SQUID that was developed for the HDMSQ1 detector during this thesis, as will be discussed in chapter 6. Marked in the plot is its optimum working point (light grey) when operated in single-stage configuration at constant bias current. Here, its energy dissipation is given by $P_{\mathrm{1st}} = U_{\mathrm{1st}} \cdot I_\mathrm{b}$, as indicated by the light grey shaded area. When this SQUID is operated as a front end SQUID in a two stage setup, then the situation changes, as the applied bias current is split up. A fraction of I_b runs through the gain resistor R_g and the remaining fraction runs through the front end SQUID and the input coil of the N-SQUID series array, as was illustrated in section 3.3.4. The corresponding working point when operated in a two-stage setup is also marked accordingly in figure 3.8 (dark grey).

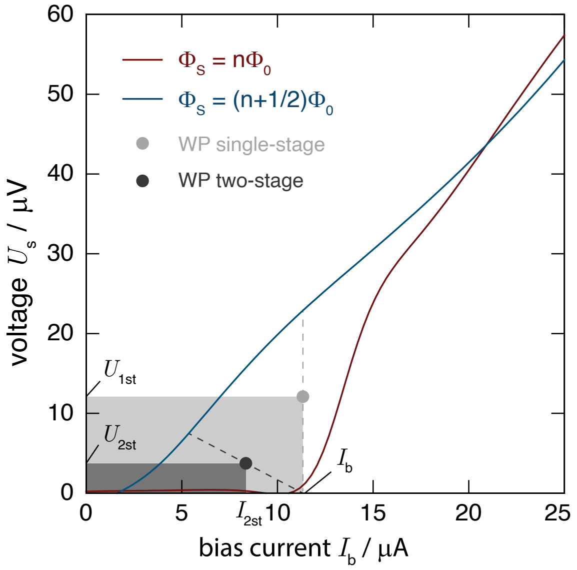

Figure 3.8: Measured IV-characteristics of a dc-SQUID that was developed for the HDMSQ1 detector, the first detector that was developed within the framework of this thesis. Marked are its working point and energy dissipation in a single-stage readout (light grey), as well as its working point and energy dissipation in a two-stage readout (dark grey).

A flux change $\delta\Phi_\mathrm{S}$ in the SQUID leads to a modulation of its critical current and the voltage response of the SQUID follows the so called load line, indicated by the dark grey dashed line. The slope of this load line is determined by $-R_{\mathrm{g}}$, as the voltage drop across the front end SQUID reduces with a decreasing R_{g}. The power dissipation is given by $P_{\mathrm{2st}} = U_{\mathrm{2st}} \cdot I_{\mathrm{2st}}$, also indicated by the dark grey shaded area. Therefore, the energy dissipation of a dc-SQUID is lower when operated in a two-stage setup in the voltage bias, compared to a single-stage readout in the current bias. A small gain resistance R_{g} should be chosen in order to minimize the energy dissipation of the front end SQUID. However, since its noise contribution is given by the last term in equation 3.28, R_g has to be large enough in order to not provide a relevant contribution to the overall noise.

Cooling fins for the suppression of the hot-electron effect

The Joule heating of a dc-SQUID that is operated in the voltage state occurs in its shunt resistors, as there is a finite current running through the normal conducting structures. The dissipated energy has to flow through insulating silicon substrate into the sample holder. Therefore, the hot electrons in the shunt resistor must first transmit their energy to the phonon system within the resistor in order to transmit energy to the phonon system of the substrate. However, the electron-phonon interaction is quite weak at millikelvin temperatures [Ens05], resulting in an electron temperature T_{e} that is much higher than the corresponding phonon temperature T_{ph}. This is called the hot-electron effect [Rou85, Wel94]. As T_{e} can be very well above 100 mK, this leads to an increased white noise level of the SQUID at MMC operation temperatures. The power dissipation P of the resistor can be described by [Gan74, Ech92]

$$P = \Lambda\Sigma(T_{\mathrm{e}}^{p} - T_{\mathrm{ph}}^{p}) \,, \tag{3.29}$$

where Λ denotes the volume of the resistor and Σ is a material dependent constant. For the exponent p, values between 4 and 5 are usually found in scientific literature [Ser00]. According to equation 3.29, increasing the volume Λ suppresses the hot-electron effect. This is usually achieved by attaching a so called cooling fin to the shunt resistor, which is just a metallic extension of the resistor in order to increase the effective volume in which the electron-phonon interaction takes place, consequently reducing the temperature of the electron system for a constant P [Wel94, Fal08]. Furthermore, the cooling fin also increases the effective contact area between the metal and the substrate, potentially reducing the impact of the so called Kapitza resistance, which describes a heat flow resistance at the interface of two materials at low temperatures [Pol69]. However, there exists an effective upper limit for such an additional interaction volume. The electron phonon interaction occurs within a characteristic interaction length $l_{\mathrm{e,ph}}$[Rou85], that increases with decreasing T_{e} and

T_{ph}, and also increases with decreasing specific conductance σ of the material that is used for the cooling fin. Therefore, when the dimension of the latter is much larger than $l_{\mathrm{e,ph}}$, only a fraction of the cooling fin volume contributes to the cooling effect.

4. Experimental methods

This chapter introduces the experimental methods that were applied within the framework of this thesis. Included is a description of the of the cryogenic system utilized for measurements at millikelvin temperatures, followed by a brief introduction of the employed data acquisition system (DAQ), as well as the signal analysis method that is part of this DAQ system. Lastly, a description of the X-ray calibration source that was used for detector characterization is given.

4.1 Cryogenics

4.1.1 Dry ^{3}He/^{4}He dilution refrigerator

The cryogenic setup used for all measurements at millikelvin temperatures in this thesis is a commercially available, pulse-tube pre-cooled ^{3}He/^{4}He dilution refrigerator BF-LD250 by Bluefors[1]. The cryostat provides a continuous cooling of experimental setups to a base temperature below 10 mK without the need for cryo-liquids, such as liquid helium. A pulse-tube cooler is a closed cycle cooling system that can reach temperatures below 3 K [Tan04, Ens05], which is used to pre-cool the dilution refrigerator before the latter can begin its operation. A schematic, as well as a photograph of the utilized a ^{3}He/^{4}He dilution refrigerator is schematically depicted in figure 4.1. The working principle of such a cryostat shall be briefly discussed.

Pure liquid ^{4}He undergoes a phase transition into its superfluid state at $T_\lambda = 2.17\,\mathrm{K}$. When mixed with ^{3}He, this transition temperature is suppressed, with $T_\lambda = 0.87\,\mathrm{K}$ for a ^{3}He concentration of $c_{^3\mathrm{He}} = 67\,\%$. For $T < 0.87\,\mathrm{K}$, a spatial phase separation of the mixture of the ^{3}He and the now superfluid ^{4}He occurs, creating a ^{3}He-rich phase and a ^{3}He-depleted phase. This is illustrated in the so called mixing chamber in figure 4.1. The concentration of ^{3}He in the depleted phase stays constant at $\sim 6.6\,\%$ for $T \to 0\,\mathrm{K}$ [Pob96]. This finite solubility is important for the operation of a dilution refrigerator and can be explained by a difference in zero-point energy and nuclear spin between the two particles. Due to their identical electron configuration, ^{3}He and ^{4}He atoms have identical van der Waals forces between each other, while ^{3}He is lighter due to having only one neutron in its nucleus. Therefore, ^{3}He has a higher zero-point motion compared to ^{4}He. As a result, the binding energy of a ^{3}He atom diluted in ^{4}He is higher than that of a ^{3}He$-$^{3}He bond, resulting in a

---

[1] BlueFors Cryogenics Oy, Arinatie 10, 00370 Helsinki, FINLAND

mixture of the two isotopes. However, the lighter ^{3}He has a nuclear spin of $S = 1/2$, meaning it has to obey the Pauli principle. This means that in this diluted phase, each of the available energy levels up the Fermi energy $E_\mathrm{F} = k_\mathrm{B} T_\mathrm{F}$ can be occupied by two ^{3}He atoms of opposite nuclear spin, setting an upper limit to the allowed ^{3}He concentration in the ^{3}He/^{4}He mixture.

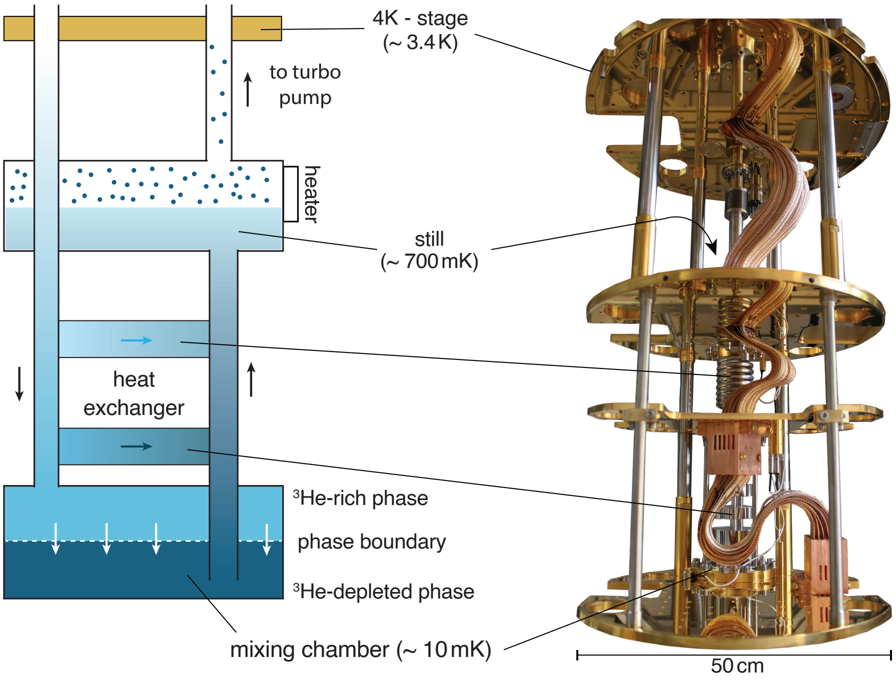

Figure 4.1: Schematic, as well as a photograph of the ^{3}He/^{4}He dilution refrigerator utilized within this thesi. The cryogenic system provides a continuous operation at lower millikelvin temperatures without the need for cryogenic liquids. Experiments are mounted to the experimental platform that is in direct contact with the mixing chamber of the cryostat.

Furthermore, the ^{3}He in the ^{3}He-depleted phase has a higher enthalpy. Therefore, a transition of ^{3}He atoms from the ^{3}He-rich phase into the ^{3}He-depleted phase requires energy that is taken up from the surrounding environment. The operation of a ^{3}He/^{4}He dilution refrigerator relies on forcing this particle transition over the phase boundary by removing ^{3}He in the still via pumping, thereby reducing the local concentration of ^{3}He. As the resulting osmotic pressure, ^{3}He atoms diffuse from the ^{3}He-depleted phase in the mixing chamber to the still. Since the concentration of ^{3}He in the depleted phase tries to stay constant at $\sim 6.6\,\%$ for $T \to 0\,\mathrm{K}$ [Pob96], ^{3}He atoms transition the phase boundary in the mixing chamber from the rich phase into the depleted phase, providing a cooling effect. The ^{3}He atoms that are pumped at the still are reintroduced back into the ^{3}He-rich phase after being pre-cooled at designated temperature stages of the pulse-tube cooler and heat exchangers of the dilution unit, creating a closed-cycle cooling system for millikelvin temperatures. During operation, the still is kept at $T \approx 700\,\mathrm{mK}$ by an energy input of a few Milliwatts via a heater. Otherwise, the stills temperature would reduce due the evaporative cooling that occurs due to the pumping of ^{3}He atoms. This reduced temperature would result in a lower vapor pressure of ^{3}He, resulting in less ^{3}He atoms being pumped, consequently reducing the cooling power of the dilution unit at the mixing chamber. Connected to the mixing chamber is an experimental platform made of annealed copper coated with gold on which experiments can be mounted.

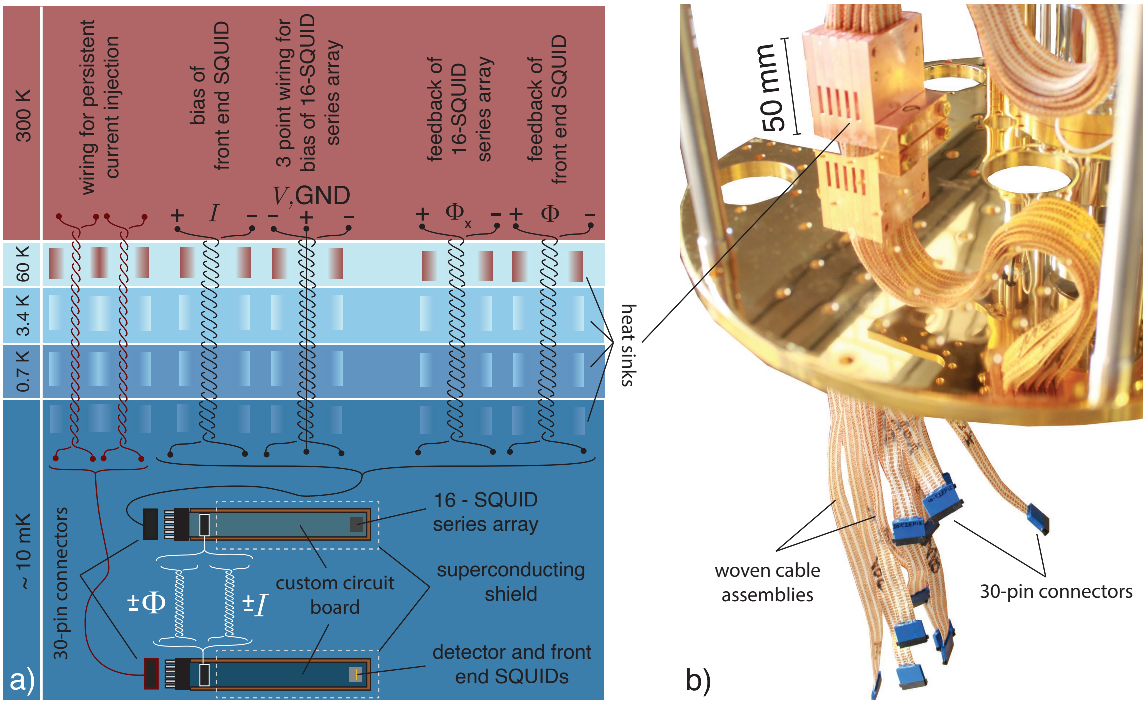

Figure 4.2: a) Schematic of a part of the wiring that is installed in the cryostat. Shown is the wiring that is required for the readout of one two-stage SQUID setup, as well as the wiring that is required for the injection of the persistent current I_0 for detector operation. Furthermore, depicted is a custom circuit board that hosts 16-SQUID series array amplifiers, as well as an additional custom circuit board that hosts front end SQUIDs and detectors. b) Photograph of the mixing chamber platform of the cryostat with the installed cable assemblies.

4.1.2 Wiring

The wiring of the cryostat is illustrated in figure 4.2 a). The black wires show the required cable assembly for one two-stage SQUID setup. This wiring is terminated with 30-pin PCB connectors[2] that fit to a custom circuit board which hosts the 16-

---

[2] Samtec Tiger Eye Socket SFM-115 series: https://www.samtec.com

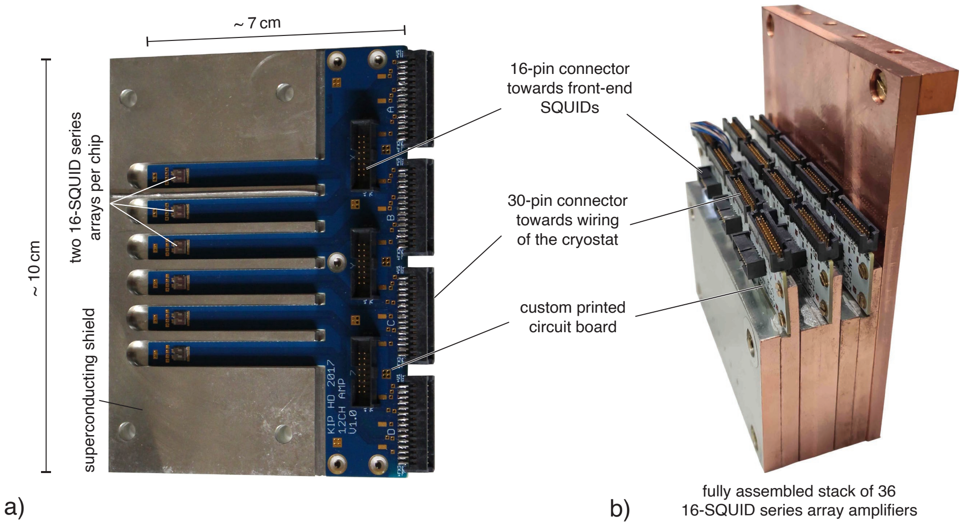

Figure 4.3: a) Photograph of a custom six-finger printed circuit board that is used to host two 16-SQUID series array amplifiers on each finger tip. Each finger is encased in a superconducting shield made of copper coated with electroplated tin. c). Photograph of a fully assembled stack of 36 16-SQUID series array amplifiers that can be installed in the cryostat.

SQUID series array amplifier for the two-stage SQUID readout. From this circuit board, a connection is made to an additional custom circuit board with the white wiring, that is used to connect the front end SQUID in the two-stage SQUID readout. The wires coming from room temperature down to the 16-SQUID series array amplifier were twisted and woven together with NOMEX by Tekdata[3]. The wires themselves are made of Alloy-30 (98 % Cu, 2 % Ni), have a diameter of 200 μm and are 2.2 m in length with a resistance of 1.56 Ω/m. To minimize their contributed heat load into the lower cooling stages of the cryogenic setup, every cable assembly is heat sunk at every cooling stage of the fridge. The white wiring has a length of 40 cm and is made of the same material as the black wiring, but are simple flat ribbon cables.

In total, 36 of the black cable assemblies are installed in the cryostat. Up to 32 16-SQUID series array amplifiers, for the readout of 32 front end SQUIDs, are usually mounted to the mixing chamber platform, leaving four cable assemblies that can be used as auxiliary wiring. The latter is for instance used for the injection of the persistent current I_0 into the field generating coils of the detector, as it will be explained in section 6.2. This auxiliary wiring is denoted in red in figure 4.2 a), where unused wires that are also part of the cable assembly are not depicted for visibility. A photograph of the mixing chamber platform of the cryostat is shown in figure 4.2 b), depicting the woven wire harnesses, 30-pin connectrors, as well as the corresponding heat sinks. The 36 cable assemblies are consolidated in 12 of such

---

[3] Tekdata interconnections ltd, sub-division cryoconnect: https://www.cryoconnect.com/

flat woven wire harnesses, i.e. one wire harness hosts the wiring for three two-stage SQUID setups. Figure 4.3 a) shows a custom circuit board that hosts 16-SQUID series amplifiers. The circuit board has six fingers, whereas a chip with two 16-SQUID series amplifiers is glued to the tip of each finger. Furthermore, each finger is individually encased in a superconducting shield that is made of copper coated with electroplated tin. Each of the depicted 30-pin connectors in the picture is used to connect three two-stage SQUID setups to the wiring of the cryostat, i.e. one of the 12 flat woven wire harnesses is connected to one 30-pin connector. The 16-pin connectors are used to connect the wiring for the front end SQUIDs, which was depicted in white in figure 4.2 a). The corresponding experimental setup for the front end SQUIDs and detectors will be introduced in section 6.4. Figure 4.3 b) shows a photograph of a fully assembled stack of 36 16-SQUID series array amplifiers that can be installed in the cryostat. What is not shown is a Mu-metal shield that also encases the entire amplifier stack during operation.

4.1.3 Thermometry

The mixing chamber platform of the cryostat is equipped with a ruthenium-oxide resistance thermometer, which increases its electrical resistance for a decreasing temperature and that is calibrated down to $T = 7\,\mathrm{mK}$. This thermometer is read out in a Wheatstone bridge setup via the Model 370 AC Resistance Bridge and Scanner model 3716 from Lake Shore Cryotronics[4]. At an operation temperature of $T = 20\,\mathrm{mK}$, the thermometer has a sensitivity of $150\,\Omega/\mathrm{mK}$. The relative resolution of the resistance bridge is denoted with $2\,\Omega$, when the thermometer is read out at a frequency of $9.8\,\mathrm{Hz}$ and an integration time of $3\,\mathrm{s}$. Therefore, the relative temperature resolution is $\Delta T/T = 6.7 \cdot 10^{-4}$. With this temperature resolution, a build in PID controller was used to operate a heater with $R = 120\,\Omega$ in order to provide an active temperature stabilization of the mixing chamber platform during measurements. In linear approximation, the additional contribution to the energy resolution of the detector due to the limited temperature resolution would be $\Delta E_{\mathrm{FWHM}}/E = 6.7 \cdot 10^{-4}$. This means, that for an energy input of $5.9\,\mathrm{keV}$, the contribution to the detectors energy resolution due to temperature fluctuations would be $\Delta E_{\mathrm{FWHM}} \approx 4\,\mathrm{eV}$, making it apparent that the utilized thermometry is insufficient for the operation of a metallic magnetic calorimeter with a potential energy resolution below $1\,\mathrm{eV}$. Increasing the integration time of the thermometer readout enhances the temperature resolution, but at the cost of time resolution, resulting in a delayed response of the PID controller in regards to temperature fluctuations. During operation, and using an integration time between $20\,\mathrm{s}$ and $30\,\mathrm{s}$ for the thermometer readout, the best achieved value for the observable temperature fluctuations was $\approx \pm 5\,\mu\mathrm{K}$. This resolution results in

---

[4] LakeShore Cryotronics Inc: www.lakeshore.com/

a contribution to the achievable energy resolution at 5.9 keV of $\Delta E_{\mathrm{FWHM}} \approx 3\,\mathrm{eV}$, which is still insufficient for a detector with a potential sub-eV energy resolution. Therefore, a different scheme to acquire temperature information was used, that will be discussed in chapter 6, where a non-gradiometric detector channel on the chip can be used to acquire relative temperature information during measurements.

4.2 Data readout

After a particle is absorbed by an MMC during operation, the corresponding voltage response that is generated by the two-stage SQUID setup connected to the detector is read out by a data acquisition system (DAQ) that was developed and described in detail in [Hen17]. It allows for the simultaneous readout of up to 32 channels with a single computer controlling the DAQ system. The DAQ system uses two 16-channel digitizer cards SIS3316[5] for analogue-digital conversion (ADC) of the SQUID output voltage, providing a maximum sampling rate of 125 MHz per channel at a voltage resolution of 16 bit. Each data channel is internally split up into a trigger channel and a data channel, featuring individual trigger engines for each channel that are based on a moving average window and a Finite-Impulse-Response filter [Ell87]. In optimal filtering, signals are assumed to have an identical rise time independent of their amplitude. Thus, all incoming signals are triggered at the same time relative to the time of maximum amplitude by a constant fraction discriminator [Bar04] that is implemented in the trigger engine. The system supports an oversampling factor of up to 512. Therefore, the high sampling rate of the DAQ allows for a precise trigger time, and the oversampling allows for a reduction the amount of data that needs to be saved. The latter would otherwise require a lot of disc space, as the acquired time windows usually have a length of up to 5 ms. In this thesis, an oversampling of 32 was used with 32768 samples taken per triggered event. The data transfer to the measurement computer is done via an RJ45 Ethernet port simultaneously to the data acquisition, which is possible due to a double-memory system incorporated in the ADC cards. Thus, one memory can be filled with acquired data while the other is read out and stored by the computer controlling the DAQ. The utilized acquisition software was also developed in [Hen17] and is written in C++. The software incorporates a signal analysis method that is based on simple least squares fitting in order to determine that signal amplitude of the detector response, which was used within this thesis and will be discussed in section 4.3.

---

[5] Struck Innovative Systeme GmbH: www.struck.de/

4.3 Signal analysis

Section 2.6.4 described a signal analysis based on the method of optimal filtering. However, a corresponding program that makes use of this analysis method for data acquired with the DAQ system described in section 4.2 was not available within the group during this thesis. Therefore, a more simple analysis method that was implemented in [Hen17] for the used DAQ system was utilized. This analysis method should be briefly discussed here. This method assumes, that the detector responses for the absorption of different energies can be projected onto each other by a simple mathematical streching in amplitude direction, such that the detector response upon an absorption of a particle with energy δE can by described by

$$p(t_i) = Ar(t_i) + n(t_i)\,, \tag{4.1}$$

where A denotes the true amplitude of the signal, $r(t_i)$ denotes a reference signal response that results from averaging several detector responses of equal energy input, and $n(t_i)$ denotes superimposed noise. The index i is a measure of the time of signal digitization within the acquired time window. The fit function that is used to describe the measured detector response has the form

$$f(t_i) = Er(t_i) + E_0\,, \tag{4.2}$$

where E denotes the apparent signal amplitude and E_0 denotes a signal offset in amplitude direction, which can occur for instance due to temperature drifts of the cryogenic setup. The factors E and E_0 are then determined by minimizing the expression

$$\chi^2 = \sum_i (p(t_i) - f(t_i))^2\,, \tag{4.3}$$

which is nothing more than a so called χ^2-fit. Assuming $n(t_i)$ denotes only a white noise contribution, the error between the actual signal amplitude A and the determined signal amplitude E can be approximated by [Fle98]

$$\Delta(A-E)_{\mathrm{FWHM}} = \frac{\sqrt{S_{\Phi,w}}}{\sqrt{t_{\mathrm{w}}}} \frac{8\sqrt{2\ln 2}}{\pi} \sqrt{1 - \frac{1}{\nu_{\mathrm{E}} t_{\mathrm{w}}}}\,, \tag{4.4}$$

Here, $\sqrt{S_{\Phi,w}}$ is the spectral density of the white noise, t_{w} is the length of the acquired time window and ν_{E} is the bandwidth of the SQUID electronics. Assuming a white noise level of $\sqrt{S_{\Phi,w}} = 1\,\mu\Phi_0/\sqrt{\mathrm{Hz}}$, a time window of $t_{\mathrm{w}} = 5\,\mathrm{ms}$, and a SQUID bandwidth of about $\nu_{\mathrm{E}} = 6\,\mathrm{MHz}$ of the XXF1-electronics, a resulting amplitude error is calculated to $\Delta(A-E)_{\mathrm{FWHM}} = 42\,\mu\Phi_0$, which corresponds to an error of $\sim 0.01\,\%$ for an assumed signal height of $\delta\Phi_{\mathrm{S}} = 0.5\,\Phi_0$. Further assuming that this signal is created by the absorption of a 5.9 keV photon, which is comparable to the detector response at this photon energy of the MMCs that were developed in this thesis, then the resulting uncertainty is 0.59 eV, which is only slightly lower compared to the calculated energy resolution at $T = 20\,\mathrm{mK}$ of the developed detectors, as will be shown in the subsequent discussion.

In [Fle03] the differences between the χ^2-fit method and the method of optimal filtering in terms of additional noise and its impact on the determined energy resolution were additionally discussed. For both analysis methods, the impact on the determined energy resolution of additional discrete noise amplitudes was investigated, for instance 50 Hz noise. Figure 4.4 a) shows a calculated plot of relative calculated energy resolution, defined by the calculated energy resolution with added discrete noise at frequency f ΔE_{FWHM} divided by the calculated energy resolution $\Delta E_{\mathrm{TEF,FWHM}}$ in which only the thermodynamic energy fluctuations were considered, i.e. the intrinsic energy resolution of the detector given by equation 2.27. The factor θ denotes the amplitude of the additional discrete noise contribution at frequency f relative to the signal amplitude Φ_{S}. As it can be seen, discrete noise contributions at lower frequencies can lead to a significant degradation of the determined energy resolution for the χ^2-fit method, whereas they have no impact when optimal filtering is applied for signal analysis.

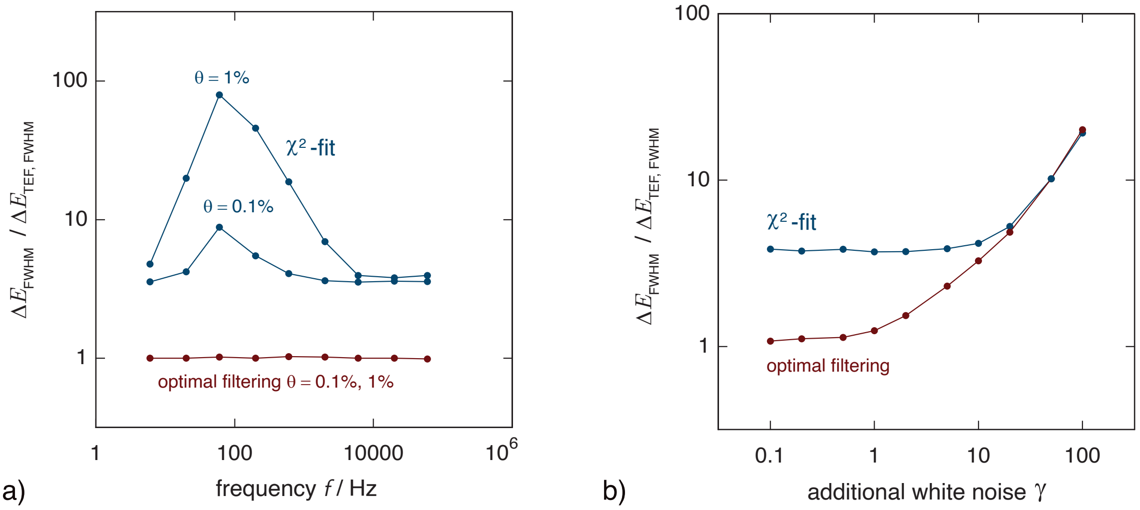

Figure 4.4: Simulations performed in [Fle03] to compare the determined energy resolution between the χ^2-fit method and the method of optimal filtering applied for signal analysis for different noise contributions that are additional to the detector intrinsic thermodynamic energy fluctuations. a) Calculated relative standard deviation of the determined linewidth as a function of additional discrete noise contributions at frequency f with an amplitude θ that is relative to the expected signal height Φ_{S}. b) Calculated relative energy resolution as a function of an assumed additional white noise contribution. The dimensionless factor γ is defined as an assumed additional noise contribution divided by the white noise level of the high frequency plateau of the detector intrinsic thermodynamic energy fluctuations.

It was discussed in section 2.6.4 how the thermodynamic energy fluctuations limit the intrinsic energy resolution of a metallic magnetic calorimeter. Therefore, [Fle03] also simulated for the two analysis methods how the determined energy resolution degrades when an additional white noise contribution is added to the high frequency noise plateau of these intrinsic thermodynamic energy fluctuations of the detector that was developed in [Fle03]. This calculation is depicted in figure 4.4 b), where the factor γ that is plotted on the x-axis denotes a dimensionless factor that is defined as an assumed additional white noise contribution divided by the noise level of the high frequency plateau of the detector intrinsic thermodynamic energy fluctuations. The plot shows, that for $\gamma > 10$ no relevant deviation in the determined energy resolution exists for the two analysis methods. This can for instance occur for MMCs that make use of the transformer coupled readout, where the additional noise contribution at high frequencies is usually dominated by the white noise of the current-sensor SQUID with a small contribution of the $1/f$-like noise of the Er ions, as it was illustrated in figure 2.8 a). However, for $\gamma < 10$ a significant deviation for the determined energy resolution between the two analysis methods occurs according to figure 4.4 b). As it was shown in figure 2.8 b) for a rather ideal case of the direct sensor readout, a γ between ~ 3 and ~ 6 can be achieved. In this case, using the χ^2-fit method for signal analysis instead of the method of optimal filtering can result in a significant degradation in the determined energy resolution. Since the former method is used in this thesis, it is therefore expected that the determined energy resolution of the developed detectors might potentially suffer from this at one point or another.

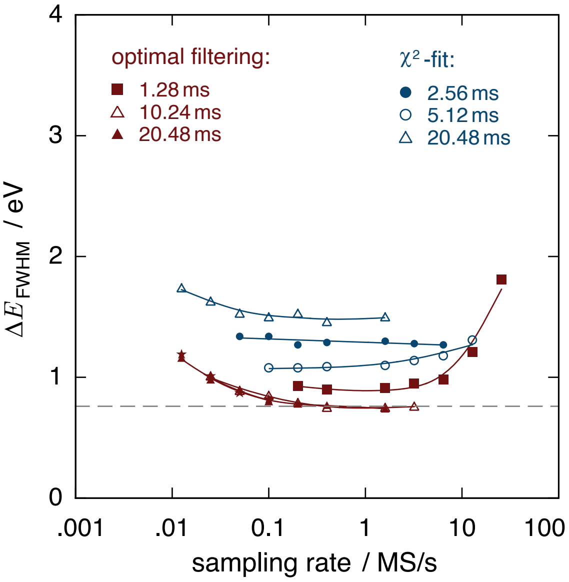

Figure 4.5: Comparison of the determined energy resolution for the two analysis methods as a function of the sampling rate used for data acquisition [Bug14]. The comparison is based on simulated data. Optimum filtering is required to achieve the baseline resolution of the detector, which is indicated by the grey dashed line. Using the χ^2-fit method degrades the energy resolution by at least a factor of 1.6 for the assumed simulation parameters. The respective data sets denote different acquired time windows.

Another comparison between optimal filtering and the χ^2-fit method was made in [Bug14] in regards to the used sampling rate for data acquisition. There, instead of only white noise, the calculated noise of the revised maXs-20 detector that was discussed in section 2.8 was used for testing the two algorithms. This noise was superimposed to simulated detector responses with a signal rise time of $\tau_0 = 1\,\mu$s, a signal decay time of $\tau_1 = 1\,$ms, and a signal amplitude of $\sim 0.6\,\Phi_0$ for a 5.9 keV energy input. The assumed amplitude is quite similar to what the detectors that were developed in this thesis achieved. Figure 4.5 shows the energy resolution that was determined with the two algorithms as a function of the sampling rate used for data acquisition. Furthermore, three sets of data for each analysis method are depicted, indicating different lengths of the acquired time windows. The grey dashed line denotes the calculated intrinsic energy resolution of the detector. The determined energy resolution degrades by a factor of 1.6 to 2.0 when the χ^2-fit method is used for signal analysis, whereas optimal filtering is required in order to achieve the intrinsic baseline resolution of the detector. Since the noise and signal amplitude that were used for these simulations are quite similar to the noise and signal amplitude of the detectors that are discussed in this thesis, one can expect do see a degradation in the determined energy resolution due to the use of the χ^2-fit method.

4.4 ^{55} Fe X-ray calibration source

An ^{55}Fe X-ray source is used to characterize the detectors that were developed in this thesis. It is encased in stainless steel with a beryllium window on one side, through which the emitted X-rays can pass. The casing is additionally glued in a brass holder in order to mount the source on the mixing chamber platform of the cryostat. The nucleus of the isotope ^{55}Fe decays with a half life of 2.74 years to a an excited ^{55}Mn nucleus via an electron capture process, which originates with a high probability from the K-shell. The ^{55}Mn de-excites by emitting X-rays or Auger electrons. The latter are absorbed by a 200 μm thick beryllium window, whereas the the dominant high energetic X-rays pass through it. In the radioactive decay process, the captured electron originates from the K-shell with a transition probability of 88%. The thereby created vacancy in the electron shell is filled with an electron from the L-shell with a probability of 90%, known as a K$_\alpha$-transition. This spectral line exhibits a fine-structure splitting due to the LS-coupling of the shell electrons, corresponding to the transitions $2p_{3/2} \rightarrow 1s_{1/2}$ with an energy of $E_{K_{\alpha_1}} = 5.899\,$keV and a natural linewidth of $\Delta E_{\mathrm{FWHM}} = 2.47\,$eV, and $2p_{1/2} \rightarrow 1s_{1/2}$ with an energy of $E_{K_{\alpha_2}} = 5.888\,$keV and a natural linewidth of $\Delta E_{\mathrm{FWHM}} = 2.92\,$eV [Höl97]. Figure 4.6 a) shows the natural lineshape of the K$_\alpha$ transition that was measured in [Höl97] with a crystal spectrometer. Table 4.1 lists the energy, the relative intensity and the natural linewidth of all spectral lines contributing to the natural K$_\alpha$ lineshape.

With a probability of 10%, the shell vacancy that is left after the electron capture is filled with an electron from the M-shell. The X-ray photon of this K$_\beta$-transition

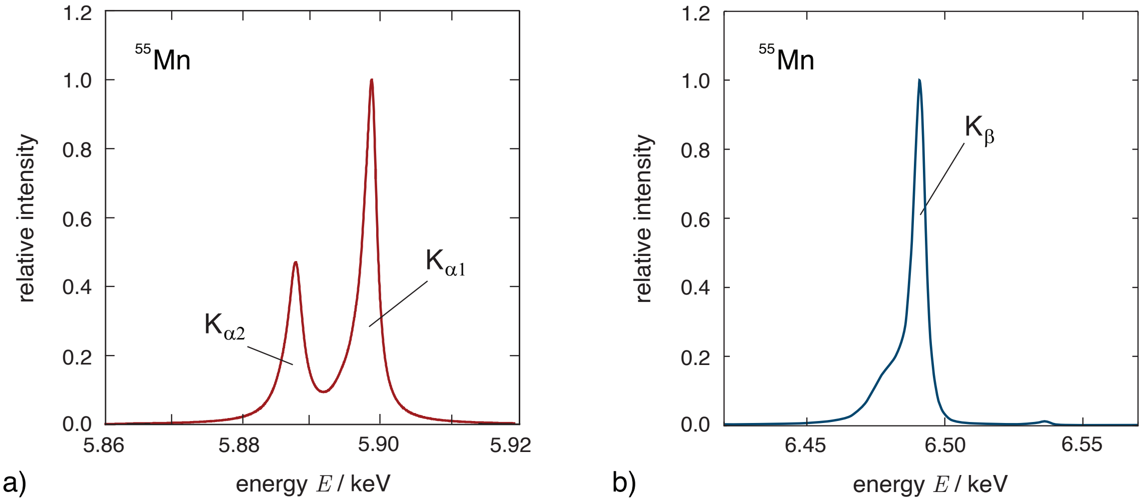

Figure 4.6: a) Natural lineshape of the ^{55}Mn K_α line, measured with a crystal spectrometer in [Höl97]. b) Lineshape of the ^{55}Mn K_β-transition, measured via X-ray fluoresence [Sak03].

spectral line	energy / eV	rel. intensity	linewidth / eV
$K_{\alpha 1}$	5898.853	0.790	1.715
	5897.867	0.264	2.043
	5894.829	0.068	4.499
	5896.532	0.096	2.663
	5899.417	0.007	0.969
	5902.712[1]	0.0106	1.5528
$K_{\alpha 2}$	5887.743	0.372	2.361
	5886.495	0.100[2]	4.216

Table 4.1: List of the energy, relative intensity and natural linewidth of the spectral lines that compose the ^{55}Mn K_{α_1} and K_{α_2} lines, respectively [Höl97]. [1] Additional line not reported in [Höl97], added from private E-mail between E. Förster, C. Enss and S. Porter. [2] Denoted as 0.01 in [Höl97], also corrected via this private E-mail.

has an energy of 6.49 keV. Its measured lineshape is shown in figure 4.6 b), measured with a crystal spectrometer [Sak03]. The remaining vacancy in the L-shell or M-shell is filled gradually with electrons from higher shells. However, the thereby emitted photons have a much lower energy and are absorbed by the protective casing of the used X-ray source, making their detection in the present setup impossible.

5. Fabrication technology

The microfabrication of some of the detectors that were developed in this thesis use up to 20 lithographic layers, and even more deposition and etching processes. For this reason, these detectors are among the most advanced detectors that have been developed in this group so far. This chapter hence discusses the optimization of state-of-the-art fabrication processes, as well as the development of entirely new processes, which were performed in order to ensure a reliable fabrication with high yield of such advanced detectors. The chapter consists of two main parts. The first one focuses on SQUID related processes, which begins with the fabrication of Josephson tunnel junctions, followed by a discussion of the quality of junctions that were fabricated with the state-of-the-art fabrication process. Afterwards, the optimization of this fabrication process is discussed, as well as the quality of junctions that were fabricated with the newly optimized fabrication process. The second main part focuses on MMC related processes, which includes the fabrication of the detector geometry that incorporates a separate field generating coil, the fabrication of overhanging absorbers on posts, and lastly the development of a fabrication process for high ampacity superconducting vias that are used to electrically connect different Nb wiring layers. Furthermore, an overview of the in-house microfabrication is given in the appendix A.1, where, for instance, the basics of a Lift-off process and an etching process are outlined.

5.1 SQUID fabrication technology

This section discusses the fabrication and characterization of high-quality Josephson tunnel junctions building one of the key elements for implementing the detectors developed within this thesis. In this context, the junction yield, the actual value of the critical current density j_c, as well as its spread Δj_c for different tunnel Junctions across the wafer area are of particular importance. This results from the fact that the energy sensitivity ϵ_s of a dc-SQUID is minimized for $\beta_\mathrm{C}, \beta_\mathrm{L} \approx 1$ and a hysteretic behavior of the Josephson tunnel junctions occurs for $\beta_\mathrm{C}, \beta_\mathrm{L} > 1$. Therefore, the design values of β_C and β_L for a dc-SQUID must be chosen in a way, so that the spread of the critical current ΔI_c, as well as the predictability of j_c is accounted for and $\beta_\mathrm{C}, \beta_\mathrm{L} \leq 1$ is guaranteed for all fabricated SQUIDs. At the beginning, the fabrication process for Nb/Al-AlO$_\mathrm{x}$/Nb Josephson tunnel junctions that was established prior to the start of this thesis will be discussed, followed by an overview of the quality of a selection of Josephson junctions that were fabricated with this process. Afterwards, the optimization of this fabrication process will be discussed, which includes the investigation of the surface morphology of Nb and Nb/Al thin films via atomic force microscopy (AFM), as well as the investigation of a potential hydrogen contamination of metallic Nb structures, that can potentially lead to a suppression of the superconductivity of Nb, or to a damage of the AlO_x tunneling barrier. The section concludes with a characterization of Nb/Al-AlO_x/Nb Josephson tunnel junctions that were fabricated with the newly optimized process.

5.1.1 Anodization-free fabrication of window-type Nb/Al-AlO_x/Nb Josephson junctions

The various steps of the state-of-the-art fabrication process for Nb/Al-AlO_x/Nb tunnel junction that has been developed prior to the start of this thesis are summarized in [Kem13] and also illustrated in figure 5.1. The process starts with an in-situ sputter deposition of an Nb/Al-AlO_x/Nb trilayer. The deposition of the metallic layers was done in the UHV sputtering system that is discussed in the appendix A.1.3. For the trilayer deposition, a 250 nm thick Nb bottom electrode is deposited at a sputtering power $P = 400\,\mathrm{W}$, an Ar pressure $p_{\mathrm{Ar}} = 0.27\,\mathrm{Pa}$, and with a deposition rate $\dot{d}_{\mathrm{Nb}} = 0.74\,\mathrm{nm/s}$ onto a pre-cleaned Si-substrate that is electrically insulated with an SiO_2 layer. Afterwards, 20 nm of Al are deposited at $P = 200\,\mathrm{W}$, $p_{\mathrm{Ar}} = 1.33\,\mathrm{Pa}$, and $\dot{d}_{\mathrm{Al}} = 0.26\,\mathrm{nm/s}$.

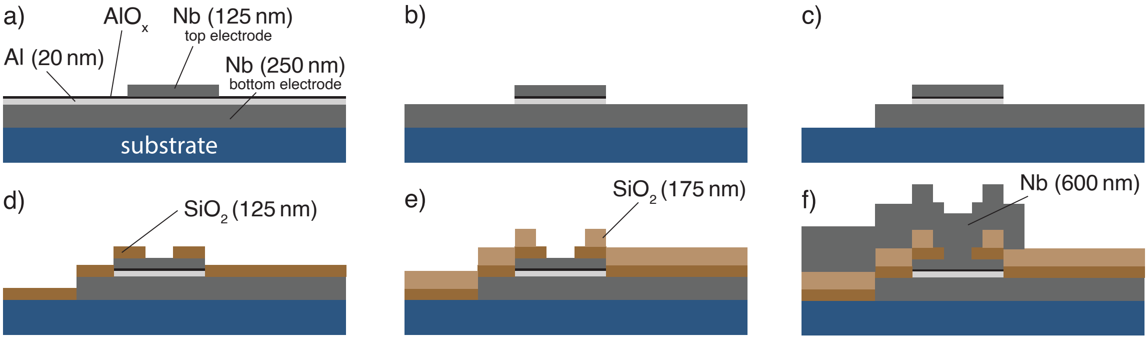

Figure 5.1: Schematic overview of the fabrication process for window-type Josephson tunnel junctions developed and used within this working group. Shown is the actual states of a single junction as intermediate steps of the process a) After sputter deposition of an Nb/Al-AlO_x/Nb trilayer, the top electrode is structured via ICP-RIE. b) The Al-AlO_x layer is chemically wet etched with an alkaline solution. c) The base electrode of the junction is etched via ICP-RIE. d) Deposition of a first insulation layer via a Lift-off process. e) Fabrication of a second insulation layer via a Lift-off process. f) Deposition of the Nb wiring contacting the top electrode via a Lift-off process.

The insulating AlO_x junction barrier is created via natural oxide formation induced by static O_2 exposure of the wafer in the load lock of the UHV sputtering system at room temperature. Under these conditions, the critical current density j_c of the junction follows a power law dependency $j_c \propto (p_{\mathrm{ox}} t_{\mathrm{ox}})^{-0.54}$ [Kem13]. Here, p_{ox} denotes the O_2 pressure in the load lock during oxidation and t_{ox} denotes the exposure time. A target critical current density of $j_c \approx 25\,\mathrm{A/cm^2}$ was chosen for all wafers that are discussed in this thesis. For this, an O_2 pressure of 41.3 mbar and an oxidation time of 16 hours was used. As it was discussed in section 3.2.3, the energy resolution of a dc-SQUID reduces for a reduced specific junction capacitance C and an increasing critical current density j_c. As C scales with the junction area A_{jj}, the latter should be chosen as small as possible. Due to accuracy limitations of the employed microfabrication techniques, the smallest window-type junction that we can fabricate is $A_{\mathrm{jj}} = 4 \times 4\,\mu\mathrm{m}^2$, whereas a size of $A_{\mathrm{jj}} = 5 \times 5\,\mu\mathrm{m}^2$ was chosen for the detectors in this thesis in order to enhance the yield of the fabricated detectors, as well as to reduce the effects of a potential deviation of the junction's edge length from the target value that might occur due to the limited accuracy of the microfabrication process. At this junction size, a critical current density of $j_c \approx 25\,\mathrm{A/cm^2}$ is used in order reach the required design values of β_{C} and β_{L}, as will be further discussed when the design of the developed detectors is introduced in section 6.1.2.

After Al oxidation, 125 nm of Nb are deposited as top electrode using the same sputtering parameters as for the bottom electrode. This finalizes the trilayer fabrication. Afterwards, using the positive resist AZ MIR 701 29cps, the top electrode is structured and etched via ICP-RIE. The Nb is etched using a $p_{\mathrm{ICP}} = 2\,\mathrm{Pa}$ SF_6 atmosphere, a substrate bias power of $P_{\mathrm{rf}} = 50\,\mathrm{W}$ and an ICP-power of $P_{\mathrm{ICP}} = 100\,\mathrm{W}$. During this process, the wafer is kept at 5 °C, resulting in an etch rate of $\dot{e}_{\mathrm{Nb}} \sim 1\,\mathrm{nm/s}$. The cross section of the resulting structure is shown in figure 5.1 a). Figure 5.1 b) depicts the state-of-the-art fabrication process after the Al-$\mathrm{AlO_x}$ was wet chemically etched with the developer AZ 351B (1:4 diluted in water), which is an NaOH based alkaline. During this step, no photoresist is applied and the Nb top electrode structured before acts an etching mask. It is worth mentioning, that we have never observed indications for a junction quality degradation due to a potential underetch and subsequent damage of the Al-$\mathrm{AlO_x}$ layer below the top electrode. After the wet etching of Al, the bottom electrode is structured with an etch process via ICP-RIE using the same process parameters as for the top electrode. Figure 5.1 c) shows the Josephson junction after the bottom electrode was structured. Next, a first insulation layer is deposited via a Lift-off process, for which the negative resist AZ 5214E is used, as it is the case for all the other Lift-off processes in the discussed junction fabrication. The deposited 125 nm thick SiO_2 layer covers the entire wafer, except for a small window that is left open on top of the junction for a later created electrical contact, hence the name window-type Josephson junction. The SiO_2 is rf-sputtered in either the UHV sputtering system or in the Alcatel system (see appendix A.1.2). When deposited in the UHV sputtering system, a sputter power $P_{\mathrm{rf}} = 250\,\mathrm{W}$, an Ar/O_2 (60 %/40 %)

pressure $p_{\mathrm{Ar/O_2}} = 0.67\,\mathrm{Pa}$, and a deposition rate $\dot{d}_{\mathrm{SiO_2}} = 1.73\,\mathrm{nm/min}$ is used. When the SiO_2 is deposited in the Alcatel system, a sputter power $P_{\mathrm{rf}} = 250\,\mathrm{W}$, an Ar/$O_2$ (60 %/40 %) pressure $p_{\mathrm{Ar/O_2}} = 0.7\,\mathrm{Pa}$, and a deposition rate $\dot{d}_{\mathrm{SiO_2}} = 1.3\,\mathrm{nm/min}$ is used. This first insulation layer has to be thick enough so that the edges of the Nb/Al-AlO_x post forming the top electrode and tunnel barrier is sufficiently covered. The thereby insulated junction is depicted in d). Afterwards, a second 175 nm thick insulation layer is deposited via a Lift-off process, where the window on top of the Josephson tunnel junction is slightly larger than before, as it can be seen in e). As a last step, the 600 nm thick Nb wiring to contact the top electrode is deposited via a Lift-off process, using the same deposition parameters as for the junction electrodes. The finished Josephson junction is depicted in figure 5.1 f).

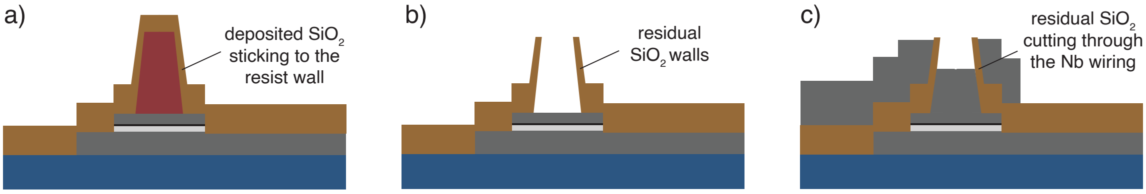

Figure 5.2: Illustration of the Nb/Al-AlO_x/Nb tunnel junction fabrication with only a single SiO_2 layer. a) After sputter deposition, SiO_2 can potentially stick to the side walls of the photoresist that is used to define the window on top of the junctions. b) The SiO_2 walls remain even after photoresist removal. c) The SiO_2 walls cut through the later deposited Nb wiring, preventing a galvanic contact between the wiring and the top electrode of the junction.

The reason why the deposition of the insulation layer is split into two separate layers is illustrated in figure 5.2 a). What is shown is the structured photoresist on top of the Junction that is used to define the window. When the process was developed in [Kem13], a positive resist was used, indicated by the direction of the slanted edges of the resist, as a structuring of such small resist posts with a negative photoresist was not possible in the group at that time. As a result of this resist shape, the deposited SiO_2 covered the entire photoresist. What could sometimes then occur in this case is depicted in b). Shown is the junction after the photoresist was removed in a suitable solvent, with SiO_2 walls remaining on the wafer. These walls could prevent an electrical connection between the later deposited 600 nm thick Nb wiring and the top electrode of the junction, as it is depicted in c). It was therefore decided to use two separate insulation layers of equal combined thickness and different window sizes compared to the single layer option, so that the height of the residual SiO_2 walls could not exceed the layer thickness of the later deposited Nb wiring. The latter was not made thicker as this could potentially introduce high mechanical stress to the wafer, consequently damaging the tunnel junctions, as was will be discussed in section 5.3.1.

Fabricating such small resist posts with a negative photoresist was made possible in the group at a later point in time and the process was adapted accordingly. However, even then was a creation of the illustrated SiO$_2$ walls observed, albeit on a much smaller scale. At that point, the subsequent junction fabrication was also done with two separate insulation layers in order to allow for a reduced thickness of the deposited Nb wiring layer, as a Lift-off process with such small resist structures becomes more reliable as a result.

5.2 Quality of Nb/Al-AlO$_x$/Nb Josephson junctions prior to this thesis

This section discusses the quality of a selection of Nb/Al-AlO$_x$/Nb Josephson junctions that were fabricated with the state-of-the-art fabrication process. The latter was originally established in [Kem12, Kem13] in the group, yielding high quality junctions with a measured sub gap voltage U_g of up to 2.9 mV, an I_cR_N-product as high as 1.8 mV and a ratio of subgap to normal state resistance $R_{sg}/R_N > 30$, all measured at $T = 4.2\,K$. However, such a quality was not always achieved with this process. In fact, some wafers showed a large spread ΔI_c of the critical current for junctions of equal size, a strong deviation between the target critical current density j_c and the actual j_c, or a low yield of working Josephson junctions, whereas other wafers exhibited a high junction quality with excellent yield, as it was reported in [Zim18] for instance. This section therefore presents the characterization of a selection of wafers in order to illustrate why an optimization of the junction fabrication process was performed within this thesis.

5.2.1 Measurement setup

To characterize the quality of the Josephson junctions, their IV-characteristics were measured using the experimental setup that is schematically depicted in figure 5.3. For the characterization based on a 4-point probe measurement, a chip containing Josephson tunnel junctions was glued to a circuit board, connected via Al wire bonds and cooled down to $T = 4.2\,K$ in a liquid ^{4}He transport dewar. Via a PCB connector, the circuit board was connected to a circuit board hosting second order RC low-pass filters that are required to filter out parasitic high frequency signals that could emerge, for instance, from pickup of electromagnetic signals from the environment. Both circuit boards were encased in a magnetic shielding, which consists of an outer Mu-metal shield and an inner shield made out of niobium, the latter being superconducting at this temperature.

Twisted pair CuNi wiring connects the cryogenic setup to a room temperature filter box. To the input side of this box, were RC low-pass filters are hosted, a voltage

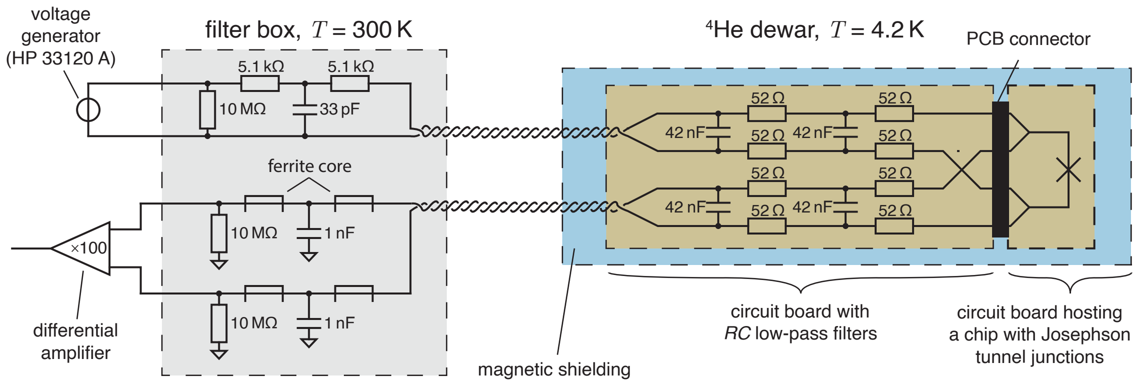

Figure 5.3: Schematic of the experimental setup that was used within this thesis to measure the IV-characteristics of Josephson tunnel junctions.

generator (HP 33120 A) was connected. This generator was used to create a bias current I by applying a voltage U, with triangular waveform and a frequency of $f = 3\,\mathrm{Hz}$, to the series connection consisting of two $R = 5.1\,\mathrm{k\Omega}$ resistors, four $52\,\Omega$ resistors, and the Josephson tunnel junction. On the output side of the filter box, LC filters are situated, as well as a $10\,\mathrm{M\Omega}$ connection to ground in order to prevent electrostatic discharge damage of the junction. A customized differential amplifier[1] was used to boost the output signal by 20 dB. The input voltage of the generator as well as the amplified output voltage were read out with an oscilloscope and saved for later data evaluation.

5.2.2 Quality of Josephson junctions from a selection of wafers

Figure 5.4 a) shows a measured IV-characteristic of a tunnel junction of $6 \times 6\,\mu\mathrm{m}^2$ in size from the wafer internally labeled HDSQ10a #w1, which is one of the selected wafers that are discussed in this section. Also shown are corresponding figures of merit that were discussed in section 3.1.1, i.e. the critical current I_c, the gap voltage U_g, the subgap resistance R_sg, and the normal state resistance R_N. The target critical current density of this wafer was $j_\mathrm{c} \approx 25\,\mathrm{A/cm^2}$. Therefore, the measured critical current $I_\mathrm{c} = j_\mathrm{c} A_\mathrm{jj}$ is a factor of 7 lower than anticipated. The gap voltage $U_\mathrm{g} = 2.52\,\mathrm{mV}$ is $0.2 - 0.3\,\mathrm{mV}$ lower than for the high quality junctions reported in the past [Kem13, Zim18], whereas the corresponding resistance ratio $R_\mathrm{sg}/R_\mathrm{N} = 17.6$ is more than a factor of 2 lower. The depicted junction was not randomly chosen. Instead, it belongs to the Josephson tunnel junction with the highest determined U_g and $R_\mathrm{sg}/R_\mathrm{N}$ out of all investigated junctions from the selected wafers. Most of the remaining measured tunnel junctions exhibited an even further degraded quality to a point, that a determination of I_c, U_g or R_sg was not even possible, because they either

---

[1] Burr Brown, INA110

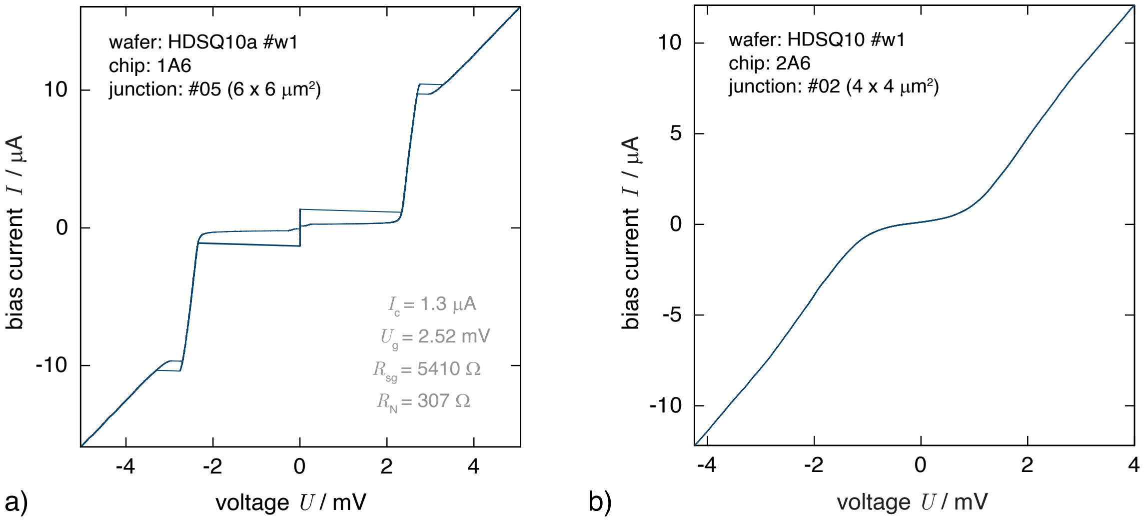

Figure 5.4: a) IV-characteristic of a $6 \times 6\,\mu\mathrm{m}^2$ sized Josephson tunnel junction from the wafer HDSQ10a #w1, as well as determined values for its corresponding figures of merit, depicting the investigated junction with the highest U_g and $R_\mathrm{sg}/R_\mathrm{N}$ from the discussed wafer selection. b) IV-characteristic of a $4\times4\,\mu\mathrm{m}^2$ sized Josephson tunnel junction from the wafer HDSQ10 #w1. The junction shows no hysteretic behavior, which is usually achieved by connecting a shunt resistor in parallel. The junction of the depicted IV-characteristic is called self-shunted, indicating that a normal conducting connection between the bottom and top electrode exists.

showed a completely ohmic behavior, or very high sub gap leakage currents in the quasiparticle regime at $U < U_\mathrm{g}$. The IV-characteristic of such a low quality junction from the wafer HDSQ10 #w1 is depicted in figure 5.4 b). No hysteretic behavior can be observed because the junction is damped due to a normal conducting connection between the bottom and top electrode. Such a connection can potentially occur for a damaged AlO$_\mathrm{x}$ tunneling barrier, where formed pinholes short the electrodes.

Figure 5.5 shows the measured critical current I_c as a function of the junction area A_jj for five selected wafers that were fabricated within the group, all of which had the same target $j_\mathrm{c} \approx 25\,\mathrm{A/cm}^2$, indicated by the red line. What can be observed is that none of the investigated junctions, except for one, reached its target critical current. The y-axis is plotted on a logarithmic scale in order to illustrate the large spread in I_c. As it can be seen, large deviations of more than one order of magnitude for junctions of equal size even from the same wafer were observed. Furthermore, the shown plot includes only 36 data points. This is due to an extremely low yield of working junctions on these five wafers, which made a statistical analysis of the junction quality across an entire wafer futile. The large I_c spread can not be attributed to a deviation in the junction area A_jj because the accuracy limitations of the employed microfabrication techniques could explain an error of the edge length of a junction

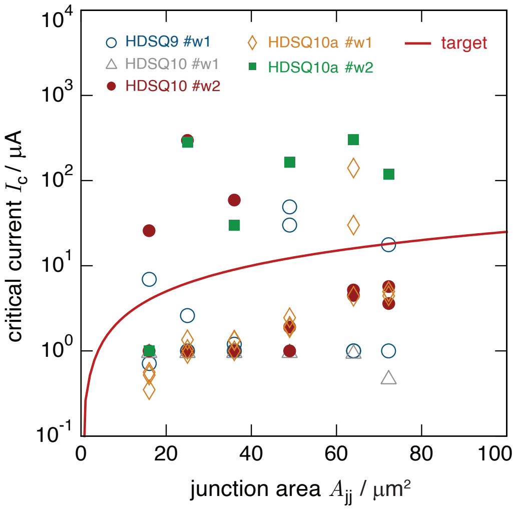

Figure 5.5: Measured critical current I_c as a function of the junction area A_jj of Josephson tunnel junctions from five selected wafers that were fabricated within the group, indicating a very high critical current spread ΔI_c, as well as a large deviation between the determined I_c and its target value. The y-axis is logarithmic in order to illustrate the large parameter spread.

of up to 200 nm, which would result in an error of the junction area of $\sim 10\,\%$ for the smallest investigated junctions, and which becomes negligible for the larger ones. The presented data however would imply an error in A_jj of at least a factor of three, which is an unrealistic assumption that would have been easily observable during a mandatory quality check under a microscope during wafer fabrication. In addition, the used experimental setup was also used for the characterization of the high quality Josephon junctions that are discussed in [Zim18]. Therefore, the large parameter spread can not be attributed to a faulty experimental setup or to an insufficient magnetic shielding, which could otherwise result in a suppression of the critical current of the junctions due to external magnetic fields. The discussed data makes it quite apparent why an optimization of the junction fabrication process within this thesis was essential.

5.3 Optimization of metallic thin film properties for Josephson junction fabrication

For the development of metallic magnetic calorimeters with direct sensor readout, as it was the main goal of this thesis, a low junction yield could lead to a significant loss of available detector channels for fabricated chips, especially when considering that present day MMC developments move towards larger, two-dimensional detector arrays with several tens or hundreds of individual detectors [Hen17, Weg18, Dev19, Gam19, Sch19]. Therefore, the used Nb/Al-AlO$_\mathrm{x}$/Nb junction fabrication process was optimized in several aspects as part of this thesis. This section first presents an introduction of requirements for a reliable Nb/Al-AlO$_\mathrm{x}$/Nb Josephson junction fabrication process. Afterwards, the characterization of sputtered metallic thin films in regards to surface roughness and morphology is discussed, as well as a potential hydrogen contamination of Nb thin films, which can potentially degrade the superconducting properties of niobium, as well as damage the $\mathrm{AlO_x}$ tunneling barrier within the junction.

5.3.1 Introduction

Ideally, the individual layers that are sputter deposited during the fabrication of Nb/Al-$\mathrm{AlO_x}$/Nb Josephson junctions should have a very high purity, should exhibit either no or slightly compressive intrinsic stress, feature a perfectly flat surface and possess an identical layer thickness across the entire substrate. In fact, all of these quality factors deviate in practice from this ideal case for a non-optimized fabrication process. When the material deposition is done via sputter deposition, as it was the case in this thesis, then the film quality depends for instance on the applied sputter cathode voltage U_{sp} during film deposition, the Ar sputter pressure p_{Ar}, or the substrates temperature [Cuo82, She83, Spa00, Oko04, Aba18]. The quality and yield of the Nb/Al-$\mathrm{AlO_x}$/Nb junction fabrication strongly depends on these thin film quality factors and their optimization is highly beneficial for the development of a reliable fabrication process [Ima92b, Hin08, Xu11].

In practice, the process parameters that lead to a deposition of thin films of excellent quality are inherently connected to the utilized sputtering system. For instance, various combinations of the cathode voltage U_{sp}, or sputter power P, can lead to a deposition of Nb thin films with minimum stress [Ima92b]. In addition, an Ar sputter pressure p_{Ar} ranging from 0.6 Pa to 1.9 Pa was found to yield a minimized intrinsic film stress [Wu79, Kur88, Tsu93, Du07b]. The exhibited film stress also depends on the substrate material [Oko04], on the substrate preparation prior to sputtering [Bas03], scales with the deposited film thickness [Qui99] and lastly, as already mentioned, depends on the substrates temperature during sputtering [Cha10]. The impact of highly compressive or highly tensile stress can lead to a reduction of the critical temperature T_{c} of a superconductor [Wu79], which would consequently reduce the gab voltage U_{g} in Nb/Al-$\mathrm{AlO_x}$/Nb Josephson junctions [Kur88]. Furthermore, a slight bending of the silicon substrate can occur when films with intrinsic stress are deposited. In this case, when for instance most of the high stress Nb is removed during the etching of the Nb/Al-$\mathrm{AlO_x}$/Nb trilayer, the wafer relaxes and potentially damages individual Josephson junctions due to the mechanical impact of the relaxation process.

The surface roughness and morphology of thin films is also directly linked to intrinsic stress [Oko04, Eng16], and consequently also depends on the chosen sputter parameters [Liu09, Bor12], as well as on the substrate material and temperature [Her15]. In terms of surface morphology, large grain sizes in deposited Nb thin films are an indicator that the film exhibits the superconducting properties of its bulk material[Jin09]. Even further, deposited Nb thin films with grain size diameters of $> 25\,\mathrm{nm}$ exhibit bulk superconductivity, whereas films with a grain size $< 8\,\mathrm{nm}$ exhibit no superconductivity at all [Bos05]. Between these two limiting cases, the superconducting ampacity, as well as the critical temperature T_c, are usually reduced.

For niobium, high quality sputter deposited films usually grow as elongated grains with a grain length of up to 100 nm, and also show a parallel growth orientation for grains that are in close proximity to each other [Du07a, Roa11, Kit18], which is true for sputtered Nb films on Si, SiO_2, MgO and sapphire substrates [Kan13]. However, a larg grain size usually results in a high surface roughness of the deposited Nb film. A flat surface of Nb and Al thin films is important in order to assure a consistent coverage of the Nb bottom electrode by the AlO_x barrier, as illustrated by figure 5.6 a). When the surface flatness is insufficient, as depicted in figure 5.6 b), a formation of pin holes can occur, shorting the bottom and top electrode of the junction, leading either to its destruction, or at least to large leakage currents in the quasiparticle regime at $U < U_g$ [Tsu93, Du07b]. It is known that Al deposited onto Nb smoothens the surface, making the creation of a well defined AlO_x tunneling barrier through natural oxide formation possible [Ima92a, Du07b]. In this meterial system, the surface coverage can be enhanced by increasing the Al layer thickness. However, this is possible only up to a certain point, as the intrinsic stress and surface roughness of Al scale with layer thickness [Agu02, Ott14], and the gap voltage U_g of the junction decreases with increasing Al thickness due to the proximity effect [McM68, Hou93, Zeh99]. Therefore, a small surface roughness of the Nb bottom electrode and an Al layer as thin as possible are preferred.

When the established fabrication process for Nb/Al-AlO_x/Nb Josephson junctions, that was discussed in section 5.1.1, was originally developed in [Kem12], experimental methods for the in-situ investigation of sputter deposited thin films were not accessible within the research group. Hence, the optimum fabrication parameters

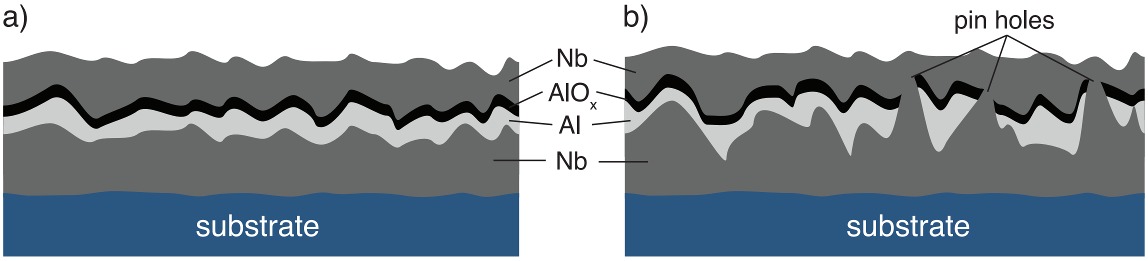

Figure 5.6: Illustration of the cross section of a Nb/Al-AlO_x/Nb trilayer. a) A sufficiently flat Nb bottom electrode can be completely covered by an Al-AlO_x layer. b) A high surface roughness of the Nb bottom electrode can lead to the formation of pin holes, potentially shorting both junction electrodes.

were found empirically via a trial-and-error approach that included the fabrication and characterization of Josephson junctions from more than 30 wafers. At a later point, an investigation of the surface roughness and morphology via atomic force microscopy was made available. This method was used in this thesis to characterize the surface morphology of Nb and Al thin films in order to reduce the surface roughness by varying the sputter power P, the Ar sputter pressure p_{Ar}, the thin film thickness t, and the substrate temperature T for thereby fabricated test samples. These characterizations are discussed in the following section. It is worth mentioning that the means to investigate film stress became available later in this thesis, but the findings of corresponding investigations could not be incorporated into the fabrication of the developed detectors, as the latter were already fabricated, but not yet fully characterized at the time the film stress investigation system became available.

5.3.2 Figures of merit to characterize the surface morphology

Within this thesis, the surface morphology of Nb and Al thin films was investigated by means of atomic force microscopy (AFM) with a Bruker Multimode 8 AFM[2]. The relevant figures of merit for the characterization of the surface roughness are illustrated in figure 5.7. Relevant for the discussion are the average height $\langle z \rangle$, the average roughness R_{a}, and the peak-to-valley depth R_{max} within an investigated area of the sample.

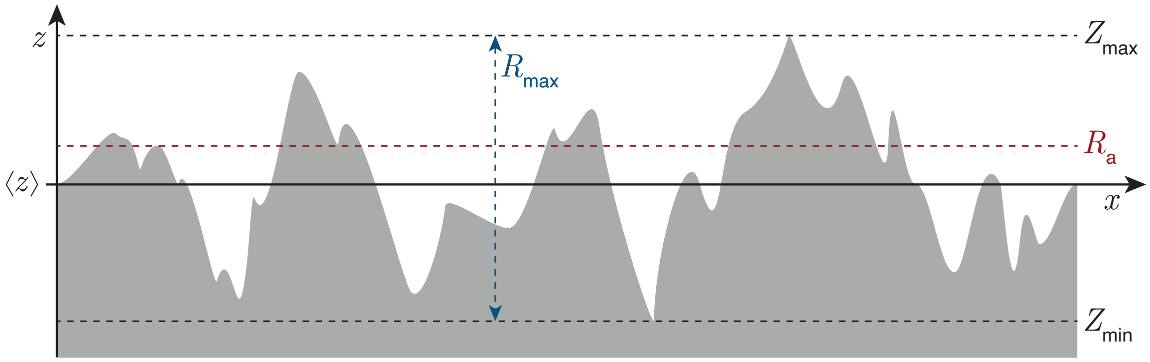

Figure 5.7: Schematic cross section of an arbitary surface used to illustrate the corresponding figures of merit that are explained in the text. $\langle z \rangle$ denotes the average height, R_{a} the average roughness, and R_{max} the peak-to-valley depth in z-direction.

The average height $\langle z \rangle$ is given by the average of all measured height values

$$\langle z \rangle = \frac{1}{MN} \sum_{m=1}^{M} \sum_{n=1}^{N} z(x_{\mathrm{m}}, y_{\mathrm{n}}) \,, \tag{5.1}$$

---

[2] Bruker Corporation:www.bruker.com

where M and N denote the number of taken data points in x- and y-direction respectively. The average roughness R_a is the arithmetic mean of the absolute deviations from the average height $\langle z \rangle$:

$$R_\mathrm{a} = \frac{1}{MN} \sum_{m=1}^{M} \sum_{n=1}^{N} \left| z(x_\mathrm{m}, y_\mathrm{n}) - \langle z \rangle \right| . \tag{5.2}$$

The peak-to-valley depth R_max is defined as the difference between the maximum measured height Z_max and the minimum measured height Z_min:

$$R_\mathrm{max} = \left| Z_\mathrm{max} - Z_\mathrm{min} \right| . \tag{5.3}$$

5.3.3 Substrate preparation

Prior to material deposition, the utilized substrate for each sample underwent a nearly identical preparation process. Small substrates made of high-purity silicon with a thickness of $375 \pm 25\,\mu$m were used, which are insulated by 240 nm of thermal SiO_2. Potential intrinsic stress contributions of the substrates themselves that might have an impact on the deposited film morphology was not accounted for. The substrates were clamped to a copper holder roughly 3 inch in diameter and vacuum grease was applied between substrate and holder to provide an adequate heat sinking during material deposition. In the load lock of the employed UHV-sputter system (see appendinx A.1.3), the substrate surface was cleaned via argon ion milling for 5 minutes (see appendix A.1.4). Afterwards, the substrate was transferred into the main UHV chamber for material deposition.

5.3.4 Surface morphology investigation of Nb thin films

The process parameters that were deliberately varied for the deposition of the characterized films were the sputter power P, the Ar sputter pressure p_Ar and the thin film thickness t in order to find a suitable parameter set for minimized surface roughness. A reference surface morphology was measured on an Nb thin film that was fabricated with the standard process parameters used fabricating Nb/Al-AlO_x/Nb Josephson junctions in the group prior to the start of this thesis, i.e. a sputter power $P = 400\,\mathrm{W}$, an Ar pressure $p_\mathrm{Ar} = 0.27\,\mathrm{Pa}$, a deposition rate $\dot{d}_\mathrm{Nb} = 0.74\,\mathrm{nm/s}$ and a layer thickness $t_\mathrm{Nb} = 250\,\mathrm{nm}$. Figure 5.8 a) shows a measured AFM image of a $5 \times 5\,\mu\mathrm{m}^2$ sized section of this sample. Also shown are the corresponding figures of merit, as well as a zoom into a smaller section. Both pictures show, that the Nb surface is built by elongated grains with a length of up to $\sim 100\,\mathrm{nm}$ and a width that varies between 20 nm and 50 nm. In addition, grains that are grouped together in close proximity are oriented in parallel to each other. These correspond to literature

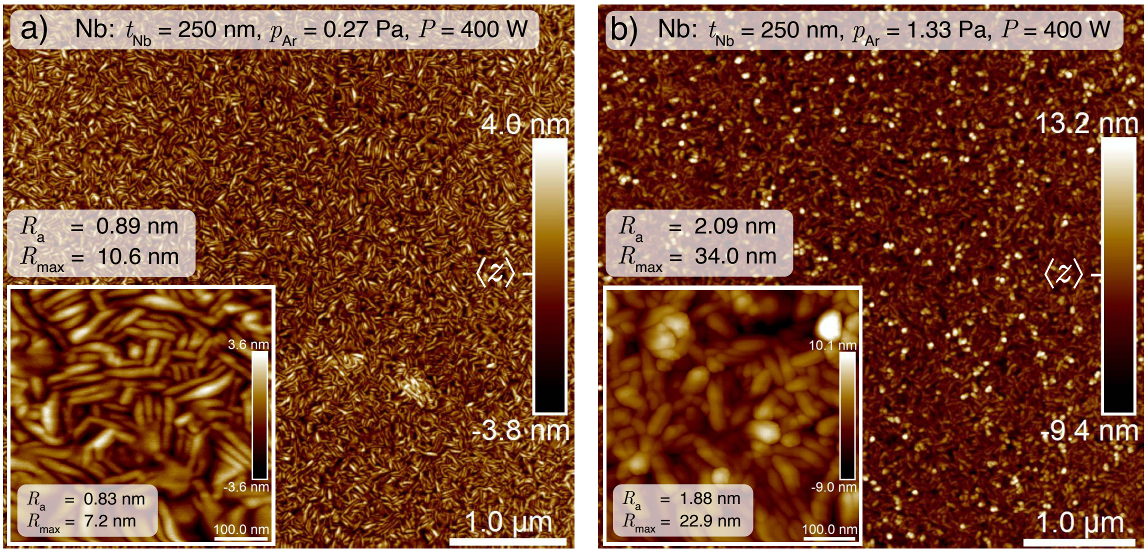

Figure 5.8: Measured AFM images of a surface morphology of Nb thin films, sputter deposited at $P = 400\,\mathrm{W}$ and $T = 300\,\mathrm{K}$. Shown are surface sections of $5 \times 5\,\mu\mathrm{m}^2$ and a zoom into a region with an area of $500 \times 500\,\mathrm{nm}^2$. a) The film was deposited at $p_{\mathrm{Ar}} = 0.27\,\mathrm{Pa}$ and $\dot{d}_{\mathrm{Nb}} = 0.74\,\mathrm{nm/s}$. b) The film was deposited at $p_{\mathrm{Ar}} = 1.33\,\mathrm{Pa}$ and $\dot{d}_{\mathrm{Nb}} = 0.93\,\mathrm{nm/s}$.

reports that were discussed in the introduction of this section. In order to study the dependence of the average surface roughness R_{a} and the peak-to-valley depth $R_{\max}$ on the gas pressure p_{Ar}, several AFM images of samples fabricated with different values of p_{Ar} were evaluated. Figure 5.8 b) shows, for example, the AFM image for a film deposited at $p_{\mathrm{Ar}} = 1.33\,\mathrm{Pa}$ and figure 5.9 a) shows the overall determined dependence of R_{a} and $R_{\max}$ on the sputter pressure p_{Ar}. The average surface roughness R_{a} is between $0.8\,\mathrm{nm}$ and $1.0\,\mathrm{nm}$ and $R_{\max}$ is $\sim 10\,\mathrm{nm}$ for an investigated sputter pressure $p_{\mathrm{Ar}} < 0.67\,\mathrm{Pa}$. For $p_{\mathrm{Ar}} = 1.33\,\mathrm{Pa}$, R_{a} is significantly increased by a factor of ~ 2.5, whereas $R_{\max}$ shows an increase by a factor of 3.4. With a length of up to $\sim 60\,\mathrm{nm}$, the elongated grains are now shorter compared to the samples that was deposited at $p_{\mathrm{Ar}} < 0.67\,\mathrm{Pa}$. This film growth behavior is also known from literature [Tsu93]. In addition, this measurement confirms the observations in [Du07a], were the surface roughness is shown to be rather constant for low sputtering pressures and that a significant increase occurs for $p_{\mathrm{Ar}} \geq 1.2\,\mathrm{Pa}$. The measurements show a comparably rough surface of our Nb films and that the average surface roughness can potentially be reduced by a factor of ~ 2 when compared to values found in literature [Du07b].

The effects of the substrate temperature T during film deposition are illustrated in figure 5.9 b), showing that the measured roughness increases with T. Therefore, the film with the smallest surface roughness was deposited at room temperature, a finding that also agrees with literature [Wan17]. During further investigation of Nb

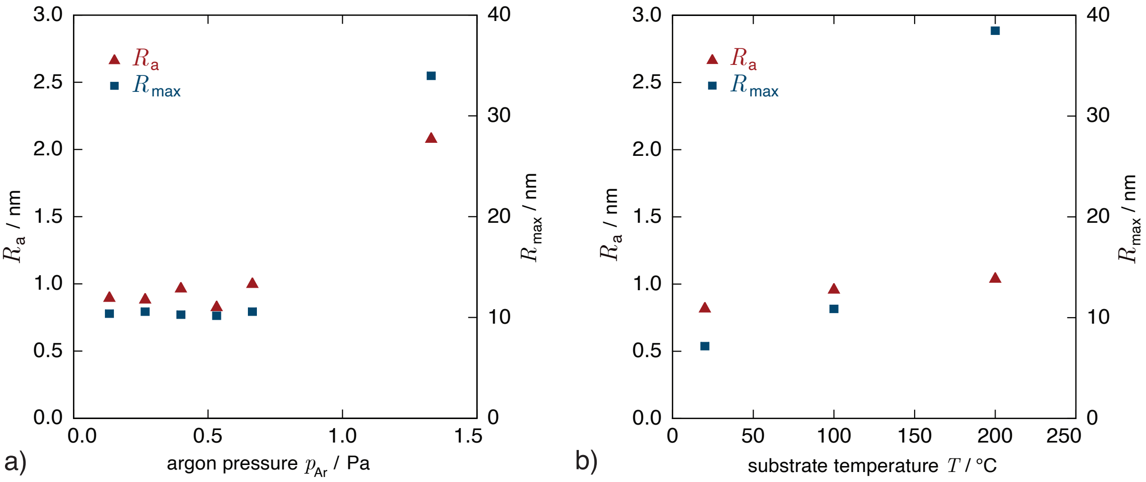

Figure 5.9: a) Average surface roughness R_a and peak-to-valley depth R_{max} as a function of sputtering pressure p_{Ar} for 250 nm thick Nb layers, that were dc-magnetron sputtered at $P = 400\,W$ and $T = 300\,K$. The deposition rate was between 0.64 nm/s and 0.93 nm/s, increasing roughly linear with p_{Ar}. b) R_a and R_{max} as a function of substrate temperature T. The 250 nm thick Nb layer was deposited at $p_{Ar} = 0.27\,Pa$, $P = 400\,W$, and $\dot{d}_{Nb} = 0.74\,nm/s$.

thin films, the impact of the film thickness t_{Nb} and the sputter power P on the surface roughness was investigated. The measured surface roughness as a function of film thickness t_{Nb} is illustrated in figure 5.10 a). It is shown, that the average roughness R_a scales with film thickness, whereas the peak-to-valley depth R_{max} heavily scatters. The dependence of R_a on the film thickness t_{Nb} agrees well with literature [Kan13].

The results indicate that the bottom electrode of an Nb/Al-AlO$_x$/Nb trilayer should be thin in order to minimize the surface roughness, which consequently minimizes the formation of pin holes within fabricated Josephson junctions. However, the Nb layer can not be made arbitrarily thin. When the film thickness is smaller than the London penetration depth λ_L, the energy gap of the Nb gets reduced, consequently reducing its critical temperature T_c and the gap voltage U_g of fabricated Josephson junctions. Values for the London penetration depth λ_L of Nb thin films can be found in scientific literature with $\lambda_L = 85\,nm$ for $T \rightarrow 0$ [Hen77, Duz81, Hin88]. Considering its temperature dependence $\lambda_L(T) = \lambda_L(0)/\sqrt{1-(T/T_c)^4}$, the penetration depth yields $\lambda_L(4.2K) = 87\,nm$ for liquid helium temperatures, at which Josephson junctions are commonly characterized in our group. Therefore, fabricating Nb/Al-AlO$_x$/Nb Josephson junctions of high quality with an Nb bottom electrode thickness $>\sim$ 100 nm is possible and was experimentally proven [Kai11]. However, Nb layer thicknesses below 250 nm were not considered for the process optimizations discussed this thesis, because past measurements for sputter deposited Nb in this group indicated a λ_L as high as 270 nm [Foe12].

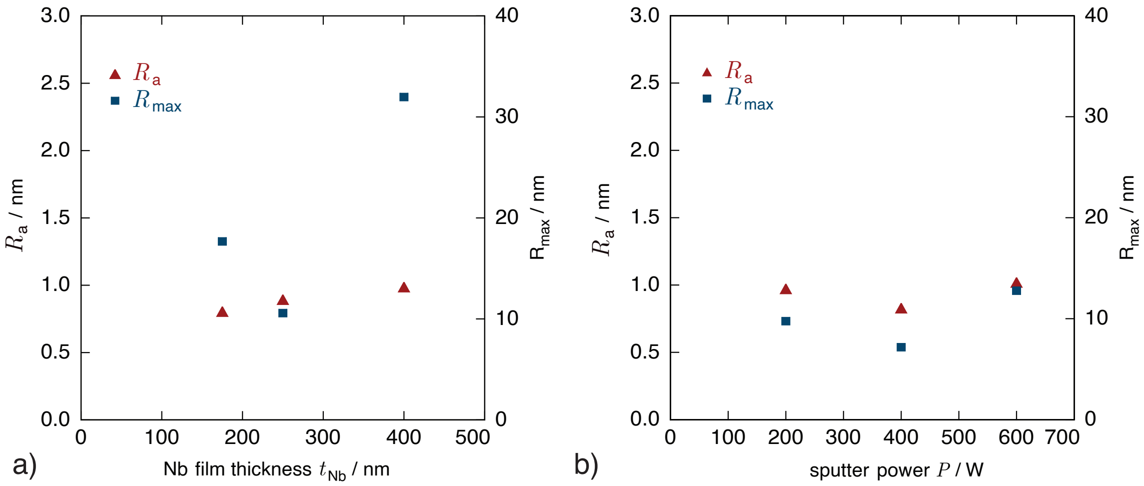

Figure 5.10: Measured figures of merit R_a and R_max of dc-magnetron sputtered Nb films deposited at $T = 300\,\mathrm{K}$ as a) a function of film thickness t_Nb for $P = 400\,\mathrm{W}$, $p_\mathrm{Ar} = 0.27\,\mathrm{Pa}$ and $\dot{d}_\mathrm{Nb} = 0.74\,\mathrm{nm/s}$, and b) as a function of the sputter power P for $p_\mathrm{Ar} = 0.27$. The deposition rate $\dot{d}_\mathrm{Nb}(P)$ is between $0.36\,\mathrm{nm/s}$ and $1.1\,\mathrm{nm/s}$.

Furthermore, the surface roughness of Nb as a function of sputtering power P was investigated on a 250 nm thick film that was dc-magnetron sputtered at $p_\mathrm{Ar} = 0.27\,\mathrm{Pa}$ and $T = 300\,\mathrm{K}$. The results are depicted in figure 5.10 b), showing that the in the past empirically chosen value of $P = 400\,\mathrm{W}$ results in the smallest surface roughness. A similar investigation [Du07a] also shows no apparent correlation between Nb surface roughness and sputter power.

5.3.5 Surface morphology investigation of Nb/Al bilayers

In order to investigate the coating of Nb by Al, in-situ sputtered Nb/Al bilayers were fabricated and characterized. The parameters of the deposited Nb layer were kept identical for each sample, i.e. $P = 400\,\mathrm{W}$, $p_{\mathrm{Ar}} = 0.27\,\mathrm{Pa}$ and $t_{\mathrm{Nb}} = 250\,\mathrm{nm}$. A reference measurement was performed in which the Al was deposited with the empirically determined parameters of the standard fabrication process, as was discussed in section 5.1.1. The corresponding AFM images are illustrated in figure 5.11 a). In addition, the measured figures of merit $R_{\mathrm{a}} = 1.25\,\mathrm{nm}$ and $R_{\max} = 25.3\,\mathrm{nm}$ are given. A comparison between these values and the measured ones of the corresponding Nb layer below (see figure 5.11 b)) shows, that the average surface roughness R_{a} increased by 40 % and the peak-to-valley depth $R_{\max}$ increased by 240 %, even though the total layer thickness was increased by only 7.5 %. This is not consistent with the finding reported in literature.

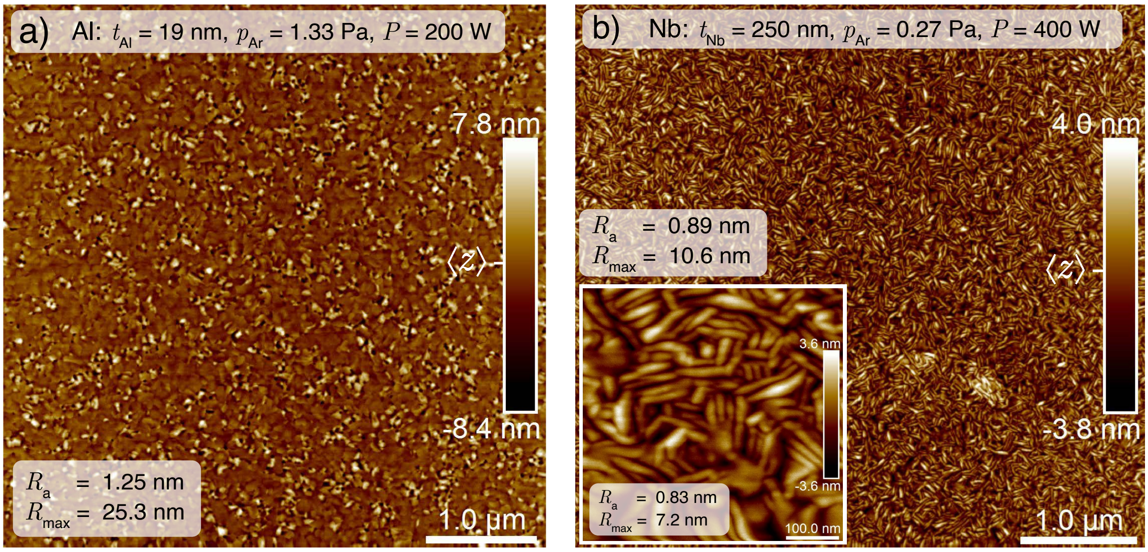

Figure 5.11: a) AFM image of a $5 \times 5\,\mu\mathrm{m}^2$ area of a 19 nm thick Al layer that was in-situ sputter deposited onto Nb. The Al was deposited at $P = 200\,\mathrm{W}$ at an argon pressure $p_{\mathrm{Ar}} = 1.33\,\mathrm{Pa}$ b) The corresponding surface morphology of the Nb below the Al, measured on a separate sample, as it was already depicted in figure 5.8 a).

When the sputter pressure was reduced to $p_{\mathrm{Ar}} = 0.27\,\mathrm{Pa}$, the average Al surface roughness was reduced by $\sim 30\,\%$ compared to the sample in figure 5.11 a), whereas $R_{\max}$ was halved. Using an argon sputter pressure of $p_{\mathrm{Ar}} = 0.27\,\mathrm{Pa}$ for sputtering the Al layer, the dependence of the Al surface morphology on the Al sputter power P was investigated. The results are summarized in figure 5.12 a). Similar to the results for Nb, the surface roughness of Al shows no clear correlation to the applied sputter power P and the empirically chosen value of $P = 200\,\mathrm{W}$ yields the smoothest surface. Furthermore, the dependence of the surface roughness on the Al layer thickness was investigated. The results of this investigation are illustrated in figure 5.12 b), showing an increase of surface roughness increasing the layer thickness. While this only confirms the expectations, no affirmation can be made whether or not the lowest investigated film thickness also provides a sufficient coverage of the bottom electrode.

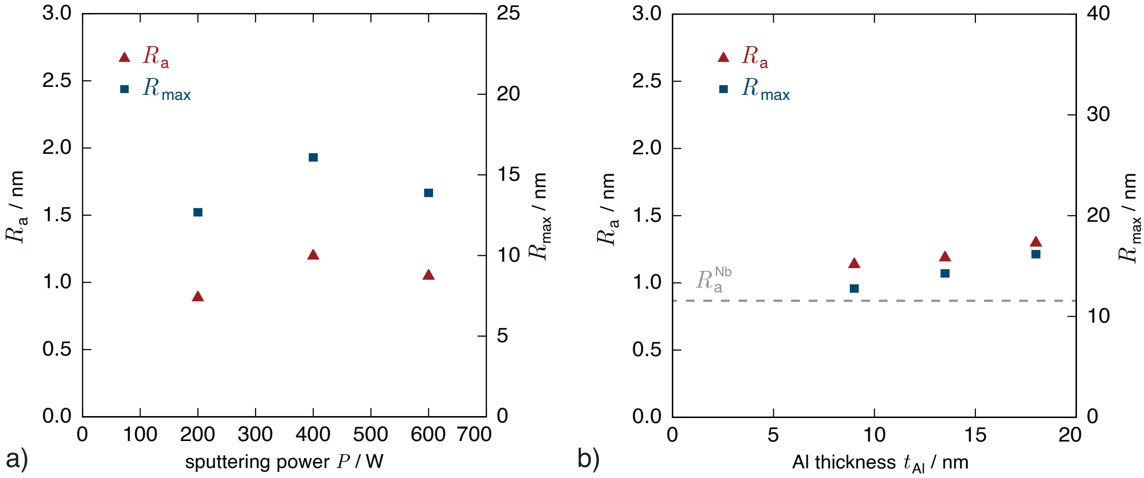

Figure 5.12: Measured figures of merit R_a and R_{max} of dc-magnetron sputtered Nb/Al bilayers deposited at $T = 300\,K$. a) Surface roughness as a function of the sputter power P used for Al deposition at $p_{Ar} = 0.27\,Pa$ and a rate $\dot{d}_{Al}$ between 0.3 nm/s and 0.9 nm/s. b) Surface roughness as a function of the Al film thickness t_{Al}, deposited at $P = 200\,W$, $p_{Ar} = 0.27\,Pa$ and $\dot{d}_{Al} = 0.3\,nm/s$. Also denoted by the grey dashed line is the average surface roughness R_a of the 250 nm thick Nb layer below the Al.

5.3.6 Hydrogen contamination of metals

A contamination of metallic structures by hydrogen is a well known phenomenon [Ste83]. The process of hydrogen entering and diffusing through a metal is generally denoted as permeation, whereas the deformation of the host materials lattice, that consequently follows this permeation, is known as hydrogen damage [Gu18]. Its derogatory effects are usually observed in the form of embrittlement [Con19], which leads to severe changes of the mechanical [Far80, Dwi18] and electrical [Sco85, Cab10] properties of the host metal, such as an increase of intrinsic stress, as well as a reduction of electrical conductance.

In general, it is found that hydrogen can permeate a metal if its metallic surface is exposed to an environment that has a sufficient hydrogen content. However, when an oxide layer is present on the surface of the metal, the oxide functions as a passivation layer, preventing the permeation of the metal by hydrogen [Bar12]. Materials with a very low permeation rate $J(T)$, or a very low hydrogen solubility c_{H}, like Al or Au, can also be used as a so called permeation barrier [Hen07]. Hydrogen can also diffuse from one structure to another when their metallic surfaces are brought into contact, depending on the hydrogen concentration present in the structures and also depending on the hydrogen solubility of the metals in question [Fuk85, Cal16]. The permeation rate can be expressed by Richardson's Law [Hen07] as

$$J(T) = \frac{\phi(T)\Delta {p_{\mathrm{H}}}^{1/2}}{d}\,, \tag{5.4}$$

where the permeation coefficient $\phi(T) = D(T) \cdot K(T)$ is the product of the diffusion coefficient $D(T)$ and the Sievert's constant $K(T)$, whereas $\Delta {p_{\mathrm{H}}}^{1/2}$ is the hydrogen pressure difference over the thickness d of the material. The Sievert's constant $K(T)$ is defined as

$$K(T) = \frac{c_{\mathrm{H}}}{\Delta {p_{\mathrm{H}}}^{1/2}}\,, \tag{5.5}$$

with c_{H} denoting the hydrogen solubility in the metal. The temperature dependent permeation rate $J(T)$ results in an increased permeation at elevated temperatures for all materials. When comparing relevant permeation parameters for different materials of interest, one finds that niobium has a very high hydrogen solubility $c_{\mathrm{H,Nb}}$ of up to 50 atomic percent (at. %) at room temperature [Fuk85] and a hydrogen diffusion constant of $D_{\mathrm{H,Nb}} \sim 10^{-5}\mathrm{cm}^2/\mathrm{s}$ [Fuk85]. In contrast, aluminium has an extremely low hydrogen solubility as low as $c_{\mathrm{H,Al}} \sim 2.6 \cdot 10^{-17}$ at. % [You98], whereas its hydrogen diffusion constant is found to vary by a few orders of magnitude with $D_{\mathrm{H,Al}} \sim 10^{-7}$–$10^{-10}\mathrm{cm}^2/\mathrm{s}$ [Has83, Ish86, You98]. The highest reported value is still two orders of magnitude smaller than $D_{\mathrm{H,Nb}}$. It is therefore easy to see why Al functions as a permeation barrier against hydrogen.

Aside from intrinsic stress, change of electrical conductance, or a suppression of superconductivity, another important effect of hydrogen damage in regards to the integrity of the interface between Al and AlO_x layers at elevated temperatures is illustrated in scientific literature [Li17]. Here, cylindrical structures with a diameter of several hundred nanometers and a length of $\sim 2\,\mu$m, that were made of deliberately hydrogenated Al with a natural oxide layer on their surface, were investigated. When these structures were heated to temperatures above 100 °C, the formation of multiple nanometer-sized cavities filled with H_2 directly at the Al/AlO_x interface was observed. It was further observed that the AlO_x could partially detach, creating inter-cavity H_2 diffusion pathways below the oxide shell. This results in the formation of even larger cavities filled with H_2, whereas the cavities that got depleted of H_2 shrunk in size. When cooled down, the AlO_x re-bonded with the Al. This phenomenon might be relevant when microfabricating SQUIDs, where wafers are heated to temperatures between 100 °C and 120 °C to reduce the solvent content in photoresists, or to induce chemical reactions. Therefore, a damage of the AlO_x barrier within a Josephson junction can occur when hydrogen is present in the metal films.

Several conclusions can be drawn from these aspects for the fabrication of not only $Nb/Al\text{-}AlO_x/Nb$ Josephson junctions, but also for the fabrication of SQUIDs and metallic magnetic calorimeters. A possible hydrogen damage can occur in Nb whenever its surface is exposed to hydrogen during any fabrication step that removes the permeation barrier protecting the metal, like argon ion milling, ICP-RIE or wet etching [Ant03, Hin10, Ric10]. The result is either a degradation of junction quality and spread of critical current I_c across a wafer [Tol09, Hin08, Ai12, Ula15], or a destruction of the junctions due to the formation of high intrinsic film stress. The Al/AlO_x layer within a junction functions as a permeation barrier, so that hydrogen can not diffuse from one junction electrode to the other. This means that the lattice constant might differ in the contaminated electrode compared to the non-contaminated electrode, giving rise to intrinsic stress. Such effects can not only occur at the time of hydrogen permeation, but also on long time scales when hydrogen diffuses through the wiring of the connected circuit [Sco85, Tol11]. The mentioned H_2 cavity formation at the Al/AlO_x interface can potentially damage the tunneling barrier, leading to a creation of pin holes. The formation of H_2 cavities might be even worse in $Nb/Al\text{-}AlO_x/Nb$ junctions as compared to the Al sturctures that were investigated in [Li17], as hydrogenated Nb provides a significantly larger hydrogen content for cavity formation compared to Al due to its very high hydrogen solubility. Lastly, the critical temperature of fabricated Nb wiring can be reduced, consequently reducing their ampacity [Wel77, Gup84]. Therefore, the prevention of hydrogen permeation of Nb especially during junction fabrication is essential to ensure the reliability and yield of the process.

Contamination of niobium by hydrogen

The degraded Josephson junction quality that was discussed in section 5.2 can potentially be attributed to a hydrogen damage of the Nb bottom electrode wiring. When an Nb/Al bilayer, or an Nb/Al/Nb trilayer is in situ sputtered, the Al serves as a permeation barrier, protecting the lower Nb layer. When the Al is wet etched, the applied NaOH-containing developer AZ 351B that was used comes in direct contact with the lower metallic Nb once the Al is fully removed. Hydrogen can therefore easily permeate the Nb, as no natural oxide layer exists. Material properties that can indicate a potential hydrogen damage of Nb are an increased sheet-resistance $\rho_{300\mathrm{K}}$ at room temperature, a reduced superconducting ampacity $j_{\mathrm{c,Nb}}$[3], as well as a reduced critical temperature T_{c}, and a reduced residual-resistivity-ratio (RRR). The latter ca be used as a measure of sample purity, as the electrical conductance of a metal at low temperatures degrades for an elevated impurity concentration within the material. In this thesis, 250 nm thick single-layer Nb wiring that was fabricated either via a Lift-off process, or an etch process using ICP-RIE, both exhibited a sheet resistance between $\rho_{300\mathrm{K}} = 0.6\,\Omega/\square$ and $0.7\,\Omega/\square$, an ampacity between $j_{\mathrm{c,Nb}} = 10\,\mathrm{MA/cm^2}$ and $12\,\mathrm{MA/cm^2}$, and a RRR between 4.7 and 5.6. For Nb wiring that was structured out of the bottom electrode of an Nb/Al-AlO$_{\mathrm{x}}$/Nb trilayer, therefore requiring the wet etching of Al, the measured sheet resistance $\rho_{300\mathrm{K}}$ increased to values between $1.0\,\Omega/\square$ and $1.2\,\Omega/\square$, and the RRR degraded to values between 2.3 and 4.6. The measured ampacity $j_{\mathrm{c,Nb}}$ of this wiring degraded to values between $0\,\mathrm{MA/cm^2}$ and $70\,\mathrm{MA/cm^2}$. Therefore, the possibly contaminated wiring exhibited an increase of $\rho_{300\mathrm{K}}$ by a factor of ~ 2, a reduction of the RRR by a factor of ~ 2, and a reduced $j_{\mathrm{c,Nb}}$ with large spread, whereas the wiring sometimes didn't even transition into its superconducting state at all at $T = 4.2\,\mathrm{K}$.

An additional verification of the fact that a property degradation of Nb occurs when the Al on top is wet etched with an alkaline solution was found by fabricating samples of Nb wiring out of an Nb/Al (250 nm/20 nm) bilayer via a Lift-off process, followed by a wet etching of the Al with two different alkaline solutions. For these samples, the Al was etched either with 3 % KOH diluted in water, or with 5 % NH$_4$OH diluted in water. The subsequently determined $\rho_{300\mathrm{K}}$, $j_{\mathrm{c,Nb}}$ and RRR of these Nb wiring samples degraded in a similar fashion compared to the wiring that was structured out of the bottom electrode of an Nb/Al-AlO$_{\mathrm{x}}$/Nb trilayer. Thus, the alkaline wet etching of Al with either NaOH, KOH or NH$_4$OH consistently degraded the thin film quality of the Nb layer below the Al by increasing its sheet resistance $\rho_{300\mathrm{K}}$, reducing

---

[3] In the context of this thesis $j_{\mathrm{c,Nb}}$ denotes the measured ampacity of Nb wiring divided by its cross section area. Ideally, this is given by the critical current density j_{c} that is predicted by the BCS-theory for a bulk superconductor, but can be reduced, for instance due to current crowding at sharp edges or corners of the thin film wiring.

its RRR and reducing its $j_{\mathrm{c,Nb}}$.

In order to verify whether or not the natural oxide on the surface of Nb wiring forms a sufficient permeation barrier against hydrogen, fabricated wiring that showed no degraded thin film quality was exposed to the developer AZ 351B for 2 minutes. Afterwards, prior measurements were verified again, showing a normal state sheet resistance $\rho_{300\mathrm{K}} = 0.7\,\Omega/\mathrm{Square}$, a critical current density $j_{\mathrm{c}} = 120\,\mathrm{MA/cm^2}$ and a $RRR = 5.15$, i.e. no hydrogen damage of the wiring occurred. This is very important, since a possible hydrogen damage of Nb during the regular development process of photoresists can therefore be excluded.

To prevent hydrogen damage of the Nb structures, literature shows that in order to remove the Al during the fabrication of Nb/Al-$\mathrm{AlO_x}$/Nb Josephson junctions, either argon ion milling [Tol11, Kai11] or wet etching with an acidic solution can be used [Sau95, Che03, Ker03]. The process for a reliable removal of Al via argon ion milling on a 3 inch wafer scale is currently in development in this group. For the acidic wet etching of Al, a solution consisting of 65 % $\mathrm{HNO_3}$, 100 % $\mathrm{CH_3COOH}$, 85 % $\mathrm{H_3PO_4}$ and $\mathrm{H_2O}$, mixed at a ratio of 1:1:16:2, is used. The corresponding chemical reactions are

$$\mathrm{2Al + 2HNO_3 \rightarrow Al_2O_3 + 2NO + H_2O} \tag{5.6}$$

$$\mathrm{Al_2O_3 + 2H_3PO_4 \rightarrow 2AlPO_4 + 3H_2O}\,. \tag{5.7}$$

Once the Al is removed, the $\mathrm{HNO_3}$ creates a permeation barrier by oxidizing the Nb, minimizing the time frame in which hydrogen can diffuse into the niobium:

$$\mathrm{6Nb + 10HNO_3 \rightarrow 3Nb_2O_5 + 10NO + 5H_2O}\,. \tag{5.8}$$

The thereby oxidized Nb also functions as an etch stop, since the removal of $\mathrm{Nb_2O_5}$ requires hydrofluoric acid, which is not present in the used acidic solution. However, the Nb should not be exposed to the acidic solution for too long as the oxide layer thickness increases with time. As this oxide layer is comparably hard to remove, this could otherwise prevent the forming of an electrical contact between the oxidized Nb and a subsequently deposited Nb wiring layer. During further optimization of the fabrication process, a sub-optimal wetting of the wafers surface by the acidic solution was observed due to its comparably high viscosity. This resulted in micrometer-sized structures, that were located on corresponding test samples, to still contain Al on their surface, even after a prolonged exposure to the acidic solution. This residual Al prevented a subsequent ICP-RIE of the Nb below the remaining Al. The wet etching was significantly improved by wetting the wafer with $\mathrm{H_2O}$ first, and then applying the acidic solution second. That this process reliably minimizes hydrogen damage in Nb structures was thoroughly tested and the thereby investigated structures exhibited a normal state sheet resistance of $\rho_{300\mathrm{K}} = 0.7\,\Omega/\square$, an ampacity of $j_{\mathrm{c,Nb}} = 120\,\mathrm{MA/cm^2}$ and a $RRR = 5.15$.

5.3.7 Characterization of Nb/Al-AlO$_x$/Nb Josephson junctions

This section discusses the quality of Josephson tunnel junctions from a wafer that was fabricated with the newly optimized process. As the prior discussion showed, only two fabrication parameters were adjusted compared to the empirically established parameters. The Ar sputter pressure for the deposition of Al was reduced to $p_{\mathrm{Ar}} = 0.27\,\mathrm{Pa}$, and the wet etching was done with an acidic solution instead of an alkaline one. The discussed results are representative for numerous wafers that were fabricated in recent times within the group.

Characterization of wafer HDSQ11b #w1

Figure 5.13 a) shows the names and locations of the investigated junction test chips on the wafer with the internal name HDSQ11b #w1, which had a target critical current density of $j_{\mathrm{c}} \approx 25\,\mathrm{A/cm^2}$. Figure 5.13 b) shows the measured IV-characteristic of a Josephson tunnel junction with a design area of $8\,\mu\mathrm{m} \times 8\,\mu\mathrm{m}$ from chip 2A16. Also shown are the important figures of merit (see section 3.1.1), i.e. the critical current I_{c}, the gap voltage U_{g}, the subgap resistance R_{sg}, and the normal state resistance R_{N}, that are used to evaluate the junction quality. The resistance ratio $R_{\mathrm{sg}}/R_{\mathrm{N}} = 35.4$ indicates a very high junction quality, and is also a factor of two higher than the one that was depicted in figure 5.4 a). The gap voltage $U_{\mathrm{g}} = 2.70\,\mathrm{mV}$ is still slightly smaller than the expectation based on equation 3.10, but this can be attributed to the proximity effect, as the Al layer in the fabricated Josephson tunnel junctions is rather thick. A statement about the critical current density $j_{\mathrm{c}} = I_{\mathrm{c}}/A_{\mathrm{jj}}$ can not yet be made from this raw data. One reason for this is, that the actual junction area A_{jj} usually shows slight deviations from the design value due to the limited accuracy of the lithographic fabrication process. The other reason is, that the measured critical current I_{c} is influenced by thermal noise, leading to a suppression of the actual critical current [Dan84]. Therefore, the noise suppression leads to a measured critical current that is apparently smaller, whereas a deviation of the junction area compared to its design value can lead to junctions of smaller or larger area, consequently decreasing or increasing the measured critical current compared to the target value.

The deviation of the area of a square Josephson tunnel junction can be addressed by introducing an offset ΔW to the edge length W of the junction, so that $A_{\mathrm{jj}} = (W + \Delta W)^2$. After several junctions of different area are characterized, their normal state resistance $R_{\mathrm{N}} \propto 1/A_{\mathrm{jj}}$ plotted as a function of the inverse area can be used to determine the actual junction area $A_{\mathrm{jj,corr}}$ by fitting the functional depen-

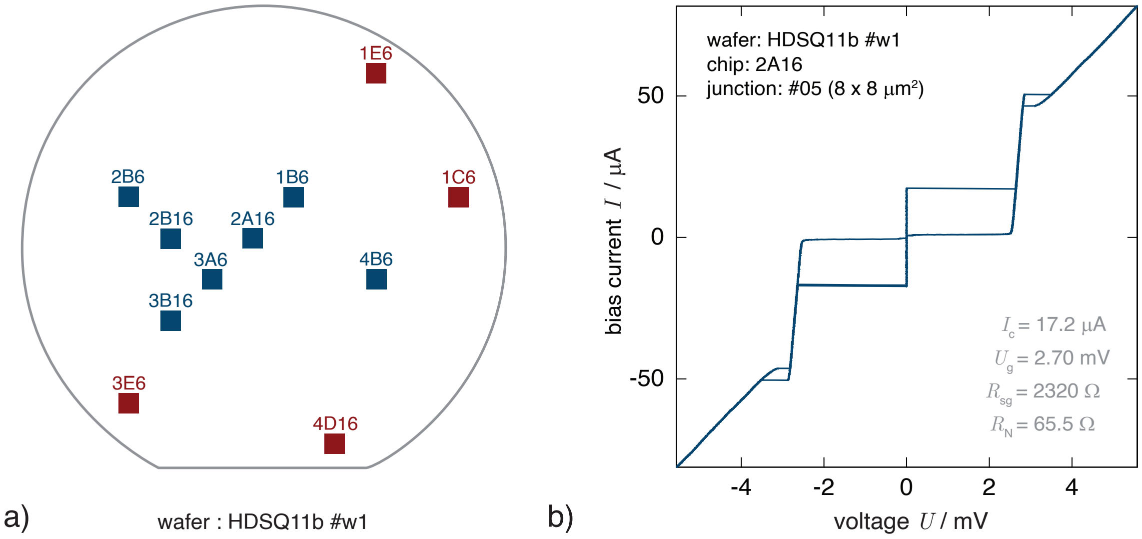

Figure 5.13: a) Labeling and location of the test chips from the wafer HDSQ11w #w1, that were used in order to investigate the reliability of the newly optimized fabrication process for Nb/Al-AlO$_\mathrm{x}$/Nb tunnel junctions. The two-color scheme denotes a distinction between chips from the center of the wafer and chips from the edge of the wafer. b) Measured IV-characteristic of a Josephson tunnel junction of chip 2A16 with a design area of $8\,\mu$m $\times$ $8\,\mu$m, as well as its corresponding figures of merit.

dence

$$R_\mathrm{N} = \rho_\mathrm{N} \frac{1}{(W + \Delta W)^2} \tag{5.9}$$

to the data, where ρ_N denotes the specific normal state resistivity of the junctions. The result of this evaluation is shown in figure 5.14 a) for wafer the HDSQ11b #w1, where the normal state resistance R_N is plotted as a function of the corrected area $A_\mathrm{jj,corr}$. The determined offset is $\Delta W = -0.13\,\mu$m, i.e. the edge length W of the fabricated Josephson tunnel junctions is $0.13\,\mu$m shorter than their corresponding design value. The specific resistivity is $\rho_\mathrm{N} = 4059\,\Omega\mu\mathrm{m}^2$. The plot also shows, that small junctions from chips located at the edge of the wafer can show a significant increase in their normal state resistance, indicated by the red data points.

The noise suppression of the critical current I_c can be calculated by [Dan84]

$$\frac{I_\mathrm{c}^\mathrm{sup}}{I_\mathrm{c}} = 1 - \left[\frac{3}{\sqrt{2}\gamma} \ln \left(\frac{\omega_\mathrm{p} I_\mathrm{c}}{\pi \sqrt{2} \gamma \dot{I}} \right) \right]^{2/3} , \tag{5.10}$$

where $\omega_\mathrm{p} = \sqrt{2eI_\mathrm{c}^\mathrm{sup}/\hbar C}$ is the plasma frequency of the junction, $\gamma = \hbar I_\mathrm{c}/(2ek_\mathrm{B}T)$, and $\dot{I}$ denotes the alteration rate of the applied bias current I that is created with the voltage generator. Furthermore $I_\mathrm{c}^\mathrm{sup}$ now denotes the suppressed critical current, i.e. the measured value, during further discussion, whereas I_c now denotes the actual critical current that is corrected for the noise suppression at the given temperature

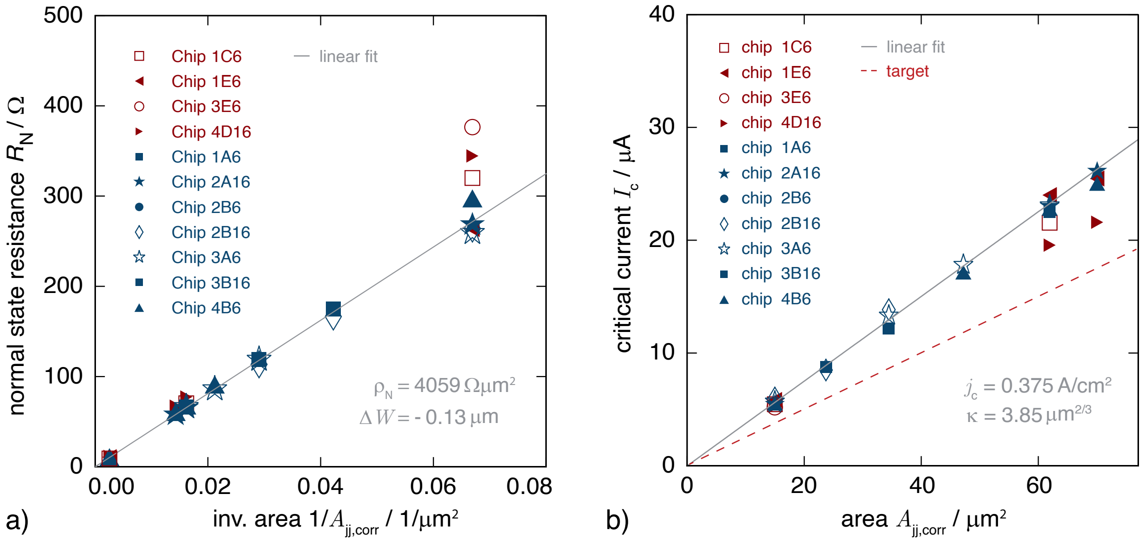

Figure 5.14: Measured parameters of the fabricated Josephson tunnel junctions. a) Normal state resistance R_N as a function of the inverse of the corrected junction area $A_\mathrm{jj,corr}$. Determined from the fit is the specific resistance ρ_N of the junctions b) Critical current I_c that is corrected for thermal noise as a function of the corrected area $A_\mathrm{jj,corr}$. Determined from the fit is the critical current density j_c.

$T = 4.2\,\mathrm{K}$. The only factor in equation 5.10 that has a dependence on the junction area $A_\mathrm{jj,corr}$ is the critical current I_c. Thus, the logarithmic term is independent of $A_\mathrm{jj,corr}$. Therefore, the equation can be expressed as

$$\frac{I_\mathrm{c}^\mathrm{sup}}{I_\mathrm{c}} = 1 - \kappa A_\mathrm{jj,corr}^{-2/3} \qquad \text{with} \qquad \kappa = \left[\frac{3}{\sqrt{2}}\frac{2ek_\mathrm{B}T}{j_\mathrm{c}}\ln\left(\frac{\omega_\mathrm{p}I_\mathrm{c}}{\pi\sqrt{2}\gamma\dot{I}}\right)\right]^{2/3}, \tag{5.11}$$

which can be used to calculate I_c in analogue to the calculation of the actual junction area $A_\mathrm{jj,corr}$. This is shown in figure 5.14 b), where the noise corrected critical current I_c is plotted as a function of the corrected junction area $A_\mathrm{jj,corr}$. The critical current density of the Josephson tunnel junctions is determined to be $j_\mathrm{c} = 0.375\,\mathrm{A/cm^2}$, whereas $\kappa = 3.85\,\mu\mathrm{m}^{2/3}$. Therefore, the measured critical current density is about 50 % higher than the expected design value. Deviations of this magnitude were already observed in the past, where high quality Josephson tunnel junctions fabricated with identical oxidation parameters, but from different wafers, showed a critical current variance of up to a factor of two. Figure 5.15 shows the relative deviation $\Delta I_\mathrm{c}/I_\mathrm{c}$ of the critical current of the measured Josephson tunnel junctions as a function of the corrected area $A_\mathrm{jj,corr}$. It can be seen, that the values deviate only up to 10 % from $I_\mathrm{c} = j_\mathrm{c}A_\mathrm{jj,corr}$, except for two junctions of large area that were located at the edge of the wafer. In total, 61 Josephson tunnel junctions were characterized with a yield of 90 %. When the junctions from the edge of the wafer are excluded in this calculation, a yield of nearly 100 % was achieved.

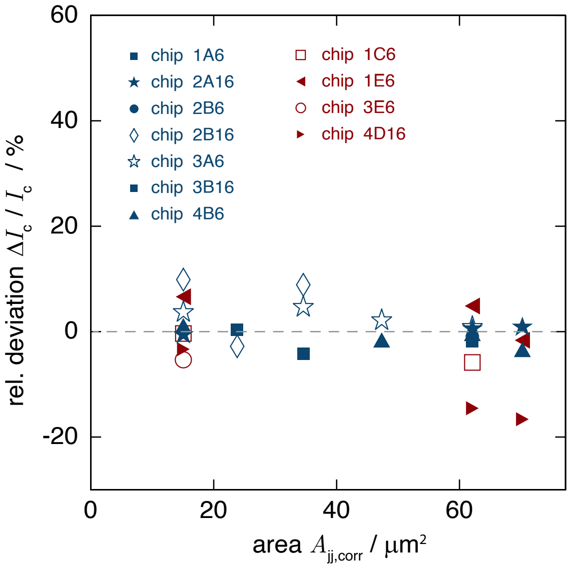

Figure 5.15: Relative deviation $\Delta I_c / I_c$ of the noise corrected critical current from the actual value of the critical current as a function of the corrected junction area $A_{jj,corr}$.

In summary, the presented data of a wafer that was fabricated with the newly optimized fabrication process for Nb/Al-AlO$_x$/Nb tunnel junctions showed an increase of 50 % in its critical current density j_c compared to the target value, a deviation that is well within an expected margin of error. Additionally, its spread Δj_c was below 10 % across the entire wafer area, except for two out of 61 investigated junctions. Furthermore, a drastic improvement of the yield of working Josephson tunnel junctions was achieved, reaching nearly 100 % in the wafer area of interest. Therefore, the main goal of the conducted process optimizations was sufficiently achieved. A reduction of the layer thickness of the Nb bottom electrode can potentially be considered for future applications, which would reduce the Nb surface roughness, as well as its intrinsic stress contribution. The determined value for the London penetration depth of $\lambda_L = 270\,\text{nm}$ in [Foe12] for sputter deposited Nb was also verified via calculation from a measured $RRR = 2.67$. In this chapter, a $RRR = 5.2$ was determined for Nb. Calculating λ_L in analogue to [Foe12] with the increased RRR yields a reduced London penetration depth of $\lambda_L = 168\,\text{nm}$, a value that might require an experimental verification before considering a reduction of the Nb bottom electrode thickness.

Either way, the wafer HDSQ11b #w1 that was discussed in this section was fabricated in July 2018. Since then, more than 30 wafers hosting Josephson tunnel junctions were fabricated in this group, among them the detectors that were developed in this thesis, all exhibiting a comparable junction quality and yield. However, the process optimizations that were performed in this thesis were not the only factor that contributed to this long term reliability of the fabrication process. What was also done since then, was a consistent monitoring of the sputter cathode voltage U_{sp} for the deposition of Nb, which reduces over time when the target material in the sputtering system erodes due to ongoing use. The voltage can be used as a measure of target erosion and should be kept above a minimum threshold for junction fabrication, as it is also reported in literature [Ima92b]. Therefore, once the cathode voltage U_{sp} was reduced to a certain threshold, the Nb target in the UHV sputtering facility was exchanged for a new one.

5.4 MMC fabrication technology

This section discusses the development and optimization of microfabrication processes for realizing the detector HDMSQ1, which is the first detector that was developed in this thesis. The discussion includes the fabrication process for a dedicated on-chip field generating coil by making use of a third niobium layer in the design, as well as the optimization of a fabrication process for overhanging absorbers on posts. Lastly, the development of a fabrication process for high ampacity vertical interconnect accesses (vias) between separate Nb wiring layers is summarized.

5.4.1 Detector geometry with independent field generating coil

For microfabricated wiring, in order for a second wiring layer to cross over a first wiring layer, the former usually requires a higher film thickness than the latter, in order to reliably cover the step created by the first layer. The SQUIDs and detectors that are developed in this group use a 250 nm thick Nb1 layer, which is insulated by 300 nm of SiO_2. For the Nb2 layer to sufficiently cross over the thereby formed step of ~ 300 in height, and also to still provide a high ampacity of this wiring layer, a Nb layer thickness of 600 nm is used in this group. For a third layer to cross over the Nb2 layer, an even higher film thickness for the SiO_2 and the Nb would be required. This is why the fabrication of multi-layered circuits usually employs chemical-mechanical planarization (CMP), a method where the surface of a wafer is flattened after each deposited layer [Ola19]. This allows for an overlayed fabrication of theoretically an infinite number of layers, all electrically insulated from each other [Ban08]. However, this method is technologically very challenging and a dedicated machine for developing such a process was not available within the framework of this thesis. The development of the integrated detectors within this thesis required an independent field generating coil for which a third Nb layer was added to the design. This coil is positioned directly below the pickup coil, as it is illustrated in figure 5.16, which depicts a sketch of the detector geometry of the first detector that was developed in this thesis. The detector geometry uses a meander-shaped field generating coil that is positioned directly below a meander-shaped pickup coil.

In order to fabricate such a detector geometry, a new fabrication process had to be developed. This process is illustrated in figure 5.17, which depicts a cross sectional view of the fabrication of two nearly congruent meander-shaped coils. The process starts with the fabrication of the meander-shaped field generating coil, which is done with an etching process via ICP-RIE. For this, after a wafer cleaning via argon ion milling, 250 nm of Nb are deposited in the UHV sputtering system (see appendix A.1.3) at room temperature with $P = 400\,\mathrm{W}$, $p_{\mathrm{Ar}} = 0.27\,\mathrm{Pa}$, and $\dot{d}_{\mathrm{Nb}} = 0.74\,\mathrm{nm/s}$,

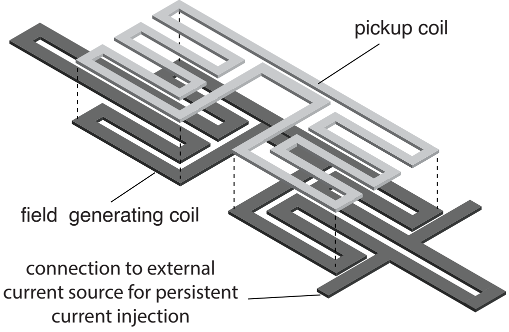

Figure 5.16: Schematic of a meander-shaped field generating coil situated below the meander-shaped pickup coil. The sketch is representative for the detector geometry used in this thesis. The coils are electrically insulated from each other by 300 nm of SiO_2.

followed by an application of the AZ MIR 701 29cps positive photoresist. After resist structuring, the Nb is etched via ICP-RIE at $T = 5\,°\mathrm{C}$ with a substrate bias power of $P_{\mathrm{rf}} = 50\,\mathrm{W}$, an ICP-power of $P_{\mathrm{ICP}} = 100\,\mathrm{W}$ and at an etch rate of $\dot{e}_{\mathrm{Nb}} \sim 1\,\mathrm{nm/s}$. However, contrary to the usual etching process, the photoresist on top of the Nb wiring is not removed, as it is depicted in a). Instead, SiO_2 is rf-sputter deposited at $P_{\mathrm{rf}} = 250\,\mathrm{W}$, at an Ar/O_2 (60 %/40 %) pressure $p_{\mathrm{Ar/O_2}} = 0.67\,\mathrm{Pa}$, and at a deposition rate $\dot{d}_{\mathrm{SiO_2}} = 1.73\,\mathrm{nm/min}$, resulting in a rounded SiO_2 layer between meander stripes, as it is shown in b). The structures after the removal of the photoresist are shown in c). At this point, an insulation layer between, but not on top of the meander stripes exists. The depicted rounded shape of this layer is due to a shadowing effect of the photoresist during material deposition, i.e. the resist blocks sputtered SiO_2 particles, reducing the effective sputter rate closer to the walls of the resist. The magnitude of this shadowing effect depends on the thickness of the photoresist and on the distance between resist structures, meaning that this process might require a renewed optimization when applied to a design with a smaller meander pitch p.

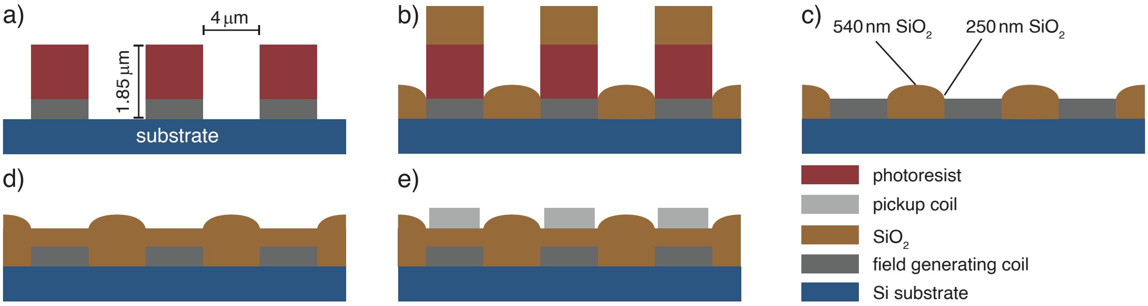

Figure 5.17: Schematic overview of the fabrication process of the detector geometry with independent field generating coil. a) Fabrication of the field generating coil via ICP-RIE. Afterwards, the photoresist is not removed. b) Sputter deposition of SiO_2. c) Removal of photoresist. d) Deposition of another layer of SiO_2 via a Lift-off process, with photoresist protecting only parts of the wafer where later an electrical connection from the field generating coil to a custom circuit board is made. e) Fabrication of the pickup coil via ICP-RIE with a slightly reduced line width compared to the field generating coil.

In the presented process, the niobium has a thickness of 250 nm with a spacing between meander stripes of 4 μm. The photoresist AZ MIR 701 29cp was spin coated to yield a film thickness of 1.6 μm. In order to fully cover the edges of the NB stripes, as it is depicted in figure 5.17 c), 540 nm of SiO_2 had to be effectively sputtered. The SiO_2 at the apex between meander stripes has a thickness of 540 nm, i.e. no observable shadowing effect occurs there, while the SiO_2 close to the niobium has a thickness of 250 nm. Both values were confirmed via atomic force microscopy. In a next step, an additional 300 nm of SiO_2 are deposited, completing the insulation of the Nb structures. This is depicted in d), where no steep edges exist in the fabricated structures and it is therefore quite easy for a subsequently deposited wiring layer to cross over the first Nb layer, whereas this layer can also have a thickness of only 250 nm, and not the 600 nm that is usually used in the group. In the last step of the fabrication process, the pickup coil situated above the field coil is fabricated using an etching process. For this, a 250 nm thick Nb layer is sputter deposited on top of the entire wafer without using a photoresist mask for protection. The meander-shaped coil is then etched via ICP-RIE, identical to the fabrication of the field generating coil. The stripe width w_2 of the pickup coil was chosen to be slightly smaller than the stripe width w_1 of the field generating coil due to the limited accuracy of the mask alignment (see appendix A.1.2). The third Nb layer that is not shown in the schematic but is required in the design, has a thickness of 600 nm and forms for instance part of the feedback coil of the SQUID. Therefore, it has to cross over the pickup coil at one point or another. No electrical shorts between the two independent coils were observed and the superconducting ampacity for both Nb wiring layers was at $j_{\mathrm{c,Nb}} \approx 12\,\mathrm{MA/cm^2}$, as long as no via was part of the wiring.

5.4.2 Overhanging absorber on posts

A fabrication process using two layers of photoresist to yield 5 μm thick overhanging absorbers on posts was developed in [Sch12]. A part of this fabrication process is illustrated in figure 5.18. Shown is a detector that is fabricated up to the sensor layer. In order to fabricate the depicted structures, the following fabrication steps were required. First, the positive resist AZ 6632 was applied, and the cylindrical posts were structured with steep edges. Afterwards, a thermal reflow of photoresist is done in a baking step at a comparably high temperature of 150 °C, which leads to the rounded resist structures that can be seen. In a next step, 100 nm of Au and 50 nm of Nb were in-situ sputter deposited. The Au functions as the cathode for the later employed electroplating of the absorbers, whereas the Nb functions as a protective layer in order to keep the Au as clean as possible. Then, a second layer of photoresist was applied and structured, the negative resist AZ nLOF 2070, which was used as molds for the absorbers. This resist requires temperatures of 115 °C for a so called post exposure bake, a temperature low enough so that the thermal reflow

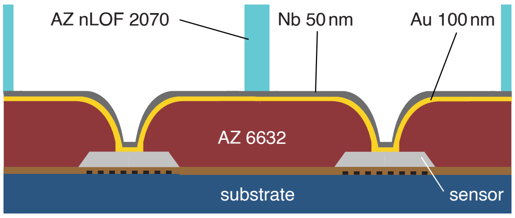

Figure 5.18: Illustration of one part the fabrication process for overhanging absorbers on posts that was developed in [Sch12].

of the AZ 6632 does not occur a second time, which would result in a wrinkling of the seedlayer and the Nb protective layer. Before electroplating, the Nb protective layer had to be etched via ICP-RIE.

Several difficulties were identified in this process over time. After electroplating the absorbers, the removal of the AZ nLOF 2070 relied on the solvent N-Methyl-2-pyrrolidon (NMP), which also slowly attacks niobium and silver structures situated on the wafer. In addition, insoluble polymerized negative photoresist was sometimes found stuck in the 5 μm wide gaps between separate absorbers, creating an unwanted thermal link between them, and also between absorbers and substrate. Furthermore, the baking step at 150 °C that was used for the thermal reflow of the AZ 6632 sometimes resulted in a polymerization of the photoresist. As a result, it became insoluble and could therefore no longer be reliably removed below the absorbers. Especially important for the detectors developed in this thesis is the fact, that using backing steps above 120 °C can potentially damage Josephson junctions, which has to be avoided when developing MMCs based on the direct sensor readout. And finally, the AZ 6632 is no longer commercially available. Therefore, this process was developed anew within the framework of this thesis, relying only on the positive photoresist AZ 4533, simplifying the fabrication while increasing its reliability.

The newly developed fabrication process for overhanging absorbers on posts is illustrated in figure 5.19, starting with a wafer that is fabricated up to the sensor layer in a). The AZ 4533 is applied at 4000 rpm, followed by a softbake at $T = 100\,^\circ\mathrm{C}$ for 3 minutes on a hotplate. Afterwards, the posts are structured as cylinders with steep edges. The depicted rounded shape of the resist is created by a subsequent baking at 120 °C for 120 s, as the AZ 4533 starts to soften at $T > 90\,^\circ\mathrm{C}$, resulting in a thermal reflow of photoresist. This rounded shape significantly increases the structural integrity of the finished absorbers for a later required ultrasonic cleaning of the wafer. Furthermore, this reduces any steep edges in the created structures, which allows for the Au seedlayer to sufficiently cover the entire area of the wafer so that none of the photoresist is exposed anymore. This seedlayer is deposited in a next step, where 100 nm of Au are sputter deposited at room temperature with $P = 200\,\mathrm{W}$, $p_{\mathrm{Ar}} = 1.33\,\mathrm{Pa}$, and $\dot{d}_{\mathrm{Au}} = 2.2\,\mathrm{nm/s}$, covering the entire wafer. This seedlayer functions as the cathode for the later employed electroplating procedure for the absorbers. The Nb protective layer used in the old process is no longer required, as the Au surface stays sufficiently clean during the subsequent wafer handling.

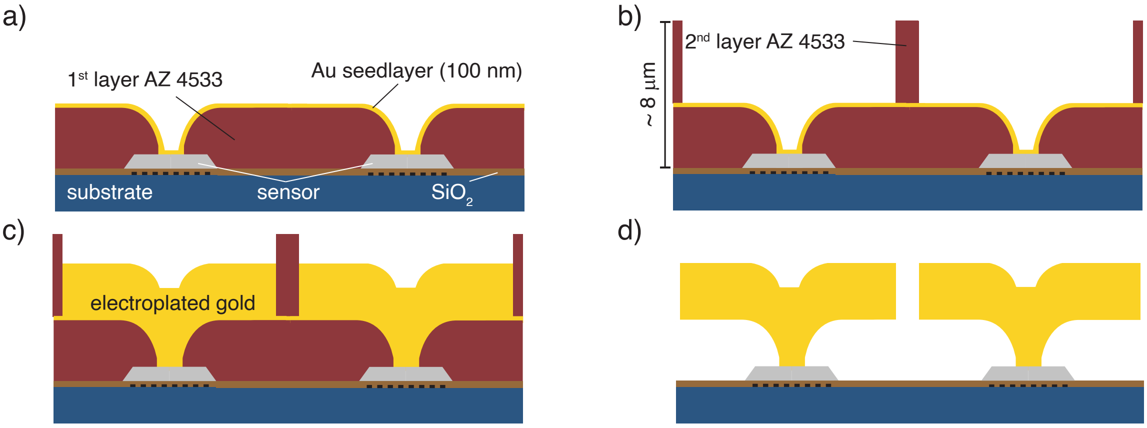

Figure 5.19: Schematic overview of the developed fabrication process for overhanging absorbers on posts. a) The posts are structured on top of the senors in a first layer of AZ 4533, followed by a sputter deposition of a 100 nm thick Au seedlayer. for electroplating. b) The AZ 4533 is applied a second time in order to structure the absorber molds. c) Simultaneous electroplating of posts and absorbers. d) Removal of photoresist followed by a weak ultrasonic cleaning, creating overhanging absorbers on posts.

After the seedlayer is deposited, the AZ 4533 is applied a second time. This time, the softbake is done at a lower temperature of $T = 80\,°\mathrm{C}$ for 12 minutes, in order to prevent a thermal reflow of the lower AZ 4533 layer, which would otherwise result in the formation of wrinkles in the seedlayer. In this resist layer, the molds for the absorbers are structured, as it is depicted in b). Afterwards, the posts and absorbers are simultaneously electroplated, as shown in c). The utilized electrolyte for this is the TechniGold 25 ES[4]. The electroplating is done at a temperature of 60 °C and at a current density of $1\,\mathrm{mA/cm^2}$, resulting in a Au deposition rate of 1.04 nm/s. To finalize the fabrication process, the photoresist is removed by immersing the wafer in dimethylformamid (DMF) or acetone for at least 24 hours, followed by a weak ultrasonic cleaning that is required to remove the remaining 100 nm of seedlayer that still connects neighboring absorbers. The finished absorbers are depicted in d). During the development of this process, it was tried to circumvent the use of the ultrasonic cleaning by removing the residual seedlayer between absorbers either via Ar ion milling or wet etching. However, it was observed that the lower layer of the AZ 4533 became partly insoluble in DMF or acetone as a result. This was not further investigated in this thesis, but is a significant point for a future optimization of this process, as using ultrasonic cleaning is the only remaining factor left in this process that might reduce the reliability of absorber fabrication, as they are sometimes torn off as a result, or at least the electroplated Au starts to bend for absorber thicknesses

---

[4] Technic Deutschland GmbH, Glärbach 2, 58802 Balve, Germany

$< 5\,\mu$m.

It shall be noted, that the photoresist AZ 4562 can also be used for this process, as it only differs from the AZ 4533 in its solvent concentration, allowing for higher resist thicknesses. In addition, both photoresists support a successive multilayer application, creating even larger resist thicknesses. Given these properties, absorbers of up to $20\,\mu$m in thickness were reliably fabricated with the process established in this thesis. For higher absorber thicknesses of even more than $100\,\mu$m, the negative resist AZ 125 nXT, or the positive resist AZ 40 XT can be used for the absorber molds [Kra13, Li18].

5.4.3 High ampacity superconducting Nb vertical interconnect accesses

The pickup coil of metallic magnetic calorimeters, as well as the coil arrangement of current-sensing dc-SQUIDs that are developed in this group, are usually build by using two individual lithographically structured superconducting layers made of Nb. However, the detectors that were developed in this thesis even require three Nb layers and recent many-pixel MMC prototypes make use of even up to six Nb wiring layers [Dev19]. Electrical connections between these layers, if required, is done with so called vertical interconnect accesses (vias). These vias are formed by small holes in the insulation layer, as it is schematically depicted in figure 5.20, showing a via that connects the first and second Nb layer in the designs that are developed in this group. The necessity for two insulation layers was discussed in section 5.1.1.

Ideally, the superconducting ampacity of Nb wiring that extends over multiple layers should only be limited by the smallest dimension of the wiring, i.e. its cross sectional area A_{Nb}. The latter is $A_{\mathrm{Nb}} = 6\,\mu\mathrm{m}{\times}250\,\mathrm{nm}$ for the meander-shaped wiring that carries the persistent current I_0 for the detectors developed within this thesis, consisting of only a single Nb layer with a measured superconducting ampacity $j_{\mathrm{c,Nb}}$ between $10\,\mathrm{MA/cm^2}$ and $12\,\mathrm{MA/cm^2}$ at $T = 4.2\,\mathrm{K}$. That the superconducting ampacity is reduced compared to its bulk value is most likely due to current crowding at sharp 90° bends in the meander-shaped wiring, and can be enhanced by rounding these bends in future designs [Ili14]. However, we observed that once vias between different Nb layers were introduced, the critical current $I_{\mathrm{c,Nb}} = j_{\mathrm{c,Nb}} A_{\mathrm{Nb}}$ decreased by at least one order of magnitude. The conductive contact area of the vias ranges from $4\,\mu\mathrm{m}^2$ to $100\,\mu\mathrm{m}^2$, which is significantly larger than the cross sectional area of the corresponding Nb wires. Therefore, introducing these vias to connect separate Nb layers should consequently not present a limiting factor for their critical current $I_{\mathrm{c,Nb}}$.

It was ascertained, that a reduction of $I_{\mathrm{c,Nb}}$ is only observed when the wiring of the first Nb layer was structured with an etch process using ICP-RIE, but not when it

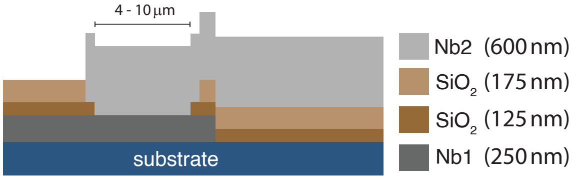

Figure 5.20: Schematic cross section of a vertical interconnect access (via) of wiring fabricated during this thesis between the first and second Nb layer. The need for two SiO_2 layers was discussed in section 5.1.1.

was structured with a Lift-off process (see appendix A.1.6). Furthermore, even when excluding the SiO_2 layers shown in figure 5.20, and using an etch process for the first Nb layer, the same reduction of $I_{\mathrm{c,Nb}}$ was observed. Therefore, the used insulation layer has no negative impact on $I_{\mathrm{c,Nb}}$. This means, that a fabrication of multilayer wiring where the first Nb layer was structured with ICP-RIE yielded vias that obviously limit the critical current $I_{\mathrm{c,Nb}}$ of the overall wiring by a factor of up to 100. The currents running in the different SQUID structures during operation are usually well below 100 μA when reading out metallic magnetic calorimeters. However, the persistent current I_0 that is required to bias the paramagnetic temperature sensor of an MMC is usually several tens of milliampere [Fle09], even going above 100 mA for the detectors developed in this thesis. In order to fabricate high ampacity multi-layer wiring, the corresponding fabrication process was started to be optimized during this thesis. In the following, the present workaround for yielding multi-layer Nb structures with a $\sim 30\,\%$ reduced ampacity compared to single-layer Nb wiring is summarized. However, it should be noted that no fully optimized process has been found and that there is no satisfying explanation for reduced via performance so far.

One hypothesis as to why vias with low performance show up is, that a solvent-resistant film is created on top of the Nb structures by a chemical reaction of the photoresist with the SF_6 used for ICP-RIE. This was observed on the side walls of etched structures in [Ade93], where etch-resistant walls with a thickness of ~ 100 nm were created. In addition, polymerized photoresist can be created during ICP-RIE [Sau95], which is also resistant to solvents and would reduce the effective contact area of a via once an additional wiring layer is put on top. If such a polymerized resist layer exists on top of the fabricated Nb wiring, then it seems to have no impact on the Nb surface morphology. Figure 5.21 a) shows an AFM image of a $2.5 \times 2.5\,\mu\mathrm{m}^2$ surface of fabricated Nb wiring that was structured via ICP-RIE. For comparison, figure 5.21 b) shows a $5 \times 5\,\mu\mathrm{m}^2$ and 500×500 nm surface of Nb wiring that was fabricated with the identical deposition parameters than the one in a), but with a Lift-off process, i.e. at no point during fabrication was photoresist on top of the deposited material. The elongated grains are observed in both pictures, and their corresponding surface roughness also shows no significant deviation.

In order to remove a potential polymerized resist layer during fabrication, oxygen

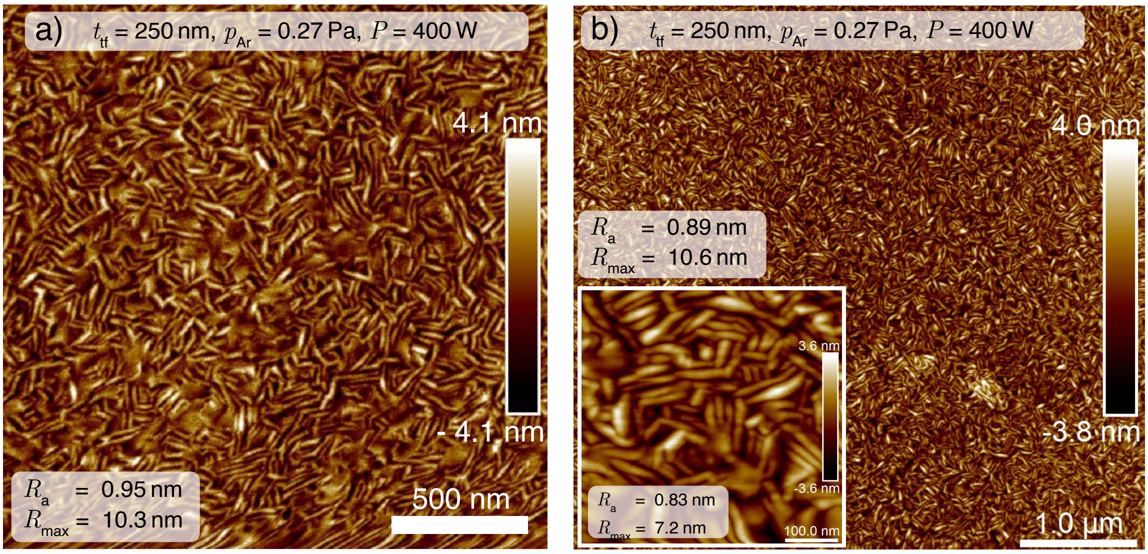

Figure 5.21: Measured AFM images of a surface of Nb wiring deposited with $P = 400\,\mathrm{W}$, $p_{\mathrm{Ar}} = 0.27\,\mathrm{Pa}$, $\dot{d}_{\mathrm{Nb}} = 0.74\,\mathrm{nm/s}$. a) Structured with an ICP-RIE process. b) Structured with a Lift-off process.

can be added to the process gas during ICP-RIE. O_2 contents of 16.6 %, 25 % and 50 % within the process gas were investigated for fabrication, resulting in no relevant improvement of the via performance. Furthermore, extensive Ar ion milling was used in order to clean the wiring surface prior to the sputter deposition of the second Nb layer. Milling times equivalent to the removal of up to $\sim$ 500 nm of Au were investigated, corresponding to an Nb removal of $\sim$ 40 nm. This also resulted in no improvement in the via performance. Additionally, the via performance did not depend on the applied photoresist during ICP-RIE (see appendix table A.1). Lastly, using an Al hardmask instead of photoresist for ICP-RIE, followed by a subsequent wet etching of the Al with an acidic solution, as well as an extensive surface cleaning via Ar ion milling, also yielded vias of significantly reduced performance. The found fabrication process that reliably yields an optimum via performance, but reduces the ampacity $j_{\mathrm{c,Nb}}$ of the Nb wiring itself, is discussed in the following.

The process starts with an in-situ sputtering of 250 nm of Nb, followed by 100 nm of Au, as it is depicted in figure 5.22 a). The Au functions as a protective coating. Afterwards, the photoresist AZ MIR 701 29cps is applied and the respective etch mask is structured. Then, the 100 nm of Au are removed via argon ion milling in the dry etching system utilized for ICP-RIE. Without breaking vacuum, the Nb is subsequently etched at $T = 5\,^{\circ}\mathrm{C}$, a substrate bias power of $P_{\mathrm{rf}} = 50\,\mathrm{W}$, an ICP-power of $P_{\mathrm{ICP}} = 100\,\mathrm{W}$ and at an etch rate of $\dot{e}_{\mathrm{Nb}} \sim 1\,\mathrm{nm/s}$. The photoresist is then removed with DMF or acetone, followed by a wet etching of the remaining Au on top of the Nb with a potassium-iodine solution diluted in water $I_2/KI/H_2O$ (1:4:40), as

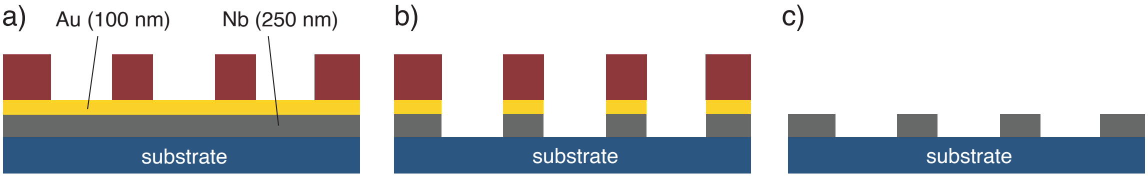

Figure 5.22: Schematic illustration of the fabrication steps of the present workaround for creating vias that do not limit the ampacity of Nb wiring. a) Sputtering of an Nb/Au bilayer and structuring of the etch mask with photoresist. b) Removal of Au with argon ion milling and ICP-RIE of the Nb. c) Removal of the photoresist with DMF and wet etching of the Au with a potassium-iodine solution.

shown in c). The thereby created wiring exhibits a $\sim 30\,\%$ reduced superconducting ampacity of $j_{\mathrm{c,Nb}} \approx 80\,\mathrm{mA}/\mu\mathrm{m}^2$, even when there is no constituting via. However, $j_{\mathrm{c,Nb}}$ stays constant when vias are introduced, even for a series connection of up to 8000 vias that part of investigated test samples. This is now the current standard fabrication procedure for the first Nb layer of fabricated MMCs within the group when vias are an essential part of the design. The detectors that were developed in this thesis require an even higher ampacity, hence the developed workaround was not used and their field generating coil consists of only a single Nb layer, i.e. the bottom electrode layer of the Nb/Al-AlO$_\mathrm{x}$/Nb trilayer.

It is possible that $j_{\mathrm{c,Nb}}$ is reduced also due to hydrogen damage, as it was discussed in section 5.3.6. While the Au on top of the Nb prevents the formation of an Nb oxide layer for protection, the Au itself presents a permeation barrier, as the hydrogen permeation of Au is even lower than for Al [Ste83]. Therefore, hydrogen can potentially permeate the Nb once the Au is removed during wet etching. In order to circumvent the use of a wet etch to remove the Au in a final test, the Au layer was removed via argon ion milling. However, the Nb wiring still exhibited the same reduced $j_{\mathrm{c,Nb}}$, indicating that the degraded performance must originate from a different step in the fabrication process. This was not further investigated in this thesis.

6. The HDMSQ1 detector

The HDMSQ1[1] detector that was developed within the framework of this thesis is the first integrated detector, i.e. detector and dc-SQUID are combined in a single device, that was developed completely within the group. The purpose of this detector was to surpass the benchmark energy resolution of the revised maXs-20 detector that was briefly discussed in section 2.8. Furthermore, the development of this detector should answer several questions, for instance the impact of the on-chip energy dissipation of the SQUID on the detector performance at millikelvin temperatures, the impact on the SQUID performance by placing a paramagnetic senor directly on top of its loop, or the feasibility of the joint fabrication of dc-SQUIDs and MMCs to create such integrated detectors. The experiments discussed within this chapter will show, that a successor of the HDMSQ1 was needed to be developed in order to exploit the full potential of the direct sensor readout of metallic magnetic calorimeters. This chapter first discusses the HDMSQ1 design and the experimental methods that are required for detector operation. Afterwards, the detector characterization is presented and discussed, concluding with a summary and an outlook towards its successor, the HDMSQ2A detector.

6.1 Detector design

6.1.1 Overview of the HDMSQ1 detector chip

Figure 6.1 a) shows a schematic of the HDMSQ1 detector that is structured on a chip with an edge length of 8 mm. In addition, figure 6.1 b) shows a photograph of one of the fabricated chips that was mounted on the experimental setup that will be discussed in section 6.4. In the center of the chip, 32 metallic magnetic calorimeters are located, forming an 8×8 pixel array. The 64 pixels cover a total area of $\sim 1.6\,\mathrm{mm}^2$. The spatial separation between the absorbers is $10\,\mu$m, resulting in an active area of about 90 %.

The chip is divided into four identical quadrants, each rotated by 90° compared to its neighboring quadrants. Each quadrant of the detector chip has bias lines for the field coils and corresponding persistent current switches in order to inject the persistent current I_0. The bondpads of these bias lines are located at each corner of the chip. The current injection procedure will be explained in section 6.2. The bondpads that

---

[1] Abbreviation for Heidelberg Meander-SQUID

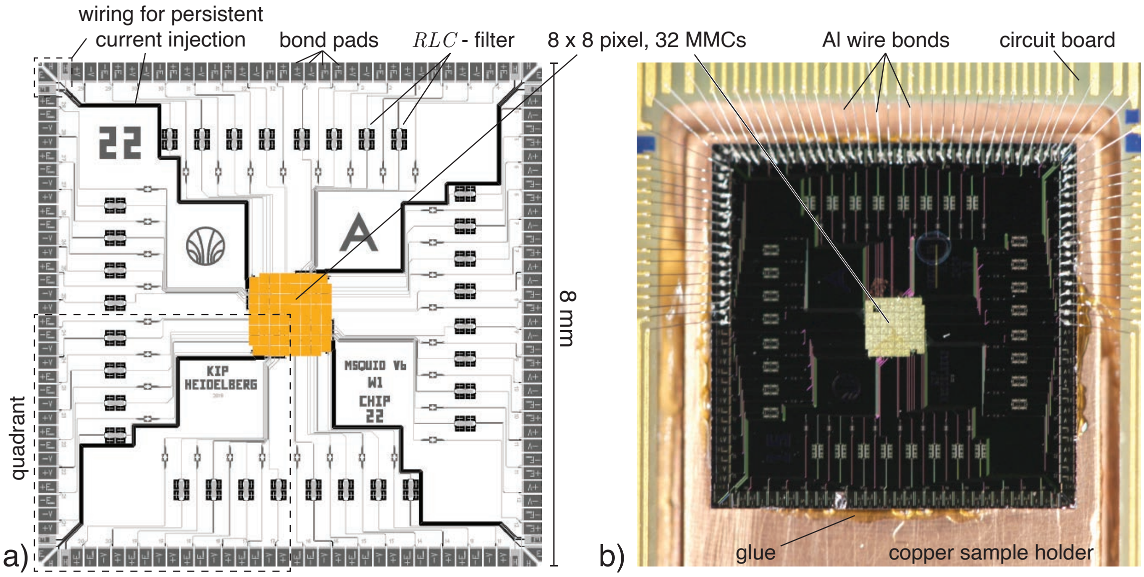

Figure 6.1: a) Design schematic of the HDMSQ1 detector chip. The chip is divided into four identical quadrants, each rotated by 90°. The detector is build of 32 metallic magnetic calorimeters with direct sensor readout, that are located in the chip center, forming an 8×8 pixel array. b) Photograph of a fabricated HDMSQ1 detector glued to a custom sample holder made of copper.

are required to connect the SQUID bias lines and feedback lines to a circuit board are located at the edge of the chip. Furthermore, an RLC-filter is located at the SQUID bias lines in order to filter out parasitic high frequency signals. The specifics of this filter are discussed in section 6.1.2.

6.1.2 Single detector of HDMSQ1

Figure 6.2 a) shows an explosion drawing of an individual integrated detector on the HDMSQ1 detector chip, that shall be explained in the order of layer fabrication, i.e. from bottom to top. All layers that are shown have the correct relative scaling to each other, except for the particle absorber. Only one temperature sensor and corresponding particle absorber are shown for visibility, whereas the 300 nm of SiO_2 that are used for insulation between each Nb layer are also omitted. Furthermore, the equivalent circuit diagram of the dc-SQUID is depicted in 6.2 b), whereas a colorized scanning electron microscope picture of the fabricated SQUID is shown in c), without the corresponding temperature sensors and particle absorber on top.

The lowest layer (dark grey) is the Nb bottom electrode of the Nb/Al-AlO_x/Nb trilayer, which also forms a meander-shaped field coil that carries the persistent current I_0 that is required to magnetize the sensor. No vias constitute this coil, which has

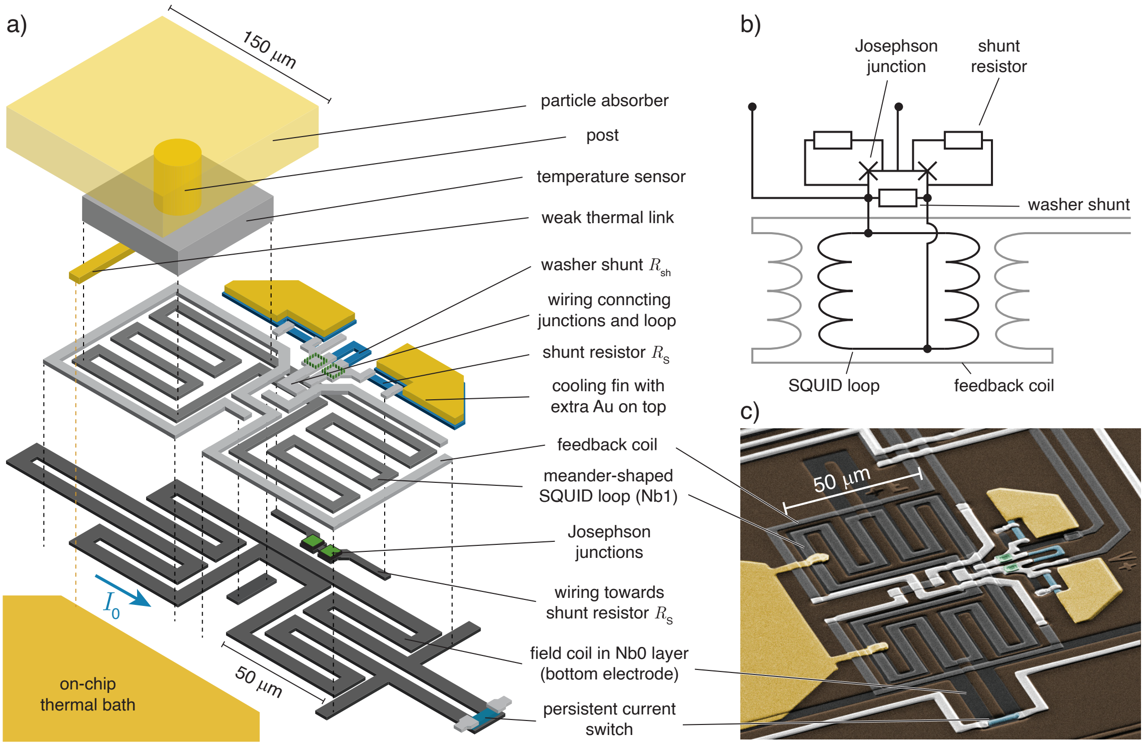

Figure 6.2: a) Explosion drawing of a single metallic magnetic calorimeter on the HDMSQ1 detector chip. b) Equivalent circuit diagram of the developed dc-SQUID. c) Colorized scanning electron microscope picture of the fabricated SQUID without temperature sensors and particle absorbers.

a superconducting ampacity of 160 mA. It has a layer thickness of $t_{\mathrm{Nb}} = 250\,\mathrm{nm}$, a meander pitch $p_1 = 10\,\mu\mathrm{m}$ and stripe width $w_1 = 6\,\mu\mathrm{m}$. Each Josephson junction (green) has a target critical current of $I_{\mathrm{c}} \approx 6.25\,\mu\mathrm{A}$. The smallest junction area that we can reliably fabricate is $A_{\mathrm{jj}} = 4 \times 4\,\mu\mathrm{m}^2$ due to accuracy limitations in the microfabrication process. To reach the target I_{c}, an area of $A_{\mathrm{jj}} = 5 \times 5\,\mu\mathrm{m}^2$ with a target critical current density of $j_{\mathrm{c}} \approx 25\,\mathrm{A/cm}^2$ was chosen. A meander-shaped SQUID loop (grey) is placed on top of the field coil in the Nb1 layer, with nearly identical parameters compared to the latter. It has an Nb layer thickness of $t_{\mathrm{Nb}} = 250\,\mathrm{nm}$, a meander pitch $p_2 = 10\,\mu\mathrm{m}$ and stripe width $w_1 = 4\,\mu\mathrm{m}$. The meander-shaped loop is connected in parallel to the Josephson junctions, forming a 1st-order gradiometer, resulting in a SQUID inductance of $L_{\mathrm{S}} = L_{\mathrm{M}}/2 = 75\,\mathrm{pH}$. Here, $L_{\mathrm{M}} = 150\,\mathrm{pH}$ is the inductance of each meander, which was determined by numerical simulations with the program InductEx [Fou15] during the design process. The structures close to the tunnel junctions have a parasitic contribution to the total inductance of less than 4 pH. After fabrication, the inductance L_{S} was determined by evaluating the critical current modulation ΔI_{mod} of the SQUID from IV-characteristics and using equation 3.14, and the results of the numerical simulations in [Tes77], to determine β_{L} and consequently L_S. The measured L_S and calculated L_S agree within 5 %.

An Au:Pd shunt resistor with $R_\mathrm{S} = 5\,\Omega$ is connected in parallel to each junction, with corresponding Au:Pd cooling fins attached to each shunt resistor. This cooling fin is comparably small in the design due to the limited available area within the 64 pixel detector array. The characteristic length that is required for electrons to thermalize with the phonon system in the Au:Pd cooling fin can be approximated by $l_\mathrm{T} \approx 11\,\mu\mathrm{mK}^{3/2} \cdot \mathrm{T}_\mathrm{e}^{-3/2}$ [Ple09], with T_e being the electron temperature within the shunt resistor. Assuming $T_\mathrm{e} = 100\,\mathrm{mK}$, this results in a thermalization length of $l_\mathrm{T} \approx 350\,\mu\mathrm{m}$, which is significantly larger than the dimensions of the cooling fin, as can be seen in figure 6.2 c). Hence, it was decided to also deposit the Au thermalization layer of the MMC on top of this cooling fin in order to increase its effective cooling volume without adding an additional lithographic layer to the design.

An Au:Pd washer shunt with $R_\mathrm{sh} = 10\,\Omega$ is connected in parallel to the SQUID loop in order to dampen resonances in the IV-characteristics of the SQUID, as it was discussed in section 3.3.1. With the presented parameters, a target $\beta_\mathrm{C} = 0.25$ is calculated with equation 3.8, where a specific junction capacitance of $c_\mathrm{jj} = 17\,\mathrm{fF}/\mu\mathrm{m}^2$ was assumed [Dee16]. A target $\beta_\mathrm{L} = 0.45$ is calculated with equation 3.14. Therefore, $\beta_\mathrm{C} < 1$ and $\beta_\mathrm{L} < 1$ should hold, even if the critical current density j_c is increased compared to the target value (see section 5.3.7). A feedback coil (light grey) surrounds the SQUID loop for flux-bias and flux-locked loop operation with a simulated mutual inductance between this coil and the SQUID loop of $M_\mathrm{fb}^{-1} = 44.5\,\mu\mathrm{A}/\Phi_0$, also agreeing with the measured value. The persistent current switch is an Au:Pd resistor with $R_\mathrm{H} = 4\,\Omega$ and its use will be explained in section 6.2.

Damping of intrinsic resonances

The occurrence of intrinsic resonances within a dc-SQUID, and how these can be dampened by resistive shunting of the SQUID loop, was discussed in section 3.3.1. Such resonances were observed in prototypes of the developed dc-SQUID discussed in this section, that did not yet include the washer shunt that is shown in figure 6.2 a). The measured IV-characteristic of one of these prototypes without a washer shunt is shown in figure 6.3 a). The characteristics shows an intrinsic resonance, as well as other distortions resulting from that. In order to investigate the SQUID's behavior and dampen this resonance, a washer shunt varying between $10\,\Omega$ and $25\,\Omega$ was added to the design and several prototypes were fabricated. In addition, prototypes without washer shunt were fabricated as control samples. All prototypes were fabricated on a single chip to minimize the impact of possible variations in the critical current I_c of the Josephson tunnel junctions, as well as to minimize potential variations of the thickness of the Au:Pd shunt resistors that can occur accross a 3 inch wafer. The measured IV-characteristics of the prototype with a washer shunt with $R_{\mathrm{sh}} = 10\,\Omega$ is plotted in figure 6.3 b), showing a smooth characteristic without any visible intrinsic resonance occurring in the bias current range of interest. Other prototypes with larger washer shunts showed characteristics of similar form. Therefore, the smallest washer shunt with $R_{\mathrm{sh}} = 10\,\Omega$ was chosen for the HDMSQ1 design, as it requires the least amount of space on the chip. What is also observed is that the critical current I_{c} of one Josephson junction is increased compared to its target value of $6.25\,\mu\mathrm{A}$. This is due to the fact that this wafer design had a higher than usual target critical current density of $j_{\mathrm{c}} = 30\,\mathrm{A/cm^2}$, whereas an even further increased value of $j_{\mathrm{c}} = 44\,\mathrm{A/cm^2}$ was determined after wafer fabrication. It is worth mentioning, that placing the paramagnetic temperature sensors on top of the SQUID loop, as it was done for realizing the HDMSQ1, did not cause other disturbing features in the IV-characteristics. That the curves in figure 6.3 b) still appear slightly distorted is due the fact that a comparably small amount of data points were taken, resulting in the depicted curves being influenced by the noise of the oscilloscope that was used for data acquisition.

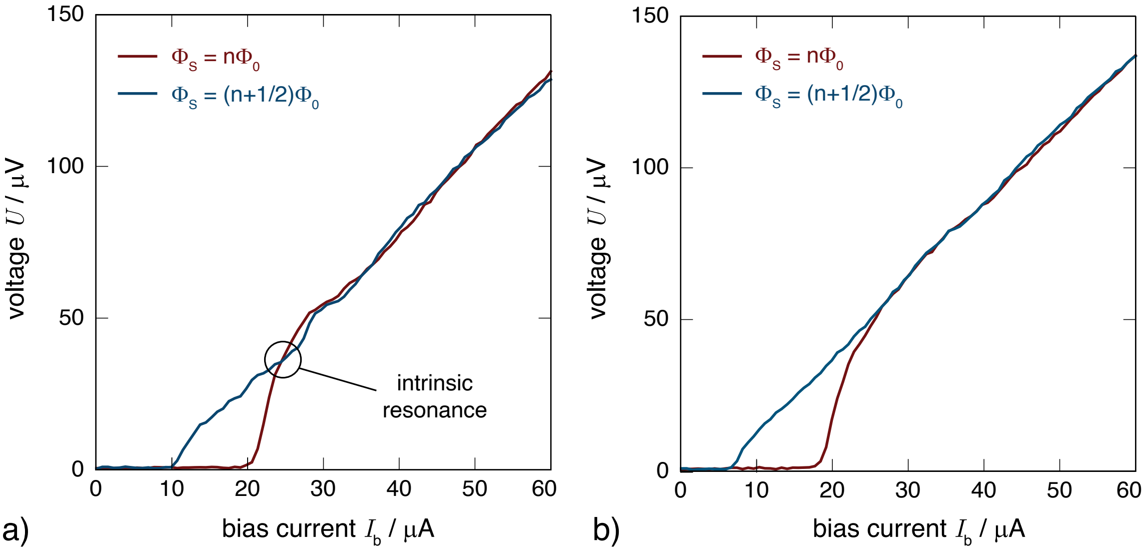

Figure 6.3: Measured IV-characteristics of the dc-SQUID building the basis for the HDMSQ1 detector for different values of the magnetic flux Φ_{S} threading the SQUID loop. a) Prototype SQUID without washer shunt. An intrinsic resonance occurs at $U \approx 40\,\mu\mathrm{V}$. b) Prototype SQUID with a washer shunt with a resistance of $R_{\mathrm{sh}} = 10\,\Omega$. No intrinsic resonance occurs in the bias range of interest.

Microfabricated RLC-filter

The equivalent circuit diagram of the on-chip RLC-filter is shown in figure 6.4 a). In this filter, dc-currents can pass through the superconducting inductances L without dissipating energy in the resistors. However, ac-currents see the impedance $i\omega L$, forcing the current to run through the resistors at high frequencies ω. Thus, the circuit exhibits an RC-low pass behavior. Each Au:Pd resistor within the filter has a resistance of $R = 18\,\Omega$, whereas each coil has an inductance of $L = 1\,\mathrm{nH}$. The inductance of the latter was determined with the program InductEx. The plate capacitor in the center has an area of $250 \times 50\,\mu\mathrm{m}^2$ and its superconducting electrodes are spatially separated from each other by 600 nm of insulating $\mathrm{SiO_2}$. Its calculated capacitance is $C = 0.7\,\mathrm{pF}$, assuming a dielectric constant of $\mathrm{SiO_2}$ of $\epsilon_\mathrm{r} = 3.9$. Also part of the circuit is the dc-SQUID, contributing with an assumed resistance of $2.5\,\Omega$, i.e. a parallel circuit of the shunt resistors that are connected in parallel to the Josephson tunnel junctions. Figure 6.4 b) shows the filters design schematic, as well as a legend of its lithographic layers without insulation. Figure 6.4 c) shows the simulated response of the filter with a cutoff frequency $f_{-3\mathrm{dB}} \approx 100\,\mathrm{MHz}$. The simulation was conducted with the LTSpice software from analog devices[2].

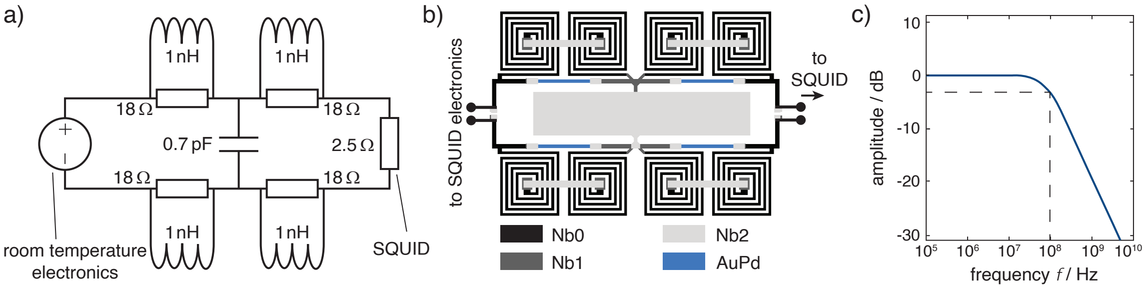

Figure 6.4: Overview of the on-chip RLC-filter that is inserted into the bias wires of each detector of HDMSQ1. a) Equivalent circuit diagram of the filter. b) Design schematic of its lithographic layers. c) Simulated filter response. Using this simulation, the cutoff frequency is determined to be $f_{-3\mathrm{dB}} \approx 100\,\mathrm{MHz}$.

Temperature sensor and particle absorber

Figure 6.5 a) shows a microscope photograph of an individual integrated detector on the HDMSQ1 detector chip with detached particle absorber. Shown is the already discussed dc-SQUID, now with corresponding Ag:Er temperature sensors on top of the meander-shaped SQUID loop. In addition, rounded Au structures on top of the sensor can be seen, that are the residuals of the single post that connects the sensor

---

[2] LTSpince from analogue devices: www.analog.com

and the absorber. Figure 6.5 b) shows a colorized scanning electron microscope picture of an individual detector that was equipped with only one particle absorber and temperature sensor.

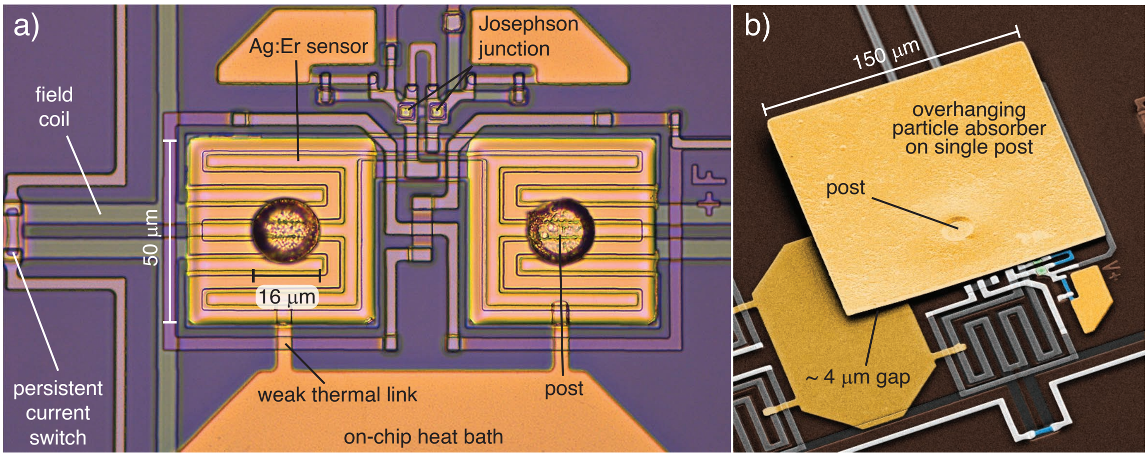

Figure 6.5: a) Microscope photograph of the HDMSQ1 detector. For visibility, both particle absorbers were removed. b) Colorized scanning electron microscope picture of an HDMSQ1 detector which was equipped with only one particle absorber and temperature sensor.

The overhanging particle absorbers are made of electroplated gold and have a dimension of $150 \times 150 \times 3\,\mu\mathrm{m}^3$. With a thickness of $3\,\mu$m, the absorbers have a quantum efficiency of QE = 98 % for photon energies of up to $E_\gamma = 5\,\mathrm{keV}$, and QE = 50 % for $E_\gamma = 10\,\mathrm{keV}$. The heat capacity of each absorber is $C_\mathrm{abs} = 0.1\,\mathrm{pJ/K}$ at $T = 20\,\mathrm{mK}$. A single post with a diameter of $16\,\mu$m connects the particle absorber to its sensor, whereas its cross section area is 8 % of the total sensor area. This is rather large compared to other MMCs like the maXs-20 detector (~ 2 %) [Sch12, Kra13], or the maXs-30 detector (~ 0.3 %) [Hen17]. However, the development of the fabrication process for overhanging absorbers on posts that was discussed in section 5.4.2 showed, that a single post of large diameter is much more structurally stable than several posts of smaller diameters for absorbers with a thickness of only $3\,\mu$m. The latter were often ripped off during the ultrasonic cleaning that is required for the developed fabrication process. It was therefore decided to use a single, uncommonly large post in the HDMSQ1 design in order to provide a high reliability of the fabrication process.

The Ag:Er temperature sensor has a dimension of $50 \times 50 \times 1.2\,\mu\mathrm{m}^3$ with an erbium concentration $c_\mathrm{Er} = 450\,\mathrm{ppm}$. The Er concentration in the sensor was fixed by the Er concentration of the Ag:Er target that was mounted in the employed UHV sputtering system at the time of fabrication, whereas the sensor area was predetermined by the available area the of meander-shaped SQUID loop. The sensor height of $1.2\,\mu$m was chosen based on numerical simulations which did not incorporate all key features of the detector geometry at the time. Therefore, the sensor was not fully optimized for $T = 20\,\mathrm{mK}$, but still yields an excellent energy resolution, assuming the detector will reach this operation temperature despite the on-chip energy dissipation of the dc-SQUID. Assuming various achievable operation temperatures for the HDMSQ1 detector, the expected energy resolution is $\Delta E_{\mathrm{FWHM}} \approx 1.3\,\mathrm{eV}$ at $T = 20\,\mathrm{mK}$, $\Delta E_{\mathrm{FWHM}} \approx 1.9\,\mathrm{eV}$ for $T = 30\,\mathrm{mK}$, and $E_{\mathrm{FWHM}} \approx 2.6\,\mathrm{eV}$ for $T = 40\,\mathrm{mK}$. These calculations are based on numerical simulations that will be discussed in section 6.3. Furthermore, since absorber and sensor are directly coupled to each other, a signal rise time of $\tau_0 \approx 100\,\mathrm{ns}$ is expected.

When one temperature sensor on top of the dc-SQUID is omitted by design, as it is the case for the detector depicted in figure 6.5 b), then this detector channel is sensitive to temperature fluctuations of the cryogenic setup because it is no longer a gradiometer. When the temperature changes, the subsequent change of the sensor magnetization $M(T)$ of this channel leads to a change of magnetic flux in only one of the meanders within the SQUID loop, leading to corresponding drifts of the output voltage of the SQUID. Thus, this detector channel can be used to measure relative temperature fluctuations. This is done by determining the offset-level of their measured untriggered noise, which in turn can be used as temperature information in order to correct the signal height of the other pixels for these temperature fluctuations in a signal spectrum analysis. This procedure will be further illustrated in section 6.5.6. The HDMSQ1 detector chip has four of these non-gradiometric channels, one located in each corner of the active area in the chip center.

6.2 Persistent current injection

In this section, the procedure and technique for a simultaneous injection of the persistent current I_0 into the field generating coils of the individual detectors of the HDMSQ1 is illustrated. Within this context, the reason for using a separate field generating and pickup coil will be discussed.

Figure 6.6 a) schematically illustrates the electrical wiring of the meander-shaped field generating coils of three single detectors of the HDMSQ1. The coils are connected in series with an external current source I_{F}. Each field generating coil has the inductance $L_{\mathrm{M}} + L_{\mathrm{sw}}$, which is formed by the large inductance on the right side of the electrical connection, as well as the small inductance on the left side of the connection. A series connection of resistors R_{H} having a resistance of a few ohms is placed in the vicinity of the inductances L_{sw}. When a field current $I_{\mathrm{F}} > 0$ (blue) is injected into the wiring via the external current source, most of the current is flowing through the inductance L_{sw}, since $L_{\mathrm{sw}} \ll L_{\mathrm{M}}$, (see fig. 6.6 b)).

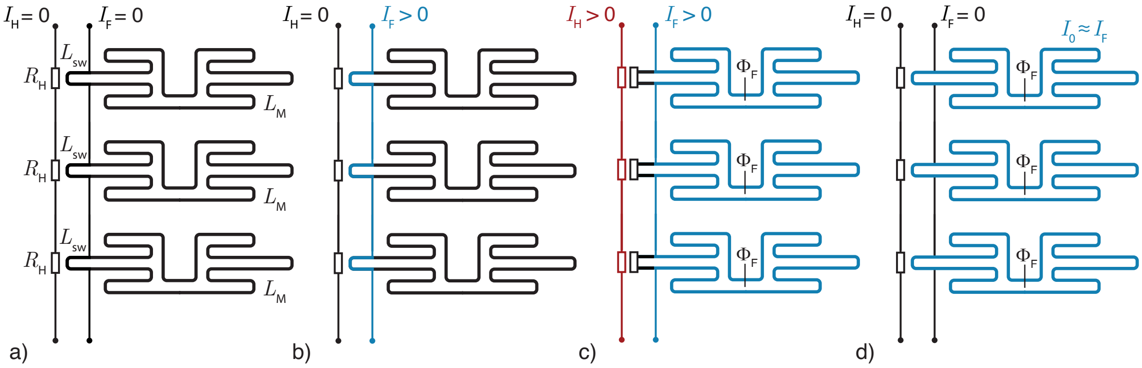

Figure 6.6: a) Schematic illustration of the electrical wiring of the meander-shaped field generating coils of three single detectors of the HDMSQ1 design. A current source I_F is connected in series to the coils, with each the latter having the inductance $L_\mathrm{M} + L_\mathrm{sw}$. L_M denotes the inductance on the right side of the electrical connection and L_sw denotes the inductance on the left side. A series connection of resistors, each having the resistance R_H, is placed in close vicinity to L_sw. b) The injected current $I_\mathrm{F} > 0$ is carried mostly by the inductance L_sw, as $L_\mathrm{sw} \ll L_\mathrm{M}$. c) A localized heat pulse switches the nearby wiring into the normal conducting state, forcing I_F to run through the remaining superconducting wiring, changing the magnetic flux threading the field coil to $\Phi_\mathrm{F} = L_\mathrm{M} I_\mathrm{F}$. d) L_sw thermalizes back below its critical temperature and Φ_F is now a conserved quantity in the closed superconducting loop. When I_F is reduced to zero, an inducted screening current I_0 keeps the magnetic flux Φ_F constant.

Once the field current I_F is injected, a rather short current pulse I_H (red) is send through the resistors, leading to a highly localized temperature increase of the surrounding structures to $T > 9.2\,\mathrm{K}$. As a result, the inductance L_sw switches into the normal conducting state, forcing I_F to go through the remaining superconducting part of the field coil (see fig. 6.6 c)). Therefore, I_F changes the magnetic flux $\Phi_\mathrm{F} = L_\mathrm{M} I_\mathrm{F}$ within the field coil. After the heat pulse, which lasts only for a fraction of a second, the structures thermalize with the substrate, and the inductance L_sw switches back into the superconducting state. The field coil is again a closed superconducting loop in which the magnetic flux Φ_F is a conserved quantity. Therefore, when I_F is reduced to zero, a screening current I_0 is induced in each field generating coil that accounts for magnetic flux quantization (see fig. 6.6 d)). Since $L_\mathrm{sw} \ll L_\mathrm{M}$, $I_0 \approx I_\mathrm{F}$ is an adequate approximation. With the presented setup, the persistent current I_0 is simultaneously prepared in all field coils that are part of the series connection. In the HDMSQ1 chip design, the field coils of the 8 integrated detectors in each chip quadrant are connected in series.

In previous detector designs [Fle09, Pie12b, Hen15, Kem18], the pickup coil and field coil are one and the same. As the description of the persistent current injection in this section made apparent, this injection requires a series connection of the coils

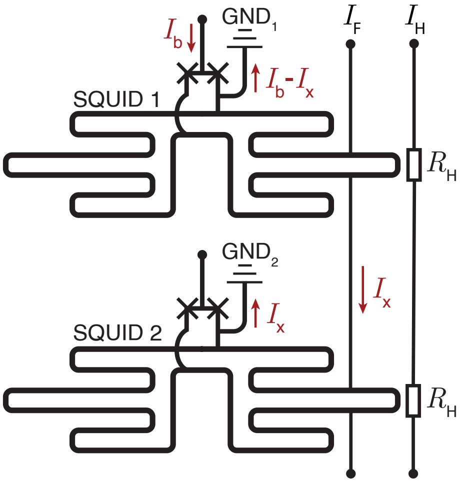

Figure 6.7: Schematic illustration of two dc-SQUIDs with meander-shaped SQUID loop that are electrically connected to each other in a way that a persistent current could be simultaneously injected in both SQUID loops. Due to this wiring, a part of the bias current I_b of SQUID 1 can run through the loop of SQUID 2 towards its ground conncetion, and vice versa, making an optimum SQUID operation challenging.

that carry the persistent current I_0. For an MMC with direct sensor readout, this would obviously mean that the SQUID loops need to be connected in series. Such an electrical wiring scheme is illustrated in figure 6.7. Shown are two dc-SQUIDs with meander-shaped SQUID loop that are connected in series, as well as bias lines I_F and I_H for persistent current injection. As the SQUID bias lines (I_b) can be easily disconnected by removing the room temperature electronics, and the Josephson junctions are normal conducting for currents larger than their critical current I_c, this scheme presents no obstacle for the injection of the persistent current I_0. However, the SQUID operation itself becomes rather challenging. When SQUID SQ1 is biased with a bias current I_b, a fraction I_x of this bias current I_b can go towards the ground connection of SQUID SQ2. When starting to operate the SQUIDs, this means SQ1 is usually biased at its optimum working point first. Afterwards, when SQ2 is biased at its optimum working point, a part of its bias current can now go towards the ground connection of SQ1, consequently changing the current running through its loop. As a result, SQ2 is now optimally tuned, while SQ1 has lost its optimum working point. Finding the optimum working point for both SQUIDs therefore requires an iterative adjustment of the bias currents, which is challenging but possible for a small number of SQUIDs, but hardly possible for a rather large number of SQUIDs, i.g. for 32 SQUIDs used in HDMSQ1 detector.

To circumvent this obstacle, an individual persistent current injection into every detector channel could be done. As this significantly increases the amount of required wires into the cryostat consequently increasing the heat load into the system, this scheme limits the amount of channels, making the use of larger detector arrays impractical. In addition, this scheme would require additional wiring structures that are part of the SQUID loop, marked by L_sw in figure 6.6, as the persistent current switch needs to be placed at a certain distance to the SQUID loop, so that the latter stays in its superconducting state during the heat pulse in the persistent current preparation procedure. As there would be no temperature sensor on top of these additional structures, they would present a non-negligible, parasitic contribution to the total usable SQUID inductance, which is undesirable for a detector that is geared towards the best possible energy resolution. Therefore, an independent field generating coil was used, giving rise to the development of the corresponding microfabrication process that was discussed in section 5.4.1.

6.3 Calculations of the HDMSQ1 detector properties

It was discussed in section 2.5.1 and 2.6, that the signal height $\delta\Phi/\delta E$ of a metallic magnetic calorimeter that makes use of a meander-shaped detector geometry can be predicted when the magnetic field distribution within the sensor is known. In order to simulate the magnetic field distribution, the paramagnetic temperature sensor is divided into small elements and the probability distribution of the magnetic field $P(B)$, which is created by the persistent current I_0 running through the meander-shaped coil, as well as a geometry factor $G(\boldsymbol{r}/p)$, are extracted using FEMM simulations. With these, the signal height $\delta\Phi/\delta E$ can be calculated.

This approach for the prediction of the signal height $\delta\Phi/\delta E$ can't be used for the HDMSQ1 detector, as the magnetic field distribution that determines the sensor heat capacity $c_{\mathrm{sens}}(B(\boldsymbol{r}))$, as well as the temperature dependence of the sensor magnetization $\partial M(B(\boldsymbol{r}))/\partial T$, is created by the current I_0 running in the field coil, whereas the geometry factor $G(\boldsymbol{r}/p)$, that describes the pickup of a magnetic flux change, has to be determined with respect to the pickup coil, i.e. the meander-shaped SQUID loop. Therefore, equation 2.11 has to be rewritten to

$$\frac{\delta\Phi}{\delta E} = \frac{V_{\mathrm{sens}}}{C_{\mathrm{abs}} + \sum\limits_{V}[c_{\mathrm{sens}}(B_{\mathrm{fc}}(\boldsymbol{r}))]_{x,y,z}} \cdot \frac{\mu_0}{p} \sum_{V} \left(G(B_{\mathrm{pc}}(\boldsymbol{r}/p)) \frac{\partial M(B_{\mathrm{fc}}(\boldsymbol{r}))}{\partial T} \right)_{V} , \tag{6.1}$$

where $c_{\mathrm{sens}}(B_{\mathrm{fc}}(\boldsymbol{r}))$ is the heat capacity of the volume element that sees the magnetic field $(B_{\mathrm{fc}}(\boldsymbol{r}))$ at location $\boldsymbol{r}$ that is created by the current I_0 running in the field coil. $G(B_{\mathrm{pc}}(\boldsymbol{r}/p))$ is the geometry factor of the volume element that sees the magnetic field $(B_{\mathrm{pc}}(\boldsymbol{r}))$ at location $\boldsymbol{r}$ that is created by the current I that runs through the pickup coil in the FEMM simulations, and $\partial M(B_{\mathrm{fc}}(\boldsymbol{r}))/\partial T$ is the temperature dependence of the sensor magnetization of this same volume element that sees the magnetic field $(B_{\mathrm{fc}}(\boldsymbol{r}))$ at location $\boldsymbol{r}$ that is created by the current I_0 running in the field coil. The sum over all elements within the sensor volume V yields the corresponding sensor properties that are required to calculate the signal height $\delta\Phi/\delta E$. Therefore, two simulations of the magnetic field distribution within the sensor have to be done. For the first one, a current I_0 is send through the field coil to extract the magnetic field distribution in order to calculate $c_{\mathrm{sens}}(B_{\mathrm{fc}}(\boldsymbol{r}))$ and $\partial M(B_{\mathrm{fc}}(\boldsymbol{r}))/\partial T$. The result of this FEMM simulation is shown for two meander stripes of the HDMSQ1 detector as a pseudocolor plot in figure 6.8 with a current $I_0 = 1\,\mathrm{mA}$ running through the field coil. For the second simulation, this current is send through the pickup coil, whereas the corresponding geometry factor $G(B_{\mathrm{pc}}(\boldsymbol{r}/p))$ for each element can be calculated with equation 2.9. In order to have an exact representation of the rounded sensor geometry between the meander stripes, the surface of this shape from a test sample was measured with an atomic force microscope. From this measurement, corresponding x- and y- coordinates were extracted, where the x-coordinates represent the horizontal direction in figure 6.8, and the y-coordinates represent the vertical direction. These coordinates were used to reconstruct the rounded sensor shape in the FEMM simulations. In order to extract the relevant factors from both simulated

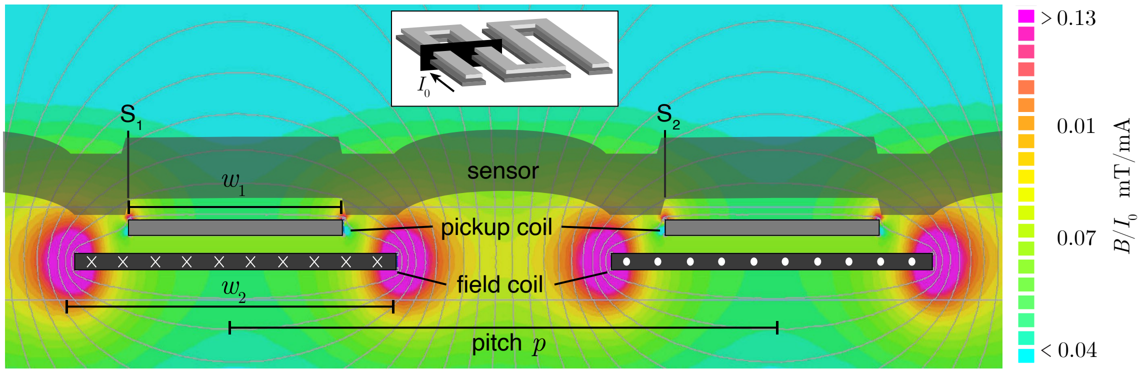

Figure 6.8: Pseudocolor plot of the calculated magnetic field distribution of the HDMSQ1 detector geometry for a cross section of two meander stripes simulated using FEMM. The depicted magnetic field is created by a persistent current $I_0 = 1\,\mathrm{mA}$ running through the field coil. The semi-transparent grey area marks the sensor location, whereas the sensor area that is delimited by the lines S_1 and S_2 is used for the numerical simulation of the detector performance.

magnetic field distributions and calculate equation 6.1 accordingly, as well as the expected energy resolution, a corresponding program was written in Python during this thesis. This program allows for the numerical simulation of the HDMSQ1 detector, as well as of other metallic magnetic calorimeters that employ different, arbitrary geometries that can be simulated using FEMM. For the HDMSQ1 detector, the sensor within the semi-transparent grey area in figure 6.8 between S_1 and S_2 was segmented into 200 elements of length $p/200 = 50\,\mathrm{nm}$ in the horizontal x-direction. The sensor height $h_{\mathrm{sens}} = 1.2\,\mu\mathrm{m}$ was divided into elements of 100 nm height in y-direction. Calculating the properties of the entire sensor volume can be done with periodic boundary conditions when edge effects are neglected. Therefore, creating magnetic field simulations of just two meander stripes is sufficient. As the meander pitch is $p = 10\,\mu\mathrm{m}$ and the sensor edge length is $50\,\mu\mathrm{m}$, the simulation results repeat themselves five times in x-direction for a total of 1000 volume elements, and also

1000 volume elements in the in-plane direction. With these considerations, the total sensor volume of $50 \times 50 \times 1.2\,\mu\text{m}^3$ was essentially divided into 12 million volume elements. The edge effect that was not considered in the simulation stems from the assumption, that the edge of the sensor is a steep wall, whereas in reality it is slanted, or rounded, due to the use of a Lift-off process for sensor fabrication, as it is discussed in the appendix A.1.6. Such an edge effect becomes more prominent the smaller the sensor becomes and might be considered in future design simulations, where for instance the SQUID loop inductance L_S stays fixed, but meander pitch p and stripe width w are greatly reduced in order to increase the signal coupling. Reducing p and w for a fixed L_S consequently means a reduction of the available sensor area. In order to account for the slanted sensor edge in this case, one would have to surrender the periodic boundary conditions and create a magnetic field simulation for the entire detector geometry, not just for a small segment of two meander stripes.

Figure 6.9 a) shows the calculated energy resolution ΔE_{FWHM} of the HDMSQ1 detector as a function of temperature T for a selection of injected persistent currents I_0. Figure 6.9 b) shows the same calculation for the predicted signal height $\delta\Phi/\delta E$ per energy input. All the factors that were used for the numerical simulations are summarized in the appendix table A.1.

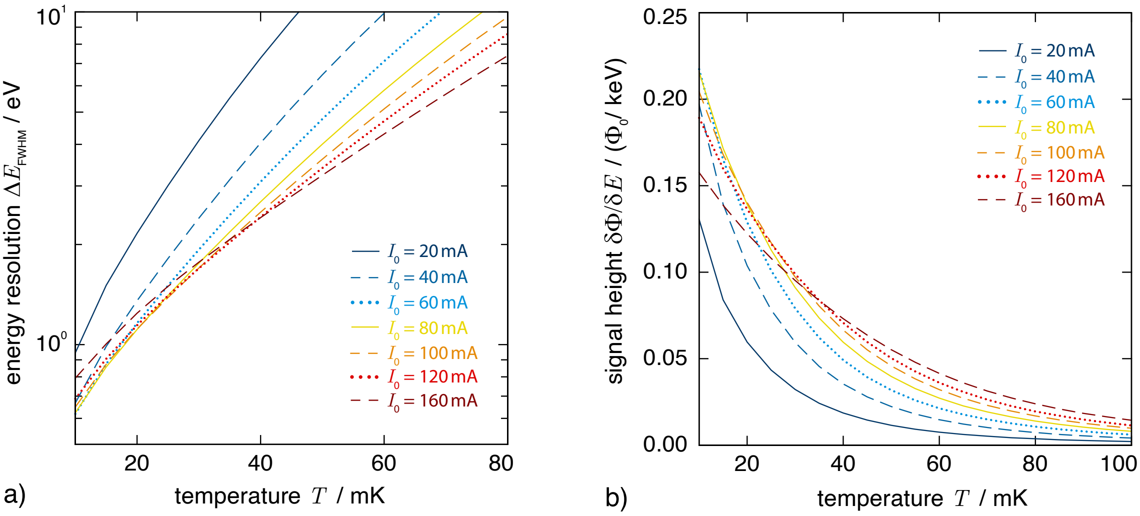

Figure 6.9: Calculated properties of the HDSMQ1 detector as a function of temperature T for a selection of injected persistent currents I_0 running in the field generating coil. a) Expected energy resolution ΔE_{FWHM}, and b) expected signal height $\delta\Phi/\delta E$ per energy input.

6.4 Experimental setup

The experimental setup designed and employed in this thesis to operate the developed detectors was mounted directly to the mixing chamber platform of the dilution refrigerator. A schematic side view and top view of the entire setup is illustrated in figure 6.10 a). Here, also a cover made of Al is shown, which becomes superconducting at the operation temperature of MMCs and should screen the setup against environmental background magnetic field fluctuations. Figure 6.10 b) shows the top view without Al cover. The main constituent of this setup is a sample holder that has the shape of a ”T” with a tiny bar. It has a length of 105 mm and is made of annealed copper to provide an excellent thermal conductivity between detector and mixing chamber platform. The detector chip is glued with GE 7031 Varnish on a small designated platform situated close to the tip of the sample holder. A custom made circuit board[3] is mounted directly on top of the sample holder in order to connect the detector to the wiring of the cryostat via electrical connectors[4]. For the SQUID bias and feedback lines of 16 SQUIDs, four 16-pin connectors are hosted on the circuit board. A 30-pin connector is used to connect the field coils and persistent current switches on the chip to the croystat wiring. The Al casing has a small notch located directly above the detector chip, allowing X-rays from a nearby calibration source to reach the detector.

Figure 6.10 c) shows a magnified, more detailed schematic cross section of the part of the detector setup where the chip is placed. The chip’s wiring is connected to the circuit board via Al wire bonds. A collimator is positioned $\sim 500\,\mu$m above the chip, preventing X-rays from hitting areas other than the absorbers of the detector array. This collimator is a microstructured foil made of electroplated gold with a thickness of $15\,\mu$m, in which square openings of $130 \times 130\,\mu\mathrm{m}^2$ were structured for each particle absorber on the chip. However, this collimator did not exist during the operation of the HDMSQ1 detector, but was fabricated and used for the HDMSQ2A detector, which will be discussed in the next chapter. The collimator is shown for completeness here, as the overall experimental setup did not change for all detectors that were developed within this thesis. Therefore, X-rays were hitting the substrate of the HDMSQ1 detector during operation, which led to potential temperature fluctuations of the chip. A soft cushion is placed between the tip of the sample holder and the Al casing, that is tightly squeezed once sample holder and casing are mounted together. This fixation prevents mechanical vibrations of the sample holder within the casing, that originate from the pulse tube cooler of the cryostat, as it occurred during testing of the setup. Since the notch in the Al casing potentially reduces the magnetic shielding of the detector, an additional aluminium collimator is mounted on

---

[3] www.multi-circuit-boards.eu

[4] Samtec Tiger Eye Socket SFM-115 series: https://www.samtec.com

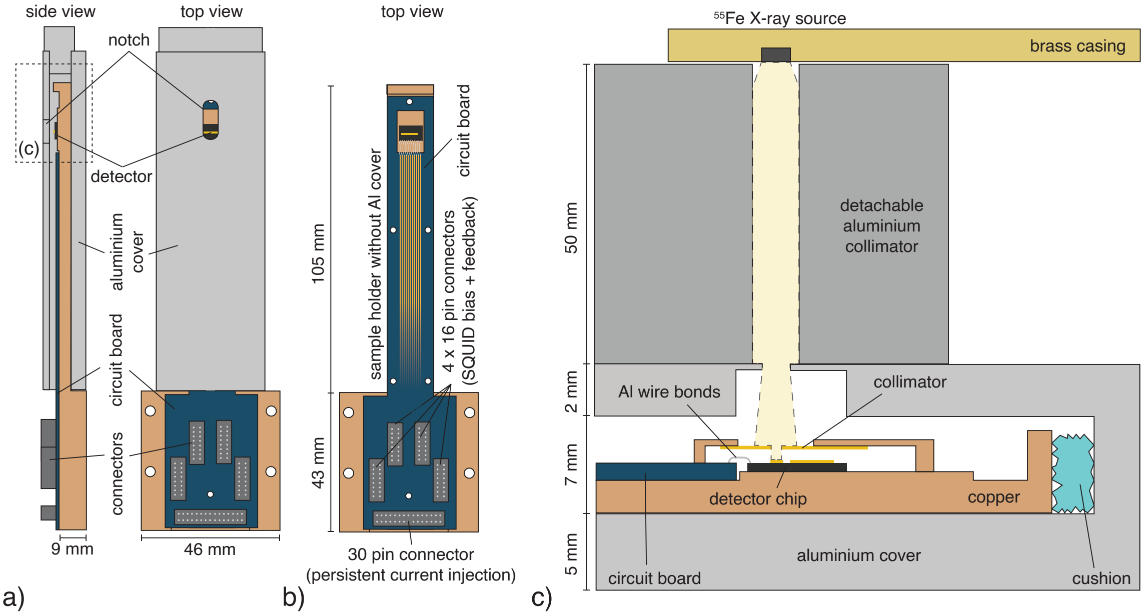

Figure 6.10: a) Schematic side view and top view of the experimental setup designed and used in this thesis with a superconducting shield made of Al, and b) top view without Al cover. The detector chip is glued to the tip of a sample holder. The chip is connected to the wiring of the ^{3}He/^{4}He dilution refrigerator via a custom circuit board and electrical connectors. c) Detailed side view of the detector region. Located above the detector chip are a collimator made of Au, one made of Al, as well as an ^{55}Fe X-ray calibration source.

top of the casing. This collimator functions as a 5 cm long tube with a high aspect ratio in order to improve the superconducting shielding of the detector. Directly above this tube, the ^{55}Fe X-ray calibration source that was discussed in section 4.4 is positioned, emitting photons of well known energy to characterize the detector. The setup provides wiring for the readout of 16 detector SQUIDs and can support chip sizes of up to $10 \times 15\,\mathrm{mm}^2$.

6.5 Experimental results

This section presents aspects of the characterization of the HDMSQ1 detector, the very first detector iteration with direct sensor readout that was fully developed inhouse. It will be made apparent, that the HDSMQ1 detector suffered significantly from design issues, which prevents the detector to achieve its full potential. These design issues are discussed in this section and were addressed in the design of its successor, the HDMSQ2A detector. The presented detector characterization includes an investigation of the signal height, the detector noise and energy resolution depending on the on-chip energy dissipation of the detector SQUID in the two-stage setup. Furthermore, the signal rise will be examined. If not denoted otherwise, all characterizations were performed at the base temperature of the utilized ^{3}He/^{4}He dilution refrigerator (see section 4.1), i.e. $T \approx 7\,\mathrm{mK}$. Of the 16 operated detector channels, 15 were working, indicating a rather high yield of the Josephson tunnel junctions. Furthermore, the critical current of these 15 SQUIDs at a magnetic flux of $\Phi_\mathrm{S} = (n + 1/2)\Phi_0$ threading their meander-shaped loop was determined to be $I_\mathrm{b} = 6.5 \pm 0.3\,\mu\mathrm{A}$, indicating a good homogeneity.

6.5.1 Optimum persistent current

Figure 6.11 a) shows a schematic of the pixels on the HDMSQ1 detector, as well as their channel labels. As the experimental setup presently only supports the operation of 16 SQUID channels, the channels 1 to 16 were operated. Most of the characterization measurements that are discussed in this section were done on Ch3 in quadrant 1, which is marked in red in figure 6.11 a).

Already during the commissioning of the HDMSQ1 detector, it turned out that the chip temperature is significantly influenced by SQUID Joule heating. As the chip's actual temperature T, which is an important parameter for determining the optimum bias conditions of the detector, was unknown, the optimum persistent current I_0, for which the detector response after photon absorption is maximized, had to be experimentally determined. For this determination, the detector SQUID of Ch3 was biased with a current $I_\mathrm{b} = 35\,\mu\mathrm{A}$. This bias current was chosen because the measured white noise level of the detector was minimized for this I_b, indicating its optimum working point, as will be discussed in detail in section 6.5.5. After applying this optimum bias current, the detector response of Ch3 that follows the absorption of ^{55}Mn K$_\alpha$ X-rays from the calibration source was measured for various injected persistent currents. Figure 6.11 b) shows the measured signal height Φ_S in the SQUID as a function of the persistent current I_0 running in its field coil. Additionally, the signal height that is expected from numerical simulations for various operation

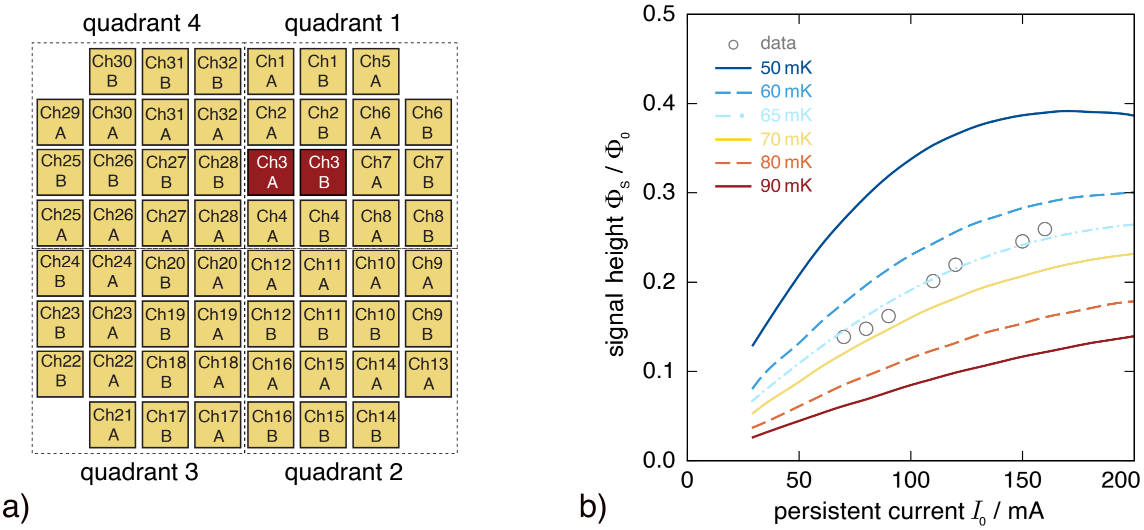

Figure 6.11: a) Schematic of the pixels of the HDMSQ1 detector with their channel labeling. b) Signal height Φ_S in the SQUID of Ch3 that resulted from the absorption of 5.9 keV ^{55}Mn K$_\alpha$ photons, measured as a function of the injected persistent current I_0 running through the field coils of all detectors in quadrant 1. Furthermore, numerical simulations of the expected signal height for various operation temperatures of the detector are shown.

temperatures of the HDMSQ1 detector is shown. The plot nicely shows that the chip, or at least the paramagnetic temperature sensor of Ch3, has an operation temperature of $T \approx 65\,\mathrm{mK}$ for the chosen bias current $I_\mathrm{b} = 35\,\mu\mathrm{A}$. Furthermore, it can be seen that the largest injected persistent current of $I_0 = 160\,\mathrm{mA}$ yielded the largest measured detector response and that even larger signal heights could have been potentially reached for a higher I_0. However, as was already mentioned in section 6.1.2, the superconducting ampacity of the field coil was about 160 mA, i.e. the actual optimum signal height at this operation temperature was unaccessible for the HDMSQ1 detector. Therefore, the persistent current was kept at $I_0 = 160\,\mathrm{mA}$ during further detector characterization.

6.5.2 Signal shape

Figure 6.12 shows the measured detector response as the flux change $\delta\Phi_\mathrm{S}$ in Ch3 after the absorption of a ^{55}Mn K$_\alpha$ photon. The measurement was performed at a rather low bias current of $I_\mathrm{b} \approx 9\,\mu\mathrm{A}$ and a persistent current of $I_0 = 160\,\mathrm{mA}$, while the cryostat was at its base temperature of $T \approx 7\,\mathrm{mK}$. The signal shape exhibits the expected fast signal rise that is followed by a much slower signal decay. Furthermore, the signal height Φ_S is roughly a factor of 2 higher than the one that was shown in figure 6.11 for the same I_0. The only difference between these two measurements is the chosen

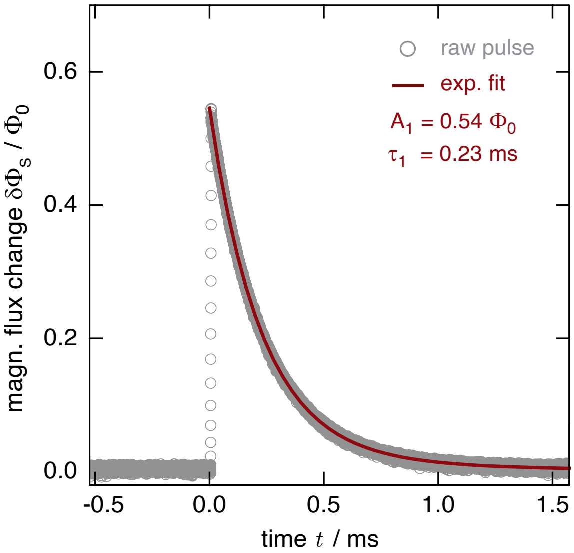

Figure 6.12: Measured magnetic flux change $\delta\Phi$ in the SQUID of Ch3 after the absorption of a ^{55}Mn K$_\alpha$ photon. The signal shape shows the expected fast signal rise, followed by a slower signal decay. The latter is described by an exponential function with a time constant of $\tau_1 = 0.23\,\mathrm{ms}$.

bias current, indicating that the reduction of I_b from $\approx 35\,\mu\mathrm{A}$ to $\approx 10\,\mu\mathrm{A}$ reduced the on-chip energy dissipation, such that the detector's operation temperature also reduced, consequently increasing the signal amplitude. Also depicted in figure 6.12 is an exponential fit with the form

$$\delta\Phi_\mathrm{S}(t) = A_1(e^{-t/\tau_1})\,, \tag{6.2}$$

in order to describe the signal decay, indicating a decay time of $\tau_1 = 0.23\,\mathrm{ms}$ with an amplitude of $A_1 = 0.54\,\Phi_0$. The predicted signal decay time is given by $\tau_1 = C_\mathrm{tot}/G$, which is the total detector heat capacity divided by the thermal conductivity of the metallic link between temperature sensor and on-chip thermal bath. The latter can be calculated according to the Wiedemann-Franz law, so that

$$\tau_1 = \frac{C_\mathrm{tot}\rho_\mathrm{Au}}{(RRR-1)\mathcal{L}T} \cdot \frac{t_\mathrm{Au} w_\mathrm{tl}}{l}\,. \tag{6.3}$$

Here, $\rho_\mathrm{Au} = 2.2 \cdot 10^{-8}\,\Omega\mathrm{m}$ denotes the literature value for the electrical conductivity, a $RRR = 2$ for sputtered Au, and the Lorenz number $\mathcal{L} = 2.44 \cdot 10^{-8}\,\mathrm{W\Omega K^{-2}}$. The width of the thermal link is $w_\mathrm{tl} = 4\,\mu\mathrm{m}$, its length is $l = 15\,\mu\mathrm{m}$ with a layer thickness of $t_\mathrm{Au} = 200\,\mathrm{nm}$. As it will be shown in the subsequent discussion in this chapter, the detector has an operation temperature of $T \approx 33\,\mathrm{mK}$ at this bias current, with a total calculated heat capacity of $C_\mathrm{tot} = 0.43\,\mathrm{pJ/K}$ for $I_0 = 160\,\mathrm{mA}$. The resulting expected signal decay time is $\tau_1 = 0.22\,\mathrm{ms}$, which is $0.01\,\mathrm{ms}$ faster then the measured value, showing a good agreement between the two. The remaining deviation of $4.3\,\%$ can be attributed to accuracy limitations in the microfabrication, found for instance in the width w_tl of the sputtered thermal link between temperature sensor and the thermal bath. An assumed reduction of w_tl by only $150\,\mathrm{nm}$ would already match the calculation to the measured value, a deviation that is well within the margin of error for structures that are microfabricated with a Lift-off process. Therefore, the signal decay of the HDMSQ1 detector can be described by a single exponential function, as it is predicted by theory.

6.5.3 Signal height

Figure 6.13 a) shows the measured signal height Φ_S of Ch3 for a 5.9 keV energy input as a function of the bias current I_b that was applied to the detector SQUID with a persistent current $I_0 = 160\,\mathrm{mA}$ running in the field coil. It is apparent, that increasing the bias current led to a significant reduction of the measured signal height Φ_S, which consequently means that the detector temperature increased with increasing I_b. Also distinctively denoted in the plot are signal heights for the two different bias currents that are relevant for the subsequent discussion, called "high bias" for $I_\mathrm{b} = 35\,\mu\mathrm{A}$, and "low bias" for $I_\mathrm{b} = 7\,\mu\mathrm{A}$ in the subsequent discussion. The latter was basically the lowest possible bias current for which a flux-locked operation could be achieved, which simultaneously is the bias current for which the maximum possible signal height was achieved. The high bias at $I_\mathrm{b} = 35\,\mu\mathrm{A}$ was the optimum working point of the SQUID, as it was already mentioned in the previous section.

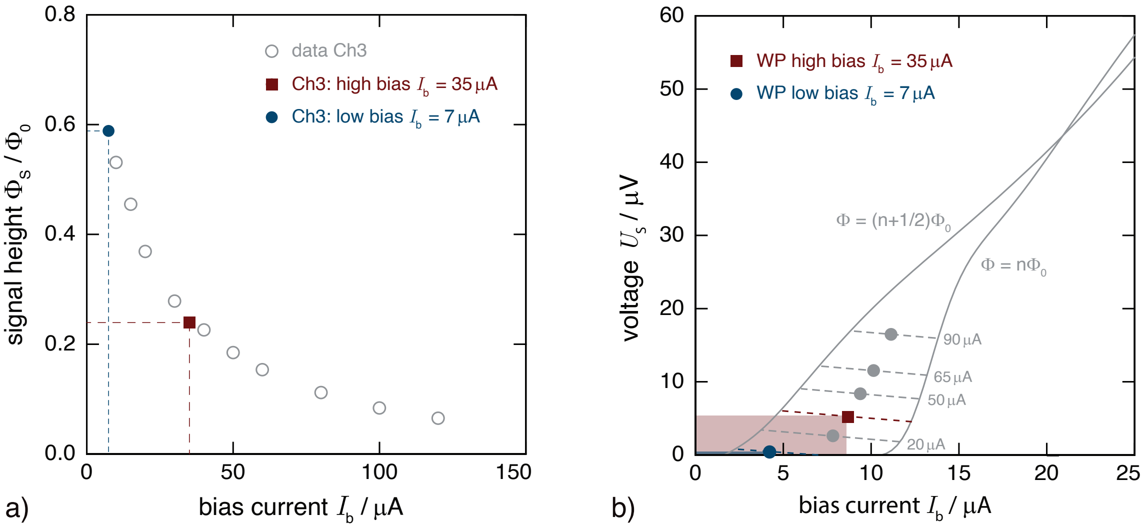

Figure 6.13: a) Measured signal height Φ_S in the SQUID of Ch3 that results from the absorption of 5.9 keV ^{55}Mn K$_\alpha$ photons, measured as a function of the applied bias current I_b b) Measured IV-characteristic of a dc-SQUID of the HDMSQ1 design, as well as the load lines and corresponding working points for this SQUID when operated in a two-stage SQUID setup for a selection of bias currents.

Figure 6.13 b) shows the measured IV-characteristic of a dc-SQUID of the HDMSQ1 design, as well as the load lines and their corresponding working points in a two-stage SQUID setup for a selection of bias currents. The amount of dissipated energy is indicated by the red shaded area for the high bias, and by the blue shaded area for the low bias. The slope of the load lines is given by the gain resistance $-R_\mathrm{g} = 0.2\,\Omega$ in the employed two-stage SQUID setup. For $I_\mathrm{b} = 7\,\mu\mathrm{A}$, the energy dissipation is significantly reduced compared to $I_\mathrm{b} = 35\,\mu\mathrm{A}$, exhibiting an energy dissipation of $P_{7\mu\mathrm{A}} \approx 4\,\mathrm{pW}$ and $P_{35\mu\mathrm{A}} \approx 40\,\mathrm{pW}$, respectively. Furthermore, the full critical current modulation $\Delta I_\mathrm{mod} \approx 7.5\,\mu\mathrm{A}$ is accessible for the high bias, but is reduced for the low bias at $\Delta I_\mathrm{mod} \approx 4\,\mu\mathrm{A}$. No stable flux-locked operation could be achieved for $I_\mathrm{b} < 7\,\mu\mathrm{A}$. It is quite apparent that the on-chip energy dissipation of only a single dc-SQUID already has a significant impact on the performance of the detector. Thus, it is important to investigate whether or not a satisfying multi-channel operation of this 64 pixel detector is possible.

For this, the signal height of Ch3 was measured at a SQUID bias current of $I_\mathrm{b} = 35\,\mu\mathrm{A}$, while this bias current was also sequentially applied to the remaining SQUIDs on the detector chip that were turned off during the determination of the optimum field generating persistent current. Figure 6.14 a) shows the measured signal height Φ_S of Ch3 as a function of the number of biased SQUIDs for two different bias currents. For this measurement, the additionally biased SQUIDs were all chosen from quadrant 1, in which Ch3 is also located. It can be seen, that for a presumedly optimum bias current of $I_\mathrm{b} = 35\,\mu\mathrm{A}$ used for all detector channels, the measured signal height of Ch3 already reduces slightly when one additional SQUID on the chip is biased, and reduces further the more channels are activated. Additionally, SQUIDs from quadrant 2 instead of quadrant 1 were biased in order to investigate a position dependence of the energy dissipation on the measured signal height of Ch3. It was assumed that energy, which is dissipated for instance in a ”far” away Ch14, has a lesser negative impact on the measured signal height of Ch3 than for instance the energy dissipation of its direct neighbor Ch4. However, no position dependence could be observed, indicating that each biased SQUID increases the temperature of the entire detector chip in a similar way.

The measurement was repeated for the low bias of $I_\mathrm{b} = 7\,\mu\mathrm{A}$, which reduces the SQUIDs energy dissipation. This measurement is also shown in figure 6.14 a). Reducing the bias current of Ch3 from $I_\mathrm{b} = 35\,\mu\mathrm{A}$ to $I_\mathrm{b} = 7\,\mu\mathrm{A}$ increased the measured signal height of Ch3 by more than a factor of two. Furthermore, the measured signal height in Ch3 stayed constant when switching on up to four additional SQUIDs, which were also biased at $I_\mathrm{b} = 7\,\mu\mathrm{A}$. Since the aim of the HDMSQ1 detector was to achieve the best possible energy resolution and not the most amount of simultaneously operated detector channels, it was decided to conduct further detector characterizations only on individually operated channels. In addition, the characterization shows that for future designs, the on-chip energy dissipation has to be reduced and the chip thermalization has to be improved in order to allow for a

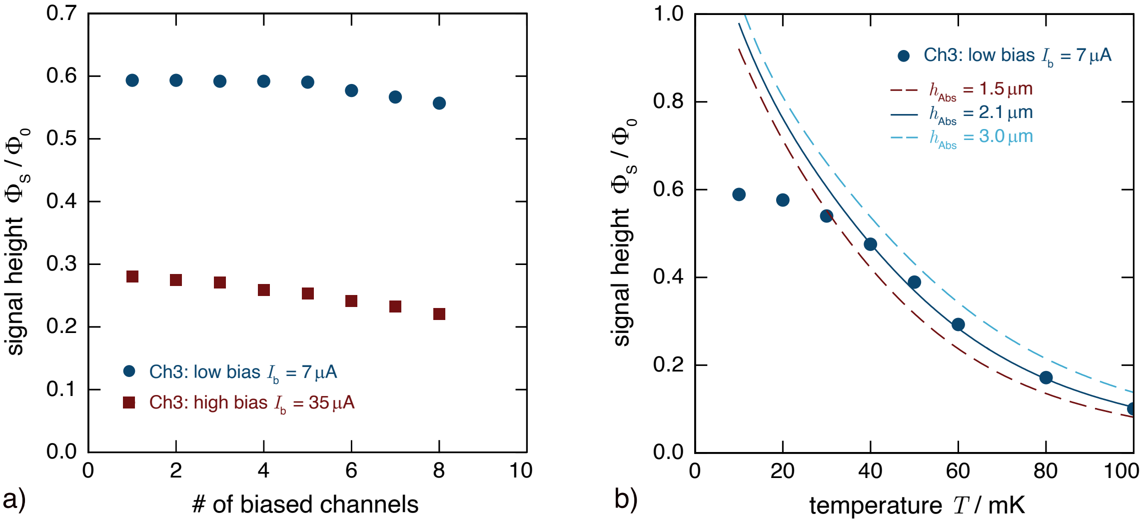

Figure 6.14: a) Signal height Φ_{S} of Ch3 that resulted from the absorption of 5.9 keV ^{55}Mn K$_\alpha$ photons, measured as a function of the number of biased SQUID channels from quadrant 1 for two different bias currents of the SQUIDs. b) Measured signal height Φ_{S} that followed the absorption of an ^{55}Mn K$_\alpha$ X-ray as a function of the mixing chamber temperature T of the cryostat for the bias currents $I_{\mathrm{b}} = 7\,\mu$A. Also shown is the signal height that is expected from numerical simulations for a persistent current $I_0 = 160\,$mA for different thicknesses h_{sens} of the particle absorber.

satisfying multi-channel operation.

Next, the signal height Φ_{S} of Ch3 for a 5.9 keV energy input was investigated as a function of the mixing chamber temperature of the cryostat and compared to the signal height that is expected from numerical simulations for the injected persistent current of $I_0 = 160\,$mA. This is depicted in figure 6.14 b), as well as the calculated signal height for three different absorber heights h_{Abs}. The target absorber height was $h_{\mathrm{Abs}} = 3\,\mu$m. However, the calculated signal height when assuming this absorber height does not describe the measured data. Instead, the data is described for $h_{\mathrm{Abs}} = 2.1\,\mu$m. The actual absorber height can be deduced by comparing the measured line intensity ratio for K_α and K_β photons to the expected line intensity ratio of the two spectral lines. This is plotted in figure 6.15 a function of the absorber height h_{Abs}. The blue dashed line denotes the expected line intensity ratio for the target absorber height of $h_{\mathrm{Abs}} = 3\,\mu$m. The red shaded area denotes the determined line intensity ratio that was measured on different pixels of the HDMSQ1 detector, giving rise to small uncertainties. The plot indicates that the actual absorber height is $h_{\mathrm{Abs}} \approx 2.1\,\mu$m. That h_{Abs} deviates from the target value can be attributed to an improper determination of the total area that is electroplated during the absorber fabrication process, i.e the area of the seedlayer that is not covered by photoresist. In the design, the total absorber area on the entire 3 inch wafer is only $\sim 0.4\,\mathrm{cm}^2$. In addition to that, a parasitic area of also $\sim 0.4\,\mathrm{cm}^2$ is required in order to electrically connect the electroplating setup to the seedlayer (cathode) on the wafer, whereas a part of the parasitic area is then blocked by this electrical connection. How much of the parasitic area is blocked was overestimated for the fabrication of the HDMSQ1 detector, i.e. the actual area that had to be electroplated was larger than the assumed area. Therefore, the target current density of $1\,\mathrm{mA/cm}^2$ of the electroplating procedure was reduced to $\approx 0.7\,\mathrm{mA/cm}^2$, which consequently reduces the Au deposition rate from 1.04 nm/s to 0.73 nm/s, resulting in an absorber height h_{Abs} that is lower than the target value for the same electroplating time of 48 minutes.

In order to deduce the actual operation temperature of the detector, figure 6.15 b) shows again the measured signal Φ_{S} of Ch3 for a 5.9 keV energy input as a function of the mixing chamber temperature T for both bias currents of interest. A detector temperature of $T \approx 3s\,\mathrm{mK}$ can be deduced for the low bias, and $T \approx 65\,\mathrm{mK}$ can be deduced for the high bias, indicating that the detector chip thermally decoupled from the experimental platform at these two temperatures for the respective bias current. Furthermore, the expected erbium concentration of the sputter target $c_{\mathrm{Er}} = 450\,\mathrm{ppm}$ was used for the calculation, as well as an interaction parameter $\alpha = 12.5$ (see section 2.3) as previously found in [Hen17, Sch19].

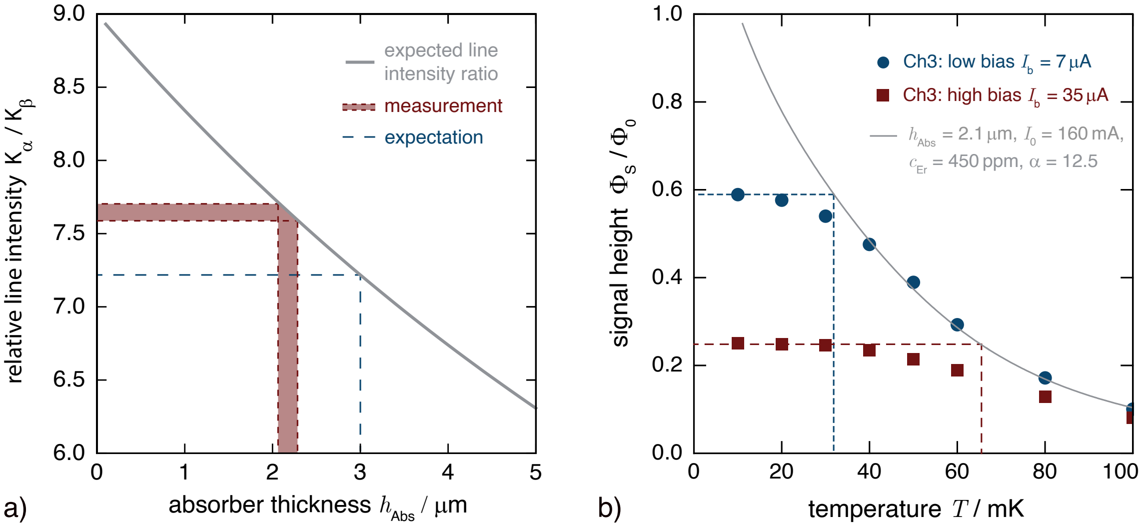

Figure 6.15: a) Expected line intensity ratio of the ^{55}Mn K_α and K_β line as a function of the Au absorber thickness h_{Abs}. The blue dashed line denotes the expected value for the target absorber thickness of $h_{\mathrm{Abs}} = 3\,\mu\mathrm{m}$. The red shaded area denotes the measured value of the line intensity ratio for several channels of the HDMSQ1 detector, indicating that the actualy absorber thickness is only about $2.1\,\mu\mathrm{m}$. b) Measured signal height Φ_{S} that followed the absorption of an ^{55}Mn K_α X-ray as a function of the mixing chamber temperature T for the two discussed bias currents for a persistent current $I_0 = 160\,\mathrm{mA}$.

6.5.4 Signal rise

In order to investigate the signal rise of the HDMSQ1 detector, signals resulting from the absorption of ^{55}Mn K$_\alpha$ photons were acquired using a short time window with a length of a few microseconds with a sampling rate of 500 MS/s (mega samples per second). Ch3 was operated with low SQUID bias, i.e. $I_\mathrm{b} = 7\,\mu$A, and at a persistent current $I_0 = 160\,$mA. Figure 6.16 a) shows the acquired detector signal for various mixing chamber temperatures. Similar to the benchmark measurement discussed in section 2.8, an exponential signal rise time of $\tau_0 \approx 100\,$ns was expected. However, the detector signal shows a linear signal rise and shifts of the time of maximum amplitude. This indicates that the detector has surpassed the maximum slew rate of the readout chain and the fast signal rise could not be resolved.

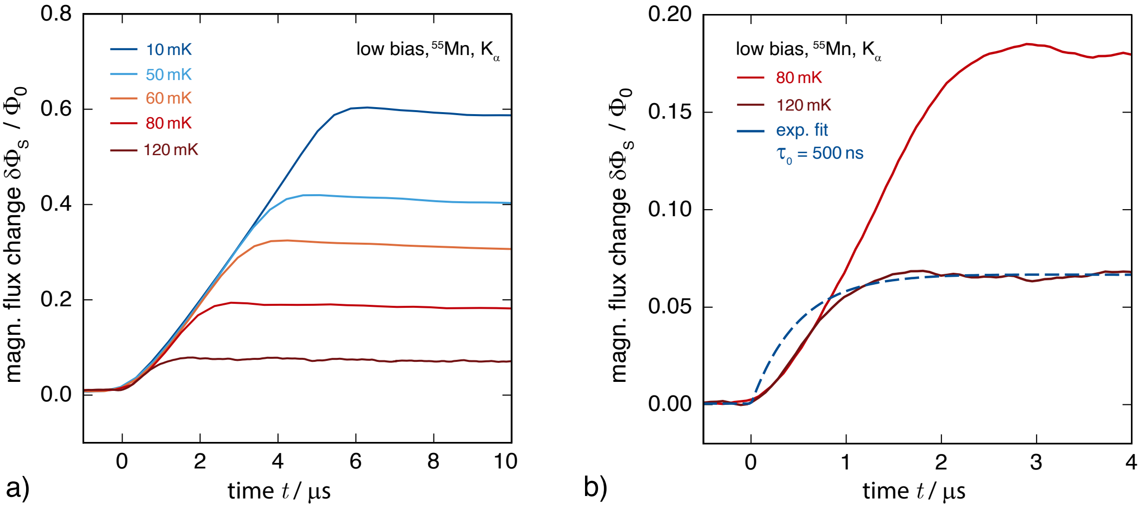

Figure 6.16: Measured flux change $\delta\Phi_\mathrm{S}$ in the SQUID of Ch3 of the HDMSQ1 detector that follows the absorption of an ^{55}Mn K$_\alpha$ X-ray for various mixing chamber temperatures T. Instead of the expected exponential signal rise where each pulse has an identical time constant, a linear signal rise was observed with corresponding temporal shifts of the time of maximum amplitude. b) Magnified plot of the two smallest depicted pulses. Even the signal rise with an amplitude of only $0.07\,\Phi_0$ did not follow an exponential rise. The blue dashed curve illustrates an exponential signal rise with a time constant of $\tau_0 = 500\,$ns.

In order to estimate the maximum slew rate of the experimental setup, the smallest recorded pulses were further investigated. Figure 6.16 b) shows a magnified view of the two smallest depicted pulses. As it can be seen, even the signal rise of the smallest pulse measured at $T = 120\,$mK with an amplitude of only $0.07\,\Phi_0$ does not follow an exponential law. To illustrate this, a curve of the form given by equation 2.30 with a time constant of $\tau_0 = 500\,$ns is also plotted in figure 6.16 b), clearly indicating that the measured signal rise does not show an exponential behavior. Therefore, the maximum slew rate of the readout chain can be approximated to be a very small

$\dot{\Phi}_{\mathrm{fb}}^{\mathrm{max}} < 70\,\mathrm{m}\Phi_0/\mu\mathrm{s}$. As the SQUID is operated in the low bias regime far from its optimum working point, its linear voltage response to external flux $\Delta\Phi_{\mathrm{lin}}$ is reduced and its full critical current modulation ΔI_{mod} is not accessible, which results in a degraded maximum slew rate of the signal readout (see section 3.3.3). However, when operating the SQUID in the high bias at its optimum working point, where the SQUID gain is increased and the signal amplitude is reduced, the signal rise could also not be resolved.

A similar result, but on a smaller magnitude, was also observed in [Sch12] for the maXs-20 detector when it was operated in a different cryostat compared to the cryostat in which its benchmark signal rise was measured. There, the signal rise with an experimentally verified intrinsic time constant of $\tau_0 = 80\,\mathrm{ns}$ and an amplitude of $\Phi_{\mathrm{S}} \approx 0.3\,\Phi_0$ could not be resolved, even with an optimally tuned front end SQUID, albeit the latter being a different SQUID design compared to the one in this thesis. The measured linear signal rise in [Sch12] required $1\,\mu\mathrm{s}$ to reach its maximum amplitude. When compared to the orange signal at $T = 60\,\mathrm{mK}$ in figure 6.16 a) that also has an amplitude of $\approx 0.3\,\Phi_0$, then the measured rise time that is required to reach its maximum amplitude is a factor of ~ 3.5 higher for the employed experimental setup in this thesis. As it was already mentioned in section 3.3.3, that a time delay t_{d} occurs between the signal input in the SQUID and the corresponding feedback response of the flux-locked circuit. When the transmission lines between the front end SQUID and the N-SQUID series array amplifier, or the transmission lines between N-SQUID series array amplifier and room temperature electronics are rather long, then this time delay t_{d} becomes the limiting factor for the achievable maximum slew rate $\dot{\Phi}_{\mathrm{fb}}^{\mathrm{max}}$ of the readout chain. It can then be approximated by [Cla04]

$$\dot{\Phi}_{\mathrm{fb}}^{\mathrm{max}} = \frac{\Delta\Phi_{\mathrm{lin}}}{4t_{\mathrm{d}}}\,. \tag{6.4}$$

It was argued in [Sch12] that the slew rate limit was reached due to the large wiring length of 30 cm between the employed front end SQUID and N-SQUID series array amplifier. As it was illustrated in section 4.1.2, the employed wiring in this thesis has a length of 40 cm between the developed front end SQUID and the corresponding N-SQUID series array amplifier modules, whereas an additional 15 cm can be added to that due to the wiring on the corresponding circuit boards. Since the wiring at millikelvin temperatures is nearly a factor of two longer than in [Sch12], it is apparent why the maximum slew rate in the here presented results is even lower.

Enhancing the maximum slew rate of the system would require a reduction of the wire length, which can only be done in a different, smaller cryostat, as the currently installed wiring length is determined by the size of the cryogenic system. Thus, in order to make the signal rise fully resolvable with the employed readout chain, the signal rise has to be slowed down to several microseconds, as will be further discussed for the HDMSQ2A detector in the next chapter.

6.5.5 Detector noise

Figure 6.17 a) shows the white noise level $\sqrt{S_{\Phi,\mathrm{w}}}$ determined at a frequency $f = 100\,\mathrm{kHz}$ of the apparent flux noise $\sqrt{S_\Phi}$ in the dc-SQUID as a function of the SQUID bias current I_b. It is obvious that the white noise level significantly depends on the SQUID bias current and that the minimum noise is achieved for $I_\mathrm{b} = 35\,\mu\mathrm{A}$, making clear why this value was initially used for the characterization measurements that were discussed in the previous sections. Figure 6.17 a) also shows, that the white noise level for the low bias at $I_\mathrm{b} = 7\,\mu\mathrm{A}$ is a factor of 2.3 higher than $\sqrt{S_{\Phi,\mathrm{w}}}$ for the high bias. However, the signal height Φ_S is a factor of ~ 2.4 larger in the low bias (see section 6.5.3), giving rise to the expectation that the optimal working point of the detector is given by $I_\mathrm{b} = 7\,\mu\mathrm{A}$, since the noise penalty is overcompensated by the gain in signal height. For this reason, it is expected that HDMSQ1 will perform best at the lowest possible bias current.

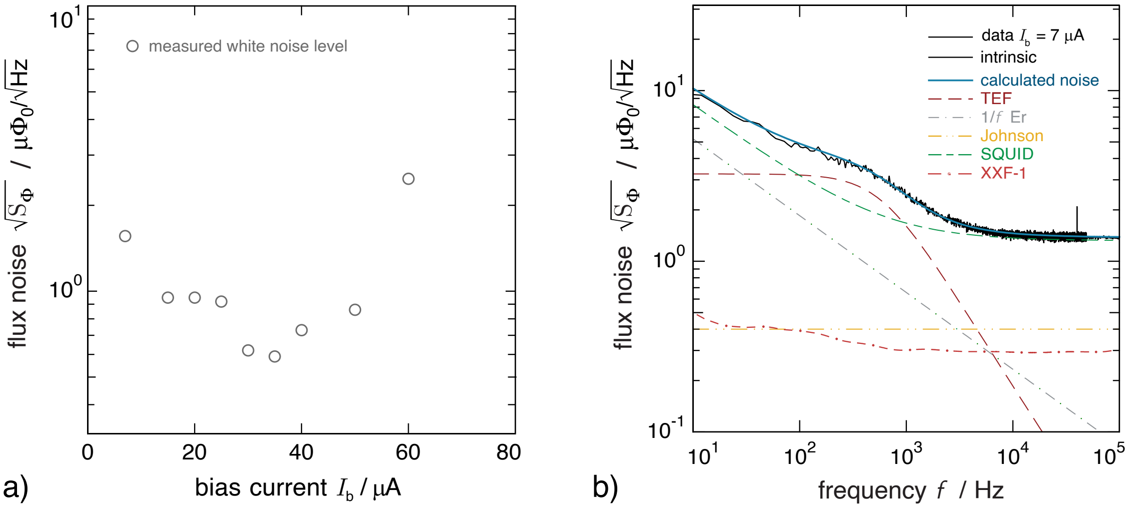

Figure 6.17: a) Measured white noise level $\sqrt{S_{\Phi,\mathrm{w}}}$ at $f = 100\,\mathrm{kHz}$ of the detector SQUID in the two-stage SQUID setup as a function of the applied bias current I_b at a mixing chamber temperature of $T \approx 7\,\mathrm{mK}$. It becomes apparent, that $\sqrt{S_{\Phi,\mathrm{w}}}$ significantly depends on the chosen I_b. b) Measured flux noise $\sqrt{S_\Phi}$ for the low bias operation. Also shown are the corresponding calculated noise contributions. The curve denoted as ”XXF-1” denotes the noise contribution of the room temperature electronics, which is negligible for the operation of the HDMSQ1 detector when operated at a low bias current.

Figure 6.17 b) shows the measured spectral density of the apparent flux noise $\sqrt{S_\Phi}$ of Ch3 for the low SQUID bias of $I_\mathrm{b} = 7\,\mu\mathrm{A}$. Furthermore, the respective calculated noise contributions that were discussed in section 2.6.3 are shown, for which the determined absorber height of $h_{\mathrm{Abs}} = 2.1\,\mu\mathrm{m}$ was used. In order to account for the degraded noise performance due to the non-optimal working point of the SQUID and match the data, a white noise level of $\sqrt{S_{\Phi,\mathrm{w}}} = 1.32\,\mu\Phi_0/\sqrt{\mathrm{Hz}}$ was added in the calculation compared to the simulation parameters of the detector that are summarized in appendix table A.1. The calculated spectral density of the apparent flux noise is in excellent agreement with the measured data, verifying the predictability of the thermodynamic properties of the MMC, as well as the SQUID based detector readout. In addition, a curve denoted as "intrinsic" is shown, which is coincident with the measured apparent flux noise, hence the same color identification was used. For this curve, the noise contribution of the room temperature electronics was subtracted. The latter is denoted as "XXF-1" in figure 6.17 b). For this calculation, the flux-to-voltage transfer coefficient $V_{\Phi,\mathrm{N}} \approx 1400\,\mu\mathrm{V}/\Phi_0$ of the 16-SQUID series array was used (see section 3.3.4). This shows, that the noise contribution of the room temperature electronics is negligible for the low bias operation of the HDMSQ1 detector in the employed two-stage SQUID setup.

6.5.6 Energy resolution

The discussion of the signal height Φ_{S} and of the apparent flux noise $\sqrt{S_\Phi}$ indicated, that the best energy resolution of the detector is achieved with low SQUID bias at $I_{\mathrm{b}} = 7\,\mu\mathrm{A}$, where the detector reaches its maximum signal amplitude for absorbed photons with given energy E. Furthermore, a persistent current of $I_0 = 160\,\mathrm{mA}$ was injected and the temperature of the mixing chamber platform was actively stabilized at $T = 10\,\mathrm{mK}$ (see section 4.1.3). But before the achieved energy resolution can be discussed, it is important to understand how the acquired data of the measured spectrum was corrected for temperature drifts of the cryogenic setup. In section 6.1.2 it was discussed, that when one of the two temperature sensors is omitted by design, or when the two temperature sensors are of different size, this detector becomes sensitive to temperature fluctuations of the cryogenic setup. As a result, its baseline voltage output changes with the operation temperature. Every time a photon was detected in Ch3, a baseline noise trace of the non-gradiometric Ch5 was automatically acquired and averaged. When the detector response of Ch3 is saved, the average value of the corresponding baseline of Ch5 is assigned to the data of Ch3 and also saved accordingly, providing a relative temperature information. Figure 6.18 a) shows the measured relative signal amplitude of the K_α-line of the ^{55}Fe X-ray calibration source of Ch3 as a function of the temperature information that was acquired with the non-gradiometric Ch5, given in arbitrary units. The amplitudes were determined from the acquired detector responses with the χ^2-fit signal analysis method (see section 4.3). The determined signal amplitude reduces for an increased temperature, as one would expect. The relative signal amplitude can be corrected

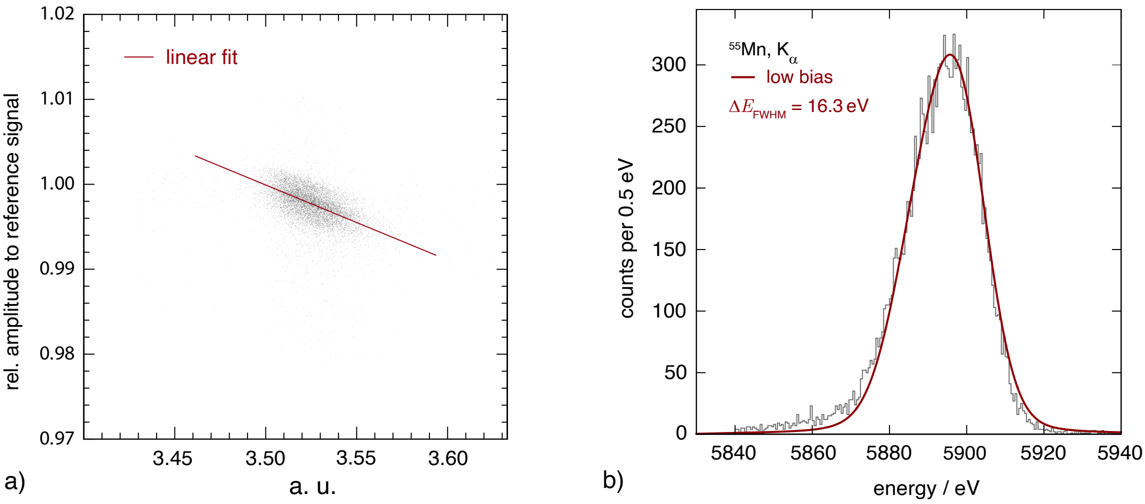

Figure 6.18: a) Measured relative signal amplitude of Ch3 of the K_α-line of the ^{55}Fe X-ray calibration source as a function of the corresponding temperature information that were acquired with the non-gradiometric Ch5, given in arbitraty units. b) Measured energy spectrum of the K_α-line of a ^{55}Mn X-ray source without any corrections for temperature fluctuations. Superimposed to the data is a convolution of the natural linewidth of the K_α-line and a Gaussian distribution with an instrumental energy resolution of $\Delta E_\mathrm{FWHM} = 16.3\,\mathrm{eV}$. The measurement was performed at a SQUID bias current of $I_\mathrm{b} = 7\,\mu\mathrm{A}$, a persistent current of $I_0 = 160\,\mathrm{mA}$, and a mixing chamber temperature of $T = 10\,\mathrm{mK}$.

for temperature fluctuations simply by dividing the data by a linear fit. This is only possible for small temperature fluctuations where the detector exhibits a linear behavior.

In order to illustrate how important the acquisition of the temperature information is, figure 6.18 b) shows the measured energy spectrum of the K_α-line of the ^{55}Fe X-ray calibration source without any correction for temperature drifts. Fitted to the data is a convolution of the natural linewidth of the K_α-line and a Gaussian distribution with an instrumental energy resolution of $\Delta E_\mathrm{FWHM} = 16.3\,\mathrm{eV}$. Figure 6.19 a) shows the same energy spectrum, but corrected for temperature fluctuations as it was shown in figure 6.18 a). Fitted to the data is a convolution of the natural linewidth of the K_α-line and a Gaussian distribution with an instrumental energy resolution of $\Delta E_\mathrm{FWHM} = 8.9\,\mathrm{eV}$. Therefore, correcting the determined signal amplitudes for temperature drifts improved the energy resolution of the HDMSQ1 detector by a factor of 1.8 for the chosen operation regime.

In order to determine the baseline energy resolution of the detector, the χ^2-fit signal analysis method was applied to untriggered noise traces (baselines) of Ch3 that were acquired during the measurement. The histogram resulting from this calculation is plotted in figure 6.19 a). A Gaussian distribution with an instrumental linewidth of

$\Delta E_{\mathrm{FWHM}} = 4.2\,\mathrm{eV}$ is fitted to the data, indicating the intrinsic energy resolution of the detector in this operation regime.

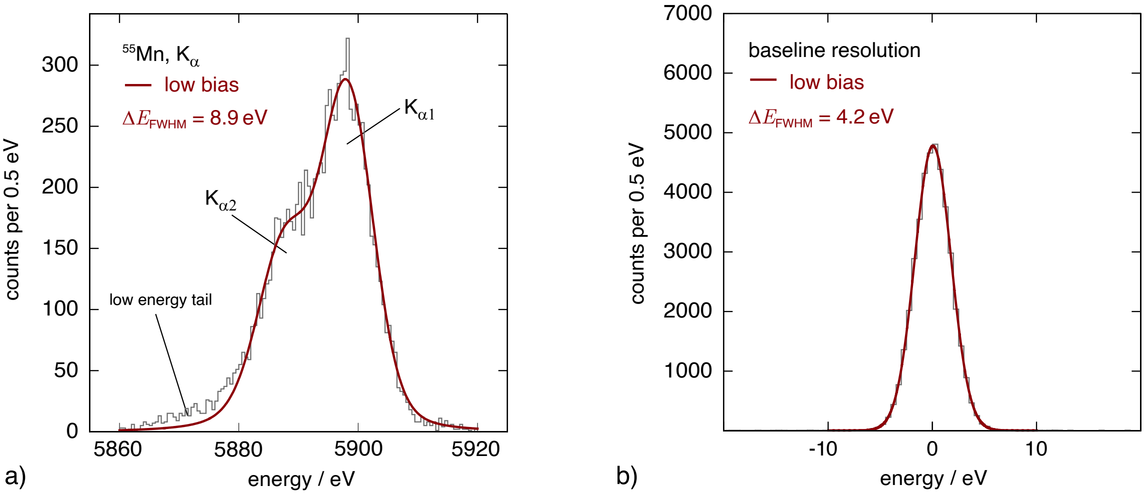

Figure 6.19: a) Measured energy spectrum of the K$_\alpha$-line of a ^{55}Mn X-ray source. Superimposed to the data is a convolution of the natural linewidth of the K$_\alpha$-line and a Gaussian distribution with an instrumental energy resolution of $\Delta E_{\mathrm{FWHM}} = 8.9\,\mathrm{eV}$. b) Histogram of the measured amplitudes of untriggered noise traces to which the χ^2-fit signal analysis method was applied. Superimposed is a Gaussian distribution with a full width at half maximum value of $\Delta E_{\mathrm{FWHM}} = 4.2\,\mathrm{eV}$, indicating the intrinsic resolution of the HDMSQ1 detector. The measurement was performed at a SQUID bias current of $I_{\mathrm{b}} = 7\,\mu\mathrm{A}$, a persistent current of $I_0 = 160\,\mathrm{mA}$, and a mixing chamber temperature of $T = 10\,\mathrm{mK}$.

The calculated energy resolution of the HDMSQ1 detector in the chosen operation regime is $\Delta E_{\mathrm{FWHM}} \approx 3.2\,\mathrm{eV}$. This calculation factored in the higher than expected operation temperature of $T \approx 32\,\mathrm{mK}$, the reduced absorber height of $h_{\mathrm{Abs}} = 2.1\,\mu\mathrm{m}$, the non-optimum persistent current of $I_0 = 160\,\mathrm{mA}$, and the degraded noise performance due to the SQUID being operated at a non-optimal working point. Therefore, the experimentally determined baseline resolution of the detector is degraded by a factor of 1.3 compared to its expected energy resolution. This can be attributed to the used χ^2-fit signal analysis method, as it was discussed in section 4.3, where simulations performed in [Bug14] of a detector of comparable performance showed, that a degradation of the determined energy resolution of up to a factor of 2 can occur compared to a signal analysis method based on optimal filtering.

That the determined energy resolution at 5.9 keV is further degraded compared to the baseline resolution can be attributed to three additional main factors, aside from the algorithm used for signal analysis. One reason for a degraded energy resolution is the loss of athermal phonons, indicated by the distinct low energy tail in figure 6.19 a). When an X-ray is absorbed at the location of the post that links the absorber and sensor, thereby created athermal phonons can potentially traverse the sensor into the substrate without depositing their energy in the sensor, as it was discussed in section 2.3.1, leading to the observed low energy tail. Another factor that degrades the energy resolution is the surpassed slew rate limit of the readout chain, which results in the measured maximum signal amplitude to not only vary in its amplitude due to noise and temperature fluctuations, but also to vary in time. The used signal analysis method assumes, that the point of maximum signal amplitude occurs at the same time after photon absorption for every detector response, independent of the energy input. This no longer holds when the slew rate limit is surpassed, as it was illustrated in section 6.5.4. As a result, K_α signals that have a slightly smaller amplitude than the reference signal of the χ^2-fit signal analysis method reach their maximum amplitude earlier than K_α signals that have a slightly larger amplitude. Thus, additional uncertainties are introduced when the algorithm tries to determine the signal amplitude via least squares fitting.

A third, and maybe the most important factor that degrades the energy resolution of the detector at 5.9 keV, are temperature fluctuations of the cryogenic setup, as well as temperature fluctuation due to photons hitting the detector substrate, as no collimator was used during the measurement. While the determined signal amplitudes were corrected for temperature fluctuations, this correction can not account for all occurring thermal effects. Acquiring temperature information with the non-gradiometric Ch5 can not account for instance for localized thermal effects of the Ch3, i.e. a potential temperature gradient on the detector chip, or photons hitting the substrate. To reduce these uncertainties, a microfabricated collimator is introduced to the experimental setup for the next detector, so that incident X-rays can only hit the particle absorbers.

6.5.7 Summary

This chapter showed, that a fully operational dc-SQUID for a direct sensor readout of a metallic magnetic calorimeter was successfully developed, fabricated and optimized. With this SQUID design, a 64 pixel two dimensional detector array for soft X-ray spectroscopy consisting of 32 metallic magnetic calorimeters was fabricated. Its characterization at millikelvin temperatures in a ^{3}He/^{4}He dilution refrigerator made several design issues apparent. Observed was a significantly increased detector temperature compared to the cryostats temperature in the lower millikelvin regime as a result of on-chip energy dissipation of the dc-SQUIDs. The detector could only reach temperatures down to $T \sim 32\,\mathrm{mK}$ for the lowest possible SQUID bias current that still allowed for a stable flux-locked loop operation. Furthermore, it could be shown that the simultaneous operation of multiple channels led to an additional increase in chip temperature, making an operation of a many-pixel array for the high resolution X-ray spectroscopy unlikely with the developed design, as there are already MMCs with an enhanced performance readily available. In addition, an expectation that was met were very large signals with a fast intrinsic rise time. As a result, the slew rate limit of the readout chain was reached. While this led to a further degradation of the detector energy resolution, it also demonstrated the significantly enhanced signal coupling between temperature sensor and SQUID of the direct sensor readout compared to the transformer coupled readout. The HDMSQ1 detector, which was not fully optimized according to numerical simulations due to its initially unknown operation temperature, reached a signal height of $\sim 0.6\,\Phi_0$ for $5.9\,\mathrm{keV}$ photons at an operation temperature of $T \sim 32\,\mathrm{mK}$. In comparison, the revised version of the maXs-20 detector that was briefly discussed in section 2.8, and which holds the demonstrated MMC benchmark in terms of energy resolution for $5.9\,\mathrm{keV}$ photons, achieved a signal height of $\sim 0.55\,\Phi_0$ for $5.9\,\mathrm{keV}$ photons during its benchmark measurement, but at a much lower operation temperature of $T \sim 12\,\mathrm{mK}$. Other design issues that will be addressed are a significant loss of athermal phonons that was observed in the measured energy spectrum of the ^{55}Mn K_α-line due to the comparably large contact area between absorber and temperature sensor. The detectors appointed aim of achieving a new benchmark energy resolution could not be achieved, while the main obstacles as to why it could not were successfully identified. In conclusion, the HDMSQ1 detector is a rather successful proof of principle for the direct sensor readout of a metallic magnetic calorimeter, whose performance was in excellent agreement with the theoretical model, but its performance in terms of energy resolution remains well below its designated aims. The challenges for a high performance operation that were identified in this chapter will be addressed by the HDMSQ2A detector, which is the topic of discussion in the next chapter.

7. The HDMSQ2A detector

The HDMSQ2A detector is the successor of the HDMSQ1 detector and addresses the main factors limiting its achievable energy resolution. In particular, the on-chip energy dissipation had to be reduced, the signal rise time constant τ_0 needed to be increased, the loss of athermal phonons should be minimized, and a potential thermal cross talk between neighboring detectors due to a shared on-chip heat bath should be prevented. This chapter first discusses how these limiting factors were addressed. Afterwards, the detector and chip design of the HDMSQ2A detector will be illustrated, followed by a presentation of its characterization results. The chapter concludes with a summary and outlook towards the HDMSQ2B detector, which is mostly identical to the HDSMQ2A detector, but explores a different customized thermalization scheme for the shunt resistors of the dc-SQUID.

7.1 From HDMSQ1 to HDMSQ2A: Design enhancements

7.1.1 Reduction of the on-chip energy dissipation

The energy dissipation of a dc-SQUID when operated in a two-stage setup was discussed in section 3.3.5. In this configuration, a reduction of the energy dissipation can be achieved in two ways. The first is a reduction of its critical current, and the second is a reduction of its shunt resistance R_S. A reduction of the critical current I_c of the Josephson tunnel junctions also reduces the critical current modulation ΔI_mod for a fixed SQUID inductance L_S, and potentially also has an impact on the occurrence of internal resonances, as was discussed in section 3.3.1. Therefore, this option might require additional optimization steps for the design. Hence, it was decided to only reduce the shunt resistance R_S of the SQUID in the HDMSQ2A detector. Just like for the gain resistor R_g, the shunt resistors can not be made arbitrarily small, as their current noise otherwise becomes a dominating noise source even at millikelvin temperatures. Furthermore, reducing R_S should only be done when the SQUID is operated as a first-stage SQUID in a two-stage setup when it is operated in the voltage bias. Reducing R_S has no impact on the critical current modulation ΔI_mod, hence the operation in the voltage bias is not impacted. For the single stage readout in the current bias, reducing R_S consequently reduces the flux-to-voltage transfer coefficient V_Φ, degrading its performance.

In order to investigate the feasibility of the operation of a SQUID with a reduced shunt resistance R_S, prototypes without temperature sensors and particle absorbers

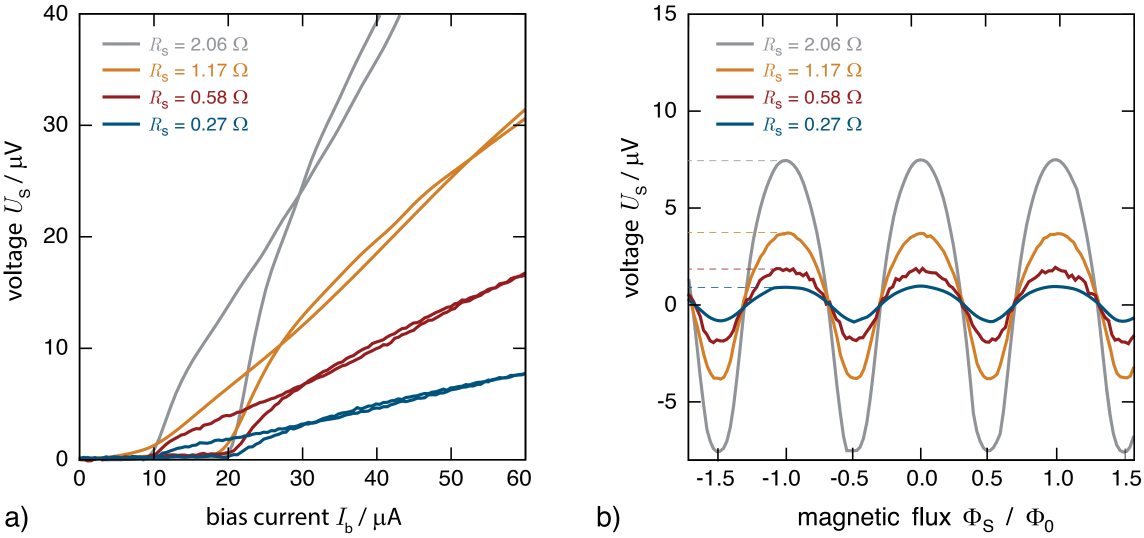

Figure 7.1: a) Measured IV-characteristics and b) $V\Phi$-characteristics of the developed dc-SQUID for various values of the shunt resistance R_S. As expected, the voltage response of the SQUID reduces with decreasing R_S without changing its critical current modulation ΔI_mod.

were fabricated. A shunt resistance of $R_\mathrm{S} = 5\,\Omega$ was used for HDMSQ1, whereas the prototypes were equipped with shunt resistances R_S of $\sim 2\,\Omega$, $\sim 1.25\,\Omega$, $\sim 0.6\,\Omega$ and $\sim 0.3\,\Omega$. After fabrication, the SQUIDs were characterized at $T = 4.2\,\mathrm{K}$ in a single-stage setup. The corresponding IV-characteristics are shown in figure 7.1 a), whereas the corresponding $V\Phi$-characteristics are show figure 7.1 b). As expected, the voltage response of the SQUIDs got reduced with decreasing R_S, whereas the critical current modulation ΔI_mod was not effected. The depicted values of the respective shunt resistances were derived from the ohmic regime of the IV-characteristic at higher bias currents. After the additional verification of the proper SQUID operation in a two-stage setup at $T = 4.2\,\mathrm{K}$, the smallest shunt resistance $R_\mathrm{S} = 0.27\,\Omega$ was chosen for the final design of the HDMSQ2A detector.

7.1.2 Minimizing loss of athermal phonons

A reduction of athermal phonon loss can be achieved in two ways. One option would be a reduction of the contact area between the particle absorber and sensor, which requires a reduction of the diameter of the post. However, this option was already excluded during the development of the HDMSQ1 detector (see section 6.1.2). The second option would be a prevention of a direct line of sight traversal for athermal phonons from the absorber into the substrate. This option was chosen for the HDMSQ2A detector and the actual implementation of this option is illustrated in figure 7.2, depicting schematics of the absorber geometries of HDMSQ1 and HDMSQ2A. The latter is an enhanced geometry consisting of the already developed HDMSQ1 absorber with a single post, now situated on top of an additional four-legged bridge, a so called tetrapod. Depicted as red lines are exemplary athermal phonon pathways following after photon absorption. For a traversal of athermal phonons through the absorber, their direct line of sight to the temperature sensor is significantly reduced in the geometry of HDMSQ2A absorber, consequently reducing the possibility of a phonon transitioning out of the gold structure before thermalizing with its conduction electrons. Furthermore, the direct line of sight travel distance for athermal phonons into the substrate was increased by nearly a factor of 10, from $\sim 3\,\mu$m to $\sim 27\,\mu$m, which consequently provides a larger interaction length for phonons to thermalize with the conduction electrons in the absorber.

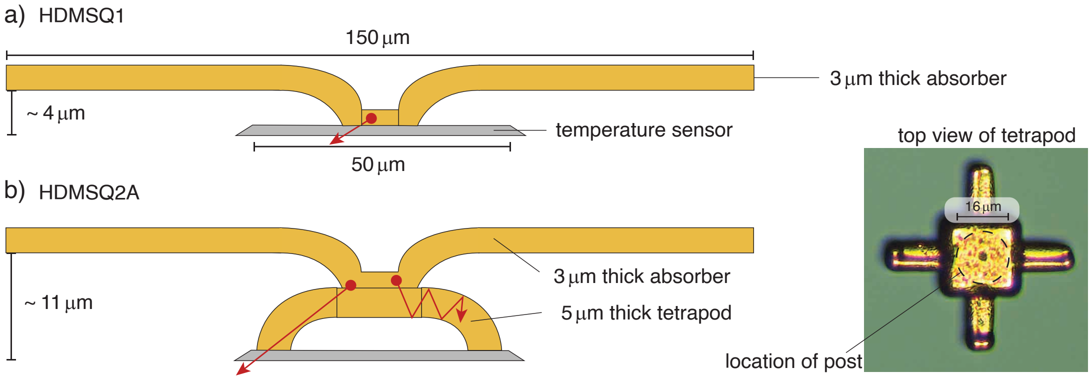

Figure 7.2: Schematic of the absorber geometry of a) the HDMSQ1 detector and b) the HDMSQ2A detector. In the latter, the absorber with a single post is positioned on top of an additional four-legged bridge, a so called tetrapod. Also shown is a microscope photograph of a tetrapod after fabrication.

The fabrication of this enhanced absorber geometry was done by applying the two-layer photoresist process that was described in section 5.4.2 for two consecutive times. First, the tetrapod was electroplated with an Au thickness of $5\,\mu$m, followed by a removal of the photoresist and seedlayer in an appropriate solvent and a weak ultrasonic cleaning. In the second application of this process, the absorbers were fabricated. For this, the first photoresist layer that is used to structure the single post has to be thick enough in order to completely cover the tetrapod, which has a total height of $\sim 8\,\mu$m, as well as provide a sufficient layer thickness so that the rounded post on top of the tetrapod has a height of 2 - $3\,\mu$m. Therefore, instead of the AZ 4533 photoresist, the AZ 4562 photoresist was used for structuring the posts, which is chemically identical, but allows for higher resist thickness due to a reduced solvent content. The AZ 4562 was spin coated at 1000 rpm for 30 s, followed by a softbake at $T = 100°$C for 5 minutes on a hotplate, yielding a resist thickness between $\sim 10\,\mu$m and $\sim 11\,\mu$m. The subsequent absorber fabrication was identical to what was already discussed in section 5.4.2. The addition of the tetrapod increases the absorber heat capacity by $\sim 5\,\%$, which has therefore only a small negative impact on the intrinsic energy resolution of the detector according to equation 2.26.

7.1.3 Slow down of signal rise

The signal rise time of a metallic magnetic calorimeter can be increased by introducing a thermal bottleneck between absorber and sensor, which slows down the heat flow between the two constituents. Figure 7.3 shows a schematic of how such a thermal bottleneck was introduced into the design of the HDMSQ2A detector. Depicted is a temperature sensor with its corresponding particle absorber placed next to it onto the substrate, instead of on top of the sensor. They are connected to each other by a thermal link made of sputtered Au. The thermal conductance is dominated by the system of the conduction electrons, as the electron-phonon coupling is very weak at such low operation temperatures, and the Kapitza resistance prevents a traversal of phonons into the substrate in the time frame of relevance, i.e. a few microseconds. Thus, the absorbed energy is transmitted to the temperature sensor without any energy being lost to the substrate. The thermal conductivity G between the two constituents can be calculated via the Wiedemann-Franz law

$$G = \frac{\mathcal{L}T}{\rho_{\mathrm{Au}}} \cdot \frac{A}{l}\,, \tag{7.1}$$

where $\mathcal{L} = 2.44 \cdot 10^{-8}\,\mathrm{W\Omega K^{-2}}$ is the Lorenz number, A is the cross section area of the sputtered thermal link, and l is the length of this link. The electrical resistivity of the thermal link is $\rho_{\mathrm{Au}} = \rho_{\mathrm{Au}}^{300\,\mathrm{K}}/(RRR-1) = 1.83 \cdot 10^{-8}\,\Omega\mathrm{m}$, with a $RRR = 2.2$ for sputtered Au. The signal rise time can then be calculated by

$$\tau_0 = \frac{C_{\mathrm{abs}}C_{\mathrm{sens}}}{G(C_{\mathrm{abs}} + C_{\mathrm{sens}})}\,. \tag{7.2}$$

Using numerical simulations to calculate the sensor heat capacity C_{sens} at an assumed operation temperature of $T = 20\,\mathrm{mK}$, different thermal links were added to individual detector channels in the HDMSQ2A design. Since the achievable operation temperature of the HDSMQ2 detector, and corresponding to that its achievable signal height, as well as the maximum slew rate of the readout chain, could only be estimated based on the results of the HDMSQ1 detector, it was decided to cover a wide range of possible signal rise times. The fastest detector channels on the HDMSQ2A detector chip received a thermal link between absorber and sensor with a target signal rise time of $\tau_0 = 2\,\mu\mathrm{s}$. The remaining detector channels have a target signal rise time between $\tau_0 = 10\,\mu\mathrm{s}$ and $\tau_0 = 40\,\mu\mathrm{s}$, increasing in $5\,\mu\mathrm{s}$ steps. The rise times were adjusted accordingly by changing the length or width of the sputtered thermal link.

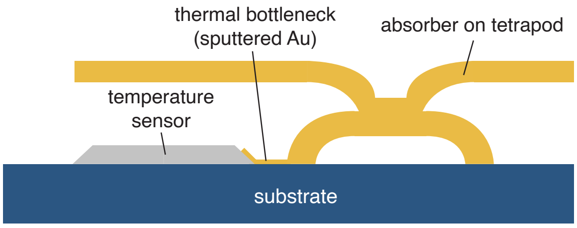

Figure 7.3: Schematic of the HDMSQ2A absorber and sensor geometry. Both constituents are connected to each other via a thermal bottleneck made of sputtered Au in order to slow down the signal rise of the detector.

7.2 Detector design

7.2.1 Single detector of HDMSQ2A

Figure 7.4 shows a microscope photograph of an individual integrated detector on a fabricated HDMSQ2A detector chip. The absorbers were deliberately removed for visibility. Since the overall design is very similar to the HDMSQ1 detector, only the design enhancements are discussed here.

The shunt resistors now have length of only 0.25 □, reducing their resistance from $R_\mathrm{S} = 5\,\Omega$ to $R_\mathrm{S} \approx 0.3\,\Omega$. In addition, its distance to the temperature sensor was doubled to $\approx 35\mu$m, which allowed to connect a cooling fin to both sides of the resistor. The total cooling fin area was increased by a factor of ~ 10. At the time of detector fabrication, the Ag:Er target in the UHV sputtering setup had a concentration of $c_\mathrm{Er} = 260\,$ppm. Assuming this Er concentration, new numerical simulations for the optimum sensor sensor height at an operation temperature of $T = 20\,$mK were performed, as the available sensor area was kept the same. As a result, h_sens was reduced from $1.2\,\mu$m to $0.8\,\mu$m. It is worth mentioning, that slight deviations from the parameters do not lead to a significant degradation of the energy resolution, as the dependency of ΔE_FWHM on c_Er and h_sens exhibits a rather flat behavior for deviations of up to 20 %. Figure 7.4 also shows the sputtered thermal link between sensor and absorber, which is structured in the same layer as the thermal link between sensor and on-chip thermal bath. The thickness of this Au layer was increased from 200 nm to 400 nm in order to guarantee a sufficient edge coverage of the $\approx 300\,$nm high steps at the location where these thermal links have to cross over the Nb1 layer in the design. Furthermore, the stripe width of the meander-shaped SQUID loop was increased from $w_1 = 4\,\mu$m to $w_1 = 5\,\mu$m, which provides a small increase in signal coupling between temperature sensor and SQUID according to numerical simulations. That this stripe width was not initially chosen for HDMSQ1 detector was to allow for a higher margin of error in the alignment process of the employed UV-laser writer (see appendix A.1.2), as the pickup coil must be placed directly on top of the field generating coil. Increasing the stripe width from $4\,\mu$m to $5\,\mu$m reduces the allowed margin of error from $1\,\mu$m to $0.5\,\mu$m, the latter being the lower accuracy limit for mask alignment of the UV-laser writer, since the field generating coil has a stripe width of 6 μm. In order to yield of reliable fabrication of HDMSQ1, which was the first prototype in this thesis, a stripe width of 4 μm was chosen. This small design enhancement did not lead to any changes in the measured SQUID characteristics, so that no additional design optimizations were required.

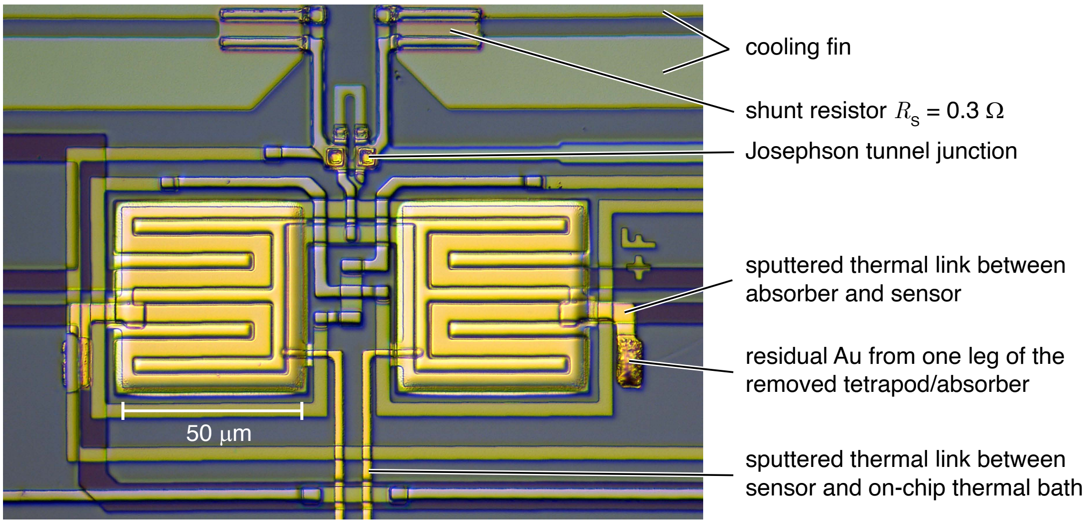

Figure 7.4: Microscope photograph of a fabricated HDMSQ2A detector. The absorbers were removed for visibility. The design changes compared to HDMSQ1 detector are explained in the text.

Lastly, the length of the weak thermal link between temperature sensor and on-chip thermal bath was significantly increased, slowing down the signal decay to a target $\tau_1 = 5\,\mathrm{ms}$ at an assumed operation temperature of $T = 20\,\mathrm{mK}$, which improves the intrinsic energy resolution of the detector according to equation 2.27. The signal decay time can be calculated with equation 6.3. In order to calculate the required length of the weak thermal link to achieve a signal decay time of $\tau_1 = 5\,\mathrm{ms}$, the following parameters were assumed: An operation temperature of $T = 20\,\mathrm{mK}$, a matching absorber and sensor heat capacity at this temperature so that $C_{\mathrm{tot}} = 0.2\,\mathrm{pJ/K}$, a literature value for the electrical conductivity of $\rho_{\mathrm{Au}} = 2.2 \cdot 10^{-8}\,\Omega\mathrm{m}$, a measured $RRR = 2.2$, a width of the weak thermal link of $w_{\mathrm{tl}} = 3\,\mu\mathrm{m}$ and a layer thickness of $t_{\mathrm{Au}} = 400\,\mathrm{nm}$. The thereby calculated length of the weak thermal link is 820 μm, which is more than five times the edge length of one particle absorber. In order to incorporate such a long thermal link into the design, the entire chip layout was changed, as will be discussed in the next section. The individual lithographic layers of the HDMSQ2A design are summarized in the appendix table A.4. The expected energy resolution of the HDMSQ2A detector is $\Delta E_{\mathrm{FWHM}} = 0.53\,\mathrm{eV}$ at $T = 20\,\mathrm{mK}$. The parameters that were used for this calculation are summarized in the appendix table A.3.

7.2.2 HDMSQ2A detector chip

Figure 7.5 shows the center part of the HDMSQ2A detector chip, where its left half is depicted by a microscope photograph and its right half is depicted by its design schematic. The detector is now a 32 pixel linear array, instead of a 64 pixel two-dimensional array. The chip's dimensions were reduced from 8 × 8 mm in the HDMSQ1 design to 8 × 4 mm, so the total number of fabricated detectors on a 3 inch wafer was identical in both wafer designs. The linear layout allows for a spatial separation of the on-chip thermal bath of each individual pixel, which should minimize thermal crosstalk. Furthermore, each on-chip thermal bath now consists of 8 μm thick electroplated Au instead of just a thin sputtered Au foil. In order to keep the layout as compact as possible, the 820 μm long weak thermal link between sensor and bath also received a meander-shaped structure.

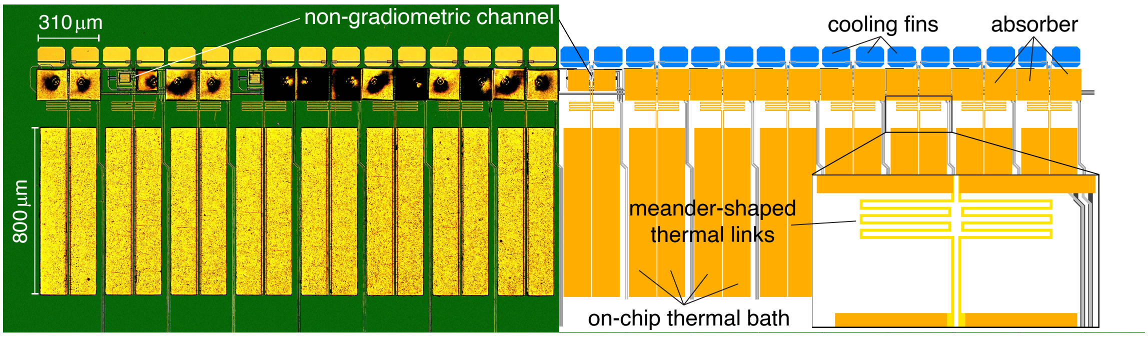

Figure 7.5: Illustration of the center of the HDMSQ2A detector chip. Its left half is depicted by a microscope photo and its right half is depicted by its design schematic. Each of the 32 pixels in the linear array has its own on-chip thermal bath. The 820 μm long thermalization link between temperature sensor and thermal bath has a meander-shaped form in order to minimize the required space on the chip.

The black areas that can be observed on the absorbers in figure 7.5 are due to refracted light that is not reflected back into the CCD sensor of the microscope camera, as the rather thin absorbers with a thickness of 3 μm start to bend during the ultrasonic cleaning that is required in their fabrication process. Two detector channels on the chip have a smaller absorber area of only 100 × 100 μm^2. These are the non-gradiometric channels that can be used to acquire temperature information. The last design change that was made compared to the HDMSQ1 chip is an increase in detector channels in which the persistent current I_0 can be injected into simultaneously. In the HDMSQ2A chip design, I_0 is injected into all 16 channels simultaneously. It is worth mentioning that it is also possible to provide an individual on-chip thermal bath for each pixel in a two dimensional pixel arrangement for future designs that incorporate more than just 16 detector channels. This can be achieved by so called through-wafer vias. For this thermalization scheme, small holes between 100 μm and 200 μm in diameter would be etched completely through the Si wafer. Afterwards, these etched holes are partly filled with electroplated gold, creating through-wafer vias in order to provide a metallic link between a thermal bath that is located on the front side of the wafer and an Au thermalization layer that is deposited onto the backside of the wafer. A microfabrication process for this thermalization scheme is currently being developed in this research group. While already showing promising results [Gam19], the process did not yet have a satisfying reliability when the HDMSQ2A detector was fabricated. Therefore, the chip layout was chosen to be a linear array in order to provide an individual thermal bath for each pixel.

7.3 Experimental results

This section presents the characterization of the HDMSQ2A detector, i.e. the signal height, the signal rise, the signal decay, the detector linearity, its noise, and the energy resolution. The detector was operated in the same experimental setup and the same dilution refrigerator as the HDMSQ1 detector. A suitable source collimator was fabricated in parallel to the HDMSQ2A detector, which was already shown in figure 6.10, and added to the experimental setup in order to prevent X-rays from hitting the substrate of the detector chip. This is the first microfabricated collimator that was used in this group, thus the corresponding fabrication process also had to be developed.

Figure 7.6 shows the IV-characteristics of a dc-SQUID from the HDMSQ1 and from the HDMSQ2A detector for comparison, both measured at $T = 4.2\,\mathrm{K}$ in a single stage setup. The HDMSQ2A characteristics are scaled up according to the ratio of the the shunt resistances of both detector designs, i.e. $R_{\mathrm{S,HMDSQ1}}/R_{\mathrm{S,HMDSQ2}} = 20$. The HDMSQ2A characteristics are impacted by the noise of the oscilloscope that was used for data acquisition, as the tiny voltage response was close to its resolution limit. The comparison shows that no additional distortions in the IV-characteristic occurred when the dc-SQUID with reduced shunt resistance R_{S} is equipped with paramagnetic temperature sensors, and that the expected behavior when operated in a two-stage setup should be similar to that of the HDMSQ1 detector, albeit exhibiting a reduced energy dissipation.

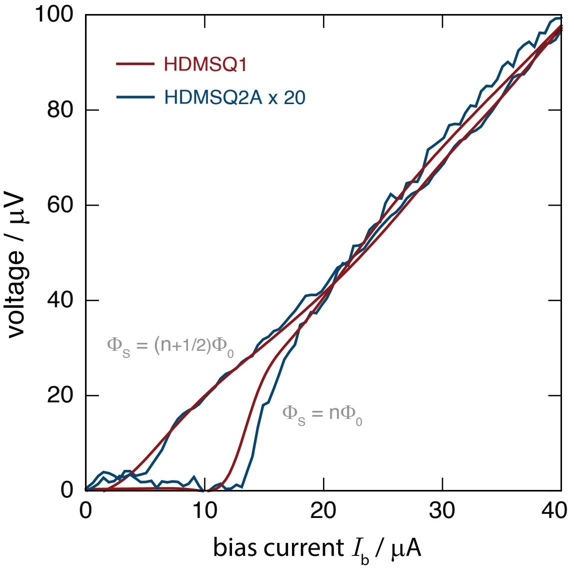

Figure 7.6: Measured IV-characteristics of a dc-SQUID of the HDMSQ1 and HDMSQ2A detector for a magnetic flux of $\Phi_S = (n+1/2)\Phi_0$ and $\Phi_S = n\Phi_0$ threading the SQUID loop. The HDMSQ2A characteristics are scaled up by factor of 20, which is the ratio of the shunt resistances of the two SQUID designs.

7.3.1 Signal shape

Figure 7.7 shows the measured detector response of the HDMSQ2A detector that follows the absorption of a ^{55}Mn K$_\alpha$ photon. The measurement was performed at a SQUID bias current of $I_b \approx 15\,\mu$A and a persistent current of $I_0 = 140\,$mA, while the cryostat was at its base temperature of $T \approx 7\,$mK. The signal shape exhibits the expected fast signal rise that is followed by a much slower signal decay. In contrast to the signal decay of the HDSMQ1 detector, the one of the HDMSQ2A detector can not be described by a single exponential function. Instead, two exponential functions are required, so that the signal decay is described by

$$\delta\Phi_S(t) = A_1(e^{-t/\tau_1}) + A_2(e^{-t/\tau_2})\,. \tag{7.3}$$

The first exponential function, with an amplitude of $A_1 = 0.5\,\Phi_0$ and a decay time of $\tau_1 = 6.14\,$ms, describes the detector thermalization to the on-chip thermal bath via the sputtered metallic link. The predicted value for τ_1 can be calculated with equation 6.3. The width of the thermal link is $w_{tl} = 3\,\mu$m, its length is $l = 820\,\mu$m with a layer thickness of $t_{Au} = 400\,$nm. As it will be shown in the subsequent discussion in this chapter, the detector has an operation temperature of $T \approx 26\,$mK at the chosen SQUID bias current of $I_b \approx 15\,\mu$A. The total calculated heat capacity is $C_{tot} = 278\,$fJ/K at an injected persistent current of $I_0 = 140\,$mA. The resulting expected signal decay time is $\tau_1 = 6.59\,$ms, which is 0.45 ms slower then the experimentally determined value. This deviation of $\sim 7\,\%$ can again be attributed to accuracy limitations in the lithographic methods used for detector fabrication. Assuming an increase in width w_{tl} by only 220 nm of the sputtered thermal link between temperature sensor and the thermal bath already matches prediction and measurement. Such a deviation is well within the margin of error for the Lift-off process that was used to microfabricate the thermal link. This error contribution can be reduced in future design iterations by increasing the width of the thermal link while reducing the layer thickness of the deposited Au in order to keep the cross section area of the thermal link constant. In this case, an additional Au deposition might be required at the locations the thermal link has to reliably cover the edges of Nb wiring it might has to cross over.

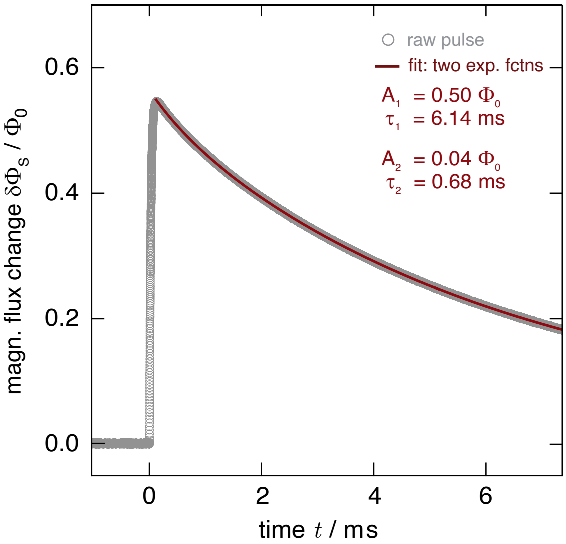

Figure 7.7: Measured magnetic flux change $\delta\Phi$ in a SQUID of the HDMSQ2A detector after the absorption of a ^{55}Mn K$_\alpha$ photon. The signal shape shows the expected fast signal rise, followed by a much slower signal decay. The latter is described by two exponential functions with the parameters denoted in the plot.

The second exponential function in equation 7.3 describes a rather fast initial signal decay with $\tau_2 = 0.68\,\mathrm{ms}$ with small amplitude of only $A_2 = 0.04\,\Phi_0$, which is 7.4 % of the total signal amplitude. Such a signal decay behavior was observed in the past for metallic magnetic calorimeters that made use of Au:Er temperature sensors instead of Ag:Er [Bur08, Sch12]. ^{197}Au has a nuclear spin of 3/2, thus it exhibits a nuclear quadrupole moment [Pow74]. The electric field tensors in an ideal fcc lattice of Au have a cubic symmetry, resulting in degenerate energy levels. When the ^{197}Au is diluted with Er^{3+}, the symmetry is broken, which leads to a hyperfine-splitting of the energy levels. As a result, the system of nuclear quadrupole moments represents another contribution to the total heat capacity of the detector, which can be observed at $T < 50\,\mathrm{mK}$ as an additional fast signal decay when the energy absorbed by the Er^{3+} ions is redistributed to the system of the nuclear quadrupole moments. This relaxation occurs with a time constant between 0.2 ms and 1 ms, depending on the applied magnetic field [Fle98, Ens00].

However, it is unclear why this behavior would be observable in the signal decay of the HDMSQ2A detector, as it makes use of am Ag:Er temperature sensor. The only Au that is found in close proximity is the 100 nm thick protective layer that coats the temperature sensor in order to prevent the oxidation of the Ag. The volume of this Au layer is $\sim 17\,\%$ of the volume of the Ag:Er in the HDMSQ2A detector. It might be possible that a part of this Au layer also experiences a break of lattice symmetry due to being in direct contact with the Ag:Er, as both layers were in-situ sputter deposited during sensor fabrication. This would then also create a hyperfine-splitting of the energy levels, consequently providing an additional contribution to the total heat capacity. Other detectors from this group with an Au coated Ag:Er sensor did not observe this behavior [Hen17, Sch19], albeit the volume of the Au coating is less than $3\,\%$ of the Ag:Er volume in these detectors, which might mean that this effect is not observable. This behavior requires additional investigation in future measurements, but was not further pursued in this thesis.

Lastly, it is interesting to see that even for the rather long thermal link of nearly 1 mm in length, no relevant relaxation between conduction electrons and phonons seems to occur, meaning no heat is transferred into the substrate before reaching the on-chip thermal bath. If this would be the case, a third exponential function would be required to describe the signal decay of the HDMSQ2A detector, as it was observed for past MMC designs [Sch00, Kem07]. Thus, it should be possible with the developed design to build a two dimensional, densely packed 64-pixel detector array whose thermalization fulfills the following requirements: Each pixel has its own thermal bath to minimize thermal cross talk. These heat baths are located on the front side of the chip without being hidden below the particle absorbers, as it was the case for the HDMSQ1 detector, and lastly, the signal decay is solely defined by the thermal conductance G of the metallic link between temperature sensor and heat bath.

7.3.2 Signal height

Figure 7.8 a) shows the measured signal height Φ_S as a function of the number of biased detector channels on the chip. The measurement was performed at a comparably high bias current of $I_\mathrm{b} \approx 25\,\mu\mathrm{A}$ and a persistent current of $I_0 = 90\,\mathrm{mA}$. It becomes apparent, that a multi-channel operation is also impractical for the HDMSQ2A detector, as the measured signal height Φ_S, and therefore also the detector's energy resolution, decreases with the number of additionally biased SQUIDs. Furthermore, similar to what was observed in the HDMSQ1 detector, the measured signal height was independent from the location of the additionally biased SQUID on the chip.

In order to deduce the actual temperature of the detector, the signal height Φ_S of one channel was investigated as a function of the temperature T of the mixing chamber platform and compared to the signal height that is expected from numerical simulations, as it is shown in figure 7.8 b). Here, the measured signal height as a function of temperature is plotted, as well as the theoretical predictions for

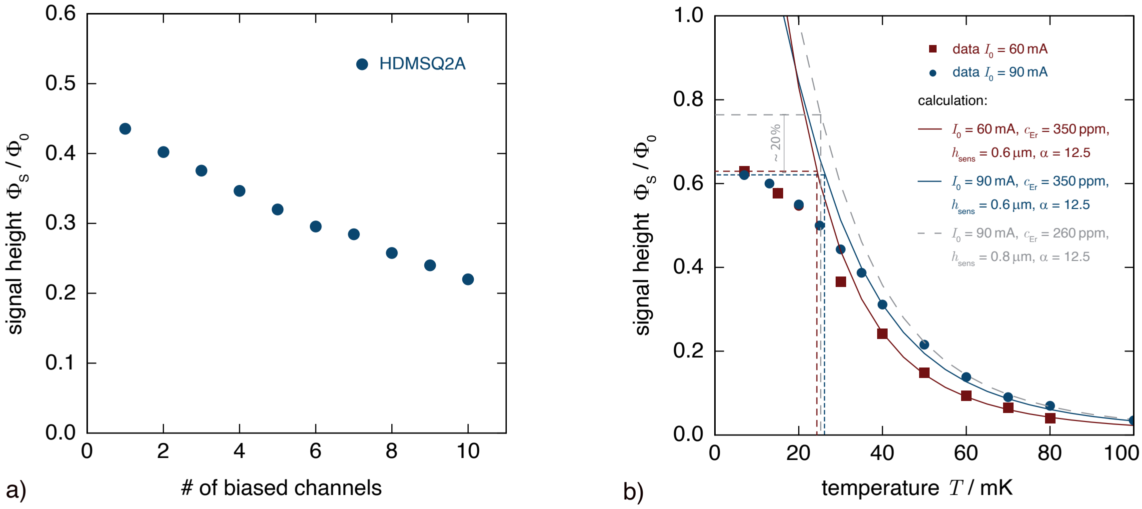

Figure 7.8: a) Signal height Φ_S in a SQUID of the HDMSQ2A detector that resulted from the absorption of 5.9 keV ^{55}Mn K$_\alpha$ photons, measured as a function of the number of biased SQUID channels. The bias current for each SQUID was $I_\mathrm{b} \approx 25\,\mu$A. b) Measured signal height Φ_S of the HDMSQ2A detector for a 5.9 keV energy input as a function of the mixing chamber temperature T for two different persistent currents. The measurement was performed at a SQUID bias $I_\mathrm{b} \approx 15\,\mu$A. The detector thermally decouples from the mixing chamber at low temperatures due to on-chip energy dissipation and reached its lowest operation temperature at $T \approx 26$ mK.

two different persistent currents, $I_0 = 60$ mA and $I_0 = 90$ mA, measured at a bias current of $I_\mathrm{b} \approx 15\,\mu$A. For the calculation of the signal height, a sensor height of $h_\mathrm{sens} = 0.6\,\mu$m with an Er concentration of $c_\mathrm{Er} = 350$ ppm was used in order to describe the data. The target values were $h_\mathrm{sens} = 0.8\,\mu$m and $c_\mathrm{Er} = 260$ ppm, as depicted by the grey curve in figure 7.8 b).

For the sputter deposition of the Ag:Er sensor in the employed UHV sputtering system, the deposition rate $\dot{d}_\mathrm{Ag:Er}$ for $P = 200\,W$ and $p_\mathrm{Ar} = 1.33$ Pa was measured at the center directly below Ag:Er target. The diameter of this target is only 2 inch and a planar sputter geometry is used. Therefore, a non-uniform layer thickness over an entire 3 inch wafer can be expected. The measurement of $\dot{d}_\mathrm{Ag:Er}$ from the center point was used to calculate the required sputter time in order to achieve the target sensor height. However, the material deposition has an angular Gaussian distribution with a peak deposition rate at the center. Therefore, chips that are located further away from the substrate center see a reduced material deposition rate, consequently resulting in a smaller h_sens. The actual Gaussian distribution of $\dot{d}_\mathrm{Ag:Er}$ was recently measured using dedicated test structuctes. From this measurement, a reduction of 150 - 200 nm for the target h_sens was deduced for the chip that is discussed in this section, as it had a distance from the substrate center of ~ 1.3 cm.

Furthermore, at the time of detector fabrication, the Ag:Er target within the employed UHV sputtering system was prepared with an erbium concentration of $c_{\mathrm{Er}} = 260\,\mathrm{ppm}$, a value confirmed on a prepared sample that was measured with a commercial magnetometer[1] at $T = 4.2\,\mathrm{K}$. Prior to the fabrication of the HDMSQ2A detector, two different detectors were fabricated in short succession. As the sensor fabrication is done via a Lift-Off process, the residual sensor material left after this process was also measured in the magnetometer, which confirmed the expected erbium concentration of $c_{\mathrm{Er}} = 260\,\mathrm{ppm}$. This concentration was therefore assumed for the optimization of the HDMSQ2A detector. However, after its fabrication, the magnetization measurement of the residual sensor material showed an Er concentration of $c_{\mathrm{Er}} = 350\,\mathrm{ppm}$. The reason why the Er concentration increased by $\sim 40\,\%$ for the deposited material compared to previous wafers is unknown. A deviation of such magnitude was not observed in the past, and was also not observed ever since.

Figure 7.8 b) shows, that similar to the HDMSQ1 detector, the HDMSQ2A thermally decouples from the cryostat due to the on-chip energy dissipation of the dc-SQUID. The lowest reached operation temperature can be estimated to be $T \approx 26\,\mathrm{mK}$, which is $\sim 6\,\mathrm{mK}$ lower compared to the HDMSQ1 detector. Additionally, no increase in signal height could be observed for bias currents of $I_{\mathrm{b}} < 15\,\mu\mathrm{A}$. This is a significant improvement compared to the HDMSQ1 detector, as the dc-SQUIDs in both designs have a comparable critical current and critical current modulation according to figure 7.6 a), whereas the dc-SQUIDs of the HDMSQ2A could be operated closer to their optimum working point without observing a negative impact on the measured signal height.

Assuming the target values for h_{sens} and c_{Er} were reached during fabrication, then the achieved signal height would be $\sim 20\,\%$ higher at the same operation temperature. This is illustrated in figure 7.8 b) by the grey dashed line, which is the calculated signal height when assuming the target values.

7.3.3 Signal rise

In order to investigate the signal rise of the HDSMQ2 detector, detector signals resulting from the absorption of ^{55}Mn K$_\alpha$ X-rays were acquired using short time windows with a length of a few microseconds with a sampling rate of 500 MS/s. For this measurement, a SQUID bias current of $I_{\mathrm{b}} \approx 25\,\mu\mathrm{A}$ and a persistent current $I_0 = 90\,\mathrm{mA}$ were used. Figure 7.9 a) shows the measured signal rise of the fastest channel on the HDMSQ2A detector, i.e. the detector channel with a target signal rise time of $\tau_0 \approx 2\,\mu\mathrm{s}$. The expected time dependence of the signal rise (see equation

---

[1] QD MPMSR XL from Quantum Design Inc, 10307 Pacific Center Court, San Diego, CA 92121, USA

2.30) with a rise time constant of $\tau_0 = 1.6\,\mu$s is fitted to the data, which it can not describe, i.e. the measured signal rise is not an exponential function. That the slew rate limit of the readout chain was reached again in this case is indicated by the linear part within the signal rise of the depicted detector response. Figure 7.9 b) shows the measured signal rise of a detector channel with a target rise time of $\tau_0 = 15\,\mu$s at $T = 20\,$mK. The expected time dependence of the signal rise with a rise time constant of $\tau_0 = 10.3\,\mu$s is fitted to the data. While the signal rise shows the expected exponential behavior, it is nearly $5\,\mu$s faster than expected.

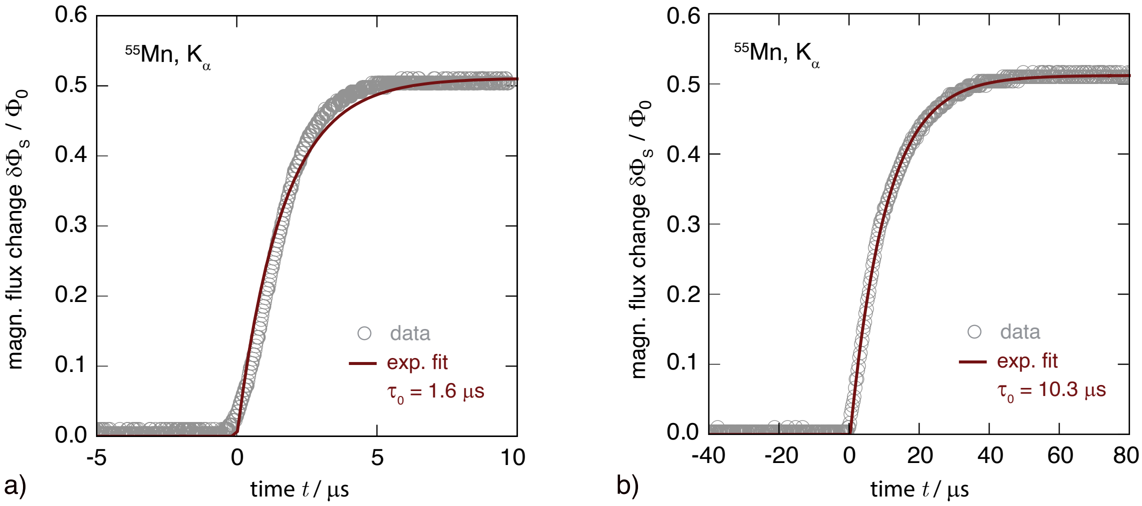

Figure 7.9: Measured signal rise of the HDMSQ2A detector at a bias current of $I_\mathrm{b} \approx 25\,\mu$A and a persistent current of $I_0 = 90\,$mA. The detector temperature is $T \approx 30\,$mK. a) Measured signal rise of the fastest channel with a target $\tau_0 = 2\,\mu$s. An exponential function with a time constant $\tau_0 = 1.6\,\mu$s is fitted to the data, indicating that measured signal rise does not follow an exponential function. b) Measured signal rise of a detector channel with a target rise time $\tau_0 = 15\,\mu$s. An exponential function with a time constant $\tau_0 = 10.3\,\mu$s is fitted to the data.

The latter can be calculated with equations 7.1 and 7.2, which requires the knowledge of the exact size of the thermal link between sensor and absorber. However, its target length of $l = 20\,\mu$m is slightly reduced due to a larger than expected sensor area after fabrication. This is illustrated in figure 7.10 a), which shows a photograph of a temperature sensor on a fabricated HDMSQ2A detector. Denoted is the design area of the sensor, its area after sensor fabrication, as well as a corrected sensor area. The depicted deviation between the target area and the deposited area is due to the use of a Lift-off process for sensor fabrication with a comparable thick photoresist, as it is depicted in figure 7.10 b). Shown is a schematic of the performed Lift-off process with the AZ nLOF 2070 photoresist that is $\sim$ 10 times as thick as the deposited Ag:Er sensor. The so called undercut of the photoresist results in an enlarged sensor area after sputter deposition compared to the design area. In order to correct this rather significant deviation, a part of this additional sensor area was removed via argon ion milling by making use of a custom photoresist mask that was drawn deliberately for this purpose. The only area on the entire wafer that was exposed to the Ar ion milling was most of the additional sensor area. The only parts of this additional area that were also protected by photoresist were the thermal link between sensor and absorber, and the thermal link between sensor and on-chip thermal bath. The resulting corrected sensor area is denoted by the green border in figure 7.10 a). Therefore, the actual length of the thermal link between temperature sensor and absorber is reduced to values between 15 μm and 16 μm. The slightly increased sensor area also means that its heat capacity is slightly increased. From figure 7.8 b) for the measured signal height of $\Phi_\mathrm{S} \approx 0.5\,\Phi_0$ and $I_0 = 90\,\mathrm{mA}$, an operation temperature of $T \approx 30\,\mathrm{mK}$ can be deduced. Furthermore, as it was already discussed, the sensor height and erbium concentration deviate from the target values, resulting in a sensor heat capacity of $C_\mathrm{sens} \approx 110\,\mathrm{fJ/K}$ at this operation temperature while accounting for its slightly increased area, whereas the absorber heat capacity is $C_\mathrm{abs} = 152\,\mathrm{fJ/K}$. The other dimensions of the thermal link are a width of $w = 6\,\mu\mathrm{m}$ with an Au thickness of $t_\mathrm{Au} = 400\,\mathrm{nm}$. With these parameters, the expected signal rise time τ_0 is between 10.0 μs and 10.6 μs, i.e. in good agreement with the experimentally determined signal rise time 10.3 μs.

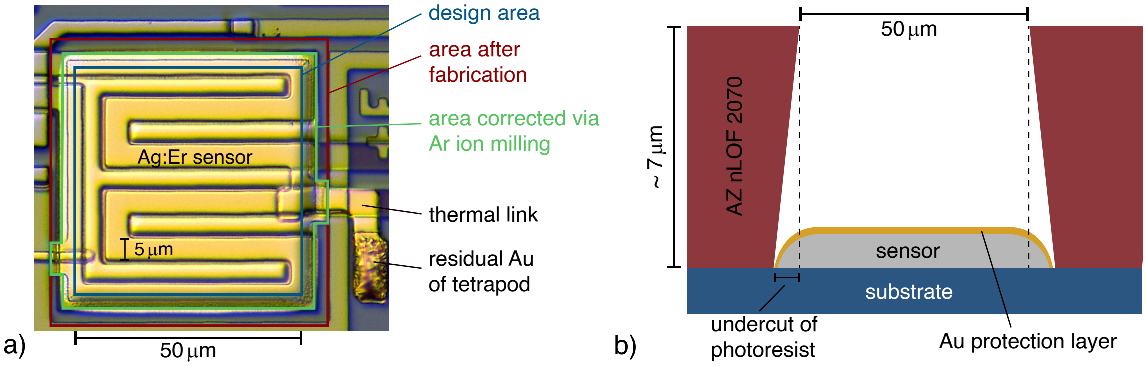

Figure 7.10: a) Photograph of a temperature sensor of a fabricated HDMSQ2A detector, illustrating the difference between the designed absorber area, the deposited absorber area, and the final absorber area that was corrected via argon ion milling. b) Schematic illustration of the Lift-off process that was used for sensor fabrication with the negative resist AZ nLOF 2070 that is much thicker than the deposited sensor. The so called undercut of the photoresist results in a larger than designed sensor area after sputter deposition.

The discussed data shows, that the signal rise of metallic magnetic calorimeters can be slowed down in a controlled and predictable manner in order to fit experimental needs. It is worth mentioning that the remaining slower channels on the HDMSQ2A detector could also be fully resolved of course. However, the fastest channel that could be fully resolved is the important one, as it allows for a rough approximation of the maximum slew rate of the employed two-stage SQUID readout, and because the energy resolution of the detector scales with $\tau_0^{1/4}$ according to equation 2.27. In future designs of this integrated detector, where the signal height can be expected to go far beyond $1\,\Phi_0$ for a 5.9 keV energy input, the discussed measurement presents a good approximation of the target signal rise time that is required in order to yield a fully resolvable detector response for photons of up to 10 keV, assuming the readout chain is not adjusted accordingly to provide a higher maximum slew rate. However, the latter would require a smaller cryostat that allows for shorter wires. Furthermore, even if a further increase of τ_0 is required in future integrated detector designs, only a minor degradation of the achievable energy resolution is to be expected [Ban12], still allowing for MMCs to reach a potential energy resolution below 1 eV.

Lastly, to yield a higher pattern fidelity in future designs for the fabrication of such comparably thin temperature sensors, the photoresist AZ 5214E should be used, just like it was the case for the other Lift-off processes during fabrication. While an undercut of the photoresist will still occur in this case, as it is intended for a Lift-off process, it will reduce the undercut below $1\,\mu$m, as the resist thickness is only $\sim 1.4\,\mu$m when spin coated at 3000 rpm.

7.3.4 Detector linearity

The linearity of metallic magnetic calorimeters was discussed in section 2.7, and shown to exhibit an excellent agreement between theory and experiment in section 2.8, where the close to perfect linearity of the maXs-20 detector was discussed.

Figure 7.11 depicts in the upper plot the measured signal height (left axis) and estimated photon energy (right axis) of the HDMSQ2A detector as a function of the actual energy of the absorbed X-ray. The red dashed line depicts a perfectly linear detector response, and the blue line denotes a second-order polynomial fit. The lower plot shows the difference between the measured signal height Φ_S and the signal height of a perfectly linear detector (left axis) and the difference between the determined photon energy E_m and the actual photon energy (right axis) E_p, as a function of the actual energy of the absorbed X-ray. The non-linearity of the detector can be determined to be $\eta(6.49\,\mathrm{keV}) = 6.05\,\%$. The measurement was performed at a SQUID bias current of $I_\mathrm{b} \approx 15\,\mu$A and an injected persistent current of $I_0 = 140\,$mA.

The expected non-linearity can be calculated according to equation 2.29. At an operation temperature $T = 26\,$mK and a persistent current of $I_0 = 140\,$mA, the detector has a calculated total heat capacity of $C_\mathrm{tot} \approx 273\,$fJ/K, a calculated signal height per energy input of $\delta\Phi/\delta E \approx 111.3\,\mu\Phi_0/$eV and a calculated $\partial/\partial T(\partial\Phi_\mathrm{S}/\partial E) \approx -3.55\,\mathrm{m}\Phi_0/(\mathrm{eVK})$. The predicted non-linearity is $\eta_\mathrm{calc}(6.49\,\mathrm{keV}) = 5.97\,\%$. Therefore, the deviation between the measured non-linearity and the calculated one at

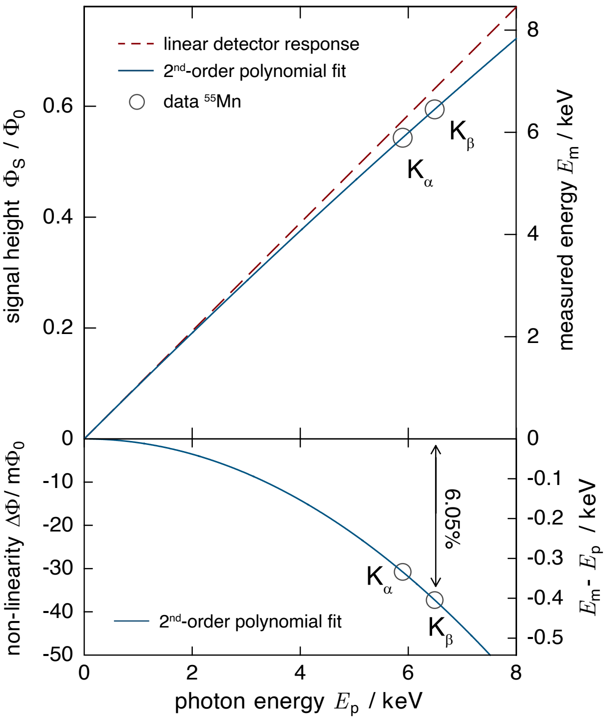

Figure 7.11: Upper plot: Measured signal height (left axis) and estimated energy (right axis) of the HDMSQ2A detector as a function of the energy of the incident photon. The red dashed line denotes a perfectly linear detector response, whereas the blue line denotes a quadratic dependence. Lower plot: difference between the measured signal height and the signal height of a perfectly linear detector (left axis) and difference between the determined photon energy and the actual photon energy (right axis) as a function of the incident photon energy. The blue line denotes a quadratic dependence of the non-linearity of the detector.

$E_\mathrm{p} = 6.49\,\mathrm{keV}$ is below $0.1\,\%$, showing that the non-linearity of the detector can be predicted and follows a simple quadratic dependence of the absorbed energy. For this calculation, the increased sensor area, the reduced sensor height, as well as the increased Er concentration compared to the target values were accounted for. Residual deviations can be explained by the limited accuracy of the sensor microfabrication.

7.3.5 Detector noise

Figure 7.12 shows the measured power spectral density of the apparent flux noise in the dc-SQUID at a bias current of $I_\mathrm{b} \approx 15\,\mu\mathrm{A}$ of the detector channel with a signal rise time of $\tau_0 = 10.3\,\mu\mathrm{s}$ in comparison with the calculated noise contributions that were discussed in section 2.6.3. The parameters that were used for the calculations are summarized in the appendix in table A.3. Compared to the actual design parameters, the erbium concentration c_Er as well as the sensor height were adjusted to the actual measured values of 350 ppm and 600 nm respectively. Furthermore, the white noise level was increased from $\sqrt{S_{\Phi,\mathrm{w}}} = 0.5\,\mu\Phi_0/\sqrt{\mathrm{Hz}}$ to $\sqrt{S_{\Phi,\mathrm{w}}} = 0.57\,\mu\Phi_0/\sqrt{\mathrm{Hz}}$ to account for the degraded noise performance of the SQUID due to being operated at a non-optimal working point. The noise exponent of the $1/f$-like Er noise contribution was reduced to 0.85 in order to match the measurement. Lastly, no thermodynamic energy fluctuations are observed in the spectrum because the measurement was performed without any persistent current I_0 running in the field generating coil, where the detector is insensitive towards incoming photons. In this case, the heat capacity C_{Z} of the magnetic moments is close to zero, as only a negligible residual magnetic field should have existed within the superconducting shield that encased the detector setup. The thermodynamic energy fluctuations are therefore not observable according to equation 2.17. With these considerations, the calculated noise is in excellent agreement with the measured data, showing that the noise performance of the integrated detector is fully predictable and behaves according to expectations.

Also shown in figure 7.12 is the noise contribution of the room temperature electronics, denoted as "XXF-1". When this contribution is subtracted from the measured noise (see section 3.3.4), one receives the curve denoted as "intrinsic", showing that the amplification of the two-stage SQUID setup is not sufficient in order to make the noise of the room temperature electronics fully negligible for $f > 10^3\,\mathrm{Hz}$. This also means of course, that the white noise level denoted as "SQUID" in figure 7.12 that was assumed for the calculations in order to match the measurement represents the white noise of the SQUID as well as the noise contribution of the room temperature electronics. The calculation shows, that the detector performance would be degraded even when the detector SQUID is operated at its optimum working point. To achieve the detector intrinsic noise performance in future applications, the flux-to-flux amplification G_Φ in the two-stage SQUID setup has to be increased. This can be done for instance by adapting the design of the employed 16-SQUID series arrays by increasing the number of constituting SQUID cells. In the presented measurement, the array had a flux-to-voltage transfer coefficient of $V_{\Phi,\mathrm{N}} \approx 1400\,\mu\mathrm{V}/\Phi_0$. To make the noise contribution of the room temperature electronics completely negligible, assuming the detector SQUID is operated at its optimum working point, a flux-to-voltage transfer coefficient of $V_{\Phi,\mathrm{N}} \approx 2000\,\mu\mathrm{V}/\Phi_0$ would be required for the SQUID array. This can be achieved for instance by increasing the number of SQUID cells from 16 to 22. Design changes in this direction are currently under consideration.

7.3.6 Energy resolution

In order to determine the energy resolution of the HDMSQ2A detector, the channel with a rise time constant of $\tau_0 = 10.3\,\mu\mathrm{s}$ was biased with a current of $I_{\mathrm{b}} \approx 15\,\mu\mathrm{A}$, where it has an operation temperature of $T \approx 26\,\mathrm{mK}$. A persistent current of $I_0 = 140\,\mathrm{mA}$ was injected. The measurement was performed at a mixing chamber temperature of $T \approx 7\,\mathrm{mK}$ without any additional temperature stabilization via the PID setup that was described in section 4.1.3, as its use resulted in an observed degradation of the determined energy resolution at 5.9 keV when operated blow 20 mK.

Figure 7.13 a) shows a histogram that results from the application of the χ^2-fit

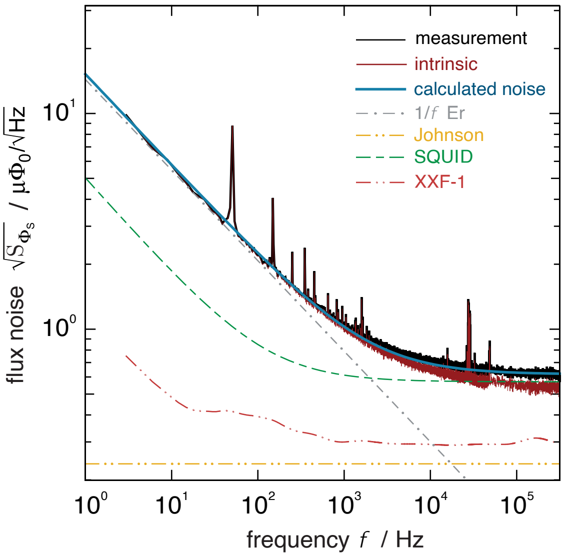

Figure 7.12: Measured power spectral density of the apparent flux noise of the HDMSQ2A detector with a signal rise time of $\tau_0 = 10.3\,\mu$s, measured at a mixing chamber temperature of $T = 10\,$mK and no persistent current running in the field generating coil. Additionally shown are the different calculated noise contributions. The thermodynamic energy fluctuations are not observed in the measured noise spectrum as the magnetic moments only have a negligible heat capacity C_Z for $I_0 = 0\,$mA.

signal analysis method to untriggered noise traces that were acquired acquired with the HDSMQ2A detector. A Gaussian distribution with an instrumental linewidth of $\Delta E_\mathrm{FWHM} = 1.7\,$eV is fitted to the data, indicating the intrinsic energy resolution of the detector in this operation regime. Figure 7.13 b) shows the measured energy spectrum of the K$_\alpha$-line of the ^{55}Fe X-ray calibration source. Fitted to the data is a convolution of the natural linewidth of the K$_\alpha$-line and a Gaussian distribution with an instrumental energy resolution of $\Delta E_\mathrm{FWHM} = 2.4\,$eV. The data is corrected for potential temperature drifts of the cryogenic setup, as it was discussed in section 6.5.6. No low energy tail can be observed in the measured spectrum, indicating that only a negligible loss of athermal phonons occurred due to the enhanced absorber geometry that was described in section 7.1.2.

The expected energy resolution of the HDMSQ2A detector at the chosen operation parameters with the discussed changes in sensor height, sensor area and Er concentration taken into account, is $\Delta E_\mathrm{FWHM} \approx 0.9\,$eV. This is 0.8 eV lower than the determined baseline resolution. Just like for the HDMSQ1 detector, the most likely candidate for this degradation is the used χ^2-fit signal analysis method, as it was discussed in section 4.3, where the determined energy resolution of a detector with lower noise but identical signal amplitude compared to the HDMSQ2A detector degraded by up to a factor of 2 when the χ^2-fit method was applied for signal analysis. Furthermore, no discrete noise peaks were factored into the simulations that were shown in figure 4.5, whereas such discrete noise contributions are observed for the HDMSQ2A detector in figure 7.12. When an analysis algorithm based on optimal filtering is available in the coming months, this hypothesis can be verified.

The energy resolution at 5.9 keV is further degraded most likely due to temperature fluctuations, which are difficult to quantify at this point. The measurement was

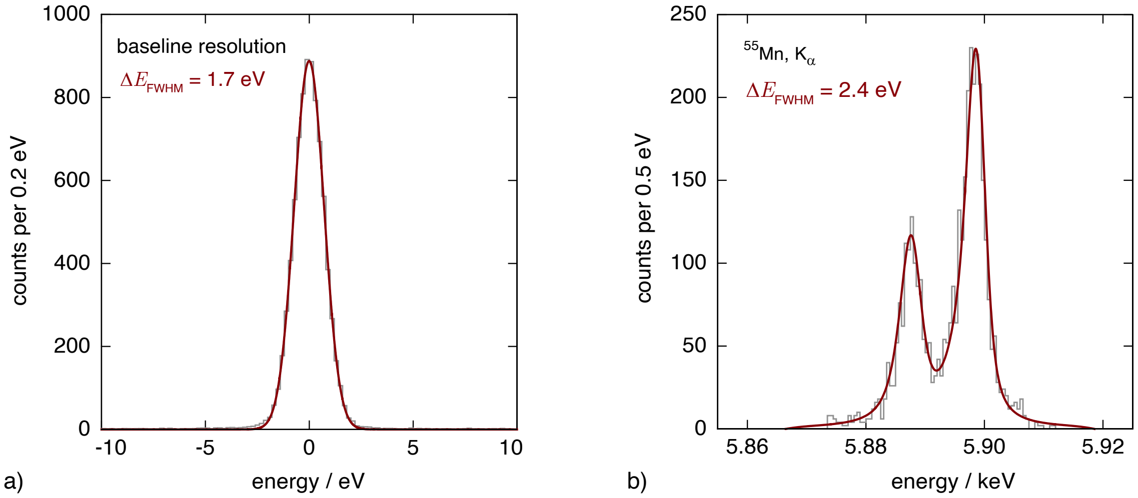

Figure 7.13: a) Determined baseline resolution of the HDMSQ2A detector setup, measured at a mixing chamber temperature $T \approx 7\,\mathrm{mK}$ without any active temperature stabilization. A SQUID bias current of $I_\mathrm{b} \approx 15\,\mu\mathrm{A}$ and a persistent current of $I_0 = 140\,\mathrm{mA}$ were used. b) Measured energy spectrum of the K$_\alpha$-line of the ^{55}Fe X-ray source. Fitted to the histogram is the expected lineshape when assuming an instrumental resolution of $\Delta E_{\mathrm{FWHM}} = 2.4\,\mathrm{eV}$.

performed at the base temperature of the cryostat, which is slightly blow $7\,\mathrm{mK}$, without any active temperature stabilization. The resistance thermometer that is installed at the mixing chamber platform is only calibrated down to $7\,\mathrm{mK}$. Therefore, no absolute temperature information is available for $T < 7\,\mathrm{mK}$ and the detector was subject to the intrinsic temperature fluctuations of the mixing chamber platform during the measurement.

The temperature fluctuations at the base temperature of this particular cryostat were observed in recent days for the first time. For this, a so called noise thermometer [Stä18] was installed at the mixing chamber platform. Such a thermometer determines the temperature by measuring the Johnson noise of a low-ohm resistor (see equation 3.15) that is in good thermal contact with the mixing chamber platform. The low-ohm resistor is connected to the input coil of a current-sensing dc-SQUID. Furthermore, this thermometry system also makes use of a two-stage SQUID setup for a reliable high precision signal readout. The temperature fluctuations at the base temperature of the cryostat that were determined with the noise thermometer are shown in figure 7.14. The depicted fluctuations are quite substantial with $\Delta T/T \approx 0.17$ when assuming a base temperature of $T \approx 6\,\mathrm{mK}$. The ^{55}Fe K$_\alpha$ spectrum that was shown in figure 7.13 b) was measured in a timeframe of 6 hours. Therefore, the temperature fluctuations of the cryostat are most likely the cause for the degraded energy resolution of the HDMSQ2A detector. Furthermore, the

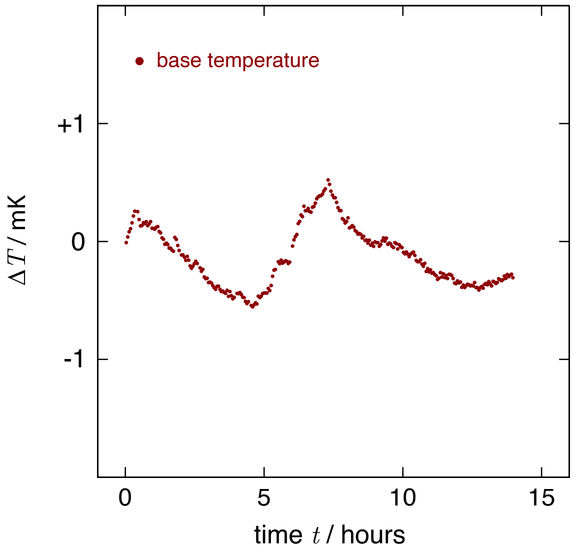

Figure 7.14: Measured temperature fluctuations as a function of time at the base temperature of the cryostat without any active temperature stabilization. The measurement was recently done with a noise thermometer mounted to the mixing chamber platform.

depicted temperature fluctuations are large enough, so that the non-gradiometric detector channel, which was used to acquire temperature information, no longer shows a perfectly linear behavior. Thus, it is quite possible that the accuracy of the performed correction of the signal amplitude for temperature drifts is also rather limited, which leads to further uncertainties for the determined energy resolution at 5.9 keV.

7.3.7 HDMSQ2A with additional Au thermalization layer

This section briefly discusses a final design adaptation that was made on an already fabricated HDMSQ2A detector chip. In this adaptation, the backside of the chip was coated with 1 μm of sputtered Au. This thermalization layer functions as a heat sink for athermal phonons traversing the silicon substrate, potentially enhancing the thermal coupling between the chip and the sample holder. In order to characterize this detector with regards to the design change, the chip was cooled down in the same experimental setup that was used for the other detectors. The characterization procedure was performed in analogue to the already discussed HDMSQ2A detector.

Figure 7.15 a) shows the measured signal height Φ_S for a 5.9 keV energy input as a function of the temperature T of the mixing chamber platform. Also plotted is the calculated signal height for a persistent current of $I_0 = 60\,\mathrm{mA}$ and an erbium concentration $c_\mathrm{Er} = 350\,\mathrm{ppm}$. An operation temperature of $T \approx 23\,\mathrm{mK}$ can be deduced from the plot, which is 3 mK lower than the determined operation temperature T of the detector version without an Au thermalization layer on its backside at the same SQUID bias current, i.e. the same on-chip energy dissipation. Therefore, putting an Au thermalization layer on the backside of the chip slightly reduced the operation

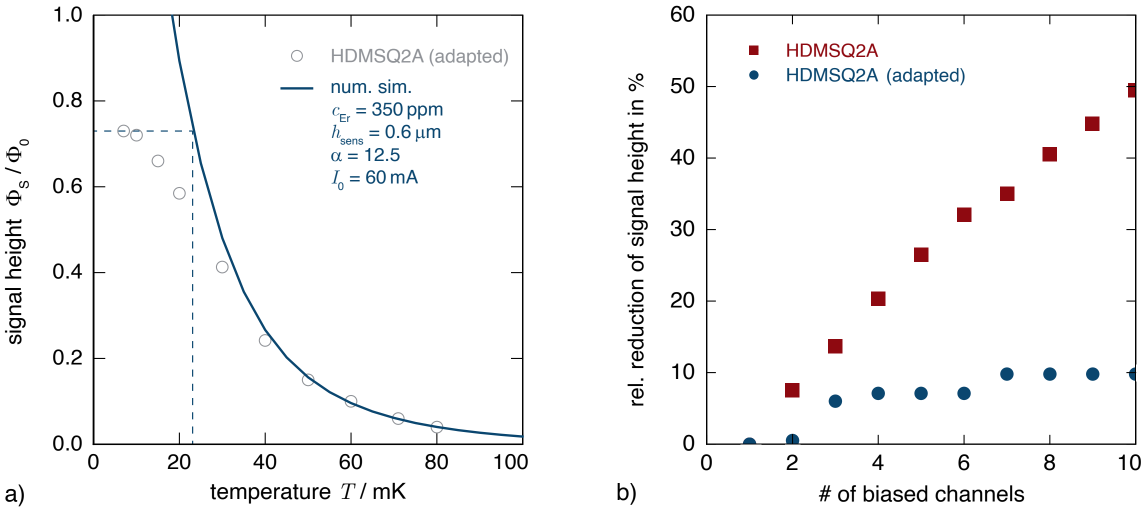

Figure 7.15: a) Measured signal height Φ_S of the HDMSQ2A detector with extra thermalization layer on its backside for a 5.9 keV energy input as a function of the mixing chamber temperature T. The measurement was performed at a SQUID bias $I_b \approx 15\,\mu$A. The detector thermally decouples from the mixing chamber at low temperatures due to on-chip energy dissipation and reached its lowest operation temperature at $T \approx 23$ mK. b) Relative reduction of the signal height in a SQUID of the HDMSQ2A detector with and without addition thermalization layer that resulted from the absorption of 5.9 keV ^{55}Mn K$_\alpha$ photons, measured as a function of the number of biased SQUID channels.

temperature of the detector.

Figure 7.15 b) shows the relative reduction of the measured signal height Φ_S for a 5.9 keV energy input in one detector pixel as a function of the number of biased detector channels on the chip for the regular HDMSQ2A and the redesigned version. The data of the former design was already shown in figure 7.8 a) plotted as the measured signal height Φ_S. For the redesigned HDMSQ2A, the measured signal height in the observed channel reduced by only 10 % for 9 additionally biased SQUIDs. It should be noted however, that the data of the regular HDMSQ2A detector was acquired at a higher total on-chip energy dissipation, as a bias current of $I_b \approx 25\,\mu$A was used, whereas the data of the adapted HDMSQ2A was acquired at $I_b \approx 15\,\mu$A.

As a last test, in order to investigate the impact of the on-chip energy dissipation on the chip temperature T, the signal height Φ_S was measured for a channel on the left side of the detector chip as a function of the bias current I_b that was applied to a different detector channel situated on the right side of the chip ~ 3 mm away, as it is illustrated in figure 7.16 a). The result is shown in figure 7.16 b), plotted as the relative reduction of the measured signal height on the left axis, and as the corresponding temperature increase ΔT on the right axis. Up to a bias current of $I_b \approx 17\,\mu$A of the additionally biased detector channel on the right side of the chip,

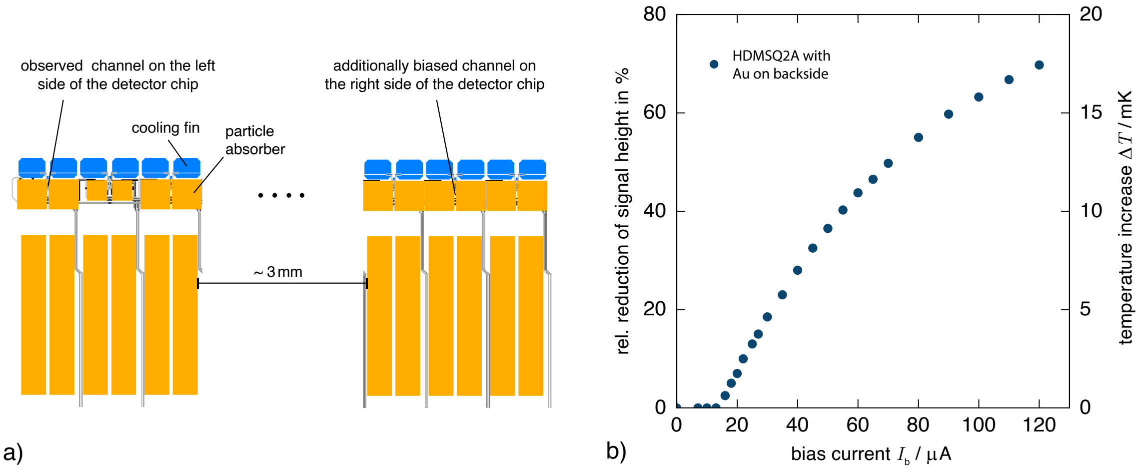

Figure 7.16: a) Illustration of where the observed channel and the additionally biased channel are located on the HDMSQ2A detector. b) Relative reduction of the measured signal height Φ_S (left axis) and temperature increase ΔT (right axis) of a channel on the left side of the HDMSQ2A detector with additional thermalization layer as a function of the bias current I_b that was applied to a dc-SQUID located at the right side of the chip.

no reduction of the measured signal height Φ_S was observed in the channel on the left side of the chip. Increasing the bias current to $I_b > 17\,\mu$A led to a significant reduction of Φ_S. Therefore, a potential multi-pixel operation for a chosen bias current of $I_b \approx 15\,\mu$ was demonstrated, whereas pushing the SQUIDs closer to their optimum working point at $I_b > 17\,\mu$A results in a significant increase of the chip temperature. This means, that while the the HDMSQ2A detector could be operated closer to its optimum working point, resulting in an improved noise performance and energy resolution compared to the HDSMQ1 detector, it also can not be operated at the optimum working point of the dc-SQUID without decreasing the measured signal height, fundamentally limiting the performance of the detector.

7.3.8 Summary

This chapter discussed the HDMSQ2A detector. The performed design changes compared to its predecessor, the HDMSQ1 detector, resulted in the anticipated performance enhancements. The signal rise time τ_0 was successfully increased in a predictable manner and the measured signal rise could be fully resolved with the employed two-stage SQUID readout. The loss of athermal phonons was successfully reduced to a non-observable level due to the enhancements of the absorber geometry. Furthermore, the on-chip energy dissipation was reduced, which led to a reduction of the operation temperature of $\Delta T \approx 6\,$mK compared to the HDMSQ1 detector and the dc-SQUIDs of HDMSQ2A detector could be operated closer to their optimum working point without observing a negative impact on the measured signal height Φ_S, resulting in an enhanced signal-to-noise ratio. In addition, the discussed detector characterizations show an excellent agreement with the theoretical model of metallic magnetic calorimeters. The performed design enhancements led to a significant improvement in the achieved energy resolution. The detector's baseline resolution could be reduced from $\Delta E_\mathrm{FWHM} = 4.2\,\mathrm{eV}$ to $\Delta E_\mathrm{FWHM} = 1.7\,\mathrm{eV}$, whereas the achieved energy resolution at 5.9 keV photon energy was reduced from $\Delta E_\mathrm{FWHM} = 8.9\,\mathrm{eV}$ to $\Delta E_\mathrm{FWHM} = 2.4\,\mathrm{eV}$. The achieved baseline resolution is a factor of ~ 2 higher than the resolution that is expected form numerical simulations, which is $\Delta E_\mathrm{FWHM} \approx 0.9\,\mathrm{eV}$ for the chosen operation parameters. The most likely cause for the degradation of the energy resolution is the used signal analysis method. The achieved energy resolution at 5.9 keV is a factor of ~ 1.4 higher than the determined baseline resolution, which can be attributed to temperature fluctuation of the cryogenic setup, as it was operated at its base temperature of $T < 7\,\mathrm{mK}$ during data acquisition without any active temperature stabilization. Furthermore, it was shown that adding a $1\,\mu\mathrm{m}$ thick Au thermalization layer to the backside of the chip led to an additional reduction of the operation temperature of $\Delta T \approx 3\,\mathrm{mK}$ down to 23 mK. This thermalization layer improved the thermalization between chip and copper substrate holder, so that a simultaneous operation of up to 10 detector channels was demonstrated without suffering a significant loss of measured signal height Φ_S at a non-optimal bias current of $I_\mathrm{b} \approx 15\,\mu$. The last remaining challenge for this detector is still the on-chip energy dissipation, which can be addressed by either reducing its critical current, or by providing a different thermalization pathway for the shunt resistors, so that they no longer dissipate their energy into the detector substrate. The latter option was investigated by developing the HDMSQ2B detector, which is the topic of discussion in the last chapter of this thesis.

8. The HDMSQ2B detector

This chapter discusses the HDMSQ2B detector. Its chip design was also part of the wafer on which the HDMSQ2A was fabricated on. Therefore, both detectors are nearly identical in their overall design parameters, the HDMSQ2B just underwent a few additional fabrication steps that were not part of the HDMSQ2A design. Thus, the HDMSQ2B also suffers from a higher than expected Er concentration within the temperature sensor, as well as a deviation between the target sensor height and target sensor area compared to the actual ones. First, this chapter illustrates the design difference compared to the HDSMQ2A, followed by a discussion of the detector characterizations. This includes an investigation of the on-chip energy dissipation on the detector performance and a determination of the energy resolution, concluding with a summary of the experimental results.

8.1 Shunt resistors on membranes

The shunt resistors that are connected in parallel to the Josephson tunnel junctions in the HDMSQ1 and HDMSQ2A detector are placed on the solid substrate at a distance of several micrometers from the paramagnetic temperature sensor. The dissipated power in these normal conducting structures when the SQUID is operated in the voltage state needs to go through the Si substrate into the sample holder. Thus, the chip temperature is increased compared to the temperature of the cryogenic setup, as was discussed in the previous chapters. With the developed HDMSQ2B detector, a different thermalization scheme for the shunt resistors was explored. The idea of this detector is to place the resistor on a thin SiO_2 membrane and to thermally anchor the shunt and the membrane through an additional metallic link directly to the sample holder. A schematic cross section of this thermalization scheme is illustrated in figure 8.1 a), and a top view is depicted in b).

Depicted in a) is a chip that is glued to a sample holder. Located on the left side are stripes of the field generating coil and of the meander-shaped SQUID loop with the Ag:Er temperature sensor located on top. The Au:Pd shunt resistor that are connected in parallel to the Josephson junction via corresponding Nb wiring are located on the right sight and are attached to a cooling fin. Below these Au:Pd structures, the Si substrate is etched away, such that they are hovering on a membrane that is made of the 240 nm thick thermal SiO_2 that insulates the wafer. This minimizes the thermal contact between the Au:Pd structures and the Si, so that the

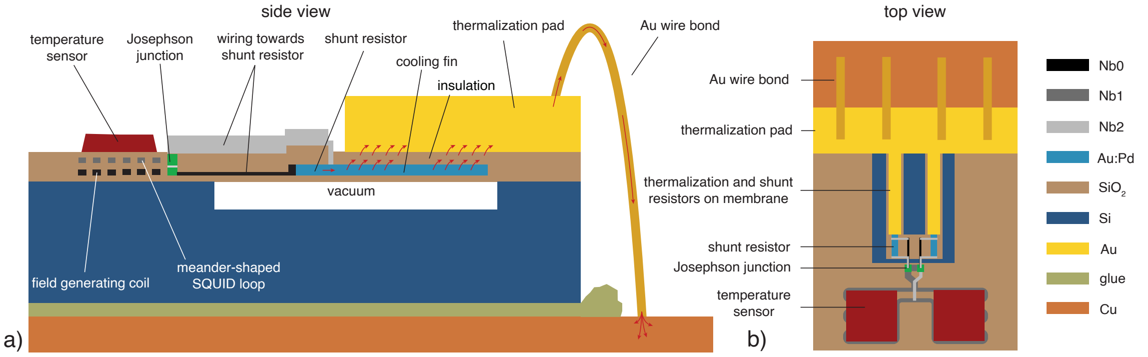

Figure 8.1: Schematic of the custom thermalization scheme of the HDSMQ2B detector. a) Side view and b) top view. The shunt resistors of the dc-SQUID are placed on a thin SiO_2 membrane, thermally decoupling them from the Si substrate. A custom thermalization structure made of electroplated Au and Au wire bonds directly transfers the dissipated energy into the sample holder.

dissipated energy can not be transferred into the substrate. Therefore, a different thermalization pathway has to be provided in order for the energy to dissipate into the sample holder. For this, an Au thermalization link is put in top of the cooling fin, as well as on a small part of the solid Si substrate for structural stability. This thermalization link is then directly coupled to the sample holder via Au wire bonds. Since the phononic thermal conductance is several orders of magnitude lower than the electronic thermal conductance at millikelvin temperatures [Ens05], as well as due to the Kapitza resistance [Pol69], only a negligible fraction of the dissipated energy is transferred from the Au thermalization link into the Si on the right side of the substrate. In addition, it is important to mention that the elongated cooling fin is electrically insulated by SiO_2. Otherwise, the SQUID's shunt resistors would be electrically connected to the sample holder via the Au wire bonds, creating a short.

8.1.1 Fabrication of shunt resistors on membranes

The process that was developed within this thesis in order to fabricate shunt resistors on membranes for the HDMSQ2B detector is introduced in this section. The fabrication of these membranes was the last step in the fabrication of the entire wafer. A top view of the actual design schematic is illustrated in figure 8.2 a). Shown is the meander-shaped SQUID loop with two Josephson junctions connected in parallel. The particle absorbers and temperature sensors on top of the SQUID loop are omitted for visibility. The Au:Pd shunt resistors are located at a distance of $\sim 20\,\mu$m from the tunnel junctions. A long thermalization bridge made of electroplated Au is fully covering the elongated Au:Pd cooling fin in the schematic. The black areas denote an etch mask, where the thermal SiO_2 on the wafer is removed to expose the

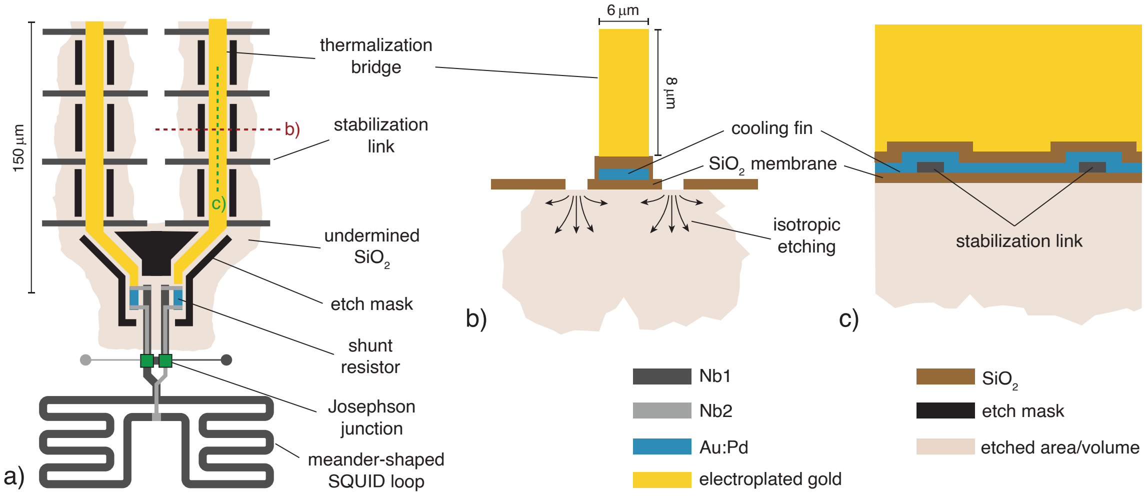

Figure 8.2: Schematic of the developed process to fabricate shunt resistors on membranes. a) Top view of the actual design sketch. The etch mask that is used to isotropically etch part of the Si substrate is marked in black. b) Cross section view of the thermalization bridge to illustrate the isotropic etching, creating floating membrane without any substrate below. c) Cross section view of a thermalization bridge at the location of the Nb stabilization links that are required to keep the membranes in place.

bare Si of the wafer. At these locations, the Si is isotropically etched, removing the substrate material below the thermalization bridges. This is further illustrated in figure 8.2 b), that shows a cross section of a thermalization bridge at the location marked by the red dashed line in a). The elongated Au:Pd cooling fin is depicted which is electrically insulated by SiO$_2$. It is situated on an SiO$_2$ membrane, as the Si substrate below is isotropically etched. Figure 8.2 c) shows a cross section of the thermalization bridge at the location marked by the green dashed line in a). Aside from the already mentioned structures, stabilization links made of Nb are depicted. These links are required to keep the membrane in place, as potential intrinsic stress in the electroplated gold on top would otherwise tear off the entire membrane. The links are made of Nb, as its thermal conductance is also highly reduced in its superconducting state compared to the normal conducting Au:Pd structures [Ens05]. Therefore, the Nb links transmit only a negligible fraction of the dissipated energy.

The 240 nm thermal SiO$_2$ were removed at the locations marked in black via ICP-RIE, for which the photoresist AZ 5214E was used for structuring the etch mask. The The ICP-RIE of the SiO$_2$ was done with CHF$_3$ at a pressure of $p_{\mathrm{ICP}} = 0.5\,\mathrm{Pa}$, an ICP-power of $P_{\mathrm{ICP}} = 500\,\mathrm{W}$, a substrate bias power of $P_{\mathrm{rf}} = 450\,\mathrm{W}$. The wafer was kept at a temperature of $T = 15\,°\mathrm{C}$, resulting in an etch rate $\dot{e}_{\mathrm{SiO_2}} \sim 1\,\mathrm{nm/s}$. Afterwards, the Si was etched isotropically to remove the substrate material that is located below the thermalization bridges. The Si etching was done via ICP-RIE with SF$_6$ at a pressure of $p_{\mathrm{ICP}} = 1.5\,\mathrm{Pa}$, an ICP-power of $P_{\mathrm{ICP}} = 650\,\mathrm{W}$, a substrate

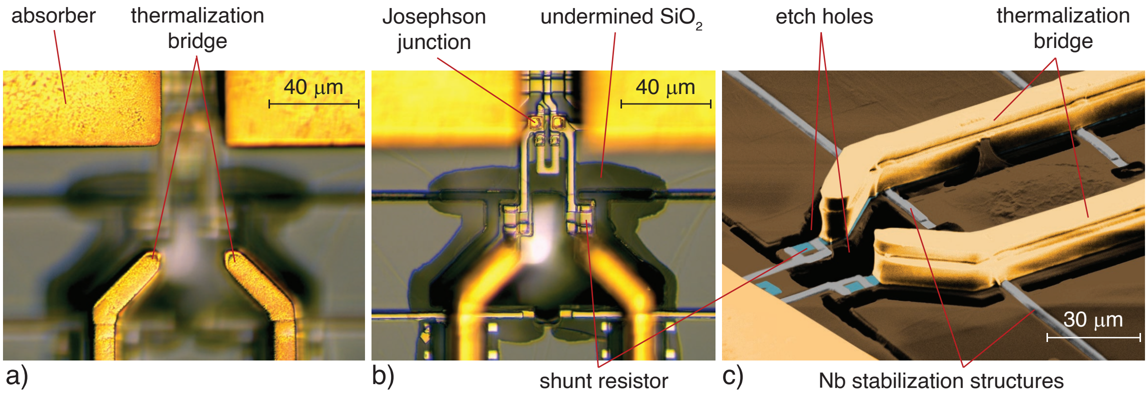

Figure 8.3: Structures of the HDMSQ2B detector with a focus on the fabricated shunt resistors on SiO$_2$ membranes. a) Microscope photo with the camera focus on the electroplated absorbers and thermalization bridges. b) Microscope photo of the same section as a) with the camera focus on the chip surface. c) Colorized electron microscope picture of the fabricated thermalization strucutres.

bias power of $P_{\mathrm{rf}} = 15\,\mathrm{W}$ and at a temperature $T = 0\,°\mathrm{C}$. The exact etch rate was unknown at that point, as the process was non-optimized and only tested three times prior to actual application. However, the undermined area is easy to see under a microscope, as the thermal SiO$_2$ is semi-transparent for visible light. Therefore, the Si etch process could be restarted several times until the desired magnitude of undermining was achieved. In order to isotropically etch the Si for $\sim 10\,\mu\mathrm{m}$ in each direction from the etch mask, an etch time of 15 minutes was required.

Figure 8.3 a) shows a microscope photograph of the section of interest of a fabricated HDMSQ2B detector with the camera focus set on the electroplated Au structures. The electroplated gold of the thermalization bridge has a total height of $8\,\mu\mathrm{m}$, given by the combined Au thickness of the absorber and its tetrapod, as was discussed in section 7.1.2. Figure 8.3 b) shows a microscope photograph of the same detector section with the camera focus set on the chip surface. Visible are the Josephson tunnel junctions of the dc-SQUID, its shunt resistors and also its washer shunt. Furthermore, the undermined semi-transparent SiO$_2$ layer can be seen, showing how the isotropic Si etching can be observed as a reliablilty check during fabrication. Figure 8.3 c) shows a colorized scanning electron microscope picture of the same chip section. The thermal conductance G of a single thermalization bridge can be calculated according to equation 7.1. With a length $l = 300\,\mu\mathrm{m}$, a height $h = 8\,\mu\mathrm{m}$, a width $w = 6\,\mu\mathrm{m}$ and a RRR of the electroplated gold between 10 and 40, the calculated thermal conductance G is between $32\,\mathrm{nW/K}$ and $138\,\mathrm{nW/K}$ at an assumed temperature of $T = 20\,\mathrm{mK}$.

8.2 HDMSQ2B detector chip

Aside from the already discussed custom thermalization scheme, the shunt resistors that are connected in parallel to the Josephson junctions have a size of $R_\mathrm{S} = 1.25\,\Omega$ in the HDMSQ2B detector, compared to $R_\mathrm{S} = 0.25\,\Omega$ in the HDMSQ2A detector. All other parameters are identical in both designs and should only show minor deviations, as both detectors were fabricated on the same wafer. Therefore, only the updated chip layout requires further illustration. Figure 8.4 shows an HDMSQ2B detector chip as it is glued on the corresponding sample holder. The chip is also identical to the HDMSQ2 chip, except for the discussed thermalization structures. Therefore, it consists of a 32 pixel linear array with each pixel having its own on-chip thermal bath. In the picture, the $300\,\mu$m long thermalization bridges are visible above the absorbers. The bridges terminate in a large thermalization pad made of electroplated gold, on which Au wire bonds are ultrasonic welded in order to create a good thermal contact with the sample holder. In addition, the chip also has a $1\,\mu$m thick thermalization layer on its backside that is made of sputtered Au to further improve the thermal coupling between substrate and sample holder, as it was discussed in section 7.3.7.

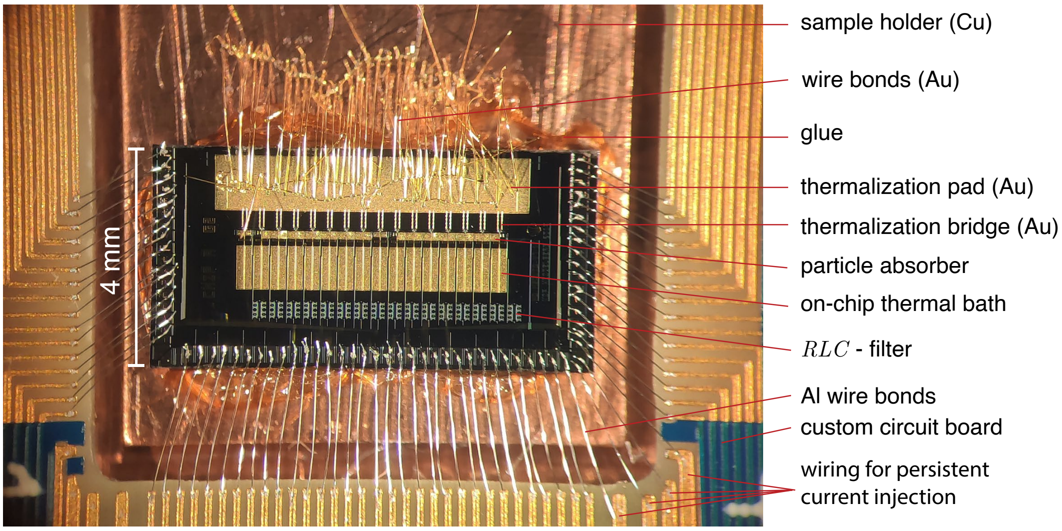

Figure 8.4: Photograph of the characterized HDMSQ2B detector chip mounted on its sample holder. Just like the HDMSQ2A, the chip hosts a linear detector array consisting of 16 integrated detectors. Each of the 32 pixels has its own on-chip thermal bath. The fabricated thermalization bridges for the shunt resistors are joined in a large pad made of electroplated gold. This pad is thermally linked to the sample holder via Au wire bonds.

8.3 Experimental results

This section discusses the characterization of the HDMSQ2B detector. Only the characterizations that correspond to the performed design changes will be discussed, as the chip is otherwise identical to the HDMSQ2A detector. This includes the impact of the on-chip energy dissipation on the signal height, the detector noise, as well as the achieved energy resolution.

8.3.1 Signal height

Figure 8.5 a) shows the measured signal height Φ_S as a function of the temperature of the mixing chamber platform for a 5.9 keV energy input. The measurement was also performed at $I_\mathrm{b} \approx 15\,\mu\mathrm{A}$, just like for the HDMSQ2A, and at an injected persistent current of $I_0 = 150\,\mathrm{mA}$. The data is in excellent agreement with the calculated signal height for a sensor height of $h_\mathrm{sens} = 0.6\,\mu\mathrm{m}$, which can be expected as both of the characterized chips (HMDSQ2A and HSMSQ2B) had a comparable distance to the wafer center, i.e. both chips experienced the same Ag:Er deposition rate during sensor fabrication. Furthermore, an increase in the sensor edge length of $4\,\mu\mathrm{m}$ was also accounting for, as it was discussed for the HDMSQ2A detector in section 7.3.3. The detector operation temperature can be deduced to be $T \approx 18\,\mathrm{mK}$, which is 5 mK less than the HDMSQ2A detector with additional Au thermalization layer on its backside has achieved, and 14 mK less than the HDMSQ1 detector achieved.

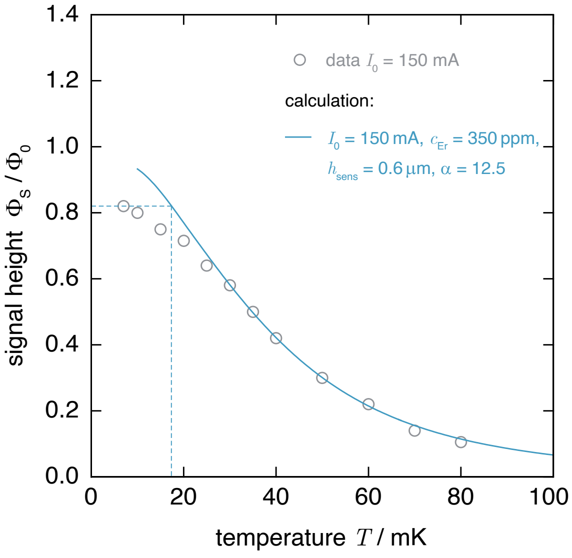

Figure 8.5: Measured signal height Φ_S for a 5.9 keV energy input as a function of the temperature T of the mixing chamber platform. The measurement was performed at a SQUID bias current of $I_\mathrm{b} \approx 15\,\mu\mathrm{A}$ and an injected persistent current of $I_0 = 150\,\mathrm{mA}$. Also depicted is the calculated signal height and the corresponding detector parameters, showing an excellent agreement between prediction and measurement. The chip thermally decouples from the cryogenic setup at $T \approx 18\,\mathrm{mK}$.

A signal amplitude of $\Phi_\mathrm{S} \approx 0.81\,\Phi_0$ was reached for a 5.9 keV energy input at the base temperature of the cryostat. This is the largest amplitude of all the detectors that were developed in this thesis. With this, the HDMSQ2B detector also surpassed the

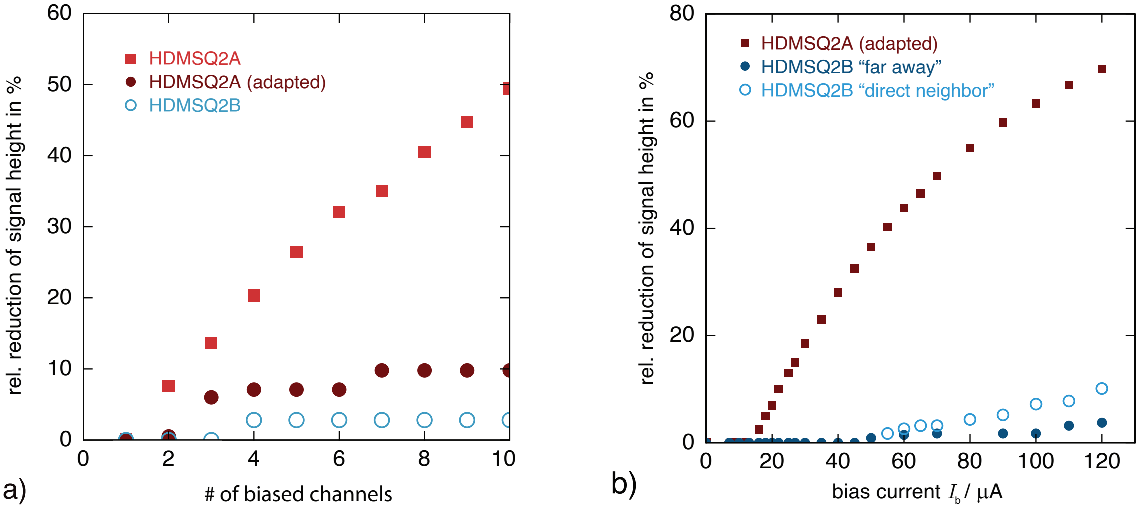

Figure 8.6: a) Relative reduction of the measured signal height Φ_S as a function of the number of biased dc-SQUIDs on the detector chip for the HDMSQ2A detector, for the adapted HDMSQ2A detector with an additional Au thermalization layer on its backside, as well as for the HDMSQ2B detector. b) Signal height Φ_S for a 5.9 keV energy input measured on a pixel on the left side of the chip as a function of the bias current I_b that is applied to a different detector channel on the chip. The shown data sets are explained in the text.

signal height of the revised maXs-20 detector (see section 2.8) by $\sim 0.25\,\Phi_0$ when it demonstrated its present MMC benchmark resolution of $\Delta E_{\mathrm{FWHM}} = 1.6\,\mathrm{eV}$ at 5.9 keV [Kem18], where it was operated at $T = 13\,\mathrm{mK}$ and at a persistent current of $I_0 = 45\,\mathrm{mA}$.

The effectiveness of the custom thermalization structures of the HDMSQ2A can also be ascertained by investigating a multi-pixel operation of the detector. Figure 8.6 a) shows the measured relative reduction of the signal height Φ_S as a function of the number of biased dc-SQUIDs on the chip for the regular HDMSQ2A detector ($I_b \approx 25\,\mu\mathrm{A}$), for the HDMSQ2A detector with Au thermalization layer on its backside ($I_b \approx 15\,\mu\mathrm{A}$), as well as for the HDMSQ2B detector ($I_b \approx 15\,\mu\mathrm{A}$). No relevant reduction in the measured signal height occurs when additional channels are biased on the HDMSQ2B detector. This indicates, that the customized thermalization structures work as intended. The full signal height is the one that was shown in figure 8.5. Thus, the signal height only reduced from $\sim 0.81\,\Phi_0$ to $\sim 0.78\,\Phi_0$ when 10 dc-SQUIDs were biased with a current of $I_b \approx 15\,\mu\mathrm{A}$.

To further illustrate the effectiveness of the custom thermalization structures, a measurement that was discussed at the end of the previous chapter was repeated. Figure 8.6 b) shows the relative reduction of the signal height Φ_S for a 5.9 keV energy input that was measured in a pixel located on the left side of detector chip as a function of the bias current I_b that was applied to a different detector channel on the chip. Three data sets are depicted in total. The one for the adapted HDMSQ2A detector (with Au on its backside) was already discussed at the end of the last chapter. The data set denoted by "far away" corresponds to the measured signal height for a pixel on the left of the HDMSQ2B detector when an additional SQUID was biased that is located on the right side of the chip $\sim 3\,\mathrm{mm}$ away from the observed pixel, just as it was the case for the data set corresponding to the adapted HDMSQ2A. The data shows, that the on-chip energy dissipation in the HDMSQ2B that results from an increased bias current barely has an impact on the operation temperature of the observed pixel, which is a significant improvement compared to the adapted HDMSQ2A. Furthermore, the last data set denoted as "direct neighbor" is for the measured signal height when the additionally biased channel was the direct neighbor of the observed channel, with a distance of only $\sim 300\,\mu\mathrm{m}$ between the two. Therefore, a position dependence of the on-chip energy dissipation was observed for the HDMSQ2B, since the measured signal height was further reduced when the direct neighbor was biased compared to when the additional energy was dissipated on the other side of the detector chip. While the dc-SQUIDs would never be operated at such high bias currents, the measurement strikingly illustrates how effective the custom shunt thermalization is compared to shunt resistors that are situated on the solid substrate. Furthermore, due to the improved shunt thermalization, the dc-SQUIDs could be operated at their optimum working point without leading to a reduction of the measured signal height for the first time.

8.3.2 Detector noise

Figure 8.7 shows the measured white noise level at a frequency of $f = 10^5\,\mathrm{Hz}$ as a function of the temperature T of the mixing chamber platform for the HDMSQ2A and the HDMSQ2B detector. The former data was acquired at a non-optimal SQUID bias current of $I_\mathrm{b} \approx 15\,\mu\mathrm{A}$, for which no reduction of the signal height was observable, and which was used to determined the energy resolution of the HDMSQ2A detector, as it was discussed in section 7.3.6. The depicted data for the HDMSQ2B detector was acquired at its optimum working point of $I_\mathrm{b} \approx 19\,\mu\mathrm{A}$. This SQUID bias current was also applied for the determination of the energy resolution of the HDMSQ2B detector, as it will be discussed in the next section. Thus, the white noise level of the HDMSQ2B detector when operated at its optimum working point is reduced by a factor of ~ 1.6 compared to the HDMSQ2A detector, when the latter is operated at the closest point to its optimum working point without reducing the signal height due to the on-chip energy dissipation. Therefore, it can be expected that the HDMSQ2B detector might achieve an enhanced energy resolution, especially when considering that it also achieved an $\sim 8\,\mathrm{mK}$ lower operation temperature.

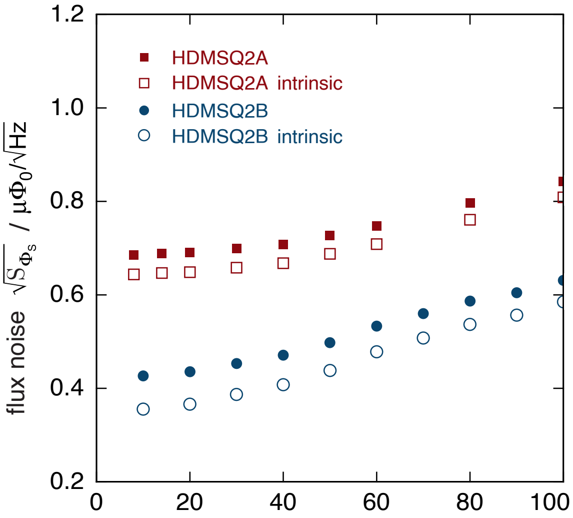

Figure 8.7: Comparison of the measured white noise level between the HDMSQ2A and the HDMSQ2B detector as a function of the temperature T of the mixing chamber platform. The chosen bias currents were $I_\mathrm{b} \approx 15\,\mu\mathrm{A}$ (non-optimal) and $I_\mathrm{b} \approx 19\,\mu\mathrm{A}$ (optimal), respectively. For the data sets denoted as "intrinsic", the noise contribution of the room temperature electronics was subtracted.

In addition, figure 8.7 also depicts data sets that are denoted with "intrinsic". For these, the noise contribution of the room temperature electronics was subtracted from the measured white noise level (see section 3.3.4). This means for the HDMSQ2B detector, that the noise contribution of the utilized XXF-1 electronics increases the total white noise level by $\sim 17\,\%$. As a result, the detector performance is slightly degraded and can not achieve its full potential with the employed two-stage readout. As it was already discussed in section 7.3.5, this can be for instance addressed by increasing the number of constituting SQUID cells in the design of the N-SQUID series array amplifiers, consequently increasing the flux-to-flux amplification G_Φ of the two-stage SQUID readout.

8.3.3 Energy resolution

In order to determine the energy resolution of the HDMSQ2B detector, it was operated at a SQUID bias current of $I_\mathrm{b} \approx 19\,\mu\mathrm{A}$ and with an injected persistent current of $I_0 = 150\,\mathrm{mA}$. The operation temperature of the detector was $T \approx 18\,\mathrm{mK}$. No active temperature stabilization was used during the measurement, i.e. the mixing chamber platform was operated at its base temperature of $T \approx 7\,\mathrm{mK}$, resulting in the detector being exposed to the intrinsic temperature fluctuations of the cyostat. In order to determine its baseline resolution, the χ^2-fit signal analysis method was applied to untriggered noise traces that were acquired during the measurement. The histogram resulting from this calculation is plotted in figure 8.8 a). A Gaussian distribution with an instrumental linewidth of $\Delta E_\mathrm{FWHM} = 1.3\,\mathrm{eV}$ is fitted to the data, indicating the intrinsic energy resolution of the HDMSQ2B detector in this setup. Figure 8.8 b) shows the measured energy spectrum of the K_α-line of the $^{55}\mathrm{Fe}$ X-ray calibration source. The curve fitted to the data is a convolution of the natural linewidth of

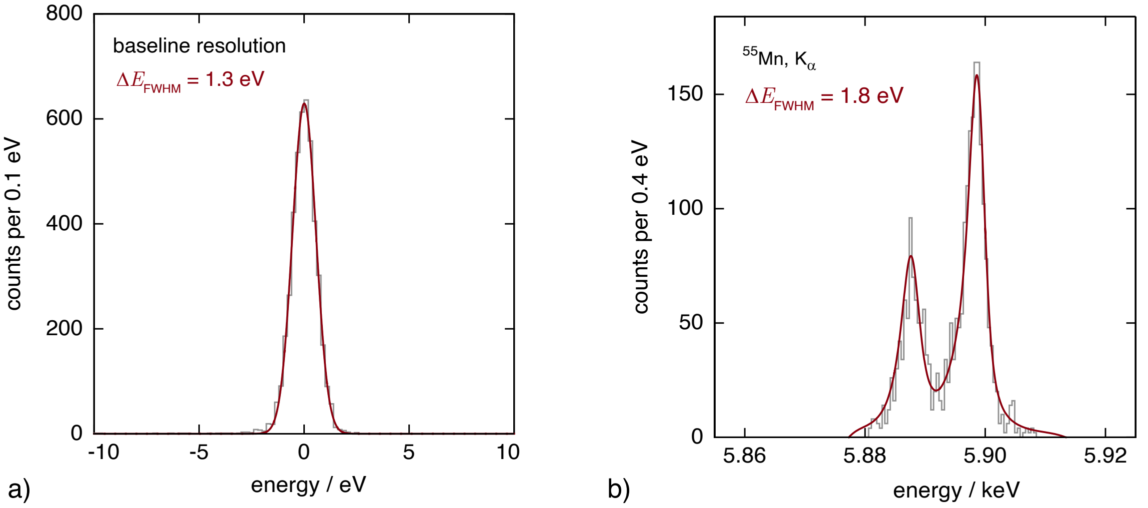

Figure 8.8: Histogram of the measured signal amplitudes of the HDMSQ2B detector. a) Superimposed is a Gaussian distribution with a full-width-half-maximum value $\Delta E_{\mathrm{FWHM}} = 1.3\,\mathrm{eV}$, indicating the baseline resolution of the HDMSQ2B detector. b) Measured energy spectrum of the K$_\alpha$-line of the ^{55}Fe X-ray calibration source. Fitted to the data is a convolution of the natural linewidth of the K$_\alpha$-line and a Gaussian distribution with an instrumental energy resolution of $\Delta E_{\mathrm{FWHM}} = 1.8\,\mathrm{eV}$. A bias current of $I_{\mathrm{b}} \approx 19\,\mu\mathrm{A}$ and a persistent current of $I_0 = 150\,\mathrm{mA}$ were used for these measurementsm where the detector has an operation temperature of $T \approx 18\,\mathrm{mK}$.

the K$_\alpha$-line and a Gaussian distribution with an instrumental energy resolution of $\Delta E_{\mathrm{FWHM}} = 1.8\,\mathrm{eV}$. The data was corrected for temperature drifts of the cryogenic setup, as it was discussed in section 6.5.6, and it was acquired in a timeframe of 6 hours.

The expected energy resolution of the detector for the chosen operation parameters is $\Delta E_{\mathrm{FWHM}} = 0.64\,\mathrm{eV}$. This calculation also accounted for the higher than expected Er concentration, the reduced sensor height, as well as the slightly increased sensor area. Similar to what was observed for the HDMSQ2A detector, the determined baseline resolution of the HDMSQ2B detector degraded by a factor of ~ 2 compared to the expected one. This can again be most likely attributed to the used χ^2-fit signal analysis method, as it was discussed in section 4.3, as well as in section 7.3.6, but requires further verification once a signal analysis algorithm based on optimal filtering is available in the coming months. Furthermore, the detector was exposed to the quite substantial intrinsic temperature fluctuations of the mixing chamber platform, as it was shown in figure 7.14, making these the most likely candidate for causing the additional degradation of the energy resolution at 5.9 keV.

While the HDMSQ2B detector was not able to surpass the benchmark energy resolution of $\Delta E_{\mathrm{FWHM}} = 1.6\,\mathrm{eV}$ at 5.9 keV of the revised maXs-20 detector [Kem18], it came rather close. When the revised maXs-20 detector achieved this benchmark, it was operated at a temperature of $T = 13\,\mathrm{mK}$ with a determined baseline resolution of $\Delta E_{\mathrm{FWHM}} = 1.5\,\mathrm{eV}$, which is only 0.1 eV lower than its determined resolution at 5.9 keV. Furthermore, the corresponding signal analysis was done with an algorithm based on optimal filtering, which was not available in this thesis. Thus, it is very likely that the determined baseline resolution of the HDMSQ2B detector, as well as its determined resolution at 5.9 keV might show a further improvement once the signal analysis based on optimal filtering is available again. Such a program which also fits to the file format of the used DAQ system that was used in this thesis is currently in development and should be available in the coming months. Then, the data of the HDMSQ2B detector can be re-evaluated in order to see whether or not the used χ^2-fit algorithm truly led to such a significant degradation in the determined energy resolution.

Since the temperature fluctuations of the cryogenic system most likely played an important role in the degradation of the energy resolution in this thesis, one can also expect that a thermometry system with an enhanced temperature resolution is required in order to exploit the full potential of the HDMSQ2B detector and potentially demonstrate an energy resolution below 1 eV at 5.9 keV. In linear approximation, the required temperature resolution would be in the range of $\Delta T/T \approx 5 \cdot 10^{-5}$. A prototype thermometry system that can achieve this is currently in development in this group, with a first characterization done in [Ger17]. At a temperature of $T = 14\,\mathrm{mK}$, the prototype achieved a temperature resolution of $\Delta T/T \approx 1.7 \cdot 10^{-4}$ with a signal integration time of only 100 ms. For comparison, the thermometry of the cryostat that was used in this thesis achieves a temperature resolution of $\Delta T/T \approx 6.4 \cdot 10^{-4}$ at $T = 14\,\mathrm{mK}$, but with a signal integration time of 3 seconds. Using the same integration time for the prototype that was characterized in [Ger17] would yield a temperature resolution of $\Delta T/T \approx 0.3 \cdot 10^{-5}$, which would be more than sufficient for the operation of the HDMSQ2B detector.

8.3.4 Summary and outlook

This chapter discussed the HDMSQ2B detector, which differs from the HDMSQ2A detector in basically just a single key factor. Implemented in this detector was a custom-designed microfabricated thermalization for the shunt resistors of the dc-SQUIDs on the chip, so that their dissipated energy is no longer transferred to the detector substrate, but directly dissipated into the sample holder. The characterization of the HDMSQ2B in this chapter showed, that these thermalization structures reduce the effect of the on-chip energy dissipation on the detector performance to such a degree, that for the first time, a satisfying multi-pixel operation of the integrated detectors could be demonstrated, as well as the operation of the dc-SQUIDs at their optimum working point where they exhibit their optimum noise performance. The detector reached an operation temperature of $T \approx 18\,\mathrm{mK}$, which is 14 mK lower than the HDSMQ1 achieved, 8 mK lower than the HDMSQ2A detector reached, and 2 mK lower that the original target value that was assumed for the detector optimizations according to numerical simulations.

The expected energy resolution of the HDSMQ2B detector for the used operation parameters is $\Delta E_{\mathrm{FWHM}} = 0.64\,\mathrm{eV}$, whereas a baseline energy resolution of $\Delta E_{\mathrm{FWHM}} = 1.3\,\mathrm{eV}$ could be demonstrated. The discrepancy between the two can be most likely attributed to the used χ^2-fit signal analysis method, which was shown to degrade the determined energy resolution compared to the method of optimal filtering (see section 4.3). The determined energy resolution at 5.9 keV X-ray energy further degraded to $\Delta E_{\mathrm{FWHM}} = 1.8\,\mathrm{eV}$. This can be attributed to temperature fluctuations of the cryogentic setup. Its thermometry and PID controlled temperature stabilization is insufficient at $T = 20\,\mathrm{mK}$ in order to provide a temperature stability that would be required for a detector with a potential energy resolution below 1 eV. Therefore, no temperature stabilization was used and the cryostat was operated at its baseline temperature of $T \approx 7\,\mathrm{mK}$ to yield the largest possible signal height, while the data analysis relied on the temperature information that was acquired on a non-gradiometric detector channel. Lastly, it was shown that the flux-to-flux amplification of the employed two-stage SQUID readout was insufficient in order to make the noise contribution of the room temperature SQUID electronics fully negligible, which led to a further limitation of the detector performance.

In the end, a new MMC benchmark energy resolution for 5.9 keV photons could not be demonstrated with the developed HDMSQ2B detector within this thesis. However, the detector characterization showed highly promising results, indicating that it can surpass the current MMC resolution benchmark of $\Delta E_{\mathrm{FWHM}} = 1.6\,\mathrm{eV}$ and push towards an energy resolution below 1 eV. Furthermore, the detector characterization also showed, that its performance is fully predictable by the theoretical model of metallic magnetic calorimeters. Future developments of this readout scheme will also incorporate the SQUID geometry into the detector optimizations according to numerical simulations, resulting in further enhancements for the intrinsic energy resolution of such an MMC, where detector responses with a signal amplitude far beyond $1\,\Phi_0$ for a 5.9 keV energy input will become a common occurrence at the already demonstrated operation temperatures.

9. Summary and outlook

This thesis discusses the development of a novel type of cryogenic micro-calorimeter for the high-resolution X-ray spectroscopy. This detector is based on the general concept of metallic magnetic calorimeters (MMCs), which are energy dispersive particle detectors operated at millikelvin temperatures, that combine a large energy bandwidth, an excellent energy resolution, a fast signal rise time, and a close to perfect linear detector response. MMCs make use of a particle absorber that is in good thermal contact with a paramagnetic temperature sensor, the latter being magnetized by a weak external magnetic field. The temperature increase of the detector that follows upon particle absorption changes the sensor magnetization $M(T)$, which leads to a change of magnetic flux in a superconducting pickup coil that is placed in close proximity to the temperature sensor. This magnetic flux change is usually read out via a superconducting flux transformer with a current sensing dc-SQUID. The latter is a flux-to-voltage transducer that can achieve a quantum-limited noise performance. Using this readout scheme, a present day benchmark energy resolution of $\Delta E_{\mathrm{FWHM}} = 1.6\,\mathrm{eV}$ at an X-ray energy of $5.9\,\mathrm{keV}$ was achieved [Kem18].

Standard MMC detectors, like the one used in the high-resolution experiment mentioned above, use a superconducting flux transformer, which has a number of advantages but impede the optimal flux coupling. The latter is due to the fact that proper transformer matching is hard to achieve, and the transformer coupled energy sensitivity is degraded by a factor of 4 compared to the energy sensitivity of the SQUID itself. The aim of this thesis was to overcome this problem, by developing an integrated design of readout SQUID and detector in which a flux transformer can be omitted. In this device, the paramagnetic temperature sensor of the MMC was placed directly into the superconducting loop of the dc-SQUID. However, the fabrication of integrated detectors is much more challenging than fabricating detector and SQUID individually. In addition, intrinsic effects of the SQUID, like its Joule power dissipation, needed to be taken care of.

The first step towards such a high performance many-pixel detector that makes use of this readout scheme was the design and development of a dc-SQUID with meander-shaped pickup coil, as well as its microfabrication and optimization. Within this context, the state-of-the-art anodization-free microfabrication process for Nb/Al-$\mathrm{AlO_x}$/Nb window-type Josephson tunnel junctions used within this research group needed to be optimized in order to guarantee the predictability of the device parameters. This optimization includes the investigation of the surface morphology of thin films used for the creation of Josephson tunnel junctions via atomic force microscopy, as well as the investigation of a potential hydrogen contamination of microfabricated niobium structures, which spoils the ampacity of fabricated wiring structures. The developed dc-SQUID is a first-order gradiometer, that is build by a parallel connection of two meander-shaped pickup coils. This allows for a readout of two temperature sensors with a single dc-SQUID. The aim of the SQUID design was a low noise device without any intrinsic resonances in its characteristics, that is read out in a flux locked loop operation mode as a front end SQUID in a two-stage SQUID setup. Furthermore, its geometry should be optimized to allow for the production of a densely packed two dimensional detector array of these integrated detectors. A device that the possesses these properties was successfully developed within this thesis.

Based on this dc-SQUID, three prototypes of integrated detectors were developed, fabricated and characterized. The first is a 8×8 pixel array with 32 integrated detectors. Each pixel is represented by a particle absorber made of electroplated gold with a detection area of $150\,\mu\mathrm{m} \times 150\,\mu\mathrm{m}$ and a thickness of $3\,\mu\mathrm{m}$, providing a quantum efficiency of $100\,\%$ for photons below $5\,\mathrm{keV}$ energy, and $\sim 50\,\%$ for $10\,\mathrm{keV}$ photons. The paramagnetic temperature sensor of each pixel is made of the alloy Ag:Er with an erbium concentration of $c_{\mathrm{Er}} = 450\,\mathrm{ppm}$ and a dimension of $50 \times 50 \times 1.2\,\mu\mathrm{m}^3$, two of which are placed directly on top of the planar meander-shaped SQUID loop in the design. The expected energy resolution at an operation temperature of $T = 20\,\mathrm{mK}$ was $\Delta E_{\mathrm{FWHM}} = 1.3\,\mathrm{eV}$. In practice, the fully operational detector array achieved a baseline resolution of $\Delta E_{\mathrm{FWHM}} = 4.2\,\mathrm{eV}$, which is the intrinsic energy resolution of the detector in the limit of low photon energies $E_\gamma \to 0\,\mathrm{keV}$, and an energy resolution of $\Delta E_{\mathrm{FWHM}} = 8.9\,\mathrm{eV}$ at an energy of $5.9\,\mathrm{keV}$. Thus, the first detector with integrated SQUID readout that was developed within this thesis is a quite successful proof of principle, whose characterized features were also in excellent agreement the theoretical model. Furthermore, all design intrinsic performance limiting factors were identified with the characterization of this detector, which allowed for its purposeful redesign in a second development iteration in order to exploit the full potential of this readout scheme. The identified factors that limited the detector performance were the on-chip energy dissipation of the dc-SQUIDs, unresolvable signal rises due to very large and very fast detector responses, as well as athermal phonon loss.

The second prototype addressed the identified problems, where two different ideas were explored in order to deal with the SQUID's energy dissipation. In one prototype, the energy dissipation was reduced by reducing the shunt resistance of the Josephson tunnel junctions to the milliohm range, which is possible without performance loss as the SQUID is read out under voltage bias in a two-stage SQUID setup. There, the critical current modulation of the front end SQUID is one of the performance defining properties, which is unaffected by a reduction of the SQUID's shunt resistance. Furthermore, a thermal bottleneck between the absorber and the temperature sensor was introduced in order to slow down the signal rise to make it fully resolvable. Within the available detector channels on one chip, different dimensions of this thermal link were implemented to successfully demonstrate the general concept, as well as the predictable adjustability of the signal rise time. In a final detector that is not suffering from SQUID or experimental setup intrinsic limitations, the rise time will then be adjusted to a value that allows for the readout of the largest signals in the target energy range using a commercial high speed SQUID electronics.

The loss of athermal phonons was reduced to a non-observable level by a introducing a "tetrapod" absorber geometry that avoids a direct line-of-sight of athermal phonons to the substrate. In addition, a potential thermal crosstalk between neighboring pixels was reduced by changing the chip layout from an 8×8 pixel array to a 32 pixel linear array, which allowed for an enhanced detector thermalization by providing an on-chip thermal bath for every individual pixel. This scheme can also be incorporated in future two dimensional detector arrays with this integrated detector design. With a further optimization according to numerical simulations, the expected energy resolution of this detector at $T = 20\,\mathrm{mK}$ is $\Delta E_{\mathrm{FWHM}} = 0.53\,\mathrm{eV}$. In characterization measurements it achieved a baseline resolution of $\Delta E_{\mathrm{FWHM}} = 1.7\,\mathrm{eV}$ at an energy of $0\,\mathrm{keV}$, and a resolution of $\Delta E_{\mathrm{FWHM}} = 2.4\,\mathrm{eV}$ at an energy of $5.9\,\mathrm{keV}$. It turned out that despite this improvement, the energy resolution was still limited by the SQUID's energy dissipation. The chip thermally decoupled from the cryostat at $T = 26\,\mathrm{mK}$ when using a low-bias operation of the SQUID, resulting in a non-optimal working point and hence an increased white noise level. For high biasing, the SQUID showed excellent performance. However, the detector thermally decouples and reaches operation temperatures above $40\,\mathrm{mK}$, degrading the energy resolution.

The second improved prototype that was developed in order to deal with SQUID's energy dissipation is based on a custom-designed on-chip thermalization for the shunt resistors of the dc-SQUIDs. This scheme thermally decouples the shunt resistors from the detector substrate by placing them on thin $\mathrm{SiO_2}$ membranes, and provides a thermalization link made of electroplated Au, so that the dissipated energy thermalizes directly with the sample holder via this metallic link. This thermalization scheme not only allowed for a SQUID operation at its optimal working point, but also a satisfying multi-pixel operation could be demonstrated. Aside from these novel thermalization structures, this prototype has a slightly higher shunt resistance, but is otherwise identical to previously discussed. Therefore, its expected energy resolution at $T = 20\,\mathrm{mK}$ is also $\Delta E_{\mathrm{FWHM}} = 0.53\,\mathrm{eV}$. The prototype achieved an operation temperature of $T = 18\,\mathrm{mK}$, a baseline energy resolution of $\Delta E_{\mathrm{FWHM}} = 1.3\,\mathrm{eV}$ at an energy of $0\,\mathrm{keV}$, and an energy resolution of $\Delta E_{\mathrm{FWHM}} = 1.8\,\mathrm{eV}$ at an energy of $5.9\,\mathrm{keV}$. This clearly shows, that such a detector can reach a performance comparable with the best micro-calorimeters world wide and has the potential to be even better. The small degradation from the expected theoretical value for the energy resolution where to due to several factors, that are not intrinsic to this kind of detector: Small temperature fluctuations of the cryogenic setup and the use of a simple least square fit pulse analysis are responsible for the major part of the degradation. These two effects can be improved in the near future. A signal analysis software based on optimal filtering that can handle the data coming from the used DAQ system should be available in the coming months, whereas a highly promising prototype of a thermometry system that has the required temperature resolution was already characterized by [Ger17].

The foundation created by this integrated detector that was developed in this thesis will be an important basis for future high resolution MMC developments in order to push their resolving power far beyond 10000 for soft X-ray detection in the coming years, making them one of the best X-ray spectrometers available. The developed detector is already an excellent candidate for instance for the operation on electron beam ion traps, where lighter highly charged ions are investigated via X-ray spectroscopy. Therefore, it can play an important role in expanding our knowledge in the field of atomic physics, as well as in the creation of astrophysical and cosmological models, to understand the inner workings of our stars and of other stellar phenomena.

A. Appendix

A.1 Microfabrication

The detector development that was carried out within the framework of this thesis relied heavily on photo-lithography and thin-film deposition techniques executed in a cleanroom environment. This included the application of standardized processes, the optimization of already established ones, and the development of completely new procedures that were previously not established in this group. This section introduces essential basics of the applied microfabrication techniques that are relevant for the understanding of the discussed processes within this thesis. The depiction of developed fabrication processes for a specific detector is be made in its corresponding chapter. The detectors that were developed in this thesis consist of up to 20 lithographic layers, all which are successively deposited onto a substrate. The fabrication of the developed metallic magnetic calorimeters was realized in the in-house, class DIN ISO 5 cleanroom, in which the detectors were microfabricated via UV-lithography, dc-magnetron sputtering, inductively coupled plasma reactive ion etching (ICP-RIE), wet etching and electroplating.

A.1.1 Photoresists

The photoresists that were used in this thesis are uniformly applied in liquid form onto a solid substrate via standard spin-coating, followed by a subsequent baking on a hot plate in order to reduce the residual solvent content. Afterwards, the photoresist is exposed to UV light in order to structure the desired design layer into the resist. This is usually done by placing a corresponding photomask between the substrate and the UV light source. For a so called positive resist, exposed areas increase their solubility for an appropriate solvent, usually an alkaline developer liquid. For a so called negative resist, exposed areas polymerize, leading to a reduction of their solubility for an appropriate developer.

Substrate: The utilized substrates were high-purity 3 inch silicon wafers with a thickness of $375 \pm 25\,\mu$m, that are also electrically insulated by 240 nm of thermal SiO_2.

Photoresists: The utilized AZ[1] photoresists and their fabrication parameters are summarized in table A.1.

---

[1] AZ Electronic Materials; now part of Merck Performance Materials GmbH

photoresist / property	AZ 5214E (negative)	AZ MIR 701 29 cp (positive)	AZ nLOF 2070 (negative)	AZ 4533 (positive)
spin-coat	500 rpm, 7 s 3000 rpm, 30 s	500 rpm, 7 s 4000 rpm, 30 s	500 rpm, 7 s 3000 rpm, 30 s	500 rpm, 7 s 3000 rpm, 30 s
thickness	1.4 µm	1.6 µm	~ 7 µm	~ 4 µm
softbake	100 °C, 60 s	90 °C, 90 s	100 °C, 10 min	100 °C, 3 min or 80 °C, 12 min
UV exposure	100 mJ/cm^2	280 mJ/cm^2	350 mJ/cm^2	350 mJ/cm^2
post exposure bake	120 °C, 120 s (image reversal)	110 °C, 90 s	115 °C, 120 s	—
developer	AZ Developer (1:1) H_2O:Dev	AZ Developer (1:1) H_2O:Dev	AZ 826 MIF	AZ 826 MIF
used for	Lift-off, except for Ag:Er sensor	ICP-RIE of Nb	Lift-off of Ag:Er sensor	fabrication of particle absorbers

Figure A.1: Overview of the utilized photoresists, their fabrication parameters and their use.

A.1.2 UV-lithography:

Two separate systems were used for the UV exposure of photoresist. The first was the mask-aligner Süss MJB3[2], in which chrome-coated photomasks[3] could be used. However, this machine was succeeded by a maskless aligner and it was therefore only used for a UV flood exposure for the image reversal procedure of the AZ 5214E photoresist.

For microstructuring, the individual design layers were written directly into the photoresist via the maskless UV-laser writer MLA150[4]. The machine provides a high resolution and high aspect-ratio exposure down to a structure size of 1.0 μm and a structure alignment accuracy of 0.5 μm over the area of a 3 inch wafer. Its light source is a 2.8 W diode laser with a wavelength of 375 nm. The exposure of a 3 inch wafer coated with the AZ 5214E, given the exposure parameters in table A.1, requires $\sim$ 25 minutes and scales linearly with the UV exposure dose.

Design software: The respective layers of the detector designs were created with the Cadence Virtuoso Layout Suite[5] and saved in the GDS file format to be used with the MLA150.

---

[2] Süss MicroTec AG, Schleissheimer Straße 90, 85748 Garching, www.suss.com

[3] Clean Surface Technology Inc., 3-20-29, Omagari, Samukawamachi, 253-0113 Koza-Gun, Japan

[4] HIMT MLA 150; Heidelberg Instruments Mikrotechnik GmbH

[5] https://www.cadence.com

A.1.3 Material deposition:

The thin film deposition was done via sputter deposition in two separate facilities. In this physical vapor deposition (PVD) method, a target material is usually bombarded by argon ions, which remove (sputter) either single atoms or clusters of atoms from the target material. The latter then redeposits onto the surface of a substrate, resulting in a homogeneous thin film deposition, assuming ideal conditions.

Alcatel SCM 601: The Alcatel SCM 601 system has a base pressure of $5 \cdot 10^{-5}\,\mathrm{Pa}$ and provides rf-sputtering of the insulator $\mathrm{SiO_2}$. This is done at a sputter power of $P_{\mathrm{rf}} = 250\,\mathrm{W}$, an $\mathrm{Ar/O_2}$ ($60\,\%/40\,\%$) pressure $p_{\mathrm{Ar/O_2}} = 0.7\,\mathrm{Pa}$, and a deposition rate $\dot{d}_{\mathrm{SiO_2}} = 1.3\,\mathrm{nm/min}$.

UHV sputtering system: The main ultra-high vacuum (UHV) sputtering system[6] has a base pressure of $4 \cdot 10^{-7}\,\mathrm{Pa}$ created by a cryogenic pump. The facility provides dc-magnetron sputtering of five different metallic targets, i.e. Nb, Al, Au, Au:Pd and Ag:Er, and also supports rf-sputtering of $\mathrm{SiO_2}$. A co-sputtering of neighboring target materials within the facility is also possible, but this option was not required for the fabrication of the detectors. Part of the main sputtering facility is a load lock chamber with a base pressure of $1 \cdot 10^{-4}\,\mathrm{Pa}$, which is created by a scroll pump and a turbomolecular pump. During the deposition procedure, the wafer is rotated around its center axis while staying in good thermal contact with the copper substrate holder, with the latter functioning as a heat sink. The following deposition parameters were used, all performed at $T = 300\,\mathrm{K}$:

- Niobium: Becomes superconducting at $T < 9.2\,\mathrm{K}$ and was used for all on-chip wiring and the superconducting constituents of the developed metallic magnetic calorimeters and dc-SQUIDs. Its deposition was done at a sputtering power $P = 400\,\mathrm{W}$, an Ar pressure of $p_{\mathrm{Ar}} = 0.27\,\mathrm{Pa}$, and with a deposition rate of $\dot{d}_{\mathrm{Nb}} = 0.74\,\mathrm{nm/s}$.
- Aluminium: Becomes superconducting at $T < 1.2\,\mathrm{K}$ and was used for the fabrication of Nb/Al-$\mathrm{AlO_x}$/Nb Josephson tunnel junctions. Its deposition was done at a sputtering power $P = 200\,\mathrm{W}$, an Ar pressure of $p_{\mathrm{Ar}} = 0.27\,\mathrm{Pa}$ or $p_{\mathrm{Ar}} = 1.33\,\mathrm{Pa}$, and with a deposition rate $\dot{d}_{\mathrm{Al}} \approx 0.26\,\mathrm{nm/s}$.
- Au: Used for detector thermalization structures and for the absorber fabrication process. Its deposition was done at a sputtering power of $P = 200\,\mathrm{W}$, an Ar pressure of $p_{\mathrm{Ar}} = 1.33\,\mathrm{Pa}$, and with a deposition rate of $\dot{d}_{\mathrm{Au}} = 2.2\,\mathrm{nm/s}$.
- Au:Pd: Used for normal conducting structures at millikelvin temperatures, i.e. shunt resistors in the developed dc-SQUIDs, as well as the persistent

---

[6] DCA Instruments Oy

current switch of the detector. Its deposition was done at a sputtering power of $P = 100\,\mathrm{W}$, an Ar pressure of $p_{\mathrm{Ar}} = 1.33\,\mathrm{Pa}$, and a deposition rate of $\dot{d}_{\mathrm{Au:Pd}} = 0.86\,\mathrm{nm/s}$.

- Ag:Er: Used as sensor material for the developed MMCs. The targets are in-house fabricated 2 inch wafers with a thickness of a few millimeters and are prepared with fixed Er concentrations, usually in the range of $c_{\mathrm{Er}} = 250 - 450\,\mathrm{ppm}$. The deposition was done at a sputtering power of $P = 200\,\mathrm{W}$, an Ar pressure of $p_{\mathrm{Ar}} = 1.33\,\mathrm{Pa}$ and a deposition rate $\dot{d}_{\mathrm{Ag:Er}} = 4.65\,\mathrm{nm/s}$. The erbium concentration of the Ag:Er sensor after deposition is determined for every fabricated wafer in an independent measurement of the residual Ag:Er after the Lift-Off process. The measurement is done in a commercial SQUID magnetometer system[7].
- SiO_2: Used for electrical insulation. Its deposition was done at a sputtering power of $P = 250\,\mathrm{W}$, an Ar/O_2 (60 %/40 %) pressure of $p_{\mathrm{Ar/O_2}} = 0.67\,\mathrm{Pa}$, and a deposition rate of $\dot{d}_{\mathrm{SiO_2}} = 1.73\,\mathrm{nm/min}$.

A.1.4 Substrate cleaning

Ar ion milling: Part of the load lock chamber of the UHV sputtering system is an ion gun that was used for substrate cleaning via Ar ion milling prior to nearly every sputter deposition procedure. The bombardment with Ar removes for instance monolayers of H_2O, or sputters material on the surface of the substrate, removing for instance residual material or natural oxide layers on metallic structures. The standard Ar ion milling procedure was done for 1 minute at a pressure of $p_{\mathrm{Ar}} = 7 \cdot 10^{-2}\,\mathrm{Pa}$ and an acceleration voltage of 300 V. The thereby achieved removal rate for material was for instance $\dot{r}_{\mathrm{Au}} \approx 20\,\mathrm{nm/min}$ for Au, or $\dot{r}_{\mathrm{Nb}} \approx 6\,\mathrm{nm/min}$ for niobium.

A.1.5 Material etching

Inductively Coupled Plasma - Reactive Ion Etching (ICP-RIE): ICP-RIE was done in the plasma etcher SI 500C[8]. In such a facility, a low pressure plasma is ignited by an electromagnetic field. The thereby created high energy ions chemically react with the material on the substrate surface and are then pumped away. Therefore, a constant reflow of gas has to be provided during the etching process. In this thesis, ICP-RIE was used for the structuring of three materials:

---

[7] QD MPMSR XL from Quantum Design Inc, 10307 Pacific Center Court, San Diego, CA 92121, USA

[8] SENTECH Instruments GmbH

- Niobium: Nb was etched in a $p_{\mathrm{ICP}} = 2\,\mathrm{Pa}$ SF_6 atmosphere, with a substrate bias power of $P_{\mathrm{rf}} = 50\,\mathrm{W}$ and an ICP-power of $P_{\mathrm{ICP}} = 100\,\mathrm{W}$. The wafer was kept at 5 °C during this process, resulting in an etch rate of $\dot{e}_{\mathrm{Nb}} \sim 1\,\mathrm{nm/s}$.

- SiO_2: For the HDMSQ3 detector that was developed in this thesis, the thermal oxide on a silicon wafer was partly removed by dry etching in a CHF_3 plasma. This was done at gas pressure of $p_{\mathrm{ICP}} = 0.5\,\mathrm{Pa}$, an ICP-power of $P_{\mathrm{ICP}} = 500\,\mathrm{W}$, a substrate bias power of $P_{\mathrm{rf}} = 450\,\mathrm{W}$, at a temperature of $T = 15\,^{\circ}\mathrm{C}$ with an etch rate $\dot{e}_{\mathrm{SiO_2}} \sim 1\,\mathrm{nm/s}$.

- Si: Isotropic etching of the Si substrate was required for the fabrication of the HDMSQ3 detector in this thesis. The isotropic etching was done via ICP-RIE with SF_6 at a pressure of $p_{\mathrm{ICP}} = 1.5\,\mathrm{Pa}$, an ICP-power $P_{\mathrm{ICP}} = 650\,\mathrm{W}$, a substrate bias-power of $P_{\mathrm{rf}} = 15\,\mathrm{W}$ and at a temperature $T = 0\,^{\circ}\mathrm{C}$. The exact etch rate was not determined, but can be estimated to be between $2\,\mu\mathrm{m/min}$ and $2.6\,\mu\mathrm{m/min}$.

Wet etching: Wet etching was required for one fabrication process in this thesis. The Al-AlO_x layer in the Josephson junction fabrication process was chemically wet etched in a solution consisting of 65 % HNO_3, 100 % CH_3COOH, 85 % H_3PO_4 and H_2O, mixed at a ratio of 1:1:16:2.

Electroplating: The absorbers of the developed detectors are made of electroplated gold. The utilized electrolyte for this is the TechniGold 25 ES[9]. The electroplating was done at a temperature of 60 °C and a current density of $1\,\mathrm{mA/cm^2}$, resulting in a Au deposition rate of 1.04 nm/s.

A.1.6 Lift-Off and etch process

Lift-Off: The Lift-off process is one standard procedure in microfabrication and is depicted figure A.2 for an example of the fabrication of niobium stripes. In the first step, the substrate is prepared with negative photoresist via spin-coating, which is the AZ 5214E in this thesis, resulting in a uniformly applied resist coating. Afterwards, the resist is exposed to UV light at the areas where no Nb is required according to the design. Then, the photoresist is developed, which is done by immersing the entire wafer in a suitable alkaline developer liquid. As a result, the photoresist is removed at the location where the Nb stripes shall be deposited. This results in slightly undermined resist structures which have the shape of an inverse pyramid with flat apex. This resist shape is crucial for a Lift-off process in order to properly disconnect the material that is deposited on top of the resist from the material

---

[9] Technic Deutschland GmbH, Glärbach 2, 58802 Balve, Germany

that is deposited onto the substrate, as it is depicted in d). The Lift-off process finalizes with the removal of the photoresist with a suitable solvent, i.e. acetone or dimethylformamide (DMF), resulting in structures with slanted edges. This process provides simplicity in fabrication at the expense of pattern fidelity, as the created structure width differs slightly from the pattern width that was written into the photoresist.

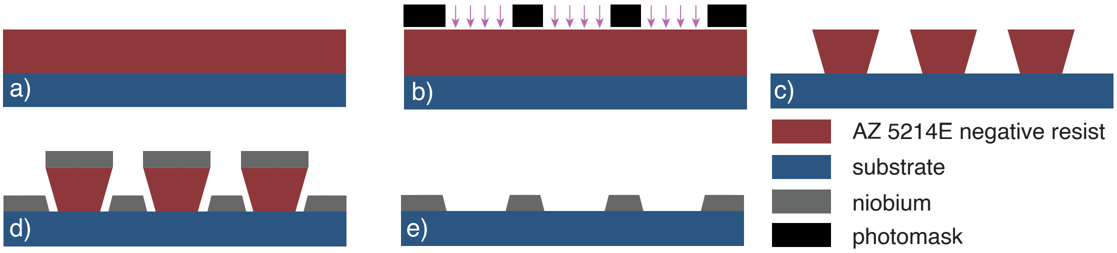

Figure A.2: Schematic of a Lift-Off process. a) Application of photoresist. b) UV exposure of resist. c) Resist development. d) Material deposition. e) Removal of photoresist.

Etch process: Another important standard procedure is the etch process that is illustrated in figure A.3 for the same example. In the first step, niobium is sputter deposited directly onto the substrate, followed by an application of a positive photoresist via spin-coating. Afterwards, the resist is exposed to UV light at the areas where the Nb needs to be removed according to the design, followed by the resist development. Afterwards, the exposed Nb is etched via ICP-RIE. The process is complete after the photoresist is removed with a suitable solvent. The result are steep-walled, rectangular structures with an enhanced pattern fidelity compared to the Lift-off process.

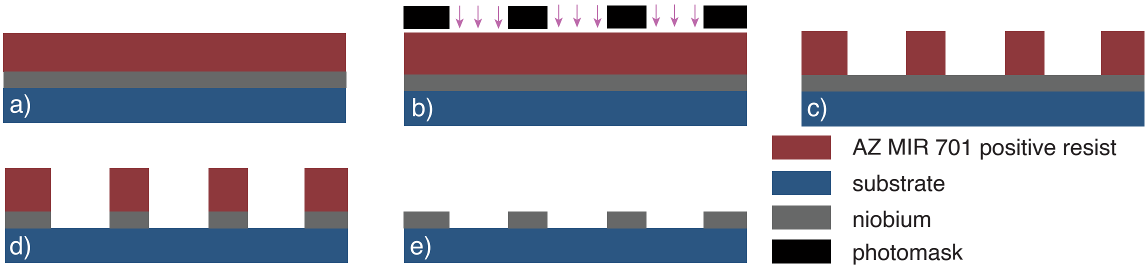

Figure A.3: Schematic of an etch process. a) Material deposition and application of photoresist. b) UV exposure of resist. c) Resist development. d) ICP-RIE of material. e) Removal of photoresist.

A.2 Detector specific amendments

This section contains additional detector specific information concerning either the microfabrication or the numerical simulations of the respective detector, summarized in tabular form.

A.2.1 HDMSQ1

Absorber	
Dimensions	$150 \times 150 \times 3\,\mu\text{m}^3$
Residual resistivity ratio RRR	10
Specific heat	$1.46 \times 10^{-5}\,\text{J/K}\cdot\text{mol}$
Distance between absorber and pickup coil	$4\,\mu\text{m}$

Temperature sensor	
Relative strength of RKKY interaction α	12.5
Residual resistivity ratio RRR	2.4
$1/f$ noise per Er ion $\sqrt{S_{\Phi,\text{Er}}}(1\,\text{Hz})$	$0.177\,\mu\Phi_0/\sqrt{\text{Hz}}$
Exponent ν of $1/f$ Er noise	0.9
Distance to pickup coil	300 nm

SQUID paramaters	
Inductance $L_\text{S} = L_\text{M}/2$	75 pH
White noise $\sqrt{S_{\Phi,\text{w}}}$	$0.4\,\mu\Phi_0/\sqrt{\text{Hz}}$
$1/f$ noise $\sqrt{S_{\Phi,1/f}}(1\,\text{Hz})$	$5\,\mu\Phi_0/\sqrt{\text{Hz}}$
Exponent of $1/f$ noise	1

Meander-shaped geometry	
Pitch and width of pickup coil	$p = 10\,\mu\text{m}$, $w = 4\,\mu\text{m}$
Pitch and width of field coil	$p = 10\,\mu\text{m}$, $w = 6\,\mu\text{m}$

Miscellaneous	
Signal rise time τ_0	100 ns
Signal decay time τ_1	$300\,\mu\text{s}$

Table A.1: Summary of the detector parameters that were used for the numerical simulations of the HDMSQ1 in order to predict its energy resolution.

Layer	Material	Thickness	Process	Structures
1	Nb	250 nm	ICP-RIE	Josephson tunnel junctions, field coils with wiring
2	Al/AlO$_x$	20 nm	wet etching	
3	Nb	125 nm	ICP-RIE	
4	SiO$_2$	540 nm	Lift-Off	lateral insulation of dedicated field coils
5	Nb$_2$O$_5$	50 nm	anodization	insulation layers
6	SiO$_2$	125 nm	Lift-Off	
7	SiO$_2$	175 nm	Lift-Off	
8	Nb	250 nm	ICP-RIE	SQUID loop, wiring
9	SiO$_2$	300 nm	Lift-Off	insulation layer
10	Au:Pd	260 nm	Lift-Off	resistive elements
11	Nb	600 nm	Lift-Off	wiring
12	Au	200 nm	Lift-Off	detector thermalization
13	Ag:Er	1.2 μm	Lift-Off	temperature sensor
	Au	100 nm		protective coating
14	Au	100 nm	electroplating and Lift-OFF	overhanging absorber on posts
	Au	3 μm		

Table A.2: Overview of the individual lithographic layers of the HDMSQ1 detector.

A.2.2 HDMSQ2A and HDMSQ2B

Absorber	
Heat capacity increased by 5 % due to the addition of the tetrapod	
Temperature sensor	
Dimensions	$50 \times 50 \times 0.8\,\mu\mathrm{m}^3$
Erbium concentration	260 ppm
SQUID paramaters	
White noise $\sqrt{S_{\Phi,\mathrm{w}}}$	$0.5\,\mu\Phi_0/\sqrt{\mathrm{Hz}}$
Meander-shaped geometry	
Pitch and width of pickup coil	$p = 10\,\mu\mathrm{m}$, $w = 5\,\mu\mathrm{m}$
Miscellaneous	
Signal rise time τ_0	$10\,\mu\mathrm{s}$
Signal decay time τ_1	$5\,\mathrm{ms}$

Table A.3: Summary of the detector parameters that were used for the detector optimizations according to numerical simulations in order to predict the energy resolution of the HDMSQ2A detector. These parameters are also representative for the HDMSQ2B. Shown are only the parameters that were changed compared to the HDMSQ1 in order to make the performed design adaptations more obvious.

Layer	Material	Thickness	Process	Structures
1	Nb	250 nm	ICP-RIE	Josephson tunnel junctions, field coils with wiring
2	Al/AlO$_x$	20 nm	wet etching	
3	Nb	125 nm	ICP-RIE	
4	SiO$_2$	540 nm	Lift-Off	lateral insulation of dedicated field coils
5	Nb$_2$O$_5$	50 nm	anodization	insulation layers
6	SiO$_2$	125 nm	Lift-Off	
7	SiO$_2$	175 nm	Lift-Off	
8	Nb	250 nm	ICP-RIE	SQUID loop, wiring
9	SiO$_2$	300 nm	Lift-Off	insulation layer
10	Au:Pd	260 nm	Lift-Off	resistive elements
11	Nb	600 nm	Lift-Off	wiring
12	Au	400 nm	Lift-Off	detector thermalization
13	Ag:Er	0.8 μm	Lift-Off	temperature sensor
	Au	100 nm		protective coating
14	Au	100 nm	electroplating	tetrapod
	Au	5 μm	and Lift-OFF	
15	Au	100 nm	electroplating	overhanging absorber on posts
	Au	3 μm	and Lift-OFF	
16	SiO$_2$	-240 nm	ICP-RIE	custom thermalization structures on membranes
	Si	$-\sim 30\,\mu$m	ICP-RIE	

Table A.4: Overview of the individual lithographic layers of the HDMSQ2A and the HDMSQ2B. It is important to mention that the membrane fabrication at the end was only done for the HDMSQ2B.

Bibliography

[Aal16] E. E. Aalseth et al., A Low-Noise Germanium Ionization Spectrometer for Low-Background Science, *IEEE Transactions on Nuclear Science*, 2016.

[Aba18] G. Abadias, E. Chason, J. Keckes, M. Sebastiani, G. B. Thompson, E. Barthel, G. L. Doll, C. E. Murray, C. H. Stoessel, and L. Martinu, Stress in thin films and coatings: Current status, challenges, and prospects, *Journal of Vacuum Science and Technology*, **36**, 2018.

[Abr12] A. Abragam and B. Bleaney, Electron paramagnetic resonance of transition metals, *Oxford University Press*, 2012.

[Ade93] D. J. Adelerhof, M. E. Bijlsma, P. B. M. Fransen, T. Weiman, J. Flokstra, and H. Rogalla, Fabrication of Nb/Al-AlO$_x$/Nb Josephson tunnel junctions using reactive ion etching in SF$_6$, *Physica C*, **209**, 477–485, 1993.

[Agu02] M. Aguilar, P. Quintana, and A. I. Olivia, Thickness–stress relations in aluminum thin films, *Materials and Manufacturing Processes*, **17**, 2002.

[Ai12] J. H. Ai, M. L. Lim, and J. R. Scully, Hydrogen Diffusion and Trapping in High Purity Al and Aluminum Alloy 5083-H131, *The Electrochemical Society*, 2012.

[Ale19] V. Alenkov et al., First results from the AMoRE-Pilot neutrinoless double beta decay experiment, *The European Physical Journal C*, **79**(791), 2019.

[Amb63] V. Ambegaokar and A. Baratoff, Tunneling between superconductors, *Phys. Rev. Lett.*, **10**(11), 486–489, 1963.

[Ant03] C. Antoine and S. Berry (Ed.), H in Niobium: Origin And Method Of Detection, Volume 671 in *AIP Conference Proceedings*, 2003.

[Arm19] E. Armengaud et al., Physics potential of the International Axion Observatory (IAXO), *Journal of Cosmology and Astroparticle Physics*, 2019.

[Bö10] H. Böhringer and N. Werner, X-ray spectroscopy of galaxy clusters: studying astrophysical processes in the largest celestial laboratories, *Astron Astrophys Rev*, **18**, 127–196, 2010.

[Ban93] S. R. Bandler, C. Enss, R. E. Lanou, H. J. Maris, T. More, F. S. Porter, and G. M. Seidel, Metallic magnetic bolometers for particle detection, *Journal of Low Temperature Physics*, **93**(3-4), 709–714, 1993.

[Ban08] G. Banerjee and R. L. Rhoades, Chemical Mechanical Planarization: Historical Review and Future Direction, *ECS Transactions*, **13**(4), 1–19, 2008.

[Ban12] S. R. Bandler, K. D. Irwin, D. Kelly, P. N. Nagler, J. P. Porst, H. Rotzinger, J. E. Sadleir, G. M. Seidel, S. J. Smith, and T. R. Stevenson, Magnetically Coupled Microcalorimeters, *J Low Temp Phys*, **167**, 254–268, 2012.

[Bar82] A. Barone and G. Paternò, Physics and Applications of the Josephson Effect, Wiley-VCH, 1982.

[Bar04] L. Bardelli, G. Poggi, M. Bini, G. Pasquali, and N. Taccetti, Time measurements by means of digital sampling techniques: a study case of 100 ps FWHM time resolution with a 100 MSample/s, 12 bit digitizer, *Nuclear Instruments and Methods in Physics Research A*, **521**, 480–492, 2004.

[Bar12] F. Barkov, A. Romanenko, and A. Grassellino, Direct observation of hydrides formation in cavity-grade niobium, *Physical Review Special Topics - Accelerators and Beams*, **15**, 2012.

[Bas03] R. B. Bass, L. T. Lichtenberger, and A. W. Lichtenberger, Effects of Substrate Preparation on the Stress of Nb Thin Films, *IEEE*, **13**(2), 2003.

[Bor12] K. Bordo and H.-G. Rubahn, Effect of Deposition Rate on Structure and Surface Morphology of Thin Evaporated Al Films on Dielectrics and Semiconductors , *Materials Science*, **18**(4), 2012.

[Bos05] S. Bose, P. Raychaudhuri, R. Banerjee, P. Vasa, and P. Ayyub, Mechanism of the size dependence of the superconducting transition of nanostructured Nb, *Physical Review Letters*, **95**(14), 2005.

[Boy09] S. T. P. Boyd and R. H. Cantor, Microcalorimeter magnetic sensor geometries using superconducting elements, *AIP Conference Proceedings*, **1185**, 595–598, 2009.

[Bro08] A.-D. Brown, S. R. Bandler, R. Brekosky, J. A. Chervenak, E. Figueroa-Feliciano, F. Finkbeiner, N. Iyomoto, R. L. Kelley, C. A. Kilbourne, F. S. Porter, S. Smith, T. Saab, and J. Sadleir, Absorber materials for transition-edge sensor x-ray microcalorimeters, *Journal of Low Temperature Physics*, **151**(1), 413–417, 2008.

[Bru82] J. J. P. Bruines, V. J. de Waal, and J. E. Mooij, Comment on: ”Dc SQUID: Noise and optimization” by Tesche and Clarke, *J. Low Temp. Phys.*, **46**, 383–386, 1982.

[Bug14] J. Bug, Investigation and comparison of different algorithms for the analysis of detector signals of metallic magnetic microcalorimeters, Bachelor Thesis, Heidelberg University, 2014.

[Bur04] A. Burck, Entwicklung großflächiger magnetischer Kalorimeter zur energieaufgelösten Detektion von Röntgenquanten und hochenergetischen Teilchen, Diploma Thesis, Kirchhoff-Institut für Physik, Universität Heidelberg, 2004.

[Bur08] A. Burck, Entwicklung großflächiger mikrostrukturierter magnetischer Kalorimeter mit Au:Er- und Ag:Er-Sensoren für den energieaufgelösten Nachweis von Röntgenquanten und hochenergetischen Teilchen, PhD Thesis, Kirchhoff-Institut für Physik, Universität Heidelberg, 2008.

[Cab10] A. L. Cabrera, J. I. Avila, and D. Lederman, Hydrogen absorption by metallic thin films detected by optical transmittance measurements, *International Journal of Hydrogen Energy*, **35**, 10613–10619, 2010.

[Cal16] S. J. Callori, C. Rehm, G. L. Causer, M. Kostylev, and F. Klose, Hydrogen Absorption in Metal Thin Films and Heterostructures Investigated in Situ with Neutron and X-ray Scattering, *Metals*, **6**(6), 2016.

[Cam10] J. Cami, J. Bernard-Salas, E. Peeters, and S. E. Malek, Detection of C_{60} and C_{70} in a Young Planetary Nebula, *Science*, **329**(5996), 1180–1182, 2010.

[Car90] J. P. Carbotte, Properties of boson-exchange superconductors, *Rev. Mod. Phys.*, **62**(4), 1027–1157, 1990.

[Cha10] R. C. Chang and F. Y. Chen, Residual Stresses of Sputtering Titanium Thin Films at Various Substrate Temperatures, *Journal of Nanoscience and Nanotechnology*, 2010.

[Che03] W. Chen, V. P. amd S. K. Tolpygo, and J. E. Lukens, Development towards high-speed integrated circuits and SQUID qubits with Nb/Al-AlO_x/Nb Josephson junctions, *IEEE Trans. Appl. Supercond.*, **13**, 103–106, 2003.

[Cho09] S. Choi, D.-H. Lee, S. G. Louie, and J. Clarke, Localization of Metal-Induced Gap States at the Metal-Insulator Interface: Origin of Flux Noise in SQUIDs and Superconducting Qubits, *Phys. Rev. Lett.*, **103**(197001), 2009.

[Cla04] J. Clarke and A. I. Braginski (Ed.), The SQUID Handbook, WILEY-VCH, 2004.

[Coh05] Y. Cohen, A. Liat, and F. Limor, Diffusion NMR Spectroscopy in Supramolecular and Combinatorial Chemistry, *Wiley, Angewandte Chemie*, **44**(4), 520–554, 2005.

[Col70] H. K. Collan, M. Krusius, and G. R. Pickett, Specific Heat of Antimony and Bismuth between 0.03 and 0.8 K, *Phys. Rev. B*, **1**, 2888–2895, 1970.

[Con19] M. Connollya, M. Martin, R. Amaro, A. Slifka, and E. Drexler, Hydrogen isotope effect on the embrittlement and fatigue crack growth of steel, *Materials Science and Engineering: A*, **753**, 331–340, 2019.

[Cuo82] J. J. Cuomo, J. M. E. Harper, C. R. Guarnieri, D. S. Yee, L. J. Attanasio, J. Angilello, and C. T. Wu, Modification of niobium film stress by low-energy ion bombardment during deposition, *Journal of Vacuum Science and Technology*, **20**, 1982.

[Dan83] V. Danilov, K. Likharev, and A. Zorin, Quantum noise in SQUIDs, *IEEE Transactions on Magnetics*, **19**(3), 572–575, 1983.

[Dan84] W. C. Danchi, J. B. Hansen, M. Octavio, F. Habbal, and M. Tinkham, Effects of noise on the dc and far-infrared Josephson effect in small area superconducting tunnel junctions, *Phys. Rev. B*, **30**, 2503–2516, 1984.

[Dan05] T. Daniyarov, Metallische magnetische Kalorimeter zum hochauflösenden Nachweis von Röntgenquanten und hochenergetischen Molekülen, PhD Thesis, Kirchhoff-Institut für Physik, Universität Heidelberg, 2005.

[Day69] L. A. Day, Conformations of single-stranded DNA and coat protein in fd bacteriophage as revealed by ultraviolet absorption spectroscopy, *Journal of Molecular Biology*, **39**(2), 265–277, 1969.

[Dee16] L. Deeg, Bestimmung der intrinsischen Kapazität von Nb/Al-AlOx/Nb-Tunnelkontakten, Bachelor Thesis, Heidelberg University, 2016.

[Dev19] A. M. Devasia, M. A. Balvin, S. Bandler, V. Bolkhovsky, P. C. Nagler, K. Ryo, S. J. Smith, T. R. Stevenson, and W. Yoon, Fabrication of Magnetic Calorimeter Arrays With Buried Wiring, *IEEE Transactions on Applied Superconductivity*, **99**, 2019.

[Dir28] P. A. M. Dirac, The Quantum Theory of the Electron, *Proceedings of the Royal Society of London*, **117**(778), 610–624, 1928.

[Dol61] R. Doll and M. Näbauer, Experimental proof of magnetic flux quantization in a superconducting ring, *Phys. Rev. Lett.*, **7**, 51–52, 1961.

[Dru06] D. Drung, C. Hinnrichs, and H.-J. Barthelmess, Low-noise ultra-high-speed dc SQUID readout electronics, *Superconductor Science and Technology*, 2006.

[Dru11] D. Drung, J. Beyer, J.-H. Storm, M. Peters, and T. Schurig, Investigation of Low-Frequency Excess Flux Noise in DC SQUIDs at mK Temperatures, *IEEE Trans. Appl. Supercond.*, **21**, 340–344, 2011.

[dS07] R. d. Sousa, Dangling-bond spin relaxation and magnetic $1/f$ noise from the amorphous-semiconductor/oxide interface: Theory, *Phys. Rev. B*, **76**(245306), 2007.

[Du07a] J. Du, A. D. M. Charles, and K. D. Petersson, Study of the Surface Morphology of Nb Films and the Microstructure of Nb/Al-AlO$_x$/Nb Trilayers, *IEEE Transactions on Applied Superconductivity*, **17**(2), 3520–3524, 2007.

[Du07b] J. Du, A. D. M. Charles, K. D. Petersson, and E. W. Preston, Influence of Nb film surface morphology on the sub-gap leakage characteristics of Nb/Al-AlO$_x$/Nb Josephson junctions, *Supercond. Sci. Technol*, **20**, 350–355, 2007.

[Dun88] R. W. Dunford, M. L. A. Raphaelian, H. G. Berry, M. S. Dewey, and D. Deslattes, Probing QED using microwave and X-ray spectroscopy in hydrogenic ions, *Nuclear Instruments and Methods in Physics Research Section B: Beam Interactions with Materials and Atoms*, 1988.

[Duz81] T. V. Duzer and C. W. Turner, Principles of superconductive devices and circuits, Elsevier New York, 1981.

[Dwi18] S. K. Dwivedi and M. Vishwakarma, Hydrogen embrittlement in different materials: A review, *International Journal of Hydrogen Energy*, 2018.

[Ech92] P. Echternach, M. Thoman, C. Gould, and H. Bozler, Electron-phonon scattering rates in disordered metallic films below 1 K, *Phys. Rev. B*, **46**(16), 10339–10344, 1992.

[Ell87] D. F. Elliot (Ed.), Handbook of Digital Signal Processing, Elsevier, 1987.

[Eng16] A. M. Engwall, Z. Rao, and E. Chason, Origins of residual stress in thin films: Interaction between microstructure and growth kinetics, *Materials and Design*, **110**, 616–623, 2016.

[Enp91] K. Enpuku and K. Yoshida, Modeling the dc superconducting quantum interference device coupled to the multiturn input coil, *Journal of Applied Physics*, **69**(10), 7295–7300, 1991.

[Enp92] K. Enpuku, R. Cantor, and H. Koch, Modeling the direct current superconducting quantum interference device coupled to the multiturn input coil. II, *Journal of Applied Physics*, **71**(5), 2338–2346, 1992.

[Ens00] C. Enss, A. Fleischmann, K. Horst, J. Schönefeld, J. S. Adams, Y. H. Huang, Y. H. Kim, and G. M. Seidel, Metallic magnetic calorimeters for particle detection, *J. Low Temp. Phys.*, **121**(3), 137–176, 2000.

[Ens05] C. Enss and S. Hunklinger, Low-Temperature Physics, SpringerLink: Springer e-Books, Springer Berlin Heidelberg, 2005.

[Epp07] S. W. Epp, J. R. C. López-Urrutia, G. Brenner, V. Mäckel, P. H. Mokler, R. Treusch, M. Kuhlmann, M. V. Yurkov, J. Feldhaus, J. R. Schneider, M. Wellhöfer, M. Martins, W. Wurth, and J. Ullrich, Soft X-Ray Laser Spectroscopy on Trapped Highly Charged Ions at FLASH, *Phys. Rev. Lett.*, **98**, 2007.

[Fal08] P. Falferi, R. Mezzena, M. Mueck, and A. Vinante, Cooling fins to limit the hot-electron effect in dc SQUIDs, *J. Phys.: Conf. Ser*, **97**, 2008.

[Fao08] L. Faoro and L. B. Ioffe, Microscopic Origin of Low-Frequency Flux Noise in Josephson Circuits, *Phys. Rev. Lett.*, **100**(227005), 2008.

[Far80] M. M. Farahani, Hydrogen embrittlement in single- and poly-crystal niobium, PhD Thesis, University of Texas, Houston, 1980.

[Fel07] A. Felten, C. Bittencourt, J.-J. Pireaux, M. Reichelt, J. Mayer, D. Hernandez-Cruz, and A. P. Hitchcock, Individual Multiwall Carbon Nanotubes Spectroscopy by Scanning Transmission X-ray Microscopy, *Nano Lett.*, **7**(8), 2435–2440, 2007.

[Fis02] B. M. Fischer, M. Walther, and P. U. Jepsen, Far-infrared vibrational modes of DNA components studied by terahertz time-domain spectroscopy, *Physics in Medicine and Biology*, **47**(21), 2002.

[Fle98] A. Fleischmann, Hochauflösendes magnetisches Kalorimeter zur Detektion von einzelnen Röntgenquanten, Diploma Thesis, Kirchhoff-Institut für Physik, Universität Heidelberg, 1998.

[Fle03] A. Fleischmann, Magnetische Mikrokalorimeter: Hochauflösende Röntgenspektroskopie mit energiedispersiven Detektoren, PhD Thesis, Kirchhoff-Institut für Physik, Universität Heidelberg, 2003.

[Fle05] A. Fleischmann, C. Enss, and G. Seidel, Metallic magnetic calorimeters, in C. Enss (Ed.), *Cryogenic Particle Detection*, 151–216, Springer Berlin Heidelberg, Berlin, Heidelberg, 2005.

[Fle09] A. Fleischmann, L. Gastaldo, J. Porst, S. Kempf, A. Kirsch, A. Pabinger, C. Pies, P. Ranitzsch, S. Schäfer, F. Seggern, T. Wolf, C. Enss, and G. Seidel, Metallic magnetic calorimeters, *AIP Conf. Proc.*, **1185**, 2009.

[Foe12] N. Foerster, Entwicklung eines kalorimetrischen Tieftemperatur-Detektors mit supraleitendem Temperatursensor fur die hochaufloesende Roentgenspektroskopie, Diploma Thesis, Heidelberg University, 2012.

[Fog89] V. Foglietti, W. J. Gallagher, M. B. Ketchen, A. W. Kleinsasser, R. H. Koch, and R. L. Sandstrom, Performance of dc SQUIDs with resistively shunted inductance, *Appl. Phys. Lett*, **55**, 1451–1453, 1989.

[Fou15] C. J. Fourie, Full-Gate Verification of Superconducting Integrated Circuit Layouts With InductEx, *IEEE Transactions on Applied Superconductivity*, **25**(1), 2015.

[Fra17] J. v. Fraunhofer, Bestimmung des Brechungs- und Farbenzerstreuungs-Vermögens verschiedener Glasarten, in Bezug auf die Vervollkommnung achromatischer Fernröhre., in *Denkschriften der Königlichen Academie der Wissenschaften zu München für die Jahre 1814 und 1815*, 193–226, Königliche Academie der Wissenschaften, 1817.

[Fuk85] Y. Fukai and H. Sugimoto, Diffusion of hydrogen in metals, *Advances in Physics*, **34**(2), 263–326, 1985.

[Gab74] A. H. Gabriel, Highly Charged Ions in Astrophysics, *Physica Scripta*, **9**(5), 1974.

[Gad17] L. M. Gades, T. W. Cecil, R. Divan, D. R. Schmidt, J. N. Ullom, T. J. Madden, D. Yan, and A. Miceli, Development of Thick Electroplated Bismuth Absorbers for Large Collection Area Hard X-ray Transition Edge Sensors, *IEEE Transactions on Applied Superconductivity*, **27**(4), 2017.

[Gam16] L. Gamer, D. Schulz, C. Enss, A. Fleischmann, L. Gastaldo, S. Kempf, C. Krantz, O. Novotny, D. Schwalm, and A. Wolf, MOCCA: A 4k-Pixel Molecule Camera for the Position and Energy-Resolving Detection of Neutral Molecule Fragments at CSR, *J. Low Temp. Phys.*, **184**(839), 2016.

[Gam19] L. Gamer, Entwicklung und Charakterisierung des 4 k-Pixel Detektorarrays MOCCA für die energie- und ortsaufgelöste Detektion neutraler Molekülfragmente, PhD Thesis, Heidelberg University, 2019.

[Gan74] V. Gantmakher, Experimental Study of Electron-Phonon Scattering in Metals, *Rep. Progress Physics*, **37**(3), 317–362, 1974.

[Gei19] J. Geist, Bestimmung der Isomerenergie von ^{229}Th mit dem hochauflösenden Mikrokalorimeter-Array maXs30, PhD Thesis, Heidelberg University, 2019.

[Geo12] S. Georgi, Röntenspektroskopie mit einem magnetischen Mikrokalorimeter an hochgeladenen Eisen- und Wolframionen, Masters Thesis, Max-Planck Institute for Nuclear Physics, 2012.

[Ger17] M. J. Gertig, High resolution susceptibility thermometers with metallic paramagnetic Au:Er sensors for millikelvin temperatures, Masters Thesis, Heidelberg University, 2017.

[Got14] L. Gottardi, H. Akamatsu, D. Barret, M. Bruijn, R. den Hartog, J.-W. d. Herder, H. Hoevers, M. Kiviranta, J. v. d. Kuur, A. v. d. Linden, B. Jackson, M. Jambunathan, and M. L. Ridder, Development of TES-based detectors array for the X-ray Integral Field Unit (X-IFU) on the future X-Ray Observatory Athena, *Proceedings of SPIE - The International Society for Optical Engineering*, 2014.

[Gu18] L. Gu and X. Y. Li, Hydrogen damage in metals, *IOP Conference Series: Materials Science and Engineering*, **380**(1), 2018.

[Gup84] M. Gupta, Why does hydrogen destroy superconductivity in niobium and lanthanum?, *Solid State Communications*, **50**(5), 439–444, 1984.

[Hah92] W. Hahn, M. Loewenhaupt, and B. Frick, Crystal field excitations in dilute rare earth noble metal alloys, *Phys. B.*, **180**, 176–178, 1992.

[Has83] E. Hashimoto and T. Kino, Hydrogen diffusion in aluminum at high temperatures, *J. Phys. F: Metal Phys.*, **13**, 1157–1165, 1983.

[Hen77] W. H. Henkels and C. J. Kirchner, Penetration Depth Measurements of Type II Superconducting Films, *IEEE Transactions on Magnetics*, **13**(63), 1977.

[Hen07] C. Henager, Materials for the Hydrogen Economy, Chapter Hydrogen Permeation Barrier Coatings, 181–190, CRC Press, 2007.

[Hen12] D. Hengstler, Untersuchung der Eigenschaften von supraleitenden Re-, Zn- und Zn:Mn-Absorbern für magnetische Mikrokalorimeter, Diploma Thesis, Kirchhoff-Institut für Physik, Universität Heidelberg, 2012.

[Hen15] D. Hengstler, M. Keller, C. Schötz, J. Geist, M. Krantz, S. Kempf, L. Gastaldo, A. Fleischmann, T. Gassner, G. Weber, R. Märtin, T. Stöhlker, and C. Enss, Towards FAIR: first measurements of metallic magnetic calorimeters for high-resolution x-ray spectroscopy at GSI, *Physica Scripta*, **2015**(T166), 014054, 2015.

[Hen17] D. Hengstler, Development and characterization of two-dimensional metallic magnetic calorimeter arrays for the high-resolution X-ray spectroscopy, PhD Thesis, Universität Heidelberg, 2017.

[Her15] S.-C. Her and Y.-H. Wand, Temperature effect on microstructure and mechanical properties of aluminum film deposited on glass substrates , *Indian Journal and Engineering and Materials Sciences*, **22**, 268–272, 2015.

[Heu11] S. Heuser, Entwicklung mikrostrukturierter magnetischer Kalorimeter mit verbesserter magnetischer Flusskopplung für die hochauflösende Röntgenspektroskopie, Diploma Thesis, Kirchhoff-Institut für Physik, Universität Heidelberg, 2011.

[Hin88] J. Hinken, Supraleiter-Elektronik, Springer-Verlag, Berlin, 1988.

[Hin08] K. Hinode, T. Satoh, S. Nagasawa, and M. Hidaka, Hydrogen-inclusion-induced variation of critical current in Nb/Al-AlO$_x$/Nb Josephson junctions, *J. Appl. Phys*, **104**, 2008.

[Hin10] K. Hinode, T. Satoh, S. Nagasawa, and M. Hidaka, Origin of hydrogen-inclusion-induced critical current deviation in Nb/Al-AlO$_x$/Nb Josephson junctions, *J. Appl. Phys*, **107**, 2010.

[Hoe06] H. Hoevers, Thermal physics of transition edge sensor arrays, *Nucl. Instr. Meth. Phys. Res. A*, **559**(2), 702 – 705, 2006, Proceedings of the 11th International Workshop on Low Temperature Detectors.

[Höl97] G. Hölzer, M. Fritsch, M. Deutsch, J. Härtwig, and E. Förster, $K\alpha_{1,2}$ and $K\beta_{1,3}$ x-ray emission lines of the 3d transition metals, *Phys. Rev. A*, **56**, 4554–4568, 1997.

[Hou93] E. P. Houwman, J. G. Gijsbertsen, J. Flokstra, and H. Rogalla, Proximity effects in Nb/Al-AlO$_x$/Nb Josephson Tunnel Junctions, *IEEE Transactions on Applied Supcerconductivity*, **3**(1), 1993.

[Hub97] M. Huber, M. W. Cromar, and R. H. Ono, Excess Low-Frequency Flux Noise in dc SQUIDs, *IEEE Transactions on Applied Superconductivity*, **7**(2), 1997.

[Ili14] K. Ilin, D. Henrich, Y. Luck, Y. Liang, M. Siegel, and D. Y. Vodolazov, Critical current of Nb, NbN, and TaN thin-film bridges with and without geometrical nonuniformities in a magnetic field, *Phys. Rev. B*, **89**(184511), 2014.

[Ima92a] T. Imamura and S. Hasuo, Fabrication of high quality Nb/$\mathrm{AlO_x} - Al$/Nb Josephson junctions. II. Deposition of thin Al layers on Nb films, *IEEE Transactions on Applied Superconductivity*, **2**(2), 84–94, 1992.

[Ima92b] T. Imamura, T. Shiota, and S. Hasuo, Fabrication of High Quality Nb/$\mathrm{AlO_x}$-Al/Nb Josephson Junctions: I - Sputtered Nb Films for Junction Electrodes, *IEEE*, **2**(1), 1–14, 1992.

[Irw05] K. D. Irwin and G. C. Hilton, Transition Edge Sensors., in C. Enss (Ed.), *Cryogenic Particle Detection, Topics in Applied Physics*, Volume 99, Springer-Verlag, Berlin, heidelberg, New York, 2005.

[Ish86] T. Ishikawa and R. B. McLellan, The diffusivity of hydrogen in aluminum, *Acta Metallurgica*, **34**, 1091–1095, 1986.

[Iyo04] N. Iyomoto, J. E. Sadleir, E. Figueroa-Feliciano, T. Saab, S. R. Bandler, C. A. Kilbourne, J. A. Chervenak, D. Talley, F. M. Finkbeiner, R. P. Brekosky, M. A. Lindeman, R. L. Kelley, F. S. Porter, and K. R. Boyce, Optimization of x-ray absorbers for TES microcalorimeters, in *Proceedings of the SPIE*, Volume 5501, 145–154, 2004.

[Jin09] Y. Jin, X.-H. Song, and D. Zhang, Grain-size dependence of superconductivity in dc sputtered Nb films, *Science in China Series G Physics Mechanics and Astronomy*, **52**(9), 1289–1292, 2009.

[Joh85] W. Johnson and G. Soff, The lamb shift in hydrogen-like atoms, *Atomic Data and Nuclear Data Tables*, 1985.

[Jos62] B. D. Josephson, Possible new effects in superconductive tunnelling, *Phys. Lett.*, **1**, 251–253, 1962.

[Kai11] C. Kaiser, High Quality Nb/Al-AlOx/Nb Josephson Junctions: Technological Development and Macroscopic Quantum Experiments, PhD Thesis, Karlsruhe Institut für Technologie (KIT), 2011.

[Kan13] X. Kang, L. Ying, G. Zhang, H. Wang, X. Kong, W. Peng, and X. Xie, Growth and Characterization of Nb films and Nb/Al-AlO$_x$/Nb Trilayers for Josephson Junctions, *IEEE 14th International Superconductive Electronics Conference, ISEC 2013*, 2013.

[Kem07] S. Kempf, Entwicklung eines vollständig mikrostrukturierten metallisch magnetischen Kalorimeters, Masters Thesis, Heidelberg University, 2007.

[Kem12] S. Kempf, Entwicklung eines Mikrowellen-SQUID-Multiplexers auf der Grundlage nicht-hysteretischer rf-SQUIDs zur Auslesung metallischer magnetischer Kalorimeter, PhD Thesis, Universität Heidelberg, 2012.

[Kem13] S. Kempf, A. Ferring, A. Fleischmann, L. Gastaldo, and C. Enss, Characterization of the reliability and uniformity of an anodization-free fabrication process for high-quality Nb/Al$-$AlO$_x$/Nb Josephson junctions, *Supercond. Sci. Technol.*, **26**, 2013.

[Kem15] S. Kempf, A. Ferring, A. Fleischmann, and C. Enss, Direct-current superconducting quantum interference devices for the readout of metallic magnetic calorimeters, *Superconductor Science and Technology*, **28**(4), 2015.

[Kem16] S. Kempf, A. Ferring, and C. Enss, Towards noise engineering: Recent insights in low-frequency excess flux noise of superconducting quantum devices, *Applied Physics Letters*, **109**(16), 162601, 2016.

[Kem18] S. Kempf, A. Fleischmann, L. Gastaldo, and C. Enss, Physics and applications of metallic magnetic calorimeters, *Journal of Low Temperature Physics*, **193**(3-4), 365–379, 2018.

[Ker03] G. L. Kerber, L. A. Abelson, K. Edwards, R. Hu, M. W. Johnson, M. L. Leung, and J. Luine, Fabrication of high current density Nb integrated circuits using a self-aligned junction anodization process, *IEEE Trans. Appl. Supercond.*, **13**, 82–86, 2003.

[Kir60] G. Kirchhoff and R. Bunsen, Chemische Analyse durch Spectralbeobachtungen, *Annalen der Physik*, **186**(6), 161–189, 1860.

[Kit18] S. Kittiwatanakul, N. Anuniwat, N. Dao, S. A. Wolf, and J. Lu, Surface morphology control of Nb thin films by biased target ion beam deposition, *Journal of Vacuum Science and Technology*, **36**, 2018.

[Knu87] J. Knuutila, A. Ahonen, and C. Tesche, Effects on dc SQUID characteristics of damping of input coil resonances, *J. Low Temp .Phys.*, **68**, 269–284, 1987.

[Koc80] R. H. Koch, D. J. V. Harlingen, and J. Clarke, Quantum-Noise Theory for the Resistively Shunted Josephson Junction, *Phys. Rev. Lett.*, **45**(2132), 1980.

[Koc81] R. H. Koch, D. J. V. Harlingen, and J. Clarke, Quantum noise theory for the dc SQUID, *Appl. Phys. Lett.*, **39**(365), 1981.

[Koc83] R. H. Koch, J. Clarke, W. M. Goubau, J. M. Martinis, C. M. Pegrum, and D. J. van Harlingen, Flicker ($1/f$) noise in tunnel junction dc SQUIDs, *Journal of Low Temperature Physics*, **51**, 207–224, 1983.

[Koc07] R. H. Koch, D. P. DiVincenzo, and J. Clarke, Model for $1/f$ Flux Noise in SQUIDs and Qubits, *Phys. Rev. Lett.*, **98**(267003), 2007.

[Koz12] A. Kozorezov, Energy Down-Conversion and Thermalization in Metal Absorbers, *Journal of Low Temperature Physics*, **167**, 473–484, 2012.

[Kra13] M. Krantz, Entwicklung, Mikrofabrikation und Charakterisierung von metallischen magnetischen Kalorimetern für die hochauflösende Röntgenspektroskopie hochgeladener Ionen., Master Thesis, Kirchhoff-Institut für Physik, Universität Heidelberg, 2013.

[Kra17] S. Kraft-Bermuth, V. Andrianov, A. Bleile, A. Echler, P. Egelhof, P. Grabitz, S. Ilieva, O. Kiselev, C. Kilbourne, D. McCammon, J. P. Meier, and P. Scholz, Precise determination of the 1s Lamb shift in hydrogen-like lead and gold using microcalorimeters, *Journal of Physics B: Atomic, Molecular and Optical Physics*, **50**(5), 055603, 2017.

[Kub14] K. Kubiček, P. H. Mokler, V. Mäckel, J. Ullrich, and J. R. C. López-Urrutia, Transition energy measurements in hydrogenlike and heliumlike ions strongly supporting bound-state QED calculations, *Phys. Rev. A*, **90**, 032508, 2014.

[Kur88] K. Kuroda and M. Yuda, Niobium-stress influence on Nb/Al-oxide/Nb Josephson junctions, *J. Appl. Phys.*, **63**(7), 2352–2357, 1988.

[LaF15] S. LaForest and R. d. Sousa, Flux-vector model of spin noise in superconducting circuits: Electron versus nuclear spins and role of phase transition, *Phys. Rev. B*, **92**(054502), 2015.

[Lam47] W. E. Lamb and R. C. Retherford, Fine structure of the hydrogen atom by a microwave method, *Phys. Rev.*, **72**, 241–243, 1947.

[Li17] M. Li, D.-G. Xie, E. Ma, J. Li, X.-X. Zhang, and Z.-W. Shan, Effect of hydrogen on the integrity of aluminium-oxide interface at elevated temperatures, *Nature Communications*, **8**, 2017.

[Li18] Y. Li, M. Kim, and M. G. Allen, A single mask process for the realization of fully-isolated, dual-height MEMS metallic structures separated by narrow gaps, *Journal of Micromechanics and Microengineering*, **28**, 2018.

[Lic87] D. L. Lichtenberger and G. E. Kellogg, Experimental quantum chemistry: photoelectron spectroscopy of organotransition-metal complexes, *Acc. Chem. Res.*, **20**(10), 379–387, 1987.

[Lik72] K. K. Likharev and V. K. Semenov, Fluctuation spectrum in superconducting point junctions, *JETP Lett.*, **15**, 442–445, 1972.

[Lik86] K. K. Likharev, Dynamics of Josephson Junctions and Circuits, New York, 1986.

[Liu09] J. Liu, J. Li, T. Li, T. Li, W. Wu, and W. Chen, Study of Stress and Morphology of Superconducting Niobium Thin Films, *IEEE Transactions on Applied Superconductivity*, **19**(3), 2009.

[Liu14] X. Liu, W. Yang, and Z. Liu, Recent Progress on Synchrotron-Based In-Situ Soft X-ray Spectroscopy for Energy Materials, *Advanced Materials*, **26**(46), 7710–7729, 2014.

[Lut06] G. Lutz, Silicon drift and pixel devices for X-ray imaging and spectroscopy, *Journal of Synchrotron Radiation*, 2006.

[McC68] D. E. McCumber, Effect of ac impedance on dc voltage-current characteristics of superconductor weak-link junctions, *Journal of Applied Physics*, **39**(7), 3113–3118, 1968.

[McC93] D. McCammon, W. Cui, M. Juda, J. Morgenthaler, J. Zhang, R. Kelley, S. Holt, G. Madejski, S. Moseley, and A. Szymkowiak, Thermal calorimeters for high resolution X-ray spectroscopy, *Nucl. Instr. Meth. Phys. Res. A*, **326**(1), 157 – 165, 1993.

[McC05] D. McCammon, Semiconductor Thermistors., in C. Enss (Ed.), *Cryogenic Particle Detection, Topics in Applied Physics*, Volume 99, Springer-Verlag, Berlin, Heidelberg, New York, 2005.

[McM68] W. L. McMillan, Tunneling Model of the Superconducting Proximity Effect, *Phys. Rev.*, **175**(537), 1968.

[Mer34] P. W. Merrill, Unidentified Interstellar Lines, *PASP*, **46**, 206–207, 1934.

[Mic18] P. Micke et al., The Heidelberg compact electron beam ion traps, *Review of Scientific Instruments*, **89**(6), 2018.

[Mos84] S. H. Moseley, J. C. Mather, and D. McCammon, Thermal detectors as x-ray spectrometers, *Journal of Applied Physics*, **56**(5), 1257–1262, 1984.

[New30] I. Newton and R. Kirchhoff, Opticks, or a treatise of the reflections, refractions, inflections and colours of light, William Innys, 1730.

[Oct83] M. Octavio, M. Tinkham, G. E. Blonder, and T. M. Klapwijk, Subharmonic energy-gap structure in superconducting constrictions, *Phys. Rev. B*, **27**(11), 6739–6746, 1983.

[Oko04] B. Okolo, P. Lamparter, U. Welzel, and E. J. Mittemeijer, Stress, texture, and microstructure in niobium thin films sputter deposited onto amorphous substrates, *Journal of Appl. Phys.*, **95**(2), 2004.

[Ola19] D. I. Olaya, M. C. C. Beltran, J. Pulecio, J. P. Biesecker, S. Khadem, T. Lewitt, and P. F. H. amd P. D. Dresselhaus amd S. P. Benz, Planarized process for single-flux-quantum circuits with self-shunted Nb/Nb$_x$Si$_{1-x}$/Nb Josephson junctions, *IEEE Transactions on Applied Superconductivity*, **29**(6), 2019.

[Ono97] R. H. Ono, J. A. Koch, A. Steinbach, M. E. Huber, and und M. W. Cromar, Tightly coupled dc SQUIDs with resonance damping, *Transactions on Applied Superconductivity*, **7**(2), 2538–2541, 1997.

[Ott14] C. Ottone, M. Laurenti, K. Bejtka, A. Sanginario, and V. Cauda, The Effects of the Film Thickness and Roughness in the Anodization Process of Very Thin Aluminum Films, *Mater. Sci. Nanotechnol.*, **1**(1), 2014.

[Pau19] M. Paulsen, J. Beyer, L. Bockhorn, C. Enss, S. Kempf, K. Kossert, M. Loidl, R. Mariam, O. Nähle, P. Ranitzsch, and M. Rodrigues, Development of a beta spectrometry setup using metallic magnetic calorimeters, *Journal of Instrumentation*, **14**, 2019.

[Pie08] C. Pies, Entwicklung eines Detektor-Arrays basierend auf magnetischen Kalorimetern für die hochaufgelöste Röntgenspektroskopie an hochgeladenen Ionen, Diploma Thesis, Kirchhoff-Institut für Physik, Universität Heidelberg, 2008.

[Pie12a] C. Pies, maXs200: Entwicklung und Charakterisierung eines Röntgendetektors basierend auf magnetischen Kalorimetern für die hochauflösenden Spektroskopie hochgeladener Ionen, PhD Thesis, Kirchhoff-Institut für Physik, Universität Heidelberg, 2012.

[Pie12b] C. Pies, S. Schäfer, S. Heuser, S. Kempf, A. Pabinger, J. P. Porst, P. Ranitsch, N. Foerster, D. Hengstler, A. Kampkötter, T. Wolf, L. Gastaldo, A. Fleischmann, and C. Enss, maXs: Microcalorimeter Arrays for High-Resolution X-Ray Spectroscopy at GSI/FAIR, *J. Low Temp. Phys.*, 2012.

[Ple09] J. Pleikies, Strongly coupled, low noise dc-SQUID amplifiers, PhD Thesis, University of Twente, 2009.

[Pob96] F. Pobell, Matter and Methods at Low Temperatures, Springer-Verlag, 1996.

[Pol69] G. Pollack, Kapitza Resistance, *Rev. Mod. Phys*, **41**(1), 48–81, 1969.

[Por11] J.-P. Porst, High-Resolution Metallic Magnetic Calorimeters for beta-Spectroscopy on 187-Rhenium and Position Resolved X-Ray Spectroscopy, PhD Thesis, Universität Heidelberg, 2011.

[Pow74] R. J. Powers, P. Martin, G. H. Miller, R. E. Welsh, and D. A. Jenkins, Muonic ^{197}Au: A test of the weak-coupling model, *Nucl. Phys. A*, **230**(3), 413 – 444, 1974.

[Qui99] P. Quintana, A. I. Oliva, O. Ceh, and J. E. Corona, Thickness effects on aluminum thin films, *Superficies y Vacío*, **9**, 280–282, 1999.

[Ric10] R. E. Ricker and G. R. Myneni, Evaluation of the Propensity of Niobium to Absorb Hydrogen During Fabrication of Superconducting Radio Frequency Cavities for Particle Accelerators, *J. Res. Natl. Inst. Stand. Technol.*, **115**, 353–371, 2010.

[Roa11] W. M. Roach, D. Beringer, C. Clavero, and R. A. Lukaszew, Investigation of epitaxial niobium thin films grown on different surfaces suitable for SRF cavities, *15th International Conference on RF Superconductivity*, 2011.

[Rod14] M. Rodrigues, M. Loidl, C. Pies, A. Fleischmann, and C. Enss, Development of large bismuth absorbers for magnetic calorimeters applied to hard x-ray spectrometry, *J. Low Temp. Phys.*, **176**(3), 610–616, 2014.

[Rot07] H. Rotzinger, Entwicklung magnetischer Mikrokalorimeter für die hochauflösende Spektroskopie des Emitters ^{36}Cl, PhD Thesis, Universität Heidelberg, 2007.

[Rou85] M. L. Roukes, M. R. Freeman, R. S. Germain, R. C. Richardson, and M. B. Ketchen, Hot Electrons and Energy Transport in Metals at Millikelvin Temperatures, *Physical Review Letters*, **55**(4), 1985.

[Sak03] K. Sakurai and H. Eba, Chemical characterization using relative intensity of manganese $K_{\beta'}$ and $K_{\beta 5}$ x-ray fluorescence, *Nucl. Instrum. Meth. B*, **199**, 391–395, 2003.

[Sau95] J. E. Sauvageau, C. J. Burroughs, P. A. A. Booi, M. W. Cromar, S. P. Benz, and J. A. Koch, Superconducting Integrated Circuit Fabrication With Low Temperature ECR-Based PECVD SiO_2 Dielectric Films, *IEEE Trans. Appl. Supercond.*, **5**(2), 2303–2309, 1995.

[Sch63] J. R. Schrieffer and J. W. Wilkins, Two-particle tunneling processes between superconductors, *Phys. Rev. Lett.*, **10**(1), 17–20, 1963.

[Sch00] J. Schönefeld, Entwicklung eines mikrostrukturierten magnetischen Tieftemperaturkalorimeters zum hochauflösenden Nachweis von einzelnen Röntgenquanten, PhD Thesis, Kirchhoff-Institut für Physik, Universität Heidelberg, 2000.

[Sch07] S. Schäfer, Development of a Fully Microfabricated Two Pixel Magnetic Calorimeter, Diploma Thesis, Universität Heidelberg, 2007.

[Sch12] S. Schäfer, Entwicklung einer Detektorzeile aus metallischen magnetischen Kalorimetern zur hochauflösenden Röntgenspektroskopie an hochgeladenen Ionen, PhD Thesis, Kirchhoff-Institut für Physik, Universität Heidelberg, 2012.

[Sch19] C. Schötz, PolarmaXs: hochauflösendes, polarisationssensitives Röntgenspektrometer basierend auf magnetischen Mikrokalorimetern, PhD Thesis, Universität Heidelberg, 2019.

[Sco85] J. H. Scofield and W. W. Webb, Resistance Fluctuations Due to Hydrogen Diffusion in Niobium Thin Films, *Phys. Rev. Lett*, **54**(353), 1985.

[See17] J. F. Seely, L. T. Hudson, A. Henins, and U. Feldman, X-ray spectrometer having 12000 resolving power at 8 keV energy, *Review of Scientific Instruments*, **88**, 2017.

[Ser00] A. Sergeev and V. Mitin, Electron-phonon interaction in disordered conductors: Static and vibrating scattering potentials, *Phys. Rev. B*, **61**(9), 6041–6047, 2000.

[Sha16] C. Shah, P. Amaro, R. Steinbrügge, C. Beilmann, S. Bernitt, S. Fritzsche, A. Surzhykov, J. Crespo, and S. Tashenov, Strong higher-order resonant contributions to x-ray line polarization in hot plasmas, *Physical Review E*, **93**(6), 2016.

[She83] R. Sherman and H. K. Birnbaum, Hydrogen permeation and diffusion in niobium, *Metallurgical and Materials Transactions A*, **14**(1), 203–210, 1983.

[Sim35] F. Simon, Application of Low Temperature Calorimetry to Radioactive Measurements, *Nature*, **135**, 763–763, 1935.

[Sjö75] M. Sjöstrand and G. M. Seidel, Hyperfine resonance properties of Er^{3+} in Au, *Physical Review B*, **11**, 3292–3297, 1975.

[Smi12] S. J. Smith, J. S. Adams, C. N. Bailey, S. R. Bandler, M. E. Chervenak, J. A.and Eckart, F. M. Finkbeiner, R. L. Kelley, F. S. Kilbourne, C. A.and Porter, and J. E. Sadleir, Small pitch transition-edge sensors with broadband high spectral resolution for solar physics, *Journal of Low Temperature Physics*, **167**(3), 168–175, 2012.

[Smi20] S. J. Smith et al., Towards 100,000-Pixel Microcalorimeter Arrays Using Multi-absorber Transition-Edge Sensors, *Journal of Low Temperature Physics*, **199**, 330–338, 2020.

[Spa00] F. Spaepen, Interfaces and stresses in thin films, *Acta Materialia*, 2000.

[Stä18] C. Ständer, Aufbau und Vergleich von zwei kreuzkorrelirten, stromsensitiven Rauschthermometern für tiefe Temperaturen, Bachelor Thesis, Heidelberg University, 2018.

[Ste68] W. C. Stewart, Current-voltage characteristics of josephson junctions, *Applied Physics Letters*, **12**(8), 277–280, 1968.

[Ste83] S. A. Steward, Review of Hydrogen Isotope Permeability Through Materials, Technical Report UCRL-53441, Lawrence Livermore National Lab, Livermore, CA (United States), 1983.

[Sto05] R. Stolz, V. Zakosarenko, L. Fritzsch, H.-G. Meyer, A. Fleischmann, and C. Enss, SQUID-gradiometers for arrays of integrated low temperature magnetic micro-calorimeters, *IEEE Transactions on Applied Superconductivity*, **15**(2), 773–776, 2005.

[Tan04] I. Tanaeva, Low-temperature cryocooling, PhD Thesis, Technical University Eindhoven, 2004.

[Tao71] L. J. Tao, D. Davidov, R. Orbach, and E. P. Chock, Hyperfine Splitting of Er and Yb Resonances in Au: A Separation between the Atomic and Covalent Contributions to the Exchange Integral, *Phys. Rev. B*, **4**, 5–9, 1971.

[Tay63] B. N. Taylor and E. Burstein, Excess currents in electron tunneling between superconductors, *Phys. Rev. Lett.*, **10**(1), 14–17, 1963.

[Tes77] C. D. Tesche and J. Clarke, dc SQUID: Noise and optimization, *J. Low Temp. Phys.*, **29**(3), 301–331, 1977.

[Tol09] S. K. Tolpygo and D. Amparo, Fabrication process-induced variations of Nb/Al-AlO$_x$/Nb Josephson junctions in superconductor integrated circuits, *Superconductor Science and Technology*, **23**(3), 2009.

[Tol11] S. K. Tolpygo, D. Amparo, R. T. Hunt, J. A. Vivalda, and D. T. Yohannes, Diffusion Stop-Layers for Superconducting Integrated Circuits and Qubits with Nb-based Josephson Junctions, *IEEE Transactions on Applied Superconductivity*, **21**(3), 119–125, 2011.

[Tsu93] K. Tsukada, J. Kawai, G. Uehara, and H. Kado, Relationship of Nb surface morphology and Al coverage to the intrinsic stress of magnetron-sputtered Nb films, *IEEE Transactions on Applied Superconductivity*, **3**(1), 2944–2946, 1993.

[Ula15] I. B. Ulanosvskiy, Hydrogen Diffusion and Porosity Formation in Aluminium, PhD Thesis, Ministry of Education and Science of the Russian Federation, National University of Science and Technology, 2015.

[Vai04] J. Vaillancourt, C. Allen, R. Brekosky, A. Dosaj, M. Galeazzi, R. Kelley, D. Liu, D. McCammon, F. Porter, L. Rocks, W. Sanders, and C. Stahle, Large area bismuth absorbers for x-ray microcalorimeters, *Nucl. Instr. Meth. Phys. Res. A*, **520**(1–3), 212 – 215, 2004, Proceedings of the 10th International Workshop on Low Temperature Detectors.

[Vel19] C. Velte et al., High-resolution and low-background ^{163}Ho spectrum: interpretation of the resonance tails, *The European Physical Journal C*, **79**(1026), 2019.

[Wan15] H. Wang, C. Shi, J. Hu, S. Han, C. C. Yu, and R. Q. Wu, Candidate Source of Flux Noise in SQUIDs: Adsorbed Oxygen Molecules, *Phys. Rev. Lett.*, **115**(077002), 2015.

[Wan17] Z. Wang, Development of Sputtering Process for High Quality Nb Thin Film, PhD Thesis, ETH Zurich, 2017.

[Weg18] M. Wegner, Entwicklung, Herstellung und Charakterisierung eines auf metallischen magnetischen Kalorimetern basierenden Detektorarrays mit 64 Pixeln und integriertem Mikrowellen-SQUID-Multiplexer, PhD Thesis, Universität Heidelberg, 2018.

[Wei96] H. Weinstock (Ed.), SQUID Sensors: Fundamentals, Fabrication and Applications, Springer-Science+Business Media, B.V., 1996.

[Wel77] J. M. Welter and F. J. Johnen, Superconducting transition temperature and low temperature resistivity in the niobium-hydrogen system, *Zeitschrift für Physik B Condensed Matter*, **27**, 227–232, 1977.

[Wel84] F. Wellstood, C. Heiden, and J. Clarke, Integrated dc SQUID magnetometer with a high slew rate, *Review of Scientific Instruments*, **55**(952), 1984.

[Wel87] F. C. Wellstood, C. Urbina, and J. Clarke, Low-frequency noise in dc superconducting quantum interference devices below 1 K, *Appl. Phys. Lett.*, **50**, 772, 1987.

[Wel94] F. C. Wellstood, C. Urbina, and J. Clarke, Hot-electron effects in metals, *Phys. Rev. B,*, **49**, 5942–5955, 1994.

[Wil69] G. Williams and L. L. Hirst, Crystal-field effects in solid solutions of rare earths in noble metals, *Phys. Rev.*, **185**, 407–415, 1969.

[Wu79] C. T. Wu, Intrinsic Stress of Megnetron-Sputtered Niobium Films, *Thin Solid Films*, 1979.

[Xu11] Q.-Y. Xu, C. H. Cao, M.-Y. Li, Y. Jiang, S.-T. Zha, L. Kang, W.-W. Xu, J. Chen, and P.-H. Wu, Fabrication of High-Quality Niobium Superconducting Tunnel Junctions, *CHIN. PHYS. LETT*, **28**(8), 2011.

[Yam94] H. Yamamori, T. Miura, A. Fujimaki, Y. Takai, and H. Hayakawa, Study on the transition width at gap voltage caused by the proximity effect in Nb-based Josephson junctions, *Supercond. Sci. Technol.*, **7**(5), 284–286, 1994.

[You98] G. A. Young and J. R. Scully, The diffusion and trapping of hydrogen in high purity aluminum, *Acta Mater.*, **46**, 6337–6349, 1998.

[Zak03] V. Zakosarenko, R. Stolz, L. Fritzsch, H.-G. Meyer, A. Fleischmann, and C. Enss, Squid gradiometer for ultra-low temperature magnetic microcalorimeter, *Superconductor Science and Technology*, **16**(12), 1404–1407, 2003.

[Zeh99] A. Zehnder, P. Lerch, S. P. Zhao, T. Nussbaumer, E. C. Kirk, and H. R. Ott, Proximity effects in Nb/Al-AlO$_x$/Nb superconducting tunneling junctions, *Phys. Rev. B.*, **59**, 1999.

[Zim18] F. Zimmerer, Beurteilung der Qualität vonNb/Al-AlO$_x$/Nb-Josephson-Kontakten und Charakterisierung des Herstellungsprozesses von Nb/Al-AlO$_x$/Nb-Dreischichtstrukturen, Bachelor Thesis, Universität Heidelberg, 2018.

[Zin06] B. L. Zink, K. D. Irwin, G. C. Hamilton, J. N. Ullom, and D. P. Pappas, Erbium-doped gold sensor films for magnetic microcalorimeter x-ray detectors, *Journal of Applied Physics*, **99**(8), 2006.

Ich erkläre hiermit, dass ich die vorgelegte Dissertation selbständig verfasst und dabei keine anderen als die angegebenen Quellen und Hilfsmittel verwendet habe.

Heidelberg, den 27.04.2020 ....

(Matthäus Krantz)